ELECTROMAGNETIC NON-DESTRUCTIVE EVALUATION XXIII

Editors:
G.Y. Tian and B. Gao

Electromagnetic Non-Destructive Evaluation XXIII

Electromagnetic Non-destructive Evaluation (ENDE) is an invaluable, non-invasive diagnostic tool for the inspection, testing, evaluation and characterization of materials and structures. It has now become indispensible in a number of diverse fields ranging from biomedics to many branches of industry and engineering.

This book presents the proceedings of the 24th International Workshop on Electromagnetic Nondestructive Evaluation, held in Chengdu, China from 11 - 14 September 2019. The 38 peer-reviewed and extended contributions included here were selected from 45 original submissions, and are divided into 7 sections: eddy current testing and evaluation; advanced sensors; analytical and numerical modeling; material characterization; inverse problem and signal processing; artificial intelligence in ENDE; and industrial applications of ENDE. The papers cover recent studies concerning the progress and application of electromagnetic (EM) fields in the non-destructive examination of materials and structures, and topics covered include evaluations at a micro-structural level, such as correlating the magnetic properties of a material with its grain structure, and a macroscopic level, such as techniques and applications for EM NDT&E. Recent developments and emerging materials such as advanced EM sensors, multi-physics NDT&E, intelligent data management and maintaining the integrity of structures are also explored.

The book provides a current overview of developments in ENDE, and will be of interest to all those working in the field.

ELECTROMAGNETIC NON-DESTRUCTIVE EVALUATION (XXIII)

Studies in Applied Electromagnetics and Mechanics

Series Editors: K. Miya, A.J. Moses, Y. Uchikawa, A. Bossavit, R. Collins, T. Honma, G.A. Maugin, F.C. Moon, G. Rubinacci, H. Troger and S.-A. Zhou

Volume 45

Previously published in this series:

Volumes 1–6 were published by Elsevier Science under the series title "Elsevier Studies in Applied Electromagnetics in Materials".

Electromagnetic Non-Destructive Evaluation (XXIII)

Edited by

Guiyun Tian

and

Bin Gao

University of Electronic Science and Technology of China, China &
Newcastle University, United Kingdom

LEGAL NOTICE

The publisher is not responsible for the use which might be made of the following information.

PRINTED IN THE NETHERLANDS

Preface

The 24th International Workshop on Electromagnetic Nondestructive Evaluation (ENDE2019) was held on September 11 to 14, 2019 at the Longemont Hotels in Chengdu, China. The workshop was organized by the University of Electronic Science and Technology of China (UESTC) and co-organized by Southwest Jiaotong University and Sichuan University. A total of 146 registered participants from 15 countries worldwide in the field of nondestructive evaluation attended the workshop.

ENDE 2019 aims to bring together engineers and scientists active in the research, development, and industrial application of Electromagnetic Nondestructive Evaluation (ENDE). It provided participants with a fantastic opportunity to exchange ideas and update on the latest developments. This year's technical sessions, poster competitions and special ENDE events focused on theoretical and applied research on ENDE methods. A total of 127 contributed technical presentations were organized into two poster sessions plus eight oral sessions covering topics on (i) QNDE and AI in ENDE and systems, (ii) ENDE sensors and numerical modelling, (iii) Analytical and numerical modelling, (iv) ENDE application, (v) ENDE application for high-speed railway, (vi) Material characterization, (vii) Inverse problems and signal processing. Through a range of technical and social activities, ENDE 2019 offered all the participants a unique opportunity to interact with the world's leading experts in electromagnetic NDE from academia, industry, and government.

Prof. Guiyun Tian, the general chair of ENDE 2019, welcomed all the attendees to the workshop and provided introductory remarks to open the workshop. The technical program commenced with two keynote speeches: (i) "Electromagnetic NDE Techniques for Inspecting Composite Materials and Additively Manufactured Components" by Prof. Satish Udpa, IEEE fellow, Michigan State University, United States; (ii) "R&D of NDT Technologies for Nuclear Power Plant and Applications" by Prof. Yong Nie, Deputy Chief Engineer, China Nuclear Power Operation Technology Corporation Ltd., CNNC, China. Three distinguished speakers from eddy current nondestructive evaluation, healthcare, and flexible tactile sensors were invited to discuss challenges confronting them and the ways in which NDE can assist in addressing these issues. An invited talk entitled "Adaptive Cross Approximations for Eddy Current Nondestructive Evaluations" was given by Prof. Jiming Song from the Department of Electrical and Computer Engineering, Iowa State University, Ames, Iowa, USA, introducing the formulation of eddy current problem using the Boundary Element Method (BEM). Another invited talk entitled "Translating Engineering to Healthcare" was given by Dr. James Avery from the Department of Surgery and Cancer, St Mary's Hospital Imperial College, UK, discussing the electromagnetic sensing and imaging from a biomedical perspective, from tracking surgical tools, medical robotics, implantable sensors, neuroscience, tomographic imaging and spectroscopy; the third invited talk entitled "Flexible tactile sensors based on patterned nanostructures of graphene and 2D materials" was given by Prof. Pingan Hu from the School of Materials Science and Engineering Harbin Institute of Technology (HIT), Harbin, China, presenting the development of highly sensitive and conformal pressures sensors for any curved surface using two dimensional (2D) nanomaterials.

The 24th book, following ENDE 2019, is proposed herein, as an Open Access publication on the IOS Press Ebooks platform, including 38 peer-reviewed extended contributions from the original 45 submissions. This suite of book covers recent studies concerning the progress and applications of Electromagnetic (EM) fields to non-destructively inspect, test, evaluate, and characterize materials and structures. More specific paper topics cover from micro-structural levels, such as correlating the magnetic properties of a material with its grain structure, to macroscopic ones, such as techniques for EM NDT&E and applications. Recent developments of emerging materials such as advanced EM sensors, multi-physics NDT&E, intelligent data management and maintaining the integrity of structures with material characterization, natural defects are included as well.

To conclude, the organizers would like to thank all members of the International Standing Committee, who provided much guidance and support through their successful ENDE experiences in past years. We also gratefully acknowledge the support of all reviewers of extended papers who have played a key role in the making of these proceedings, and Dr Yan Yan and Mr Kun Zeng for the help of editing this book. Lastly, we acknowledge the hard work of student volunteers, whose dedication and interactions with all ENDE participants ensured the smooth and successful operation of the ENDE2019 Workshop and the book preparation.

<div align="right">

University of
Electronic Science and Technology of China
Guiyun Tian
General Chair, ENDE 2019
Bin Gao
Co-Editor

</div>

ENDE 2019 – Chengdu, China Conference Organization

The 24th International Workshop on Electromagnetic Nondestructive Evaluation was held on September 11 to 14, 2019 at the Longemont Hotels in Chengdu, China.

Organized by University of Electronic Science and Technology of China

Co-organized by Southwest Jiaotong University and Sichuan University

Sponsored by National Natural Science Foundation of China, Newcastle University, The Chinese society of Nondestructive testing, State Key Laboratory for Strength and Vibration of Mechanical Structure, National Sensor Engineering Research Center and International Scientific Corporation Center for Nondestructive Detection, Guangzhou Doppler Electronic Technology Co., Ltd, International Scientific Cooperation Research Center for Nondestructive Detection.

Local Organizing Committee

General Chairman:
GuiYun Tian *University of Electronic Science and Technology of China/Newcastle University*, *UK*

Co-Chairs:
Zhenmao Chen, *Xi'an Jiaotong University, China*
Junming Lin, *Eddysun Electronic Corp, China*
Tianpeng Qiang, *Special Equipment Safety Supervision Inspection Institute of Jiangsu, China*
Xiaorong Gao, *Southwest Jiaotong University, China*

Members:
Bin Gao, *University of Electronic Science and Technology of China, China*
Jianping Peng, *Southwest Jiaotong University, China*
Jianbo Wu, *Sichuan University, China*
Yu Zhang, *Southwest Jiaotong University*, China
Yong Li, *Xi'an Jiaotong University, China*
Shejuan Xie, *Xi'an Jiaotong University, China*
Yunze He, *Hunan University, China*
Hong Zhang, *Fuqing Branch of Fujian Normal University, China*
Mengbao Fan, *China University of Mining and Technology, China*
Deqiang Zhou, *Jiangnan University, China*
Jincheng Zhao, *Eddysun Electronic Corp, China*
Qiuji Yi, *Newcastle University, United Kingdom*
Ying Yin, *Special Equipment Safety Supervision Inspection Institute of Sichuan, China*
Kai Zheng, *Special Equipment Safety Supervision Inspection Institute of Jiangsu, China*
Yunlai Gao, *Beijing Aeronautical Science &Technology Research Institute, COMAC, China*

List of Reviewers

(Alphabetical order)
Junaid Ahmed, *University of Electronic Science and Technology of China, China*
Libin Bai, *University of Electronic Science and Technology of China, China*
Sandor Bilicz, *Budapest University of Technology and Economics, Hungary*
Zhichao Cai, *East China Jiaotong University, China*
Klara Capova, *University of Zilina, Slovakia*
Tomasz Chady, *West Pomeranian University of Technology, Poland*
Zhenmao Chen, *Xi'an Jiaotong University, China*
Francesco Ciampa, *University of Surrey, UK*
Stephen Dankwa, *University of Electronic Science and Technology of China, China*
Yiming Deng, *Michigan State University, USA*
Xavier Dérobert, *Institut français des sciences et technologies des transports, France*
Mengbao Fan, *China University of Mining and Technology, China*
Bin Gao, *University of Electronic Science and Technology of China, China*
Louvain Georadar, *Austrian Institute of Technology, Austria*
Fasheng Qiu, *Nanchang Hangkong University, China*
Yunze He, *Hunan University, China*
Pan Hu, *Nanjing University of Aeronautics and Astronautics, China*
Sebastien Lambot, *FNRS Research Director Faculty of Bioscience Engineering & Earth and Life Institute, Belgium*
Jakob Juul Larsen, *Aarhus University, Denmark*
Stefano Laureti, *Università degli Studi di Perugia, Italy*
Jinyi Lee, *Chosun University, South Korea*
Dominique Lesselier, *Laboratoire des Signaux et Systèmes, France*
Changyou Li, *Northwestern Polytechnical University, China*
Yong Li, *Xi'an Jiaotong University, China*
Helena Geirinhas Ramos, *Instituto Superior Técnico Lisboa, Portugal*
B. Purna Chandra Rao, *Indira Gandhi Centre for Atomic Research, India*
Christophe Reboud, *CEA LIST, France*
Joerg Schotter, *Austrian Institute of Technology, Austria*
Sung-Jin Song, *Sungkyunkwan University, South Korea*
Ruslee Sutthaweeku, *King Mongkut's University of Technology North Bangkok, Thailand*
Klaus Szielasko, *Fraunhofer-Institutfür Zerstörungsfreie Prüfverfahren (IZFP), Germany*
Frédéric Taillade, *Électricité de France, France*
Toshiyuki Takagi, *Tohoku University, Japan*
Jianbo Wu, *Sichuan University, China*
Suixian Yang, *Sichuan University, China*
Yan Yan, *University of Electronic Science and Technology of China, China*
Norita Yusa, *Tohoku University, Japan*
Qing Zhang, *Nanjing University of Aeronautics and Astronautics, China*
Hai Zhang, *University of Laval, Canada*

This page intentionally left blank

The 24th International Workshop on Electromagnetic Nondestructive Evaluation
第 2 4 届 国 际 电 磁 无 损 评 估 研 讨 会
Bridging Micro&Macro，Safety of the World. 从微识宏，知构安然。

ENDE2019
Chengdu.2019

2019.9.12

ix.

This page intentionally left blank

Contents

Analytical and Numerical Modelling

Material Characterization

Inverse Problem and Signal Processing

Artificial Intelligence in ENDE

Eddy Current Testing and Evaluation

This page intentionally left blank

Study on Effect of Electromagnetic Characteristics of Deformed 304 Stainless Steel on Eddy Current Testing

Benli Wan [a,b], Bin Hu [b,1], Yuntao Li [b] and Yuhong Zhu [b]

[a] *School of Automation Science and Electrical Engineering, Beihang University, Beijing, China*

[b] *China Special Equipment Inspection and Research Institute, Beijing, China*

Abstract. The induced ferrite and other high magnetic microstructures content changes are studied when 304 austenitic stainless steel stripe specimens are tested under different uniaxial tension deformation, namely its deformation less than 50%. Furtherly, the correlation is plotted between the resulting magnetic permeability or coercivity caused by these microstructures and deformation. Meanwhile, the optimal eddy current excitation frequency under different deformation was obtained, which was consistent with 3-D finite element analysis (FEA). Besides, other various factors affecting the quality of eddy current testing (ECT), such as temperature and conductivity, are also considered comprehensively during the tensile test. The results of the experiment and simulation calculation show that when the deformation is within 50% that necking deformation has occurred, the magnetic permeability of specimens increases with deformation, and gradually begin to have the magnetic properties of weak ferromagnetic materials, which also changes the optimal excitation frequency, which varies from 60 kHz to 110 kHz. Because of the electromagnetic response noise increase, the impedance plane diagrams of defects distort simultaneously, which leads to the quantitative evaluation error of defects.

Keywords. 304 austenitic stainless steel, deformation, eddy current testing, the optimal frequency

1. Introduction

304 austenitic stainless steel is widely used in different branches of the industry, covering from daily life to complex industries (chemical, oil, nuclear, etc.).[1] However, due to its structural characteristics, the typical failure mode of this type of stainless steel is stress corrosion cracking (SCC), which often occurs on the surface of the component and is very suitable for ECT. Meanwhile, these steels may become ferromagnetic when the martensite phase is produced by cold work deformation, hydrogen charging, or ion irradiation. [2] Cold working deformation is ubiquitous in the service of industrial equipment. It changes the electrical and magnetic properties of 304 stainless steel, especially the magnetic properties, which affect the implementation of ECT. Therefore, it is essential to study the effect of deformation on ECT for the safety of industrial equipment made of 304 stainless steel.

---

[1] Corresponding Author, 2 Buliding Xiyuan Hepingjie, Chaoyang District Beijing, China. E-mail: hubin@csei.org.cn.

S. H. Khan [3] pointed out in his research that austenite transformation results in changes in electromagnetic properties of the material, causing variation in eddy current impedance, but didn't make a profound study. Maher Shaira [4] used eddy current probes for local measurements that were proved to be sensitive to austenite transformation and even quantitatively after calibration. A Lois [5] developed a standard curve for ECT of martensitic magnetic structure content for 304 austenitic stainless steel, but it is not clear how to select the permeability. In practice, Li Xiaoting [6] found that the best frequency of ECT for stainless steel pressure vessel was 100 kHz, but the effect of phase transformation was not taken into account.

In this paper, the relative content of micromagnetic structure after austenite transformation at different stretching stages and the change of magnetic properties of specimens are measured by experiments. On this basis, the optimal frequency of ECT for 304 stainless steel surface cracks under two typical deformation conditions was calculated by the 3-D FEA method. Furthermore, the optimal frequency under different deformation is also obtained by experiments, which is in agreement with the simulation results. Finally, the source of magnetic noise affecting ECT and the mechanism are analyzed preliminarily. The above research is expected to guide stainless steel inspection.

2. Specimens processing and measurement

Two sets of 304 stainless steel strip specimens were prepared. One group was used to measure magnetic properties, and the other group was used to fabricate artificial grooves (representing crack-like defects). EDM processed the surface opening grooves located in the middle of each specimen after specified deformation, and their sizes were all 0.2×1×15mm, as illustrated in Figure 1.
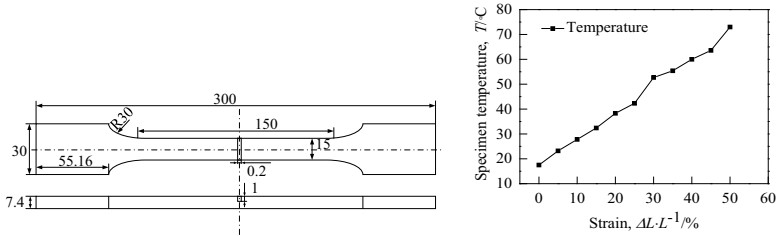
Figure 1. Specimens with grooves (unit mm). **Figure 2.** Temperature variation of specimens with deformation.

The specimens are stretched at a rate of 60 mm/min, and the ambient temperature is 17.5°C. Because these become hot during the stretching process, the temperature variation curve of the specimens under different stretching ratios in the actual test process is as shown in Figure 2. When the maximum deformation is 50%, the temperature is 73°C. A slow process of deformation occurring during the operation of actual industrial equipment can be considered that the temperature does not change.

2.1. Measurement of electromagnetic characteristics

All specimens tested are from the same batch of raw materials, using the same heat-treatment process. The total content of ferrite and martensite in standard 304 stainless steel after reliable solution treatment is generally less than 3%, measured by Fischer

FERITSCOPE FMP30, according to the magnetic induction method. The content of the magnetic microstructure at different deformation stages corresponded to Figure 3. The average error of two sets of specimens was less than 5% to ensure repeatability. Indirectly, the measured electromagnetic properties of reference specimens were considered the same as defective specimens. The experimental device can refer to the previous work[8].

(a) Magnetic properties variation.   (b) Conductivity variation.
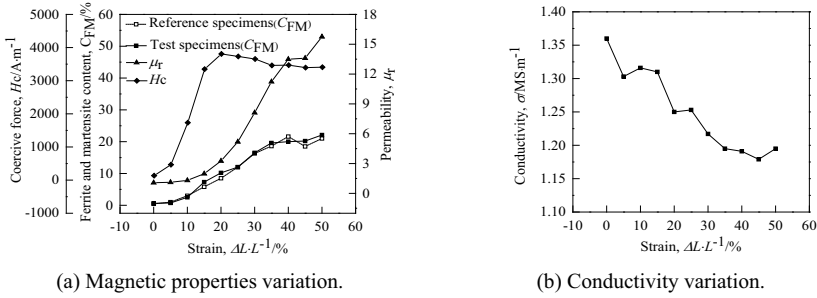
Figure 3. Electromagnetic characteristics variation with deformation.

2.2. Test results analysis

The measurement results from Figure 3 show that the surface conductivity measured by the four-probe method decreases with deformation, and the maximum change is 13%, which is little effect on eddy current distribution compared with permeability variation. The permeability and coercivity measured by FE-2100SD [8] increase during plastic deformation, as illustrated in Figure 3. Non-ferromagnetic 304 stainless steel begins to possess some magnetic properties of weakly ferromagnetic materials because of deformation. When the deformation reaches 15%, permeability increases significantly, and there is even hysteresis. These changes inevitably affect eddy current distribution in the specimen, such as detectable depth reduction at the same frequency and higher magnetic noise. Besides, it also causes a change in the optimum detection frequency.

3. Finite element simulation

The electromagnetic parameters of materials in two critical stages of deformation are selected for FEA. One is the deformation of 15%, and stress has exceeded the yield limit; the other is the deformation of 35% when the uniform deformation stage of specimens is terminated. There are key points that affect the eddy current distribution of specimens.

Table 1. Simulation parameters

Coil parameters					Flat specimen material			
Inner radius	Outer radius	Height	Interval	Turns	Strain	Permeability		Electrical conductivity
						Initial	Maximum	
r_1/mm	r_2/mm	h/mm	d/mm	n	$\Delta L \cdot L^{-1}$/%	μ_i	μ_m	σ/MS·m^{-1}
0.500	1.25	1.00	1.00	150	15	1.397	1.974	1.310
					35	3.274	11.230	1.195

When the differential eddy current probe is used, the plate specimen, size 61×22×6mm, is large enough to cause no edge effect. However, the defect size in the 3-D FEA model is quite small, and the other model size is massive, which leads to too large tolerance in mesh generation to be solved accurately or even not convergent. Air,

specimen and coil part can be meshed reasonably by using the interpolation moving boundary method [7]. In this way, the lift-off layer can be meshed effectively, as showed in Figure 4.

(a) FEA mesh   (b) FEA model
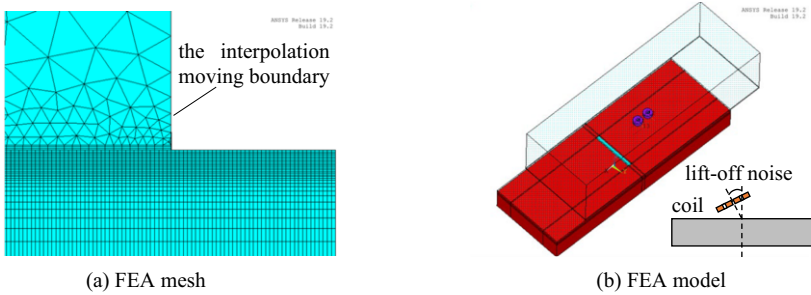
Figure 4. Simulation model and mesh.

Because the primary interference of differential probe is the probe tilt, it is necessary to calculate the coil impedance phase caused by the probe tilt and the coil impedance caused by defects at different frequencies in the simulation calculation. Since the detection frequency of 304 stainless steel without deformation is 100 kHz, 60 kHz~110 kHz is chosen as the frequency range of simulation calculation, and simulation parameters can be obtained from Table 1. The magnetic field produced by the coil is fragile; the initial permeability obtained from the test is substituted into the calculation.

From Figure 5, it can be seen that the amplitude of the lift-off signal may be much larger than that of defect signal when the probe tilt angle is large. The phase difference should be as significant as possible in the range of 0° to 90° as a reference to optimal frequency selection. According to the above principles, the following conclusions can be drawn. When the deformation is 15%, the optimal frequency is 60 kHz, and the phase difference is about 40°. When the deformation is 35%, the optimal frequency is 70 kHz, and the phase difference is about 80°.

(a) Impedance plane at 70kHz   (b) Phase difference at different frequencies
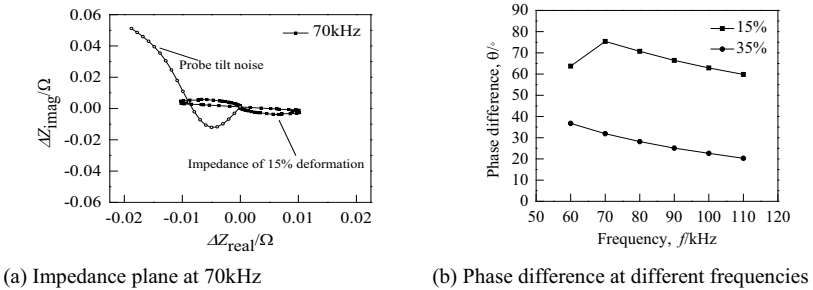
Figure 5. Impedance analysis under 15% and 35% deformation.

4. Result

The optimal frequency is not entirely determined by the phase difference but also related to other factors such as impedance amplitude and detection sensitivity. Further experimental analysis is made to consider as many factors as possible, affecting ECT. Before a 5% deformation, the phase difference does not change much between different

frequencies, roughly between 10° and 20°. When the deformation is between 10% and 35%, the phase difference varies greatly, and the optimal frequencies range from 60 kHz to 110 kHz, as illustrated in Figure 6. The results are consistent with the theoretical calculation [8]. When the deformation exceeds 35%, the optimal frequencies approach 110 kHz and do not change much. The impedance amplitude increases with the deformation, which has similar trends at different frequencies, as illustrated in Figure 7.
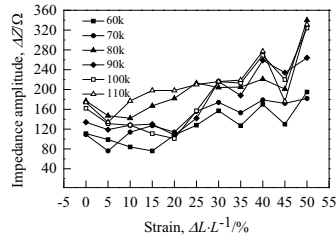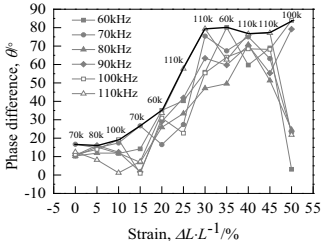
Figure 6. Phase different variation by experiment   **Figure 7.** Impedance amplitude variation by experiment

It can be concluded that if the optimal frequency is selected according to the phase difference, there is a certain correlation between the stress-strain curve of 304 stainless steel and the coercivity variation rule under different deformation. If it is selected according to amplitude, it is related to the change rule of the micromagnetic structure or its permeability under different deformation. The region with the greatest change in the optimal frequency occurs in the plastic uniform variation region corresponding to the yield point and the tensile strength. If some areas of in-service equipment are just at this stage, eddy current exciting frequency should be carefully selected.
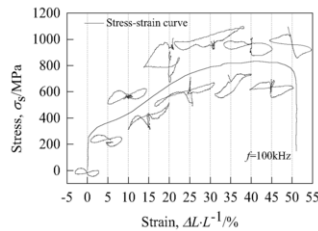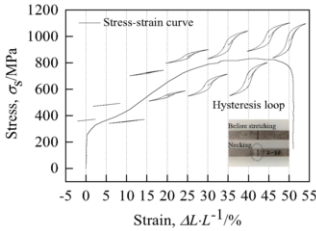
Figure 8. Hysteresis variation with deformation   **Figure 9.** Impedance plane diagrams with deformation

The magnetic properties are not only characterized by permeability, but also by hysteresis loops. It can be seen from Figure 8 that the area of the hysteresis loop increases gradually along the stress-strain curve. The magnetic noise of the probe is not only caused by the inhomogeneous permeability of the tested material but also affected by the hysteresis loop. It is considered that the micromagnetic structure is homogeneous under uniaxial tensile strain, so the magnetic noise is mainly related to the different working points of the hysteresis loop. Usually, this noise is reduced by magnetic saturation.

From Figure 9, it can be seen that the area with the greatest magnetic noise is the deformation range corresponding to the yield point to the tensile strength. Thus, the changes of real and imaginary parts of impedance (voltage in the device) with 15% deformation are studied separately. It can be found that the distance between the peak value and its value in the real part of the impedance varies slightly, but the shape remains unchanged. The imaginary part of impedance varies greatly; not only the amplitude and position of peak value change, but also it has a small additional range of variation

compared with the specimen without deformation from Figure 10. It can be concluded that the influence of micromagnetic structure on defect detection is mainly caused by the influence of coil impedance imaginary part after 304 stainless steel deformation.

(a) Real part   (b) Imaginary part
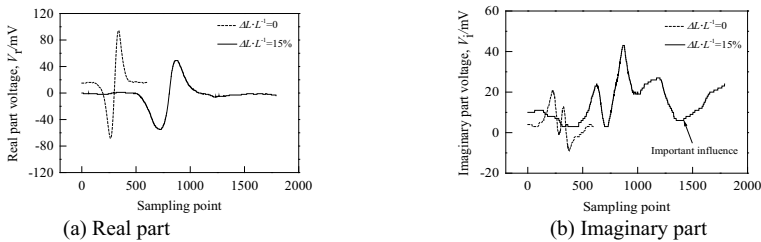
Figure 10. Change of coil inductance by deformation

5. Conclusion

In the process of ECT of industrial equipment made of 304 stainless steel in service for a long time, the high magnetic microstructures by deformation have a dominant effect on the eddy current coil impedance imaginary part, which leads to the distortion of impedance plane of defects and its quantitative evaluation error. Besides, the optimal detection frequency should be selected in the range of 60 kHz~110 kHz according to the ferrite content measured at that time or obtained by multiple ECT experiments in this range. The quantitative evaluation of 304 stainless steel defects under inhomogeneous tension will be further studied in the future.

Acknowledgments

References

[1] El Wahabi M. Caracterización termomecánica de aceros inoxidables austeníticos AISI-304[M]. Universitat Politècnica de Catalunya, 2003.
[2] Tavares S S M, Silva M R D, Neto J M, et al. Ferromagnetic properties of cold rolled AISI 304L steel[J]. Journal of Magnetism and Magnetic Materials, 2002, 242(4):1391-1394.
[3] Khan S H, Ali F, Khan A N, et al. Eddy current detection of changes in stainless steel after cold reduction[J]. Computational Materials Science, 2008, 43(4): 623-628.
[4] Shaira M, Guy P, Courbon J, et al. Monitoring of martensitic transformation in austenitic stainless steel 304 L by eddy currents[J]. Research in Nondestructive Evaluation, 2010, 21(2): 112-126.
[5] Lois A, Ruch M. Assessment of martensite content in austenitic stainless steel specimens by eddy current testing[J]. Insight-Non-Destructive Testing and Condition Monitoring, 2006, 48(1): 26-29.
[6] Xiaoting Li, Gongtian Sheng. Nondestructive testing of pressure vessels: eddy current testing technique [J]. NDT, 2004, 26(8): 411-416.
[7] Yutian Sun, Ming Yang. The moving problem in the dynamic fem of electric machines[J]. Large electric machine and hydraulic turbine, 1997(06):35-39.
[8] Benli Wan, Bin Hu, Yuntao Li. Simulation research on selection of ECT frequency[J]. Failure Analysis and Prevention, 2013, 8(05): 269-273.

Eddy Current Testing of the Lightning Strike Protection Layer in Aerospace Composite Structures

Bo FENG [a,1], Dario J. PASADAS[a], Artur L. RIBEIRO[a] and Helena G. RAMOS[a]

[a] *Instituto de Telecomunicações, Instituto Superior Técnico, Universidade de Lisboa, Lisbon, Portugal*

Abstract. The lightning strike protection layer, which is a mesh of metal stripes, is adhered to composite materials to dissipate the huge current induced during lightning strike. This paper presents an eddy current imaging method to inspect defects in the lightning strike protection layer. A tuning method was applied to tune the resonant frequency of excitation and sensing coils and enhance the testing results. Two parameters, namely the amplitude of induced voltage in the sensing coil and the amplitude of the voltage across a sampling resistor in the excitation circuit, were used to image the defects. The results show that the image formed by sensing coil voltage is less noisy and more accurate.

Keywords. Eddy current testing, composite, lightning strike protection layer

1. Introduction

Metals, especially aluminum and titanium, were extensively used to construct aerospace structures decades ago. Since 1990s, carbon fiber reinforced polymer (CFRP) composites have been increasingly used due to its high strength-to-density ratio and resistance to corrosion. Nowadays, composites can be the major part of the aircraft. For example, the Airbus A350 XWB is made of more than 50% composites while the Airbus NH90 comprises 90% composites [1]. One of the main drawbacks of changing the aerospace structure from electrical conductive metal to semi-conducting composite is the vulnerability to lightning strike damage [2]. Lightning strikes, with current up to 200 kA, could cause fiber breakage, resin deterioration and delamination in composites. In order to protect the composite structure, a lightning strike protection layer, in the form of metal mesh, is commonly incorporated in the composite to dissipate currents [3].

The lightning strike protection layer could be damaged by huge current or corrosion and lose the ability to protect the composites. In order to guarantee its functionality, its integrity must be inspected. The purpose of this paper is to present an effective method for inspecting the breakages in the lightning strike protection layer and tries to improve the testing results.

---

[1] Corresponding Author, Bo FENG, Torre Norte Piso 11, Av. Rovisco Pais, 1, 1049-001 Lisboa, Portugal; E-mail: bofeng@tecnico.ulisboa.pt.

Eddy current testing (ECT) is an efficient technique for detecting defects. In ECT, a time-varying voltage is send to a coil to generate time-varying magnetic field. When a conductive specimen is in the proximity of the coil, eddy currents are generated in the specimen and produce a secondary magnetic field. ECT has been widely used for inspecting metals due to their high conductivity [4-6]. With the emerging of new materials in industry in recent years, researchers have tried to apply ECT to inspect low-conductive composite materials [7-9]. The lightning strike protection layer is a metal mesh incorporated into composite base, therefore, ECT can be a possible method to detect the breakages in the lightning strike protection layer. However, further analysis and experiments should be done to study the effectiveness of ECT on this new structure.

2. Materials and Methods

2.1. Samples to simulate lightning strike protection layer

The lightning strike protection layer is a mesh of metals incorporated into the composite materials. Usually, the lightning strike protection layer is adhered onto the surface of the composite. There are also different types with the lightning strike protection layer located below several composite layers. It is well known that for the eddy current testing method, defects in the surface are easier to be detected than defects in the sub-surface. Therefore, a sample with lightning strike protection layer located inside the composite was made. The lay-up of the sample is shown in Figure 1. It consists five layers of CFRP material, each layer is with thickness of 0.8 mm. Copper tapes, with thickness of 100 μm and width of 5mm, were adhered onto the surface of the third layer to simulate a section of the metal mesh.
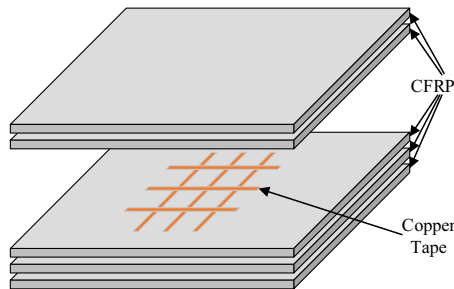
Figure 1. Lay-up of the sample.

When dissipating huge current during lightning strike, the metal mesh can be damaged due to the high temperatures attained because of Joule effect, and breakages can show up. In order to simulate the defects, the sample to be inspected was made incorporating three artificial breakages. A photo of the metal mesh described above and the defects is shown in Figure 2. The breakages were made with different width to test the resolution of the eddy current imaging system.
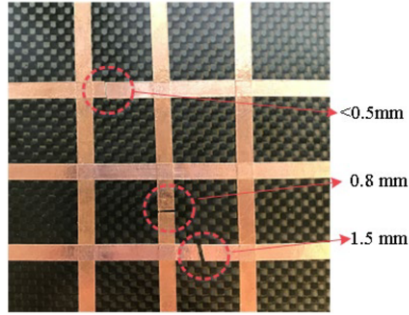
Figure 2. Artificial breakages in the sample.

2.2. Eddy current testing probe and tuning technique

The eddy current testing probe consists of an excitation coil outside and a coaxial sensing coil inside. The number of turns and dimensions of the excitation and sensing coils are listed in Table 1. As shown in Figure 3, the probe during inspection was placed above the composite sample with a lift-off of 1 mm and is fixed to a support of a two-axis positioning system.

Table 1. Specifications of excitation and sensing coils

	Excitation coil	Sensing coil
Number of turns	391	50
Height	8 mm	4 mm
Outer diameter	23 mm	4.5 mm
Inner diameter	10 mm	2 mm
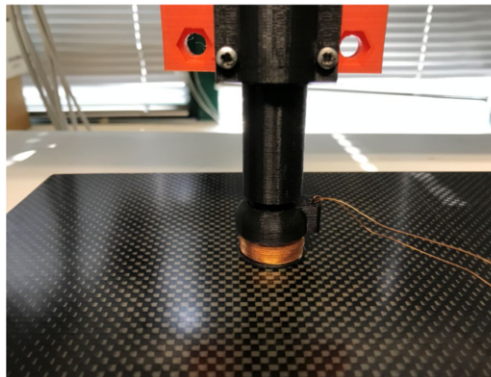
Figure 3. The eddy current testing probe.

In order to increase sensitivity, the excitation and the sensing circuits were tuned to the circuit resonant frequency. The resonant frequency of a LC circuit is given by:

$$f = \frac{1}{2\pi\sqrt{LC}} \tag{1}$$

To tune the resonant frequency to the same value of 150 kHz, the inductances of the two coils were measured when they were in air. The tuning circuits are shown in Figure 4. A capacitor of 3.9 pF was connected to the excitation coil in series to reduce the total impedance of the circuit and maximize the excitation current. A resistor of

10 Ω was also added to the excitation circuit in series as a sampling resistor to monitor the excitation current. In the sensing circuit, a capacitor of 1.5 nF was added to the sensing coil.
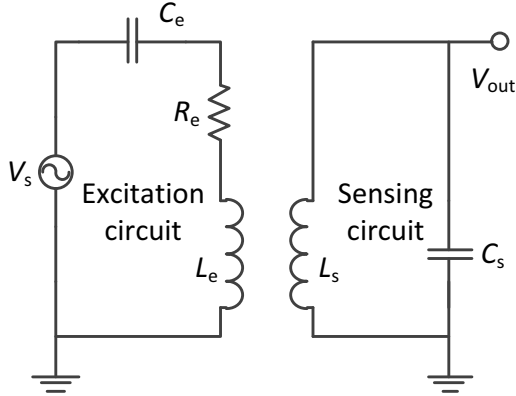
Figure 4. The tuning circuits for excitation and sensing coils.

2.3. Measurement system

A voltage with frequency of 150 kHz and peak-to-peak amplitude of 1.8 V generated by an arbitrary function generator (Tektronix AFG 3102) was amplified by a power amplifier and applied to the excitation circuit. The ECT probe was driven by a two-axis positioning system to make a scan above the sample in an area of 81 mm × 81 mm with steps of 1 mm. At each location, two quantities were acquired by an oscilloscope (Tektronix TDS5032B Digital Oscilloscope) and were send to a computer. One quantity is the peak-to-peak amplitude of the voltage across the sampling resistor in excitation circuit, which reflects the change of impedance of the excitation coil caused by the defect. The other parameter is the peak-to-peak amplitude of the sensing coil voltage, which reflects the change of secondary magnetic field.

3. Results

After the scanning, a matrix with 81 × 81 elements was obtained in each channel of the oscilloscope. Each matrix directly shows the image of the defects. However, eddy current testing signals are prone to be influenced by lift-off changes. To reduce the influence of lift-off on the scanning results, a baseline matrix was built. In the matrix of the output voltage of the sensing coil, the value obtained at the starting point was subtracted from the values at the other three corners of the scanning region. The differences were used to form a baseline matrix of 81 × 81points by interpolating linearly from the corners. The final result, which is shown in Figure 5, was obtained by subtracting the baseline matrix from the original matrix. From the ECT imaging results presented in Figure 5, it can be seen that the locations and dimensions of the copper tapes were accurately imaged, and at the junctions of two tapes, the ECT signals have larger perturbations. Furthermore, all the three breakages were successfully detected, as pointed out by the white circles. The perturbation increases with the width of the breakage. Another important detail to be noticed is the magnitude of the output voltage

is 70 V, even without amplification. The resonant technique effectively increased the output voltage.
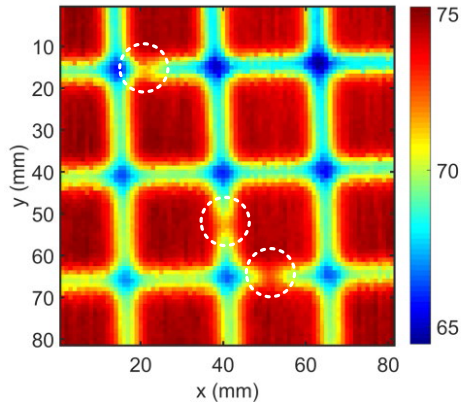
Figure 5. Output voltage of sensing coil.

The other quantity that can be used to image the defects is the voltage across the sampling resistor. The image was also adjusted to the change of lift-off by subtracting a baseline matrix. The result is shown in Figure 6. Even with baseline subtracting, the result is still noisy and severely influenced by the lift-off change. So, the defects are not able to be seen.
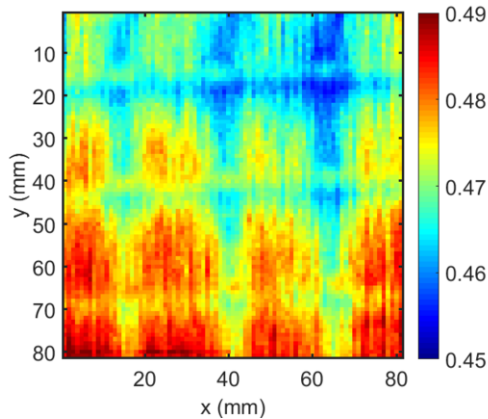
Figure 6. Voltage across sampling resistor.

4. Conclusions

This paper proposes an effective method for the inspection of breakages in the lightning strike protection layer in aerospace composite structures. An eddy current testing system with coaxial coils was used for the inspection. Both excitation and sensing circuits were tuned to the resonant frequency. This technique effectively increased the output voltage in the sensing coil. By comparing the results obtained using the output voltage at the sensing coil and the current that runs in the excitation current, it is concluded that the output voltage in the sensing coil is more suitable for imaging the defects. With the output voltage in the sensing coil, all the breakages in the sample were successfully detected even the smallest with a width of less than 0.5 mm.

References

[1]   https://www.airbus.com/newsroom/news/en/2017/02/Material-evolution.html.

[2]   T. M. Dhanya, C. S.Yerramalli, Lightning strike effect on carbon fiber reinforced composites – effect of copper mesh protection, *Materials Today Communications* **16** (2018), 124-134.

[3]   M. Gagné, D. Therriault, Lightning strike protection of composites, *Progress in Aerospace Sciences* **64** (2014), 1-16.

[4]   D. Pasadas, A. L. Ribeiro, T. Rocha, H. Ramos, 2D surface defect images applying Tikhonov regularized inversion and ECT, *NDT & E International* **80** (2016), 48 – 57.

[5]   F. Jiang, S. Liu, S. Xin, et al, Evaluation of circumferential cracks in metal tubes based on a magnetic field response model of eddy current testing, *Insight* **62** (2020), 91-97.

[6]   Y. Yu, K, Gao, B. Liu, et al, Semi-analytical method for characterization slit defects in conducting metal by Eddy current nondestructive technique, *Sensors and actuators a-physical* **301** (2020), 111739.

[7]   Z. Cai, D. Zou, C. Liu, Research on Eddy-Current Testing of Functional Polymer Composite Material, *IEEE transactions on magnetics* **54** (2018), 2501005 .

[8]   M.P. Degoeje, K. Wapenaar, Nondestructive inspection of carbon fiber-reinforced plastics using eddy-current methods, *Composites* **23** (1119), 147-157.

[9]   B. Feng, D.J. Pasadas, A.L. Ribeiro, H.G. Ramos, Locating and Imaging Impact Damage with an Integrated System of PZT and Eddy Current Probe, *in Proc. Int. Instrum. Meas. Technol. Conf.*, Auckland, New Zealand, May 2019.

15

An Eddy Current Method to Evaluate Local Wall Thinning of Carbon Steel Pipe

Shanshan SUN[a], Deqianga ZHOU[a,b,1], Noritaka YUSA[c], Haicheng SONG[c]

[a] *School of Mechanical Engineering, Jiangnan University, Jiangsu, China*
[b] *Key laboratory of nondestructive testing of Nanchang Hangkong University, China*
[c] *Department of quantum science and energy engineering, Tohoku University, Japan*

Abstract. This paper proposes to evaluate the local wall thinning of carbon steel pipe using an eddy current method. Firstly, the feature signals are determined by correlation analysis of the signals and the wall thinning sizes. Subsequently, the models for estimating the residual wall thickness rt is constructed using Gaussian process regression (GPR). Finally, the applicability of the models to the evaluation of local wall thinning is verified by simulation and experiment.

Keywords. local wall thinning, eddy current, correlation, Gaussian process regression

1. Introduction

Carbon steel pipe is widely used in industrial equipment because of their high welding ability and low price, but the wall is thinned due to flow accelerated corrosion and liquid droplet impingement [1-2]. At present, some non-destructive testing methods have been proposed, such as eddy current testing[3-6], which is an easy to implement and fast non-destructive testing technology.

This study proposes the use of eddy current method to obtain various types of signals at different frequencies to detect local wall thinning. Then the regression model for evaluating local wall thinning is established based on the correlation analysis between signals and defects. The model can evaluate the size of defects.

2. Numerical simulation

2.1. Finite element model

Numerical simulations are performed using simulation software COMSOL Multiphysics 5.2 a+ AC / DC module. The governing equation is:

$$\nabla \times (\nabla \times \mu^{-1}A) + (j\omega\sigma - \omega^2\varepsilon)A = J_e \qquad (1)$$

Where ω is angular frequency, ε is permittivity, σ is electric conductivity, μ is magnetic permeability, A is magnetic vector potential .The conductivity and relative permeability of the pipe are 5.2 Ms/m, 160, respectively. The current density J_e of the excitation coil is 2.94 x 105 A/m². Figure 1 illustrates schematic of numerical simulation.
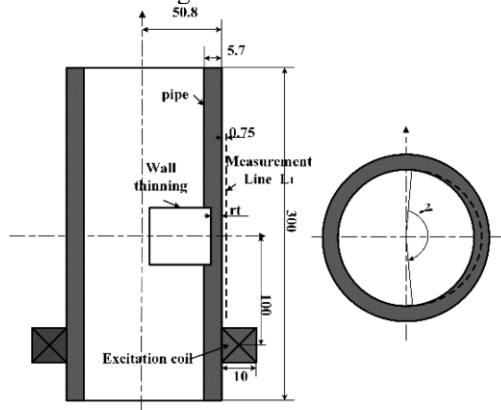
Figure 1. Schematic of numerical simulation.
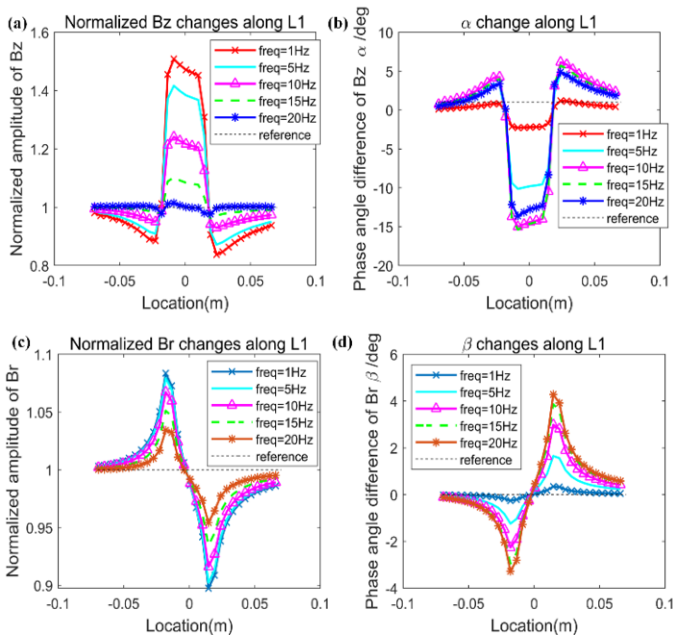
Figure 2. The change of signals along L₁.

2.2. Signal analysis

In this paper, 1Hz, 5Hz, 10Hz, 15Hz and 20Hz are used as the excitation frequency in order to evaluate the wall. Figure 2 shows the changes of normalized amplitude and phase difference along L_1 when the pipe is thinned, and the amplitude and phase of signals are abrupt and the amplitude and phase of Br appear peaks and troughs at the defect. Therefore, the extreme value of the signal on L_1 can be extracted as features of defect

signals, which are denoted as Bz_{maxi}, Br_{maxi}, Br_{mini}, α_{mini}, β_{maxi}, β_{maxi}, respectively. The subscript maxi and mini represent the maximum or minimum value of the signal on L_1 at iHz.

2.3. Correlation analysis

Correlation analysis is performed to determine the corresponding estimated defect size rt feature signals. Figure 3 shows that the correlation coefficients between the extreme value of the signals and the residual wall thickness rt is greater than 0.75, so these extreme values can be used as the feature signals for evaluating rt. The arrows in the figure indicate the largest correlation coefficient in each type of signal. These signals are Bz_{max1}, α_{min10}, Br_{min1}, β_{min20}, respectively.
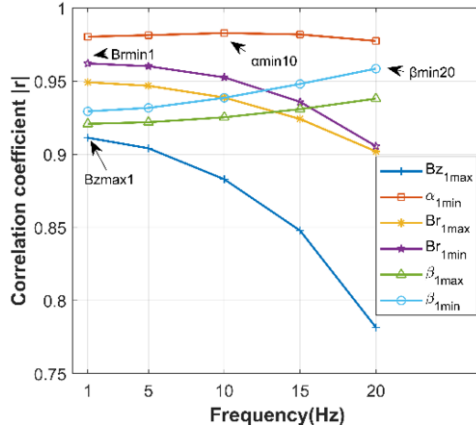
Figure 3. Correlation analysis of feature signals with rt.

2.4. Evaluation of residual wall thickness rt by Gaussian process regression

The Gaussian process has a strict theoretical foundation of statistical learning and has good adaptability for dealing with high-dimensional nonlinear small sample data [7]. According to the previous correlation analysis, the feature signals Bz_{maxi}, α_{mini}, Br_{maxi}, Br_{mini}, β_{maxi} and β_{mini} are highly correlated with rt. Assume that they satisfy them relationship:

$$y = f(X) + \varepsilon \tag{2}$$

Where y is the vector of residual wall thickness rt, X is the feature signals matrix, ε is Gaussian noise, and the posterior distribution of f(X) is obtained from the data set {x_i, y_i} by Gaussian process .y~GP(m(X), κ(X,X)), where m(X) is the mean function, κ(X,X) is the covariance function, and the squared exponential kernel is expressed as:

$$\kappa\left(x_p, x_q\right) = \sigma_f^2 \exp\left[-\frac{1}{2}\frac{(x_p - x_q)^T(x_p - x_q)}{\sigma_l^2}\right] \tag{3}$$

Where σ_f is the signal standard deviation and σ_l is the characteristic length scale.

Figure 4 shows the evaluation effect of the model when different signal combinations are used as predictors. As shown in Figure 4-(f), the RMSE=0.016, which is the smallest, the evaluated value of rt is the closest to the true value. This result corresponds to the previous correlation analysis, and the selection of signals with high correlation coefficient as predictors will improve the evaluation effect of the model.
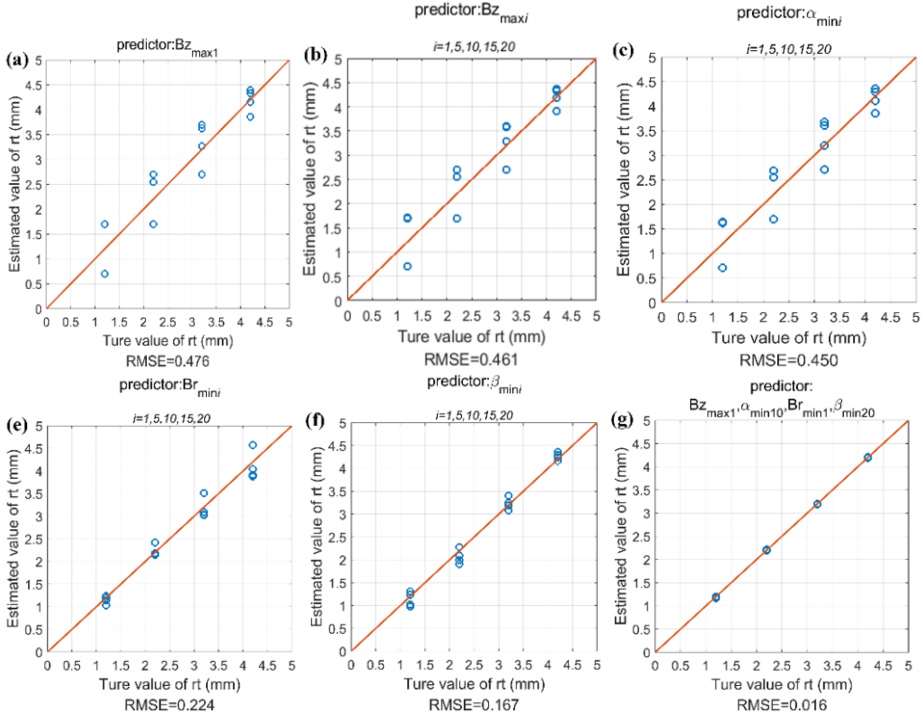
Figure 4. Compare the models with different feature signals as predictors to evaluate rt.

3. Experimental verification

3.1. Experimental setup

Figure 5 presents the experiment system. The excitation coil was excited by an AC current supplied from the function generator 1 WF1973 (NF Corporation, Yokohama, Japan). A lock-in amplifier 1 LI5640 (NF Corporation, Yokohama, Japan) and a shunt resistor monitor the current and provide a reference frequency to the lock-in amplifier 2 LI5640 (NF Corporation, Yokohama, Japan). Two sensor arraies, each consisting of ten Magneto-Impedance sensors, measure magnetic fields. The signals are measured by the lock-in amplifier 2 and automatically recorded by the PC via the A/D converter.
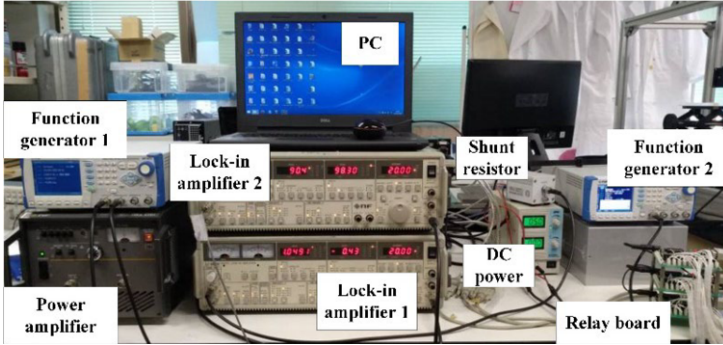
Figure 5. Experiment system.

3.2. Evaluation of residual wall thickness rt

Figure 6 shows the verification of the evaluation of the prediction model using the experimental signals. As shown in Figure 6(f), the model evaluates best, RMSE=0.497. This result is consistent with the experiment, which Bz_{max1}, Br_{min1}, α_{min10}, and β_{max20} are the best predictors, the evaluated value of rt is close to the true value.
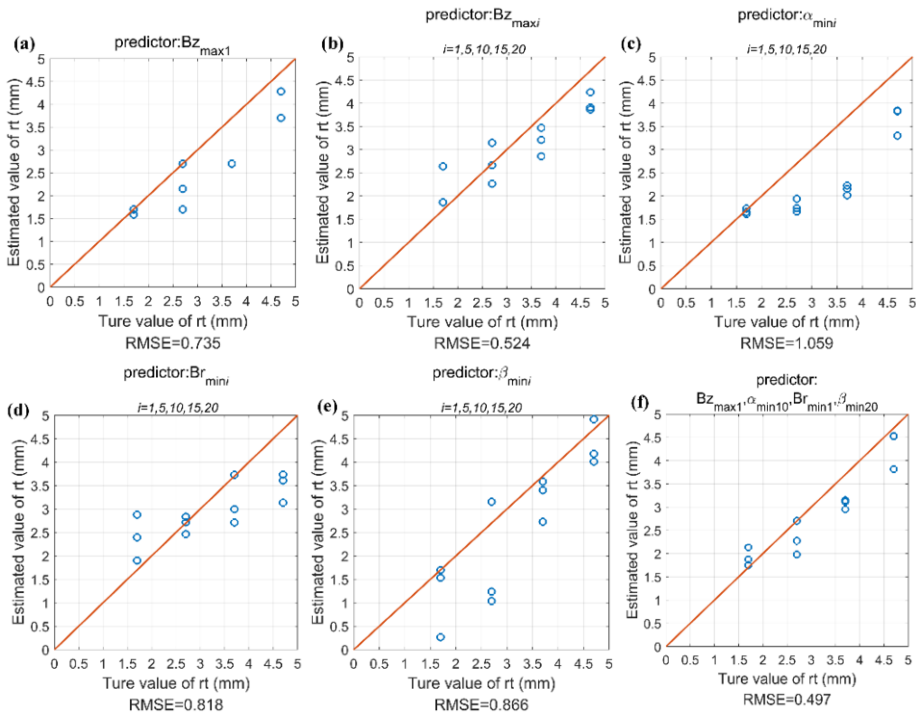
Figure 6. Experimental verification of evaluation of rt.

4. Conclusion

This paper develops the inverse algorithms for evaluating the local wall thinning of carbon steel pipe based on Gaussian process regression. Through comparative analysis, the signal with high correlation coefficient with defect size is used as the predictor, and the evaluation effect of the model is better. The simulation results are basically consistent with the experimental results, indicating the correctness of the simulation, and have a strong guiding role for the actual pipeline inspection.

Acknowledgements

References

[1]   Xie S, Chen Z, Takagi T, Uchimoto T. Quantitative non-destructive evaluation of wall thinning defect in double-layer pipe of nuclear power plants using pulsed ECT method. NDT&E International. 2015 Oct;75:87-95.

[2]   Hwang KM, Yun H, Seo HK, Lee JY, Kim KW. Development of ToSPACE for pipe wall thinning management in nuclear power plants. 2019;(1):1-5.

[3]   Zhdanov AG, Shchukis EG, Lunin VP, Stolyarov AA. Algorithms for pre-processing of eddy-current signals when inspecting heat-exchanger pipes of NPP steam generators. Russian Journal of Nondestructive Testing. 2018 Jun;54(4):283-293.

[4]   Evgeny Y, Olga G, Daniil U. Thickness measuring of electroconductive pipe walls using the dual-frequency eddy-current method. 2017 Jan;783(1):012061.

[5]   Zhu L. Development and application of eddy current inspection system for heat-exchanging tubes of horizontal steam generator. 2019;40(3):150-154.

[6]   Spikic D, Tutic R, Vasic D, Ambrus D, Bilas V. Digital eddy current probe for tube nondestructive testing using binary excitation. IEEE Instrumentation and Measurement Technology Conference. 2019 May;2019: 1091-5281.

[7]   Denzel A, Kästner J. Gaussian process regression for geometry optimization. 2018;149(9).

Research on Analysis of Eddy Current Response to Lay Length of Wire Ropes

Shaoni Jiao[a,b,c], Xiaojuan Jia[d,1], Tengyu Li[a,b,c], Shukui Jin[a,b,c], Ziming Kou[a,b,c], Juan Wu[a,b,c], Yanfei Kou[e]

[a] *College of Mechanical and Vehicle Engineering, Taiyuan University of Technology, Taiyuan,030024*
[b] *Shanxi Province Engineering Technology Research Center for Mine Fluid Control, Taiyuan, 030024*
[c] *National-local Joint Engineering Laboratory of Mining Fluid Control, Taiyuan, 030024*
[d] *College of Mechanical and Equipment Engineering, Hebei University of Engineering, Handan, 056038*
[e] *College of Mechanical Engineering, North Central University, Taiyuan, 030051*

Abstract. The lay length is one of the important parameters for the wire rope and its detection can indirectly characterize its stress and surface damage state. The eddy current testing (ECT) method is advantageous because of its easy operation, single-side detection, low requirement of surface preparation, applicability in harsh environment, and other properties. Hence the lay length of the wire ropes is measured by ECT in this paper. The eddy current (EC) response to the wire rope is simulated. The EC on the surface of the strand below the pancake coil forms a vortex, and the distribution of the EC on the curved surfaces on both sides of the strand is symmetrical. The spacing between the adjacent peaks or troughs of the scanning signal is the distance between the adjacent strands, and the number of peaks or troughs of the scanning signal in a range of the lay length is related to the number of strands of the wire rope. Finally, the experimental validation is performed. The relative error of the lay length of the wire rope assessed by the EC method is less than 0.28%.

Keywords. Wire rope, Lay length, Eddy current testing, Finite element analysis

1. Introduction

The wire rope is a flexible space spiral structure winded by the same size of the strands, and has been widely utilized as a bearing and transmission component in the fields of mining, tourism, construction, et al[1]. Guaranteeing the safety of the wire rope is important for reducing economic loss or casualties. The tension or deformation of the wire rope caused by surface wear can lead to changes in the lay length of the wire rope [2]. Therefore, the detection of the lay length can indirectly characterize the force and surface damage of the wire rope. The traditional method of measuring the lay length is mainly done manually, which is not suitable for detecting the running wire rope.

---

[1] Corresponding author: Xiaojuan Jia. Email: jiaxiaojuan@cqu.edu.cn.

Different nondestructive methods have been applied to detect the running wire ropes, such as the image recognition method and the magnetic flux leakage (MFL) method. Alberto has proposed an automatic vision measurement system for the lay length detection. The image of the running wire rope is acquired through the camera, and then the wireline contour is extracted using the image and signal processing algorithms to determine the lay length. The accuracy of the lay length obtained by this method is 1.2 mm[3]. Esther has established an image comprehensive analysis system based on the wire rope model, which can capture the actual 2-D projection of the wire rope using the camera, and construct a parametric 3-D model based on the structural parameters of the wire rope model. The accuracy of the lay length and strand space obtained by this method is 1 mm [4]. Sylvain has calculated the lay length according to the change of the scanning MFL signal with the uneven surface of the wire rope [5].

The eddy current testing (ECT) method has a series of advantages and has been applied in the wire rope testing. Cao has quantitatively tested the broken wires with symmetrically arranged the excitation and the detection coils around the wire rope [6]. Zheng has adopted a double eddy current (EC) probe placed in parallel to detect the lay length. The sensitivity is related to the distance between the probe and the probe consistency. Hence the detection difficulty is increased [7].

The image recognition method is greatly affected by the external environment. The MFL method requires the wire rope to be magnetized and its operation is relatively complicated. In this paper, the ECT for detecting the lay length of the wire rope is studied. Firstly, the EC distribution on the surface of a single strand is analyzed and the scanning signal of the wire rope with the differential bridge is obtained. Then the experimental platform is established for lay length detection.

2. Finite element analysis

2.1. $A_r, V - A_r$ formulation

The governing equations for the calculation of EC response to the wire rope are as follows

$$-\frac{1}{\mu_0}\nabla^2 A_r + j\omega\sigma\left(A_r + \nabla v\right) = -\nabla \times H_s - j\omega\sigma A_s \quad \left(\Omega_1\right) \tag{1}$$

$$\nabla \cdot \left(-j\omega\sigma A_r - j\omega\sigma\nabla v\right) = \nabla \cdot j\omega\sigma A_s \quad \left(\Omega_1\right) \tag{2}$$

$$-\frac{1}{\mu_0}\nabla^2 A_r = 0 \quad \left(\Omega_2\right) \tag{3}$$

where the wire rope model area (Ω_1) and the air domain containing the power supply (Ω_2) constitute the entire solution domain. In (1)-(3), A_r stands for the simplified magnetic vector potential (MVP). A_s and H_s represent the magnetic vector position and magnetic field strength generated by the excitation current in the solution space, respectively. μ_0 represents the magnetic permeability of the solution space. ω stands for the angular frequency. In (1) and (2), $v = V/(j\omega)$, in which V represents the simplified electrical scalar position. The eddy current density J can be calculated as follows

$$J = - j\omega\sigma\left(A + \nabla v\right)$$
(4)

where A is the vector sum of A_s and A_r.

2.2. Simulation model

The model includes the wire rope and the probe composed of a double pancake coil, as shown in Fig. 1. The $Oxyz$ global coordinate system is established and the origin is the wire rope center. Figs.1(a) and (b) are the projections of the model on the xz and yz planes, respectively. The wire rope has the total length of 240 mm, the lay length of 60 mm, the radius of the single helix is 3.48 mm, the strand radius of 1.65 mm. The conductivity is 3.0×10^7 S/m and the relative magnetic permeability of the wire rope is 10[8]. The coils are coaxially placed and are the same size. Each pancake coil has the inner diameter of 6.0 mm, the outer diameter of 8.0 mm, the height of 3.0 mm, the number of turns of 500, the lifting height of 0.5 mm and the distance of 2.5 mm between the upper and lower coils. The exciting frequency is 80 kHz. The model is solved by an FE analysis software package developed in lab.

Fig.1. Schematic of the simulation model (a) the xz plane view   (b) the yz plane view

2.3. Eddy current distribution of single strand

Fig. 2 shows the partial single strand and the probe which remains the same with the one in Section 2.2. The surface of the strand is divided into four parts. The bottom surface of the probe is just on Surface 1. Surface 3 is the corresponding back side of Surface 1. Surfaces 2 and 4 are the corresponding side faces of the strand.
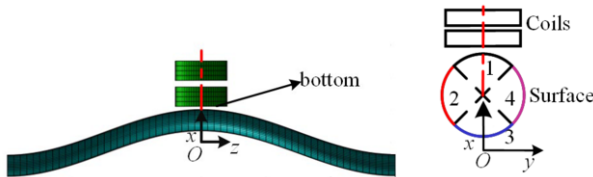
Fig.2. The single strand model with the probe

Fig. 3 shows the distribution of the real part of the EC density at the bottom center of the probe ($x = 5.63$ mm, $y= 0$, $z = 0$). Fig. 3 (a) is the partial distribution of the EC density on Surface 1. A vortex is formed on Surface 1 and the center of the vortex denoted by point A is located just under the bottom center of the probe. Fig. 3 (b)-(d) are the partial distributions of the EC density on Surface 2-4. ECs are formed on Surface 2-4 and the centers are denoted by point B, point C and point D. The distribution of ECs in the wire rope is different from the one in the traditional flat metal due to the special helical structure. When the probe scans along the axis of the wire rope, the response of EC will change with the distribution of ECs. Hence the lay length will be deduced from the change of the response of EC.

(a)

(b)

(c)

(d)
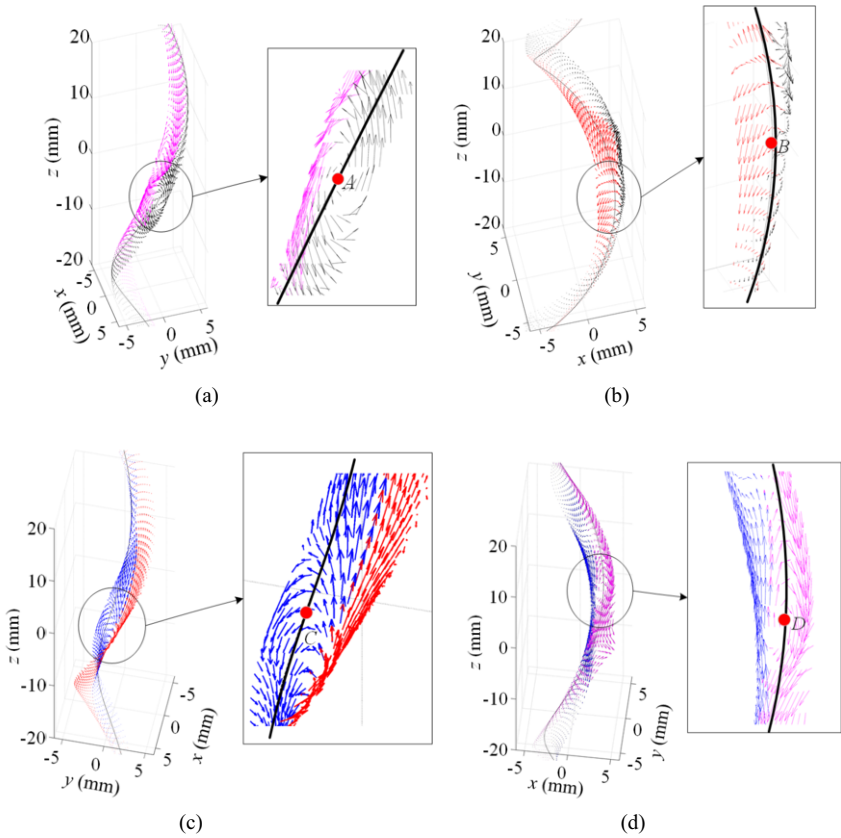
Fig.3.The real part distribution of the EC density on the single strand surfaces (a) on Surface 1(b) on Surface 2(a) on Surface 3(a) on Surface 4

2.4. Linear scan simulation
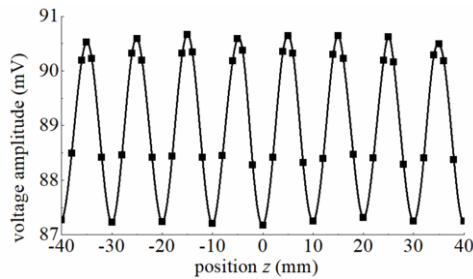
Fig.4. Simulation result of scanning the wire rope

The probe scans from $z = -40$ mm to $z = 40$ mm with a step of 2 mm. Fig. 4 shows the change of the amplitude of the differential voltage with the scanning position. It can be seen that the curve changes periodically and there are 7 peaks or troughs in one lay length range. The spacing between the adjacent peaks or troughs is just the gap of the wire strand.

3. Experiments

3.1. Eddy current testing system

To validate the simulation result shown in Fig.4, the experiment of detecting the lay length by the EC method is conducted. Fig.5 shows the platform and is mainly composed of the signal generator (DG4102), the probe, the electronically controlled displacement platform, the Native Instruments (NI) data acquisition card and the monitor. The excitation signal is with the frequency of 80 kHz and the amplitude of 10 V. The acquired data is post-processed by Labview.
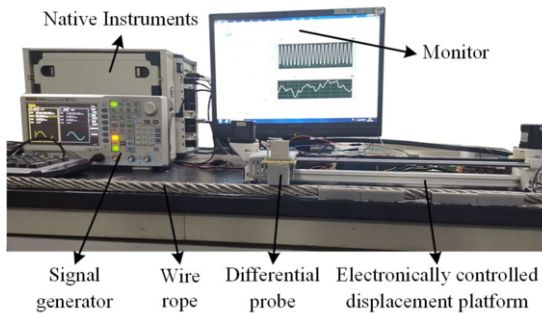
Fig. 5 The experimental platform of detecting the lay length

Fig. 6 shows the 6×19+IWRC wire rope sample with a diameter of 16.0 mm and a total length of 1200 mm. The average lay length and gap between the two adjacent strands are 104 mm and 17.33 mm, respectively. Fig 7 shows the probe with two same pancake coils arranged coaxially. The probe is connected to the differential detection circuit printed on the PCB board.
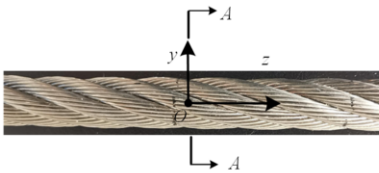
Fig.6. 6×16+IWS wire rope sample   Fig.7. The probe for the lay length detection
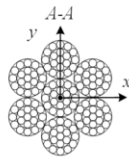
3.2. Linear scanning test

Fig. 8 shows the results of scanning the wire rope with a total scan length of 360 mm. The experiment is repeated twice and the change of the amplitude of the differential voltage with the scanning position is shown in Fig.8. The results agree well during the two experiments. The amplitude of the differential voltage exhibits alternate peaks and valleys during the scanning. The distance between the two adjacent peaks or valleys is a gap between the adjacent strands of the wire rope. The distance between the adjacent seven peaks or valleys is approximately one lay length, which is consistent with the simulation results shown in Fig.4. The average strand gap and lay length are 17.16 mm and 103.71 mm respectively. The relative error is the difference between the manually

measured lay length and the value assessed by the EC method divided by the manually measured value and is 0.28% in Fig.8.
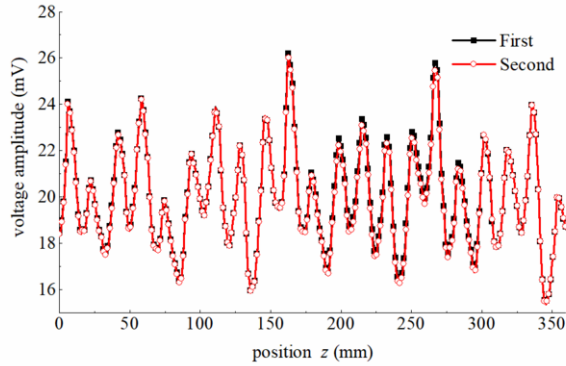
Fig.8. Experimental result of scanning the wire rope

4. Conclusions

The lay length of the wire rope is detected by the EC method in this paper. The A_r,V- A_r formulation for calculating the EC response to the wire rope is established. The finite element analysis shows that the EC forms vortex on the surface of the single helical strand. Due to the uneven surface of the wire rope, the lift between the probe and the rope changes with the scanning position. The amplitude of the differential voltage changes periodically as the probe scans. The distance between the adjacent peaks or valleys is just the space between the adjacent strands and the lay length can be deduced from the scanning signal. The relative error of the lay length obtained by the EC method and the manually measured value is 0.28%.

5. References

[1]   REN Zhiqian, YU Zongyue, CHEN Xun. Study on wire rope elastic-plastic damage constitutive model[J]. Journal of Mechanical Engineering, 2017, 53(1): 121-129.
[2]   ELATA D, ESHKENAZY R, WEISS MP. The mechanical behavior of a wire rope with an independent wire rope core[J]. International Journal of Solids and Structures, 2004, 41(5-6): 1157-1172.
[3]   VALLAN A, MOLINARI F. A vision-based technique for lay length measurement of metallic wire ropes[J]. IEEE Transactions on Instrumentation & Measurement, 2009, 58(5): 1756-1762.
[4]   WACKER ES, DENZLER J. An analysis-by-synthesis approach to rope condition monitoring[C] //International Symposium on Visual Computing. Springer, Berlin, Heidelberg, 2010: 459-468.
[5]   OUELLETTE S. Measurement of lay length of wire rope: USA, US9470657B2[P]. 2016-10-18.
[6]   CAO Qingsong, LIU Dan, HE Yuehai, et al. Nondestructive and quantitative evaluation of wire rope based on radial basis function neural network using eddy current[J]. NDT & E International, 2012, 46: 7-13.
[7]   ZHENG Xinhong, ZHANG Jiayi, ZHANG Xiaolei, et al. An on-line testing device for wire rope lay length: China, CN201520535589.5[P]. 2015-11-18.
[8]   FU Fengli, TANG Xiaogao. Asynchronous motor design manual[M]. Beijing: Machinery Industry Press, 2003.

Analysis of Lift-Off Effect on Transmitter-Receiver Probe in Eddy Current Testing

Qing Zhang [a], Xin Li [a] and Guiyun Tian [b,1]

[a] *College of Automation Engineering, Nanjing University of Aeronautics and Astronautics, Nanjing, China*
[b] *School of Engineering, Newcastle University, England, UK*

Abstract. The Transmitter-Receiver Probe (TR probe), which has improved signal-to-noise ratio, deep penetration depth, and directional measurement is used in pulsed eddy current testing (PECT). Whereas, the lift-off effect on the TR probe is one of the main obstacles. The purpose of this paper is to analyze the lift-off effects on the TR probe and presents a feature for lift-off estimation. Firstly, an analytical model of a TR probe is given based on previous studies. Secondly, on the basics of the analytical model, the spectrum of the PECT signal is studied, and the lift-off effects on the TR probe are analyzed. Then, the lift-off effects under different coil distances are studied and a *D* Intersect Point (DIP) is proposed for the lift-off estimation. Results show that the TR probe can be used to reduce the lift-off effect for the non-ferromagnetic materials and the ferromagnetic materials. And both the DIP time and amplitude can be used for lift-off estimation. However, the DIP time is better, as its evolution curve with lift-off is a straight line with the same slope. The study is believed to be helpful for the TR probe design, the lift-off measurement, and the thickness assessment and defect quantification.

Keywords. Lift-off effect, Transmitter-Receiver Probe, Eddy Current Testing

1. Introduction

Different types of Pulsed Eddy Current Testing (PECT) probe have been designed and selected for thickness measurement and defect detection in industrial applications [1]. One of the most commonly used PECT probe configurations includes excitation coil and magnetic sensor probe where a coil is used for excitation and the magnetic sensor is used to pick-up the response signal. Although this type of probe has high sensitivity, only the excitation coil could be optimized [2]. Another type of probe configuration includes two coaxial coils, which use one coil for excitation, and the other for pick-up. Whereas, the Signal-to-Noise Ratio (SNR) of this probe is low, as the signal in the receiver coil is susceptible to the magnetic field directly resulted from the excitation coil [3]. To have directional measurement e.g. stress and improve the SNR, the transmitter and receiver coils are non-coaxial placed, which is called the Transmitter-Receiver probe (TR probe). It has several advantages, such as the improved SNR, the deep penetration depth, etc. [4-5]. Ona et al. [3] validated that the TR probe sensitivity is enhanced at a higher lift-off when the coil gap exceeds a certain value. These made it a good choice for PECT.

---

[1] Corresponding Author, g.y.tian@newcastle.ac.uk

The lift-off effect of the PECT probe is one of the main obstacles [6]. It is complicated, as it may be affected by many factors, such as specimen materials and probe configurations. That is why the Lift-off Intersection point (LOI) can be easily found in non-ferromagnetic material, while, it is not obvious in ferromagnetic material [7]. Meanwhile, although the lift-off effect has already been studied on the magnetic sensor probe and the coaxial coil probe [8, 9], the influence of the lift-off effect on the TR probe has not yet been studied thoroughly [3]. The purpose of this paper is to analyze the lift-off effects on the TR probe and present a feature that can be used for lift-off measurement. Considering a theoretical model serves as a cost-effective and fairly efficient tool to explore the characteristics of the TR probe, the analytical model for the TR probe is used in this paper. Based on the analytical model, the spectrum analysis of PECT signals under different lift-off are given to examine the lift-off effect on the TR probe. Then behaviors of the TR probe under different coil distances are discussed, and a D Intersect Point (DIP) is proposed to measure the lift-off. Moreover, the lift-off effect and DIP are also studied when the specimen is a ferromagnetic plate.

The rest of this paper is organized as follows. In Section 2, the formulation of the TR probe analytical model is given. In Section 3, on the basics of the analytical model, the lift-off effects on the TR probe are analyzed. In Section 4, the lift-off effects are examined under different coil distances D, and DIP is proposed to measure the lift-off. In Section 5, the lift-off effect on the TR probe for ferromagnetic material is discussed. And finally, a brief conclusion is given in Section 6.

2. Formulation of the TR probe analytical model

Considering the specimen as a metallic plate with the thickness of c, and then the TR probe with the lift-off of l_0 located over the metallic plate is simplified as a three-layered structure shown in Figure 1(a). Layers 1 and 2 represent the air and the metallic plate, respectively. The layer over the plate is considered to be layer 3. It is divided into three sub-regions, and the TR probe which consists of non-coaxial transmitter and receiver coils with the same parameters is located in sub-region II. The probe in polar coordinates is shown in Figure 1(b).
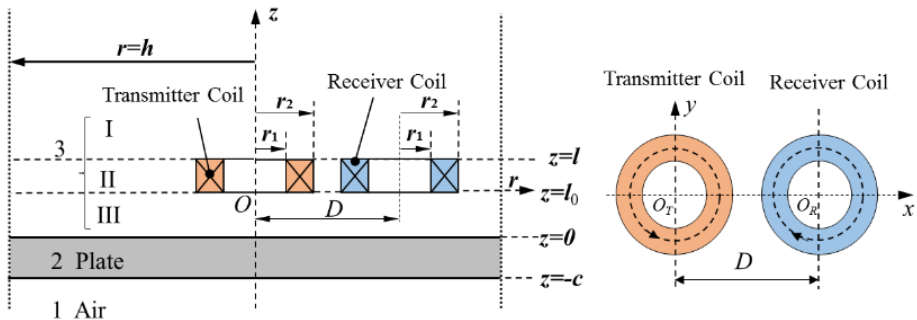
(a) A TR probe over a three-layered structure.   (b) A TR probe in polar coordinates

Figure. 1. The model of the TR probe located over a metallic plate

As the square-wave excitation current of PECT is theoretically represented by superimposing a series of sinusoidal harmonics in the frequency domain, the Fourier-

based method [10] can be used to obtain the PECT signal $\triangle U$. It can be written as:

$$\triangle U[s] = \frac{1}{N}\sum_{m=1}^{N} e^{j\frac{2\pi}{N}(s-1)(m-1)} \triangle U[\omega_m], \quad s = 1,2,...,N \qquad (1)$$

where N is the number of sampling points, m denotes the m-th sinusoidal harmonic, ω_m is the angular frequency of the m-th sinusoidal harmonic, $\triangle U[\omega_m]$ is the induced voltage of the TR probe for the m-th sinusoidal harmonic. According to [5], $\triangle U[\omega_m]$ can be expressed as:

$$\triangle U[\omega_m] = j\pi\omega_m\mu_0 I(\omega_m) \times \int_0^\infty e^{-2\alpha l_0} \times S(\alpha) \times R'_{3,2}(\alpha)\mathrm{d}\alpha \qquad (2)$$

where, j is the imaginary unit, μ_0 is the permeability of vacuum, $I(\omega_m)$ is the amplitude of the harmonic excitation current. l_0 denotes the lift-off of the probe, α can be understood as the radial spatial frequency [11], $S(\alpha)$ is the spatial frequency spectra of the TR probe, and $R'_{3,2}(\alpha)$ is the generalized reflection coefficient [12] of the three-layered structure. It can be written as:

$$R'_{3,2}(\alpha) = \frac{(\mu_{r2}\alpha - \beta_2)(\mu_{r2}\alpha + \beta_2) - (\mu_{r2}\alpha - \beta_2)(\mu_{r2}\alpha + \beta_2)e^{-2\beta_2 c}}{(\mu_{r2}\alpha + \beta_2)(\mu_{r2}\alpha + \beta_2) - (\mu_{r2}\alpha - \beta_2)(\mu_{r2}\alpha - \beta_2)e^{-2\beta_2 c}} \qquad (3)$$

where, $\beta_2 = (\alpha^2 + j\omega_m\mu_0\mu_{r2}\sigma_2)^{1/2}$, μ_{r2} and σ_2 are the relative magnetic permeability and electrical conductivity of the metallic plate, respectively.

Moreover, according to [5], the expression of $S(\alpha)$ satisfies:

$$S(\alpha) = n^2 J_0(\alpha D)[\frac{(e^{-\alpha l} - 1)}{\alpha l_2} \times \frac{Int(\alpha r_1, \alpha r_2)}{\alpha^2(r_2 - r_1)}]^2 \qquad (4)$$

$$Int(x_1, x_2) = \int_{x_1}^{x_2} x J_1(x)\mathrm{d}x \qquad (5)$$

where $J_1(x)$ denotes the first-order Bessel function, D is the center distance between the transmitter coil and the receiver coil, n is the number of the coil turns, r_1, r_2, $(l - l_0)$ are the inner radius, the outer radius and the height of the coil, respectively.

Meanwhile, as $J_0(0)=1$, substituting $J_0(0)=1$ into (4), the result is the same with $S(\alpha)$ for the coaxial coil probe in [10]. It indicates that the coaxial probe is a specific TR probe with D equals to 0. As the coaxial probe is widely used in PECT, it is used as a standard to analyze the performance of the TR probe for reducing the lift-off effect in this paper.

3. Lift-Off effect on the TR probe

The formulated model in Section 2 allows efficient and cost-effective investigation of the TR probe behaviors. As the formulated mode has been verified in [5], from now on, simulations were carried out to study the lift-off effect on the TR probe. The metallic plate is considered to be a 20-mm thick aluminum plate. The relative magnetic permeability and conductivity of the aluminum plate are set to be 1 and 21.6 MS/m, respectively. The amplitude, duty cycle, and period of the square-wave current are set to be 4 amps, 50%, and 1 s, respectively. The parameters of the coils are listed in Table 1, and the coaxial probe used in this section has the same coil parameters with the TR probe.

Table 1 Parameters of the probe

Parameters	r_1 (mm)	r_2 (mm)	$l - l_0$ (mm)	n
Value	3.0	5.0	5.0	1000

As the behavior of the PECT signal can be revealed by analyzing its spectrum, spectrums of PECT signals under different lift-offs are examined. Figure 2(a) and (b) are the spectrums obtained by the coaxial probe and the TR probe, respectively. As shown in Figure 2, the maximum values of spectrums obtained by the coaxial probe under 0 mm and 10 mm lift-offs are 7.49V and 0.42V, respectively. Whereas, those for the TR probe under 0 mm and 10 mm lift-offs are 0.434V and 0.195V, respectively. The values of the spectrum for the TR probe are much smaller, and they change much slower with the lift-offs. Therefore, it can be inferred that the signal amplitude of the TR sensor is smaller, and it is insensitive to lift-off.
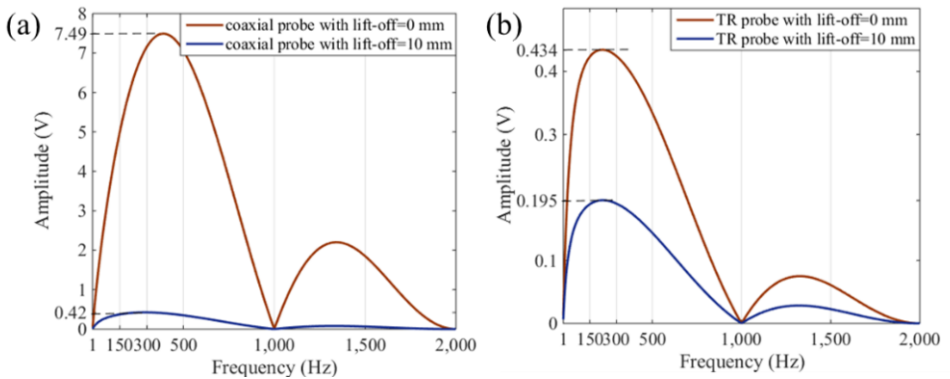
Figure. 2. Spectrum of the PECT signals obtained by (a) the coaxial probe; (b) the TR probe.
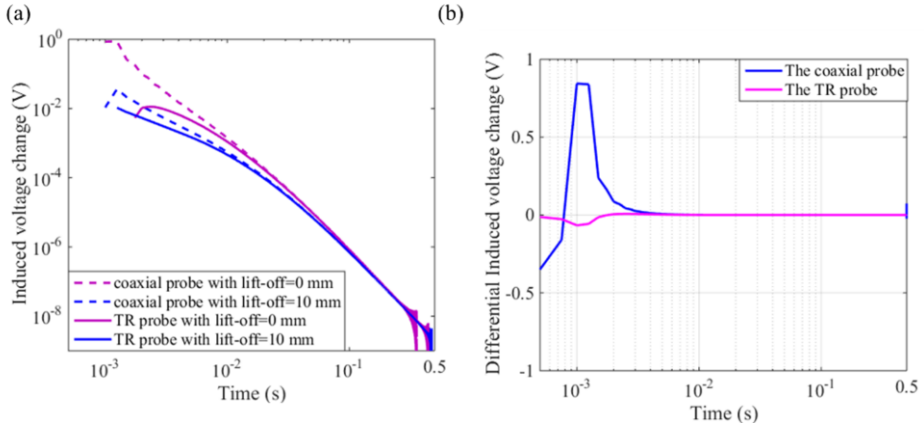
Figure. 3. (a) PECT signals obtained by the coaxial probe and the TR probe under different lift-offs; (b) the differential signals obtained by the coaxial probe and the TR probe.

To verify the above conclusions, signals under 0 mm and 10 mm lift-offs are studied. Figure 3(a) are the induced voltage changes $\triangle U$ obtained by the coaxial probe and the TR probe with D=18 mm. It shows that the signal amplitudes of the TR probe are smaller than those of the coaxial probe, especially in [0.001, 0.010]s. Moreover, to investigate the lift-off effect, the corresponding differential signal obtained by subtracting a 10-mm

lift-off signal from a 0-mm lift-off signal is given. As shown in Figure 3(b), the difference signal obtained by the TR probe is smaller than that obtained by the coaxial probe. That proves the TR probe can be used to reduce the lift-off effect. These conclusions are consistent with those obtained by the spectral analysis. Furthermore, as shown in Figure 3(b), the lift-off effect in [0.01, 0.50]s is weak, that is because the maximum spectrum values occur at 150-500 Hz.

4. Behaviors of the TR probe under different coil distances

As the coil distance D is an important parameter for the TR probe design, the lift-off effects with different D are discussed in this section. Figure 4(a) are signals of the TR probe with D=10 mm and D=18 mm. It shows that the amplitude of the PECT signal, as well as the difference of $\triangle U$ with 0 mm and 10 mm lift-offs, are affected by the coil distance D. That indicates the lift-off effect will vary with D.

To quantitatively evaluate the lift-off effect, the Euclidean distance is applied. Its calculating formula is:

$$Dis = \sqrt{\sum (\Delta U_{ref} - \Delta U)^2}$$

(6)

where Dis is the Euclidean distance, $\triangle U_{ref}$ is the signal obtained with 0 mm lift-off, $\triangle U$ is the signal obtained with other lift-offs, and the bigger value of Dis means the more obvious of the lift-off effect.

Through changing the lift-off from 0 to 10 mm with a step of 2 mm and D ranging from 10 mm to 24 mm with a step of 2 mm, the influence of D on the lift-off effect is discussed. The results are shown in Figure. 4(b), of which x-axis denotes the coil center distance and the y-axis denotes Euclidean distance Dis obtained by Eq. (6). Figure. 4(b) shows that Dis decreases with D first and then increases, which illustrates that for every lift-off, there exists a specific D which makes the least effective of the lift-off effect. Moreover, for the probe studied in this paper, D=22 mm is a good choice. These analyses will be helpful for probe design.
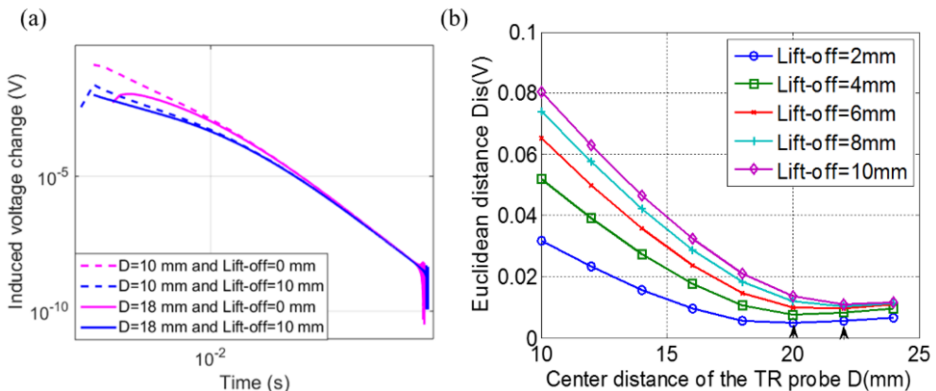
Figure. 4. (a) Signals of the TR probe under different D; (b) Euclidean distance of the TR probe under different D and lift-offs.

Furthermore, as differential PECT signals are always used for thickness measurement and defect detection, the differential PECT signals under different coil

distances are discussed in this section. The differential signal is obtained by subtracting a 16-mm thick aluminum plate signal from a 20-mm thick aluminum plate signal. Figure 5 is the differential PECT signals under 10 mm lift-off obtained by the TR probe with D=10 mm, 14 mm, 18 mm and 22 mm. The differential PECT signals under different coil distances are intersected at a point, which is called a D Intersect Point (DIP) in this paper.

As the coil distance is related to the lift-off effect on the TR probe, then DIP under different lift-offs are studied. Figure 6(a) shows the behaviors of DIP time with lift-offs and Figure 6(b) shows the behaviors of DIP amplitude with lift-offs. As the lift-off increases, the DIP time and DIP amplitude increases. However, the DIP time evolution curve with lift-off is a straight line with the same slope. This indicates that both the DIP time and DIP amplitude can be used for lift-off measurement, however, the DIP time is better. These are believed to be beneficial for lift-off measurement and high precision detection.
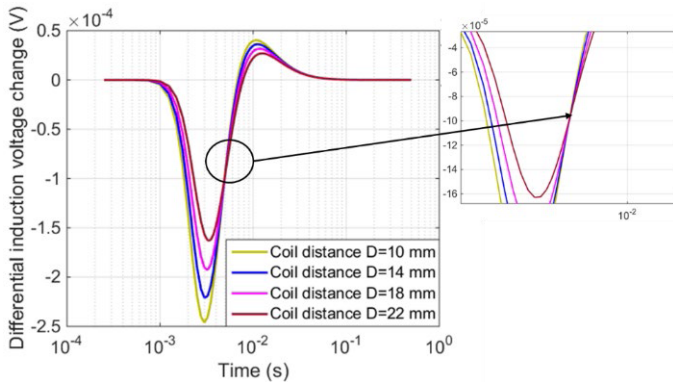
Figure.5. The D Intersect Point under 10 mm lift-off
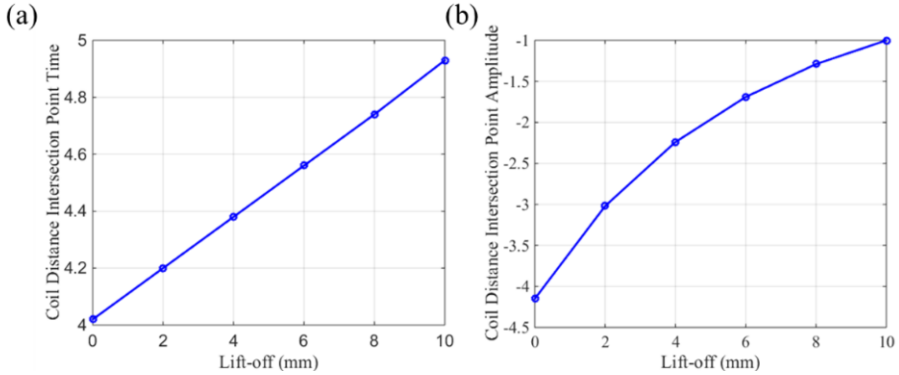
Figure.6. (a) Behavior of the DIP time with lift-offs and (b) behavior of the DIP amplitude with lift-offs

5. Discussion

As the specimen could be made by a ferromagnetic material, and the signal feature for a ferromagnetic plate and a non- ferromagnetic plate may be different, the behavior of the TR probe for a ferromagnetic plate is discussed in this section. The ferromagnetic plate

is represented by a 20-mm thick U71Mn(G) plate, which is widely used in rail. And the relative magnetic permeability and conductivity of the U71Mn(G) plate are 1000 and 2.0 MS/m, respectively.

Figure 7(a) and (b) give the induced voltage changes $\triangle U$ for the U71Mn(G) plate obtained by the coaxial probe and the TR probe with D=18 mm, respectively. Figure 7(c) and (d) are the corresponding spectrum obtained by the coaxial probe and the TR probe, respectively. Results show that the TR probe can be used to reduce the lift-off effect for the ferromagnetic materials. Moreover, different from the aluminum plate, the lift-off effect of the U71Mn(G) plate in [0.001, 0.01]s is weak, this is because of the maximum spectrum values for the U71Mn(G) plate occur at 1Hz. Moreover, as shown in Figure 8, the DIP is also found for the U71Mn(G) plate, and the DIP time evolution curve with lift-off is also a straight line with the same slope. That means the DIP time and amplitude can also be used for lift-off measurement when the specimen is a ferromagnetic plate.
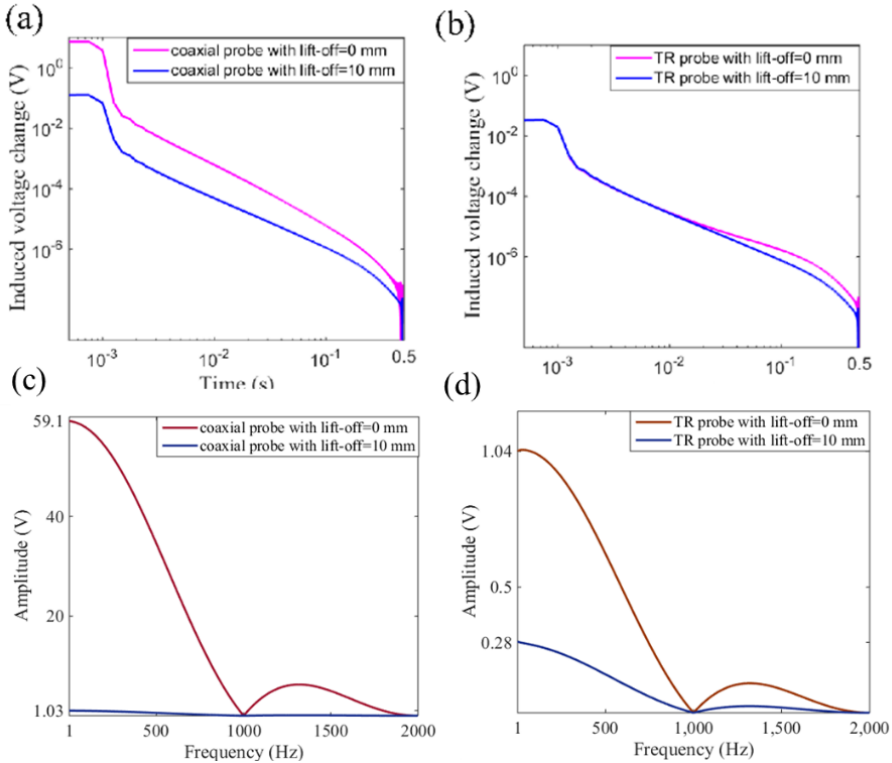
Figure.7. PECT signals obtained by (a) the coaxial probe; (b) the TR probe; and spectrum of the PECT signals obtained by (c) the coaxial probe; (d) the TR probe.
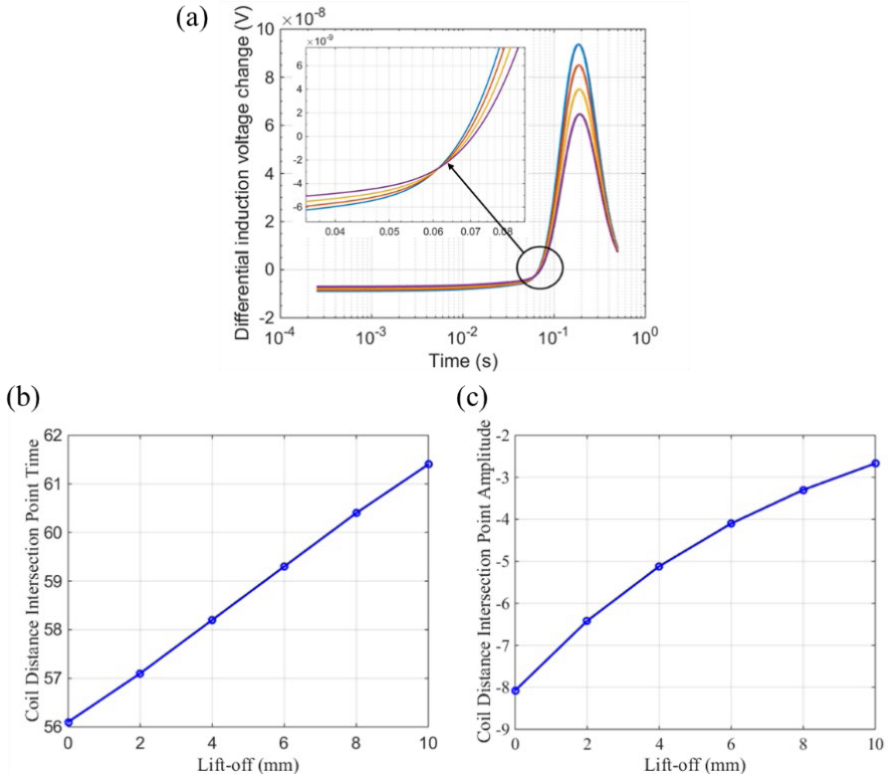
Figure.8. (a) DIP for the U71Mn(G) plate; (b) behavior of the DIP time with lift-offs and (c) behavior of the DIP amplitude with lift-offs

6. Conclusion

The lift-off effects and the *D* Intersect Point (DIP) phenomenon on the TR probe are studied in this paper based on an analytical model. Firstly, by discussing the spectrum and the signals under different lift-offs, it proves that the TR probe can be used to reduce the lift-off effect both for the ferromagnetic and non-ferromagnetic materials. Then, the lift-off effects under different coil distances and the DIP phenomenon are examined. Results show that there exists a specific *D* which makes the least effective of the lift-off effect. The DIP time and amplitude can be used for lift-off estimation, of which the linearity of DIP time and lift-off is better. These are beneficial for the probe design, the lift-off measurement, and the high precision detection. The further work will focus on the experimental study of the TR probe for the defect detection, speed effect, and the TR probe design and optimization with the variation of lift-offs.

Acknowledgment

References

[1] A. Sophian, G. Tian, and M. Fan, Pulsed eddy current non-destructive testing and evaluation, A review, *Chinese Journal of Mechanical Engineering* **30.3** (2017), 500-514.

[2] Z. Xu, X. Wang, and Y. Deng, Rotating Focused Field Eddy-Current Sensing for Arbitrary Orientation Defects Detection in Carbon Steel, *Sensors* **20.8** (2020), 2345.

[3] O. D. Ijike, G. Y. Tian, R. Sutthaweekul, S. M. Naqvi, Design and optimisation of mutual inductance based pulsed eddy current probe, *Measurement* **144** (2019), 402-409.

[4] G. Mook, O. Hesse, V. Uchanin, Deep penetrating eddy cur-rents and probes, *Mater. Test* **49** (2007), 258–264.

[5] Q. Zhang, and X. Wu, Study on the Shielding Effect of Claddings with Transmitter–Receiver Sensor in Pulsed Eddy Current Testing, *Journal of Nondestructive Evaluation* **38.4** (2019), 99.

[6] G. Y. Tian and A. Sophian, Reduction of lift-off effects for pulsed eddy current NDT, *NDT&E Int*. **38.1** (2005), 319-324.

[7] D. Wen, M. Fan, B Cao, and B. Ye, A Twice Subtraction Method for Obtaining LOI in Pulsed Eddy Current Signals of Ferromagnetic Samples. *IEEE Trans. Magn.* **55.12** (2019), 1-7.

[8] G. Y. Tian, Y. Li and C. Mandache, Study of lift-off invariance for pulsed eddy-current signals, *IEEE Trans. Magn.* **45.1** (2009), 184-191.

[9] J. Li, X. Wu, Q. Zhang, and P. Sun, Measurement of lift-off using the relative variation of magnetic flux in pulsed eddy current testing, *NDT&E Int.* **75** (2015), 57-64.

[10] Z. Xu, X. Wu, J. Li, and Y. Kang, Assessment of wall thinning in insulated ferromagnetic pipes using the time-to-peak of differential pulsed eddy-current testing signals, *NDT&E Int.* **51** (2012), 24-29.

[11] V. O. De Haan and P. A. De Jong, Analytical expressions for transient induction voltage in a receiving coil due to a coaxial transmitting coil over a conducting plate, *IEEE Trans. Magn.* **40.2** (2004), 371-378.

[12] M. Fan, P. Huang, B. Ye, D. Hou, G. Zhang, and Z. Zhou, Analytical modeling for transient probe response in pulsed eddy current testing, *NDT&E Int.* **42** (2009), 376-383.

Evaluation of Eddy Current Response Due to the Applied Stress on a Steel Plate Using Phase Diagram

Sanjeema BAJRACHARYA[a,1] and Eiichi SASAKI[a]
[a] *Tokyo Institute of Technology, Tokyo, Japan*

Abstract. Structural health monitoring of steel structures is crucial for inspection of corrosion and cracking in structural members, compromising their safety and serviceability. In the present study, the prospective of evaluation of change in stress state of structural member due to corrosion and cracking through eddy current based stress measurement is investigated. For this, three-dimensional numerical simulations are carried out in the FE software COMSOL Multiphysics 5.2a for a steel plate subjected to change in relative permeability, representative of change in stress state, whereby the eddy current indices are characterized, including the effects of additional influential parameters namely, lift-off, excitation frequency, and probe size. Phase Diagram is then proposed as a concise method to evaluate the variation of relative permeability and lift-off concurrently in a single graph for an excitation frequency and probe size. It further facilitates the selection of suitable excitation frequency and probe size to conduct the eddy current based stress measurement.

Keywords. eddy current, stress measurement, numerical simulation, phase diagram.

1. Introduction

Steel structures forming an integral part of the infrastructure suffer from corrosion due to long-term exposure to harsh environment and cracking due to fatigue as they near the end of their design life. Corrosion in the steel plate girders results in the reduction in their load-bearing capacity [1], leading to safety concerns of the overall structure, while fatigue cracking results in sudden brittle fracture [2]. Hence, inspection and monitoring of the steel structures for evaluation of the extent of effect of corrosion and detection of cracking, under structural health monitoring, have become crucial.

Various non-destructive testing methods such as ultrasonic testing, X-ray diffraction, and eddy current testing have been developed and employed for structural health monitoring of steel structures [3-6]. Among these, the eddy current testing has been selected in the present study because it is a non-contact method that does not require the use of coupling agent nor surface preparation such as clearing off the top rust layer, thus proving itself time and cost efficient, particularly for field inspection of large structures with damages such as corrosion and cracking that are widespread [6, 7].

---

[1] Corresponding author, Tokyo Institute of Technology, 2-12-1 Ookayama, Meguro-ku, Tokyo, Japan; E-mail: bajracharya.s.aa@m.titech.ac.jp

Conventionally, the extent of corrosion is determined by the remaining thickness of a structural member [6], while the cracks are detected by the change in eddy current signal due to the distortion of eddy current around them [7]. Nevertheless, it is to be noted that both corrosion and cracking cause change in stress distribution in the structural members, which can be detected by eddy current testing based on the Villari effect [8]. Hence, a more viable approach for evaluation of corrosion and cracking through the stress change in a structural member, hereby termed as eddy current based stress measurement is proposed in the present study.

Eddy current testing has been applied in the determination of the internal stresses in the mechanical equipment in the industry [4, 5] and tension force in PT tendons, pre-stressed bars and cables, etc. [9-12]. However, its application has not been tested yet in the evaluation of stress change due to corrosion and cracking in structural members. Moreover, the eddy current probes used are designed to encircle the tendons, bars, and cables, whereas, surface probes are required to move over the structural members for determination of corrosion and cracking. Hence, a methodology to conduct eddy current based stress measurement using a suitable eddy current probe needs to be devised.

In reference to the eddy current influential parameters, lift-off has been maintained at a constant minimum [5, 11] to ensure sufficient sensitivity to the change in stress due to load in the PT tendons and cables. But it is difficult to achieve in field inspections such as a corroded steel plate girder with a rust layer. Only [10] and [11] have considered the effect of frequency in view of the stress measurement, while it has been found in [10] that miniaturization of probe offers better sensitivity to stress. However, it might not hold true when factoring in the larger lift-offs due to rust layer in a corroded structural member. Hence, the effect of these influential parameters - lift-off, excitation frequency, and probe size should be investigated for the eddy current based stress measurement.

Hence, the prospective of evaluation of corrosion and cracking through eddy current based stress measurement is investigated in the present study. For this, three-dimensional numerical simulations are carried out in the AC/DC module of the general purpose, FE software COMSOL Multiphysics 5.2a, where the change in relative permeability of a steel plate, representative of stress, is evaluated by using an eddy current probe. Furthermore, a new, concise method of representing the simultaneous variation of relative permeability and lift-off, corresponding to a particular frequency and probe size, called Phase Diagram is proposed for easier evaluation of the effect of change in these influential parameters on eddy current indices, thus obtaining the criteria for selection of excitation frequency and probe size for the eddy current based stress measurement.

2. Stress Measurement by Eddy Current Testing

Eddy current testing is based on the principle of Faraday's law of electromagnetic induction. When an alternating current is passed through a coil, it generates primary magnetic field, which when brought near a conducting material induces eddy currents. The change in a material property such as magnetic permeability in the test material affects the eddy current flow, which is then reflected in the eddy current signal. When the stress is applied to a magnetostrictive material such as steel, domain reorientation occurs, causing change in its magnetic permeability, by the phenomenon known as Villari or Inverse magnetostrictive effect, thus enabling eddy current to detect the change in relative permeability due to stress. This can also be illustrated by one of the equations for linear magnetostriction [9] as shown in Eq. (1).

$$B = d^* \psi + \mu^\psi H \qquad (1)$$

Where, ψ is the stress, B and H are the magnetic flux density and applied magnetic field, respectively, μ^ψ is the magnetic permeability at constant stress, and d* is a piezo-magnetic cross coupling coefficient. Eq. (1) shows that change in stress causes change in the magnetic flux penetrating the test material, which in turn affects the eddy current. This has also been verified experimentally by Jiles et al. (2002) [13] from the changes in hysteresis loop on application of stress. For positive magnetostrictive materials like steel, magnetic permeability increases with the increase in tensile stress.

In this study, numerical simulations are first carried out using a steel plate subjected to variation of relative permeability, representative of applied stress, as well as the other influential factors namely, lift-off, excitation frequency, and probe size. Then, the eddy current indices – real and imaginary voltages, and phase detected by a reflection-type eddy current probe are used to characterize the eddy current response. From the results of this parametric study, a new, concise method called Phase diagram is proposed to observe the simultaneous variation of relative permeability and lift-off at an excitation frequency for a probe size, which proffers the criteria for the selection of suitable excitation frequencies and probe size for the eddy current based stress measurement.

3. Finite Element Modeling

The three-dimensional numerical simulations are carried out in the frequency domain of the AC/DC module of FE software, COMSOL Multiphysics 5.2a, where the relative permeability of the steel plate is increased in X-direction to represent the increase in applied tensile stress. The reflection probe, comprising of an outer excitation coil and an inner detecting coil, selected in the present study for its high gain, is used to characterize the eddy current indices – real and imaginary voltages, and phase. It is modeled by using two concentric, homogenized, multi-turn cylindrical coils as shown in Figure 1 (a).
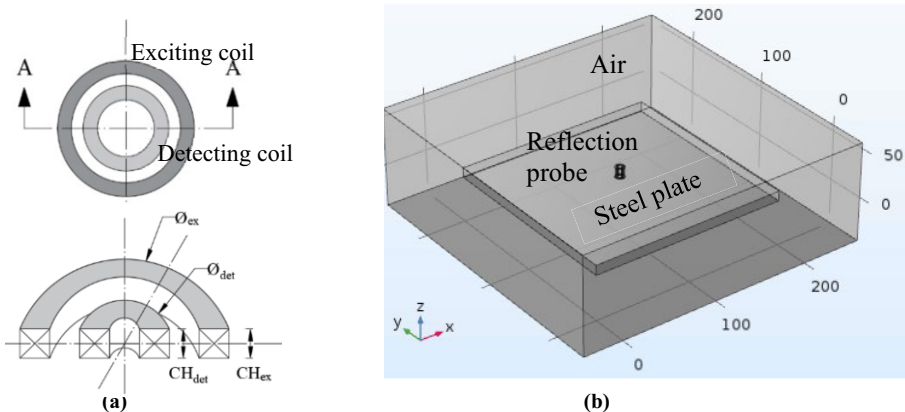
Figure 1. (a) Top view and cross-section of reflection probe, and (b) Finite element model

Here, ϕ is the coil diameter, CH is the coil height, and the subscripts *ex* and *det* denote exciting and detecting coils, respectively. The size of the computational domain

(air) is 300*300*100 mm (Figure 1(b)) and the steel plate, made up of carbon steel, is 200 mm*200mm*10mm. The boundary condition is imposed such that the tangential component of the magnetic vector potential is zero. And, the material properties assigned to the steel plate, coils, and air are listed in Table 1.

Table 1. Material properties

Properties\Domain	Air	Coils	Steel plate
Relative permeability along X-direction (μ_{rX})	1	1	100-200
Electrical conductivity (σ)	0.1	$5.998*10^7$	$4.032*10^6$

The parametric study is then conducted by varying the relative permeability of the steel plate along X-direction (μ_{rX}) from 100 to 200, lift-offs from 0 to 3 mm, and excitation frequencies of 0.5, 1, and 5 kHz for two probes 2D1CH and 10D10CH with exciting and detecting coils of diameters 2 mm and 1 mm, and 10 mm and 6mm, respectively and coil heights of 1 mm and 10 mm, respectively.

4. Numerical Results and Discussion

4.1. Phase Diagram

Instead of conventional practice of using individual eddy current indices to characterize the effect of change in influential parameters, a new, concise method, termed as Phase Diagram, is proposed to depict the variation of eddy current indices due to the concurrent changes in relative permeability and lift-off, at an excitation frequency for a probe size, in a single graph. It is constructed by plotting the real and imaginary voltages detected by the reflection probe along X- and Y-directions, respectively, as shown in Figure 2 for probe 2D1CH at an excitation frequency of 1 kHz. In doing so, a clearer and succinct view of the change in more than one parameter at a time is obtained, therefore, condensing a number of graphs into one to extract the same amount of information as will be detailed in the following section. Thus, Phase diagram is used to evaluate the effect of the eddy current influential parameters henceforth in the present study.
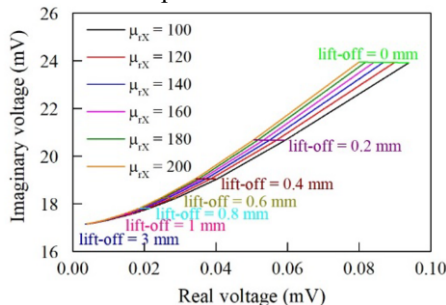
Figure 2. Phase diagram for probe 2D1CH at excitation frequency of 1 kHz.

4.2. Effect of Relative Permeability and Lift-off

It can be seen from Figure 2 that real voltage decreases and phase increases with the increase in relative permeability in X-direction of the steel plate, while imaginary voltage

is found to be less sensitive to change in relative permeability than the real voltage. Therefore, real voltage or phase could be an appropriate indicator for calibration in the future quantitative analysis. On the other hand, the well-known trend of eddy current that the detected voltages decrease as the lift-off increases is clearly observed; as the lift-off increases, the coupling between the probe and test material decreases, thus resulting in smaller value of detected voltage. In addition, the change due to relative permeability and lift-off can be easily distinguished from their distinct phase differences.

4.3. Effect of Excitation Frequency and Probe Size

Figure 3 shows the Phase diagrams for probe 10D10CH at excitation frequencies of 100 Hz, 1 kHz, and 5 kHz. It is clearly seen that at larger frequencies of 1 and 5kHz, the trend of change in eddy current indices due to relative permeability becomes non-uniform for different lift-offs. Whereas, at a lower frequency of 100 Hz, a uniform trend of change is obtained, which is invaluable for calibration of the eddy current indices for future quantitative analysis, also inferring that lower frequencies are more suited to conduct eddy current based stress measurement. However, comparing Figures 2 and 3(b), the larger probe 10D10CH showed slightly inconsistent trend of change in eddy current indices at 1kHz, while the smaller probe 2D1CH gives a consistent trend of change at the same excitation frequency. Hence, the combined contribution of excitation frequency and probe size should be taken into account for selecting a suitable excitation frequency exhibiting consistent trend of change of relative permeability, for calibration purpose.
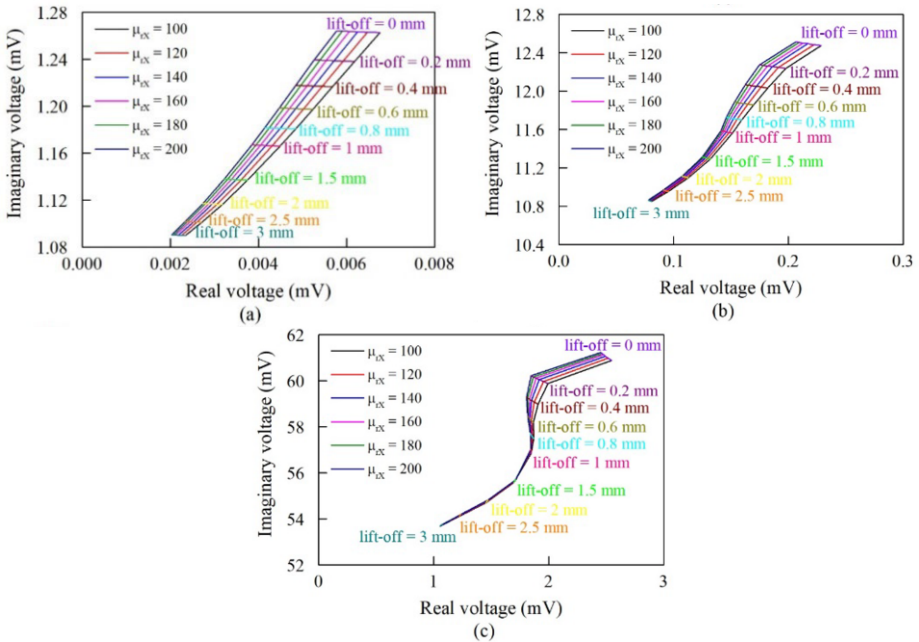
Figure 3. Phase diagram for probe 10D10CH at excitation frequencies of (a) 100 Hz, (b) 1 kHz, and (c) 5 kHz.

Furthermore, the larger probe 10D10CH showed sufficient sensitivity even at lift-offs as large as 3 mm (Figure 3), while the smaller probe showed highly diminished sensitivity at a 1 mm lift-off (Figure 2). Therefore, larger probes are deemed desirable to measure stress over a corroded surface with rust layer generating large lift-offs.

Hence, the criteria for the selection of excitation frequency and probe size for the eddy current based stress measurement is obtained from the Phase diagram as the consistent trend of relative permeability requisite of calibration and sufficient sensitivity at different lift-offs.

5. Conclusions

In the present study, a comprehensive analysis of eddy current based stress measurement was carried out through three-dimensional numerical simulations in FE software COMSOL Multiphysics 5.2a. The effects of change in relative permeability of a steel plate due to the change in stress state in a steel plate and other influential factors namely, lift-off, excitation frequency, and probe size were characterized by using eddy current indices as detected by the reflection probe. Phase diagram was established as a viable, concise method of evaluating the concurrent change in the relative permeability and lift-off at an excitation frequency for a probe size. From the phase diagram, two important criteria for the selection of excitation frequency and probe size i.e., the uniform trend of change of eddy current indices, favoring lower excitation frequency, and sufficient sensitivity to larger lift-offs, respectively were obtained. The future works in this study would be evaluation of change in eddy current indices due to application of stress in multiple directions and experimental works offering comparison to the numerical results.

Reference

[1] N. Khurram, E. Sasaki, H. Katsuchi, and H. Yamada, Experimental and numerical evaluation of bearing capacity of steel plate girder affected by end panel corrosion, *International Journal of Steel Structures* **14** (2014), 659-676.

[2] T.L. Anderson, *Fracture Mechanics: Fundamentals and Applications*, CRC Press, Boca Raton, Florida, 2017.

[3] J. W. Wilson, G. Y. Tian, and S. Barrans, Residual magnetic field sensing for stress measurement, *Sensors and Actuators A: Physical*, **135** (2007), 381-387.

[4] J. Li, W. Zhang, W. Zeng, G. Chen, Z. Qiu, X. Cao, and X. Gao, Estimation of stress distribution in ferromagnetic tensile specimens using low cost eddy current stress measurement system and BP neural network, *PloS ONE*, **12** (2017), e0188197.

[5] A. Dahia, E. Berthelot, Y. Le Bihan, and L. Daniel, A model-based method for the characterisation of stress in magnetic materials using eddy current non-destructive evaluation, *Journal of Physics D: Applied Physics*, **48** (2015), 195002.

[6] A. Akutsu, E. Sasaki, Y. Ebisawa, and H. Tamura, Analysis of corrosion damage condition of steel members using low frequency eddy current testing, *Journal of Japan Society of Civil Engineers, Ser. A1 (Structural Engineering & Earthquake Engineering (SE/EE))*, **73** (2017), 387-398.

[7] J. García-Martín, J. Gómez-Gil, and E. Vázquez-Sánchez, Non-destructive techniques based on eddy current testing, *Sensors*, **11** (2011), 2525-2565.

[8] B. D. Cullity and C. D. Graham, *Introduction to magnetic materials*, Wiley, Hoboken, New Jersey, 2009.

[9] J. M. Kim, J. Lee, and H. Sohn, Automatic measurement and warning of tension force reduction in a PT tendon using eddy current sensing, *NDT&E International*, **87** (2017), 93-99.

[10] J.-G. Liu, and W.-J. Becker, Force and stress measurements with eddy-current sensors, *Proceedings II of the SENSOR* (2001), 23-28.

[11] W. Ricken, J.-G Liu, and W.-J Becker, GMR and eddy current sensor in use of stress measurement, *Sensors and Actuators A: Physical*, **91** (2001), 42-45.

[12] W. Ricken, H.-C. Schoenekess, and W.-J Becker, Improved multi-sensor for force measurement of pre-stressed steel cables by means of the eddy current technique, *Sensors and Actuators A: Physical*, **129** (2006), 80-85.

[13] D.C. Jiles, S.J., Lee, and C.C.H. Lo, The effects of stress on magnetic properties and the use of magnetic measurements for evaluation of materials, *Conference on Resurgence of Metallic Materials* (2002).

This page intentionally left blank

Advanced Sensors

This page intentionally left blank

Capacitive Imaging for Adhesive Bonds and Quality Evaluation

Xuhui HUANG, Ciaron HAMILTON, Zonglin LI, Lalita UDPA, Satish S. UDPA and Yiming DENG[1]

Nondestructive Evaluation Laboratory, Department of Electrical and Computer Engineering, Michigan State University, East Lansing, MI 48824

Abstract. Defective adhesive bonds pose significant threats towards structural integrity due to reduced joint strength. While the nature of the adhesion of two solids remains poorly understood since adhesion phenomenon is relevant to so many scientific and technological areas. A concept that has been gaining our attention from the perspective of nondestructive testing is the properties discontinuity of the adhesion. Discontinued properties depend significantly on the quality of the interface that is formed between adhesive and substrate. In this research, discontinued electrical properties at the interface are considered. The simplified model is free from multidisciplinary knowledge of chemistry, fracture mechanics, mechanics of materials, rheology and other subjects. From a practical standpoint, this emphasizes the need to establish a good relationship between electrical properties of adhesive bonds and corresponding measurements. Capacitive Imaging (CI) is a technique where the dielectric property of an object is determined from external capacitance measurements. Thus, it is potentially promising since adhesive and substrate differ in terms of dielectric property. At the interface between adhesive and substrate, discontinuity of the dielectric properties causes abrupt changes in electric field spatial distribution and thus alters capacitance measurement. By simulating defects in adhesive joints regarding permittivity uncertainties. Further understanding of the cause of degraded adhesion quality can be obtained

Keywords. Adhesive bonds, Capacitive imaging, Coplanar electrode sensor, Electrostatic simulation model

1. Introduction

Adhesive bonds have a wide range of applications since they allow joining of dissimilar components and provides lighter structures[1]. When substrate and adhesive surface are in contact and only forming weak bonds, joint strength will be reduced, which could dramatically alter the failure strength of the joint and cause premature failure[2, 3]. To make adhesion possible, intrinsic adhesion forces across the interface between substrate and adhesion is applied, which makes interface quality a significant factor of bonding strength. However, interface usually constitute a weak link in the manufacturing as the discontinuity of the material properties causes abrupt changes in stress distribution[4]. Therefore, interface formed between the substrate and adhesion has been gaining lots of attention among recent adhesion analysis[3, 5]. Generally, any defect found in an

---

[1]Corresponding Author, Yiming Deng, Nondestructive Evaluation Laboratory, Department of Electrical and Computer Engineering, Michigan State University, Michigan MI 48824, United States; E-mail: huangxu6@msu.edu.

adhesive bond has the potential to affect the strength of the bond. According to [6] ,defect in adhesive bonds can be categorized into three types. The first type is air void, shown in Fig. 1(a) which is the inclusion of air in the adhesive. Inclusion of foreign material in the joint and adhesive is another factor illustrated in Fig. 1(b) and is bringing in complication since material properties of contamination are hardly accessible. The last category of defect is kissing bonds, which suggest that interlocking between substrate and adhesive is insufficient to form strong bonds as shown in Fig. 1(c). There are two fundamental methods in which an adhesion adheres to a substrate: mechanical interlocking and chemical interaction, with the former being investigated primarily in our research. The mechanical interlocking model is first proposed by McBain [7], which introduced mechanical keying of the adhesive into the irregularities of the substrate surface as the main source of adhesion. The motivation in this work is to model weak interlocking as kissing bonds by constructing multiple layer structure that simulate permittivity distribution of adhesion, which can be used to predict the response signal of capacitance imaging.
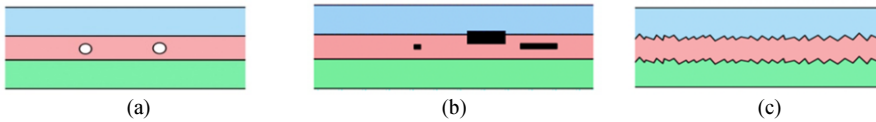
Figure 1: (a) Schematic illustration of air void;(b) Inclusion of foreign material (contamination);(c) Kissing bonds; two substrates are marked by green and blue while adhesive is denoted by light red.

A coplanar capacitive imaging (CI) probe with rectangular electrodes is applied to study adhesive bonds in this paper. The coplanar structure enable us to interrogate the sample from one side which permits a quick inspection based on coupling between sample and electric field[8]. As electric field generated from driving electrodes penetrates through the sample, it causes an electric displacement within to counter the applied field. The displacement field alters the charge stored between the sensing and driving electrodes, thus changing the inter-electrode capacitance. Therefore, the CI technique could be adopted to detect subsurface features, i.e. electrical properties of adhesion. In this work, the commercial software COMSOL Multiphysics version 5.4 is employed to numerically predict field from capacitive electrodes and response signal that were likely to be produced under experimental conditions based on finite element method (FEM). Then, details of COMSOL-based simulation model and some preliminary results are presented. In the end, imaging performance evaluation based on experimental and simulation measurement are presented.

2. Finite element (FE) based Simulation Model

Finite element (FE) modelling is employed in COMSOL to calculate the fields from capacitive electrodes and to predict the changes in response signal under various adhesion. The frequency of the voltage applied in driving electrode is 4.9 MHz which is obtained from impedance analyzer. As representative samples are placed in the fringing field region of the coplanar sensor the resonance frequency is recorded. In theory, a consequence of Maxwell's equations is that changes in time of currents and charges are not synchronized with changes of the electromagnetic fields. The changes of the fields are always delayed relative to the changes of the sources, reflecting the finite speed of

propagation of electromagnetic waves[9]. In this work, electromagnetic fields vary slowly as well as negligible coupling between the electric and magnetic fields which leads to zero magnetic induction. Therefore, quasi-static approximation is valid. This implies that it is possible to rewrite Maxwell's equations in the following manner[10].

$$\nabla \times E = -\frac{\partial \mu_0 H}{\partial t} \approx 0; \nabla \times H = \frac{\partial \varepsilon_0 E}{\partial t} + J; \nabla \cdot \varepsilon_0 E = \rho; \nabla \cdot B = 0 \qquad (1)$$

By solving the field equations with the imposed potential boundary conditions, the amount of induced charges on the sensing electrode is calculated. Thus, the relationship between capacitance of electrode pair and electrical characteristics of adhesion can be derived. With the simplified equations, the analysis of the CI system can be considered as an electrostatic analysis. The COMSOL based simulations were carried out to investigate behavior of the field and capacitance measurement given different bond conditions. Three-dimensional model that consists of a capacitor of two electrodes, attachment, lap shear sample and a holder were built up regarding different adhesion structures. It is illustrated in Fig 2(a), (b) and (c)

| (a) | (b) | (c) |
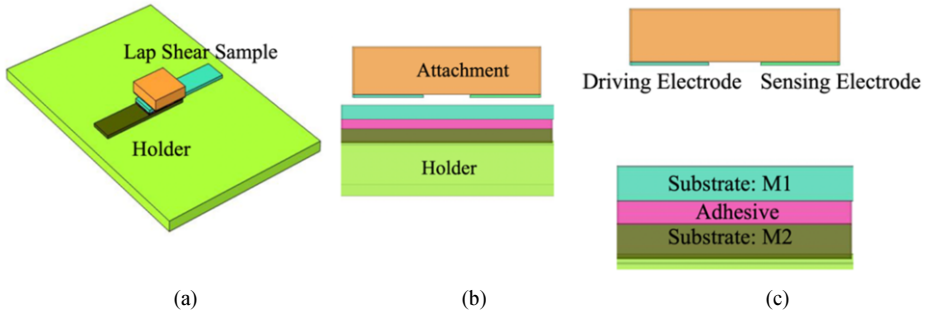
Figure 2: (a) Overview of CI simulation model with parameters described in Table 2 (b) Arrangement of substrate and holder (c) Modelling of coplanar sensor and adhesion structure

As mentioned earlier, intimate contact alone is often insufficient for good adhesion at the interface due to the presence of defects, interlocking and air bubbles. We firstly study the coupling between fringing field and lap shear sample of air voids of different sizes. For air void analysis, 9 spherical voids with size of 1% to 9% of adhesive thickness were considered. Contamination is treated as a special case of air void located at the interface of adhesion and substrate, which is modelled as a rectangular air void in simulation.

In the end, since interlocking phenomenon is often found on rough substrates, it is modelled as irregular interface between substrate and adhesive at the macroscopic level[11]. Kissing bonds are modelled as multi-layer structures and the number of knots is adopted to control roughness of interlocking surface. An increasing number of knots leads to a jump in contact area between adhesive and substrate. Electric properties for FEM modelling are illustrated in Table 1.

Table 1. Dielectric property of materials assigned in simulation

Material	Permittivity
M1	2.43
M2	2.47
Defect (Air void)	1.00
Mechanical Interlocking: layer between adhesion and M1	2.43
Mechanical Interlocking: layer between adhesion and M2	2.47
Adhesion	6.20
Contamination	1.00

Table 2. Detailed description defined in COMSOL based simulation model

Parameter	Value (length, width, thickness)
Holder	300[mm], 400[mm], 50[mm]
Substrate	40[mm], 40[mm], 10[mm]
Electrode	15[mm], 40[mm], 0.5[mm]
Substrate: M1	100[mm], 25[mm], 3[mm]
Adhesive	45[mm], 25[mm], 2[mm]
Substrate: M2	100[mm], 25[mm], 3[mm]

COMSOL-based simulation model was developed as a quasi-static problem, which assumes that the electric field is not propagating along the electrodes, and that there is no coupling between the electric and magnetic fields. To setup electrostatic FEM analysis, a set of boundary conditions were specified in Table 2 as electric potentials being applied to the given model. To accurately calculate the capacitance, it is also necessary to adopt a computation domain sufficiently large to include fringing fields.

Table 3: Boundary conditions defined in COMSOL based simulation model and corresponding explanation

Boundary Conditions	Descriptions
Ground	Sensing electrode is specified as ground along with holder and substrate, with the electric potential of 0 V while driving electrode has an applied potential of 1 V
Zero Charge Boundary	To simulate a perfectly insulating surface and is assigned to outer domain boundary
Floating Potential Boundary Condition	To simulate a perfectly conducting surface where both electrode surfaces are assigned as this BC
Computation Domain	The size of computation domain truncates the modeling space. In fact, the fringing electric field extends to infinity, but drop off in proportion to the inverse cube of the distance. They rapidly become small enough to be considered numerically insignificant. Here, it is verified that the computation domain is large enough to capture the fringing fields

Behaviour of the electric fields differs with the samples given by various conditions of adhesion, which is verified in the field contour line results. The relative closeness of the lines gives us ideas about the intensity of electric field at each point. Shown in Fig. 3(a) and 4(a), the fringing electric field emanates from the driving electrode and terminates at the sensing electrode and it can reach the inside of the testing sample through the designed air gap. The influence of adhesion on capacitive coupling can be observed as the electric field lines are distorted, thus alter the inter-electrode capacitance.
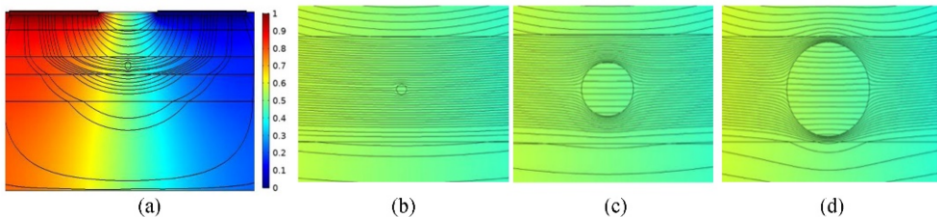
Figure 3: (a) Electric field lines distribution overview (b) air void of size 10% of adhesion thickness (b) air void of size 50% of adhesion thickness (c) air void of 90% of adhesion thickness.
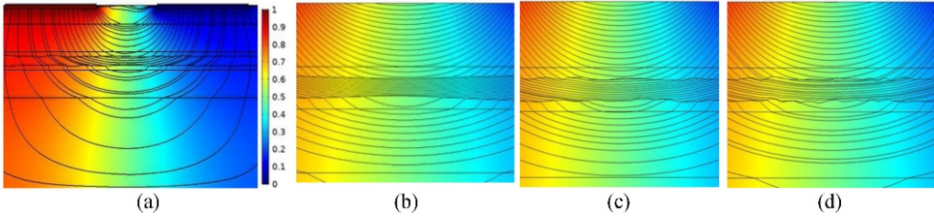
Figure 4: (a) Electric field lines distribution overview (b) irregularities associated with two interfaces generated by knots number of 20 (c) irregularities associated with two interfaces generated by knots number of 100 (d) irregularities associated with two interfaces generated by knots number of 200

In the case shown in Fig. 3(b) to 3(d), the spherical air void of various sizes is held beneath M1, placed at the center of adhesion. They are acting as dielectric resistance to the electric field since the permittivity of air is much lower than that of the sample. With larger air void presented, the field lines were pushing away as darker areas representing higher intensity of the field. The effects of interlocking, which is modelled as multi-layer structure also influence the distribution of the fringing electric field and thus impacts the charge on the sensing electrode. Therefore, they can be detected via capacitance measurement. the air gap between the specimen and probe surface will act as the dielectric media between the two electrodes of the equivalent variable capacitor, as shown in Fig. 4(a) and 5(a). Permittivity variations within the volume sampled by the probing field, such as varying lift-off distances, dent on the surface, void under the surface or other forms of defects, will result in a capacitance value change.

3. Experimental setup

The capacitive sensing setup consists of the sensor probe, and an external pick up coil is connected to a Function Generator which generates the excitation sine wave voltage of frequency ranging from 1 kHz up to 20 MHz. The measurement set up is shown in Fig 5(a). The coplanar capacitive sensor is mounted on an X-Y raster scanner and the target is placed at 1 mm above. The measurement signal is fed into the input of directional coupler and the coupler is connected to the pick-up coil of the probe. The reflected signal which carry the information on amplitude and phase difference from the pick-up coil is fed to one of the input ports of the lock-in amplifier. The reference signal from the power splitter is fed into the other input port of the lock-in amplifier. The lock-in amplifier generates voltage signals for the difference in reference and reflected signal. The output of the lock-in amplifier is fed into a National Instrument Data Acquisition card (PCIe-6341) which samples and digitizes the data using an imagining routine and the output is plotted on a computer. The output is the change in voltage signal as a function of position on the target. A low frequency directional coupler was designed for this purpose. The schematic of the imaging setup is outlined in Fig. 5(b).

<table>
<tr><td>(a)</td><td>(b)</td></tr>
</table>
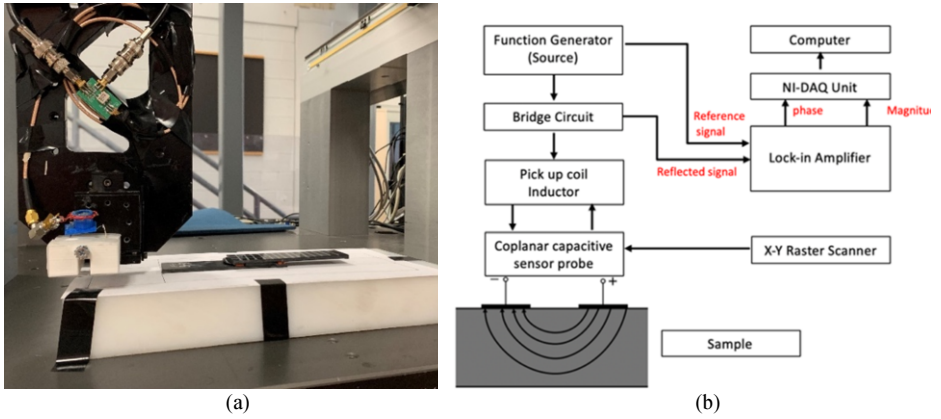
Figure 5: (a) Experimental setup (b) Scheme of the measurement system used for Adhesive bounded samples

4. Post-processing

Low frequency components extracted from both simulated and experimental results are mainly contributed by lift-off variations, coupling between fringing field and edge of sample which can mask varying adhesion indications. To enhance detectability of varying adhesion, high pass filters are generally applied for data processing. In our research, high frequency components are preserved by subtracting an approximated surface, which is also considered as a smoothing process. In this study, the smoothed value is determined by neighboring data points $N = \{x_i\}_{i=1,2,\dots}$. A local regression weight function is applied

$$w_i = \left(1 - \left|\frac{x - x_i}{d(x)}\right|^3\right)^3 \tag{2}$$

In equation (2), x is the value to be smoothed, $d(x)$ denotes the size of the span. We can infer from the equation that data points outside the span have no influence on the fit, thus it is considered as a local process. In addition, this process is very flexible, which makes it suitable when fitting a complex deterministic structure. Then we calculated

$$I = \sum_{x \in \text{Image}} \|x - \sum_i w_i x_i\|_2^2 \tag{3}$$

which is the summation of norm of subtracted value on entire region, indications of varying adhesion quality are comparable. We take defect-free sample as an example of surface approximation and it is presented in Fig. 5(a)-(b)

<table>
<tr><td>(a)</td><td>(b)</td></tr>
</table>
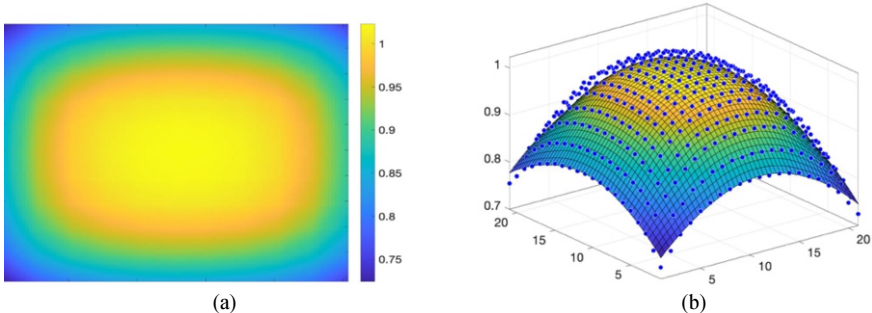
Figure 6(a) Simulated defect-free sample (good bonds) scanning results (b) Surface approximation

Table 4: Calculated *I* in terms of ratio to air void of size 0.02, simulation results are calibrated by defect-free measurements. Air void size is given in terms of percentage of adhesive thickness

Air void size ratio	1%	2%	3%	4%	5%	6%	7%	8%	9%
I	I_1	$1.00I_1$	$1.01I_1$	$1.08I_1$	$2.32I_1$	$6.95I_1$	$8.24I_1$	$8.80I_1$	$9.06I_1$

Table 5: Calculated *I* in terms of ratio to regularities generated from knots =5, simulation results are calibrated by defect-free measurements. Interlocking level representing irregularities is constructed by predefined number of knots

Interlocking level	5	10	20	40	80	100	150	200	250
I	I_2	$1.02I_2$	$1.08I_2$	$4.92I_2$	$15.44I_2$	$76.29I_2$	$925.02I_2$	$2665.9I_2$	$3737.25I_2$

Simulation of various adhesive bond conditions were designed and carried out to study the effect of air void and irregularities associated with interlocking. In Table 3, *I* exhibited larger value as increasing size of the air void. This trend is more significant in Table 4 as the number of knots increased to simulate interlocking with larger contact area. Electrical coupling between electrodes and sample varies when different interlocking and air void parameters are incorporated into the model, which are causing abrupt changes to capacitance measurements spatially. Since local changes in intensity value (measured capacitance) are captured by subtracting approximation surface. Bonding strength is inversely proportional to the value of *I* under the condition of air void as well as contamination. Compared with the results obtained from interlocking model, it can be seen in Table 4 that the irregularities associate with substrate-adhesion interface have much higher impact on the performance. From previous studies, adhesion strength is assumed to be proportional to contact area. In this way, surface irregularities could contribute to the increase of interfacial area, thus enhancing adhesive strength performance. Therefore, the relationship between bond quality in terms of interlocking and I should be positive which is opposite to the air void model. However, according to[11], it is possible to establish good adhesion between perfectly smooth surfaces. Thus, it is insufficient to conclude that mechanical interlocking would undeniably add more joint strength, which makes simulation results from interlocking model alone insufficient to draw conclusions.

5. Experimental Results Analysis

A set of experiments were performed to study the effects of adhesive bond with different qualities. To obtain information about the sample, a raster scanning system was used which controls the movement and data acquisition (DAQ) of the coplanar capacitive probe. A function generator was set up to send an excitation signal of 4.9 MHz to the driving electrode. The sensing electrode yields the reflected signal towards a lock-in amplifier. The lock-in amplifier sends the real and imaginary potential components of probe to a DAQ unit connected to the computer, in which the analogue to digital data is saved for processing.

<center>(a)   (b)</center>
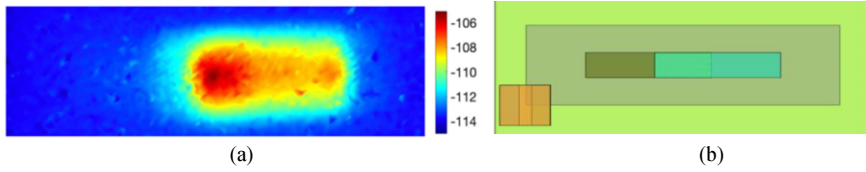
Figure 7: (a) Capacitive imaging experimental results in phase variation with scanning step size of 1mm, taken at lift-off distances of 1 mm. (b) The scan was performed at the region marked by black box.

In the experiment, CI is performed over multiple samples categorized into 13 types, representing 6 defective types of bad and mixed adhesive bond located in substrate(M1)-adhesion, substrate(M2)-adhesion respectively, plus a group of good bond samples.

<center>(a)   (b)   (c)</center>
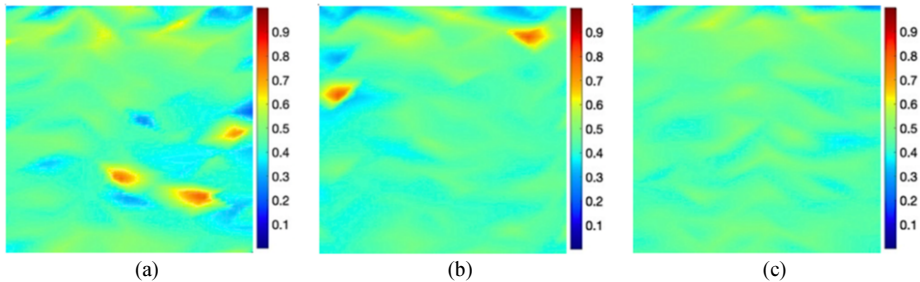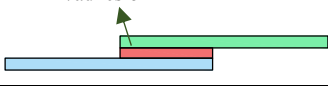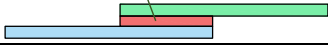
Figure 8 (a) Postprocessing results of bad bonds experimental measurements (b) mixed bonds results (c)Good bonds results

In the defective cases, sudden changes in the phase after value showed up as a brighter spot and darker shade on the colormap image. Compared with Fig. 7(a)(b), Fig. 7(c)is smoother, which suggest higher value of I for capacitive imaging of defective bond.

Table 6: Ratio of I/I_0 calculated by Equation 3 for experimental results

Interface	Bond Quality	Bond Type	Ratio of I/I_0
	Bad Bond	Type I	0.945
		Type II	1.211
M1/adhesion		Type III	1.061
	Mixed Bond	Type IV	1.197
		Type V	1.113
		Type VI	1.049
	Bad Bond	Type I	1.471
		Type II	1.079
M2/adhesion		Type III	1.028
	Mixed Bond	Type IV	1.280
		Type V	1.272
		Type VI	1.162

In the end, we calculate I for all types of bonds. The ratio of I to good bonds I_0 is then computed and compared with others in Table 5. It is worth noting that, the ratio achieves lowest value (the only one lower than 1) for bad bond of Type I. The ratio of 0.945 is in adhesive of bad bonds, Type I, is opposed to previous observations found in void simulation. This could be explained partly by interlocking model. It is thus thought interesting to embark on a study of how well capacitive imaging could detect the

presence of kissing bonds for future study as well as taking more factors that affect bonds strength into account in simulation.

6. Conclusion and Future Work

In the research, we highlighted some factors that affect adhesive bonds. Following adhesion bond analysis, three important factors: interlocking, air void, contamination are incorporated into adhesion modelling. The COMSOL-based capacitive imaging model unveils the electric field distribution over the adhesion region given different conditions. It shows that capacitance measurement not only indicates electric field distribution but also provide information about bond strength. Then, a data analysis framework based on high pass filter is proposed and being tested on both simulation and experimental study. For simulation, extracted high frequency components indicate that spatial variation of adhesion greatly affects smoothness of capacitive imaging results, which would be advantageous in quality detection, as illustrated in experimental results analysis. However, uncertainty associated with interlocking model is not studied thoroughly which leads to poor explanation of experimental results of bad bonds Type I.

Future work will involve an investigation into the more factors that influence bond strength. Which means that simulation model for various bonding quality could be modified and enhanced while different sources of uncertainties would also be interpreted in a better way. Applications of CI in the narrative is also restricted by limited access to the MUT and it is sensitive to lift-off distances as single electrode pair is adopted in this study. The robustness of capacitive imaging should be further enhanced via optimizing sensor design, especially with novel arrangement of electrodes.

References

[1]   Ebnesajjad, S., Handbook of Adhesives and Surface Preparation. Chapter 8: AdhesiveApplications and Bonding Processes. William Andrew, 2009: p. 183-208.
[2]   Jeenjitkaew, C., Z. Luklinska, and F. Guild, Morphology and surface chemistry of kissing bonds in adhesive joints produced by surface contamination. International Journal of Adhesion and Adhesives, 2010. **30**(7): p. 643-653.
[3]   Fourche, G., An Overview of the Basic Aspects of Polymer Adhesion. Part I: Fundamentals. Polymer Engineering and Science, 1995. **35**.
[4]   Harold Schonhorn and H. L. Frisch*, B.L., Murray Hill, Environmental Aspects of Adhesion and Adhesive Joint Strength. Journal of Polymer Science, 1973.
[5]   Fourche, G., An Overview of the Basic Aspects of Polymer Adhesion. Part II: Application to Surface Treatments. Polymer Engineering and Science, 1995.
[6]   Waugh, R.C., Adhesive Bonding, in Development of Infrared Techniques for Practical Defect Identification in Bonded Joints. 2016. p. 9-20.
[7]   Hopkins, J.W.M.a.D.G., In Second Report of the Adhesives Research Committee. London, 1926.
[8]   Yin, X., et al., Investigations into the measurement sensitivity distribution of coplanar capacitive imaging probes. NDT & E International, 2013. **58**: p. 1-9.
[9]   5.2, C., AC/DC Module User's Guide. 2015.
[10]   Haus, H.A., and James R. Melcher, Electromagnetic Fields and Energy. Massachusetts Institute of Technology: MIT OpenCourseWare.
[11]   Baldan, A., Adhesion phenomena in bonded joints. International Journal of Adhesion and Adhesives, 2012. **38**: p. 95-116.

Design of Power Grid Intelligent Patrol Operation and Maintenance System Based on Multi-Rotor UAV Systems

Qunying Liu[a,1], Haifeng Zeng[a], Shaojian Ni[a], Bowen Li[a], Jingsong Meng[a], and Yiguo Zhang[b]

[a]*School of Automation and Engineering, University of Electronic Science and Technology of China*
[b]*Guangzhou Polytechnic of Science and Trade*

Abstract. Complex geographical conditions and bad weather have caused great difficults to inspect transmission line of power grids. This work aims to develop a micro multi-rotor Unmanned Aerial Vehicle (UAV) system for inspecting power grid. The proposed system integrates with an intelligent robot and mobile communication networks. The high-resolution aerial images of the inspection line can be obtained to improve the operational efficiency and safety. The time period from the front-end signal acquisition to terminal decoding and playback is 1.5s for condition-based maintenance. The system supports TDD-LTE, FDD-LTE, WCDMA, CDMA2000, and other network standards. It also supports the video input signals with the resolution of standard 576i, HD 720p, FHD 1080i, and FHD 1080p. It is compatible with a variety of transmission formats and codes, help to achieve timely, comprehensive and efficient high-resolution aerial image acquisition of patrol lines, and improve operational efficiency and safety, real-time monitoring and condition-based maintenance of power transmission lines.

Keywords: Multi-Rotor UAV System, Intelligent Patrol Operation, Path Planning, Power Grid Maintenance

1. Introduction

The fault detection technology developed for the power grid includes the methods based on impedance, methods based on the traveling wave, and methods based on sample training [1]. Impedance-based methods [2] have been applied to determine the fault position typically by using voltage and current measurements from one or more terminals to calculate line impedance. The impedance-based method, especially for the one using local-measurements, is only based on reactance by ignoring the influence of fault resistance and load current. However, this method may produce significant errors caused by remote end current infeed, load impedance, power transmission angle and angle difference between the transmission line and electricity source impedances [3]. To meet the increasing demand for electricity and the safe operation of grid, automation and modernization of line patrol maintenance have increasingly shown their urgency[4]. With the development of Unmanned Aerial Vehicle (UAV) technology [5], the

---

[1]Corresponding Author, Qunying Liu, School of Automation Engineering, University of Electronic Science and Technology of China, Chengdu 611731, China; E-mail: lqy1206@126.com.

application of UAV in power grid patrol has entered an exploratory stage, it is becoming an important method for power grid maintenance. An automatic electrical equipment abnormal heat diagnosis method using infrared image sequence adopted from Unmanned Helicopter Vehicle (UHV) is proposed in [6], which automatically identifies the locations of device fault for further manual inspection. The traditional mode of operation and inspection has the following problems [7]: (1) information acquisition mode is traditional and single source; (2) equipment condition perception is restricted by power outage maintenance and off-line experiments; (3) Limited usage of advanced data utilization tools such as online monitoring, live maintenance. Under these conditions, the concept of intelligent transportation and inspection based on the modern information technology of "Big Cloud Moving" emerged as the times require [8]. UAV-assisted power grid patrol is an essential part of the three-dimensional patrol system based on Intelligent equipment. Based on the application status and possible development direction of UAV-assisted power grid patrol operation[9], this paper develops a system, namely the Power Grid Intelligent Patrol UAV System (Esmart), which significantly boosts the level of automation, intelligence and efficiency of the power grid patrol using latest computer mobile communication technology. The power grid intelligent inspection UAV system is a vital part of the three-dimensional inspection system based on the intelligent equipment and the current inspection technology research. The UAV-assisted power grid patrol can effectively solve the problems of traditional manual patrol, such as large workload, low efficiency, high risk, high cost of manned helicopter patrol, complex flight approval procedures, and limited operating environment. With the development of application technology in the UAV industry [10,11,12], UAV-assisted power grid patrol will provide a safe, efficient and comprehensive patrol mode for power grid patrol to meet the needs of daily power grid patrol, fault patrol, and emergency rescue.

   This work aims to develop a micro multi-rotor UAV system for power grid inspection. The proposed system adapts to various patrol scenarios by combining the key technologies in the intelligent robot, mobile communication, and geographic information. The intelligent patrol UAV system and software for the power grid, namely Esmart, is developed independently based on the iOS mobile operating system. Automated intelligent control software system for deep customization of Power Patrol operation. The main functions of the system include: KML, Excel files import, flexible flight parameter setting, automatic route planning, one-button takeoff and landing, automatic operation, intelligent safety inspection, real-time image transmission. Panoramic acquisition module, refined patrol module, channel/tree barrier patrol module, and rapid mapping and other intelligent business operation modes can meet the data acquisition needs of various application scenarios, can timely, comprehensive and efficient access to high-resolution aerial photographs of patrol lines, improve operational efficiency and ensure operational safety, real-time monitoring and condition-based maintenance of power transmission lines.

2. Micro multirotor multispectral UAV system equipment (UAV carrier multi-sensor integration)

2.1. The system specifications

The micro multi-rotor multi-spectral UAV system equipment is mainly composed of a micro multi-rotor UAV and a multi-spectral camera. The multi-spectral camera is used for acquisition band range including (450-520nm), (520-600nm), (630-690nm), (760-900nm) and RGB. Therefore, the processing and analysis of the multi-spectral and multi-band images rely on professional software, which provides a scientific basis for water quality by detecting and analyzing the spectral information in different environments as well as engineering monitoring.

Figure 1. Micro multirotor UAV system equipment

The micro multirotor UAV system equipment is shown in Figure 1. The detail parameters of the UAV system are shown in the following. The product positioning: professional film and television and commercial aerial photography machine weight: 1380g; Hovering accuracy: vertical: /-0.1m (ultrasonic working range); /-0.5m level:/-0.3m (within the working range of visual sensor): /1.5 m. Lift speed: maximum rise speed: 6m/s (motion mode) ,maximum drop speed: 4m/s (motion mode). flight speed 20m/s (motion mode). flight altitude: 6000 m. Flight time about 28 minutes. Wheelbase 350mm.Propeller 9450S quick-release paddle. Tele-controller: Operating frequency band: 2.4-2.5GHZ. Operating voltage:7.5v. Receiving gain: 10dB±1. Emission gain: 15dB±1. The input power range: 3~20dBm. The maximum output power is 4W(36dBm). Operating current: 435Ma@Pout28dBm9V; Noise coefficient ≤ 2.5 db. Transmission delay ≤ 1us. The operating temperature: 40~80℃. The control distance: 5,000m (No interference, no shielding); CE: 3500mm.

In this system, a Multi-spectral sensor is embedded. A 2 mega-pixel monochromatic image sensor collects data on the discrete spectral band: green light (550nm, bandwidth 40nm), red light (660nm, bandwidth 40nm), red edge light (735nm, bandwidth 10nm), and near-infrared light (790nm, bandwidth 40nm). The supported image sensor settings include green light, red-edge light, near-infrared light, RGB and so on. In addition, the system contains a 16 mega-pixel RGB trichromatic image sensor. It also includes a magnetometer, a Wi-Fi wireless network signal interface. The micro USB host port connects multispectral sensor to the sunshine sensor. The Micro USB port equipment connects multispectral sensors and unmanned drivers. The other components of the multispectral sensor are used as the inertial navigator.

3. System Functions

Esmart, which responsible for data acquisition of the power grid intelligent patrol UAV system as shown in Figure 2. Esmart is a flight control software of intelligent aerial survey UAV developed based on the iOS mobile operating system and Xinjiang SDK. It integrates functions of automatic cruise, route planning and auxiliary control. It also supports common aircraft types in Xinjiang and capture power line images as well as environment information, which are important for decision making and understanding failure mechanism in long-term studies.

Figure 2. Functional architecture of intelligent patrol UAV system in the power grid

Esmart is customized in-depth according to the characteristics of Power Patrol operation. It has KML, excel file import, flexible flight parameter setting, automatic route planning, one key takeoff and landing, automatic operation, intelligent safety inspection, real-time image transmission and other general functions. Panoramic acquisition module, fine inspection module, channel / tree barrier inspection module and rapid mapping and other intelligent business operation modes can meet the data collection requirements of various application scenarios, and can obtain high-resolution aerial photos of inspection lines in a timely, comprehensive and efficient manner, by which the Esmart can improve the operation efficiency and ensure the operation safety of UAV system. It can be further developed for Power Grid Intelligent Patrol Operation and Maintenance System.

It develops the following modules to satisfy various data acquisition of transmission/distribution lines in power industry: (1) Panoramic acquisition module, which is used for aerial photography acquisition of 360-degree panoramic images, mainly used for channel inspection of transmission and distribution lines and substation inspection, and can quickly acquire 360-degree panoramic images on site; (2) Fine patrol module, which is used for fine photographic inspection of key equipment's and key parts on poles and towers, and image collection of every potential defective part to provide data support for later intelligent classification and defect analysis; (3) Channel/tree barrier patrol module, which is used for Fully automatic patrol of corridors and corridors of lines can be realized by combining images in the later stage, which can provide reliable basis and guarantee for avoiding potential safety hazards caused by tree barrier problems; (4) Rapid mapping, which can be used to collect orthophoto and oblique photographic data of platform and sheet areas, can be realized in the later stage. Three-dimensional modeling can be widely used in planning, infrastructure, maintenance, monitoring and other processes in the power industry; (5) coordinate management, which is used to

update the coordinates of line poles and towers, facilitates the daily maintenance of basic data of power equipment, and improves the accuracy of internal network system data.

3.1. The Intelligent Control system of UAV Inspection (automatic Inspection path Planning of UAV)

To improve the efficiency of UAV inspection and realize the standardization of UAV inspection, an automatic patrol path planning technology of UAV is developed in this work. The proposed method plans a patrol route according to the positions of power grid towers, the status of the signal channel, environmental barriers, orthophoto image acquisition and tilt photography. For the route planning of orthography and tilt photography in fast mapping, path is calculated by using the inverse triangle tangent method [13] and the position of touch point on the screen of the mobile device. The multiple parameters of KML, images and videos from panoramic acquisition will be processed and monitored through feature extraction and information mining for health monitoring with spatial geographic information data, abnormal diagnostics and further prevention including condition-based maintenance.

Specifically, the patrol route of the channel or tree barrier is automatically planned by calculating the route inspected by the UAV based on the imported line file tower coordinates, the overlap parameters of the flight beat, and the parameters of the aircraft flight. Fast mapping (orthophoto and tilt photography) selects the mapping area on the map through manual interaction, then the route inspected by UAV can be automatically calculated according to the overlap parameters of aerial photography and the parameters of aircraft flight. After the route is calculated, the multi-rotor UAV enters to the autonomous flight mode. For the failed UAV, such as the whom have completed their mission or lost signal connection with the controller, will return to the departure point automatically. In addition, when the operation area is too large to allow the UAV to complete the required mission, the UAV can divide the patrol route into different sections automatically according to the battery level. Each section contains a break point to allow the UAV to land and replace the battery.

In addition, each module of the system contains mission management function, which records the mission of each flight, including the parameters of flight setting, and flight path, supports task viewing and can be loaded and executed again. In this way, the standardization of inspection operation can be guaranteed, and the efficiency of inspection is improved as well. The inspection situation of UAV can be transmitted back in real-time through satellite transmission and local wireless communication. The field situation can be displayed in controller intuitively, which provides reference for command and decision making. Ground station monitoring and remote image transmission system are compatible with the patrol multi-rotor UAV system, micro multi-rotor multi-spectrum UAV system, as well as the power patrol inspection and water conservancy patrol remote monitoring system to provide remote emergency monitoring service. The system platform supports the real-time and stable transmission of the pictures captured by the multi-rotor UAV in the sky to the ground wireless image transmission and remote-control receiving equipment. The video transmitter receives digital or analog signals from the UAV, then generates and transmits audio and video signals to the monitoring center through various network modes such as EDGE, EVDO, TD-SDCDMA, WCDMA and LTE, then broadcast the multi-media data to various platforms (TV, smart phones, and etc.) through the server for display. The whole work process of the system is shown in Figure 3.
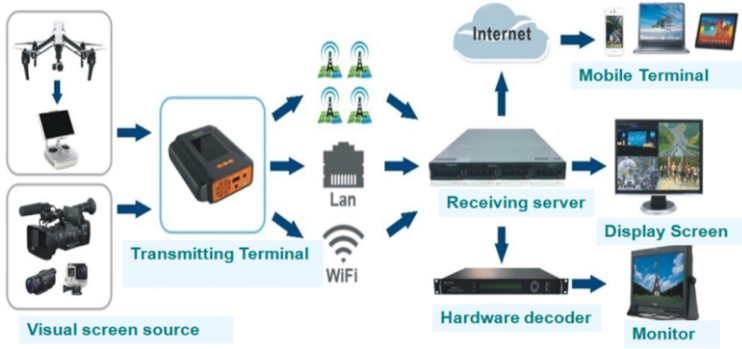
Figure 3. The work process of system

The image remote transmission terminal is based on multi-link aggregation technology and H.265 coding technology real-time video transmission terminal. Equipped with three built-in 4G modules and a USB extension interface, while supporting Wi-Fi and wired network access. The image transmission enhancement terminal is a bidirectional power amplifier developed for 2.4GHz band and in accordance with IEEE 802.11b/g/n standard. The product matches the frequency expansion techniques such as direct sequence (DSSS), orthogonal frequency division reuse (OFDM). Time Division Duplex (TDD) fast microwave detection technology and linear power amplifier technology are used to greatly expand the radio frequency communication distance under the condition that the transmission rate of 802.11b/g/n wireless equipment remains unchanged.

3.2. Intelligent Flight

The UAV has a set of intelligent operation functions, including automatic operation mode, one-button take-off, self-operation, automatic return. The workflow of the one-button automatic takeoff is as follows: set the flight mode and parameters, start the task, the software starts to automatically check the flight parameters, as shown in Figures 4 and 5, after completing the pre-flight safety check, slide key, one-button take-off of the aircraft, self-operation, automatic execution of flight tasks. The workflow of the full-automatic operation mode is as follows: click the automatic take-off key after completing the pre-flight safety check. When the flight altitude reaches 2/3 of the flight altitude of the first break point, the aircraft automatically adjusts the direction of the platform to the preset angle of the platform. After arriving at the first breakpoint, it carries out automatic flight and execution tasks according to the preset route (e.g. taking photos).

Flight status information is transmitted to controller in real time to allow the operator to check the flight status of the UAV. In case of emergency (such as signal lost or insufficient energy), one-click return, or suspension can be made to allow the aircraft return to the last take-off point or hover in the position temporarily.

Figure 4. Take off to carry out a mission

Figure 5. Suspend flight or return by one click

4. Conclusion

The inspection for power grid has always been a challenging task, because of the complex structure of electrical equipment and the physical distribution characteristics of the power grid. In addition, the long monitoring distance, harsh geographical and climatic conditions bring huge difficulties to manual inspection. To achieve low-cost high efficiency inspection of power grid, this paper presents the development of an intelligent UAV based power grid inspection system, which improves the standardized line management and emergency command. The rapid and intelligent collection processing and application of spatial geographic information data in the key areas of power grid line corridor in collaboration with failure diagnostics and health management are realized, by which the needs of fine grid inspection, channel inspection, fault inspection and special inspection can be met. One of the premises of this conclusion is that the control inputs aren't delayed. However, according to the experiment results, there is often a delay in the actual communication, and the force and torque output by the actuator such as the motor are delayed. Moreover, the response may not keep up with the change of the control amount, so the forces acting on the aircraft are delayed, which may cause the response of the flight system to be slow or even unstable. Now the problem is that when a disaster occurs at early warning, it is too easy to be impacted to implement the command of disaster monitoring and auxiliary disaster relief, providing timely, intuitive, and comprehensive auxiliary decision-making basis for disaster control. It has

practical and efficient advantages for power grid inspection and has the prospect of promotion and application. As a result, it is recommended to promote the application in a wider range of industries.

References

[1] M. Majidi and M. Etezadi-Amoli, A new fault location technique in smart distribution networks using synchronized/nonsynchronized measurements, IEEETransactionsonPowerDelivery,2018 ,33(3):1358–1368.

[2] Tirath Pal S. Bains, Tarlochan S. Sidhu, Zhihan Xu, Ilia Voloh and Mohammad R. Dadash Zadeh, Impedance-Based Fault Location Algorithm for Ground Faults in Series-Capacitor-Compensated Transmission Lines, IEEE Transactions on Power Delivery, 2018,33(1):189-199.

[3] M. Kezunovic, Smart Fault Location for Smart Grids," IEEE Transactions on Smart Grid, vol.2, no.1, pp.11-22,2011.

[4] Li Bingqiang, Wang Qian. Applying unmanned autonomous helicopter to transmission line inspection[J]. Shandong Electric Power, 2010, 171 (1):1-4(in Chinese)

[5] Chenhao Zhang, Guobing Song, Ting Wang and Liming Yang, SingleEnded Traveling Wave Fault Location Method in DC Transmission Line Based on Wave Front Information, IEEE Transactions on Power Delivery,2019,34(5):2028-2238.

[6] Zhang Wenfeng, Peng Xiangyang, Chen Ruimin, Cnen Chi, Deng Chaoyi, QIAN Jinju, XU Wenxue. Intelligent Diagnostic Techniques of Abnormal Heat Defect in Transmission Lines Based on Unmanned Helicopter Infrared Video[J]. Power System Technology,2014,38(5):1334-1338

[7] Jinju Qian, Xiaoming Ma, Ke Wang, Lin Yi, Xiaoyang Peng, Zhangquan Rao. Application and effect of large-scale Inspection Power Lines by Using Large Unmanned Helicoper in Guangdong Power Grid. Guangdong Electric Power, 2016,29(5):124-129.

[8] Zhonghua Hu, Min Zhao, Min Yao. Research and Development Trend of Path Planning for Unmanned Air Vehicle[J]. Avionics Technology, 2009, 40(2):24-29.

[9] Xiangyang Peng, Qing Zhong, Zhangquan Rao. Intelligent Diagnostic Techniques of Transmission Lines Corona Dischare Defect based on Ultraviolet Detection from Unmanned Aerial Vehicle. High Voltage Engineering,2014,40(8):2292-2298.

[10] Jianchao Li , Liming Wang , Xinwei Shen. Unmanned Aerial Vehicle Intelligent PatrolInspection System Applied to Transmission Grid.2018 IEEE Conference on Energy Internet and Energy System Integration (EI2),pp.1-6.

[11] Homma, R. Z., Sohn, O., & Bose, R. C. Analysis of the recognition and localisation techniques of power transmission lines components in aerial images acquired by drones. CIRED-Open Access Proceedings Journal, 2017(1), 29-32.

[12] Zhuofan Xu, R. Wei, Qirui Zhang, Kai Zhou and Renke He, Obstacle avoidance algorithm for UAVs in unknown environmentbased on distributional perception and decision making, 2016 IEEE Chinese Guidance, Navigation and Control Conference (CGNCC), Nanjing, 2016, pp. 1072-1075.

[13] H. Kandath, T. Bera, R.Bardhan and S. Sundaram. Autonomous Navigation and Sensorless Obstacle Avoidance for UGV with Environment Information from UAV, 2018 Second IEEE International Conference on Robotic Computing (IRC), Laguna Hills, CA, 2018, pp. 266-269.

Edge Detection of Metal Thickness of Electromagnetic Acoustic Transducer Based on Super-Heterodyne Phase-Sensitive Detector

Zhichao CAI [a,1], Zhenyong ZHAO[a], Lan CHEN[a], and Guiyun TIAN[b]
[a] School of Electrical and Automation Engineering, East China Jiaotong University
[b] School of Engineering, Newcastle University, Newcastle, UK, NE1 7RU

Abstract. In order to improve the thickness measurement accuracy of metal plate, a new method based on phase detection thickness is proposed. Two modes of ultrasonic echo are generated by electromagnetic acoustic transducer (EMAT) at the edge of specimen, and super-heterodyne phase-sensitive detection technique is used to collect the phases of the ultrasonic, then the thickness information of the tested specimen is obtained accurately. Firstly, the finite element model of EMAT is built, and the time-domain characteristics of acoustic echo are analyzed. Secondly, the 0º and 90º phase detection on echo signal are detected by the super-heterodyne phase-sensitive detection system. Finally, the relationship between phase information and specimen thickness is analyzed. The results show that the detection method, which based on super-heterodyne phase-sensitive detector of edge mode conversion, can realize the detection of metal plate thickness, and the phase error range is controlled within 0.23%.

Keywords. edge detection, super-heterodyne phase-sensitive detector, EMAT, finite element analysis

1. Introduction

In general, ultrasonic testing method is used for the thickness measurement of metal materials, the principle of piezoelectric ultrasonic energy exchange is often used to produce ultrasonic wave for the detection of solid materials. But piezoelectric transducers (PZT) needs to be coated with coupling agent in the detection, and the testing specimen needs to be pretreated, so this kind of direct contact detection method requires higher detection environment, higher detection cost and lower detection efficiency [1]. Besides, PZT usually excites primary wave (P wave), but the shear wave (S wave) with the same frequency has better resolution detection, so the higher resolution detection can only be achieved by applying higher excitation frequency.

Compared with PZT, the electromagnetic acoustic transducer (EMAT) has the characteristics of non-contact detection, no coupling agent and no pretreatment on the specimen surface in testing [2], at the same time, EMAT is more likely to excite S wave, under the same resolution detection, the excitation frequency of EMAT is only half of

---

that of PZT [3]. Therefore, the research of electromagnetic ultrasonic testing technology based on EMAT has been more extensive in recent years [4].

There are two main methods for measuring metal thickness by EMAT: 1. Pulse-echo method; 2. Electromagnetic acoustic resonance (EMAR) method. In the pulse-echo method, the thickness of metal specimen is calculated by using the peak data of two echo signals[5], when the metal thickness is relatively thick, the echo signal will be very weak, higher requirements are put forward for using pulse echo method to accurately measure echo signal. In the EMAR method, which has a high detection efficiency, the damage evaluation of 2.5mm-thick aviation aluminum plate can be carried out accurately by using EMAR method [6]. However, it is still difficult to the peak data due to the influence of acquisition frequency and noise [7]. Moreover, the EMAR method needs to increase the number of excitation cycles to realize the superposition of adjacent echoes, this will cause strong main pulse interference, so this method is often used in measuring sheet metal [8].

Based on the above shortcomings, a detection method based on ultrasonic edge detection and super-heterodyne phase-sensitive detector is proposed in this paper, accurate phase information is used to feedback thickness information of specimen. The rest of the paper is organized as follows : Section 2 introduces the principle of EMAT detection at the edge of the specimen. The principle of super-heterodyne phase-sensitive detector is demonstrated in Section 3. Section 4 introduces finite element modeling simulation and analysis, followed by the discussion in Section 5.

2. The principle of EMAT detection at the edge of the specimen

The edge detection of EMAT is similar to the principle of traditional EMAT thickness measurement, the difference is that EMAT is placed on the edge of metal material to produce multi-mode ultrasonic. When a high frequency excitation pulse current is fed into the coil, the eddy current will be induced in the skin depth of the metal surface, and the vibration of those particles are affected by Lorentz force under the static magnetic field provided by Nd-Fe-B permanent magnet, S wave and P wave propagating downward are generated in the interior of the specimen, Rayleigh wave (R wave) propagating along the surface is generated on the side of the specimen.

| (a) t=1μs | (b) t=6μs | (c) t=11μs | (d) t=20μs |
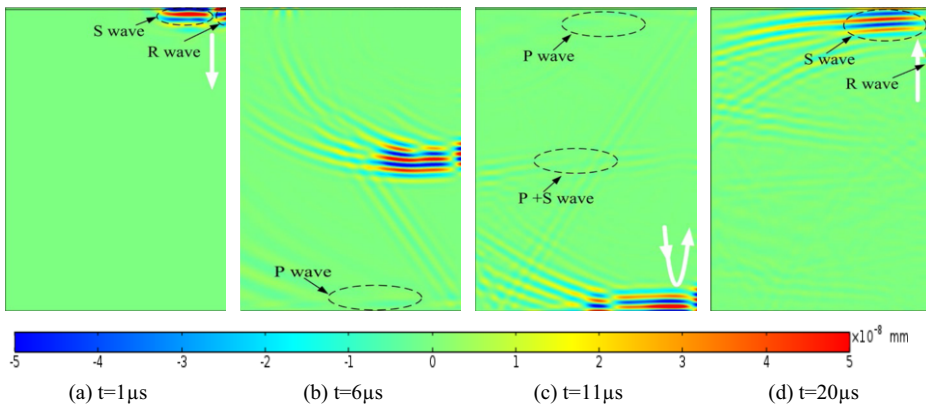
Figure 1. The propagation process of ultrasonic wave in the specimen

To simulate the ultrasonic propagation process, a two-dimensional finite element model of electromagnetic ultrasonic transceiver is established, the frequency of electromagnetic ultrasonic excitation F_S=3MHz, The displacement distribution of ultrasonic wave at different time in Y-axis direction is shown in Figure 1. At the beginning, EMAT excites both S wave and R wave on the surface of metal specimen, because ultrasonic wave speed of different modes is different, with the increase of propagation time, two modes of ultrasonic are gradually separated. When the ultrasonic wave hits the bottom of the specimen, it will reflect the ultrasonic wave and propagate to the top of the specimen according to the original path, and the magnetic flux in the coil will be changed. According to Faraday's electromagnetic induction law, the time domain voltage signal containing two modes of ultrasonic echo will be induced in the coil.

According to the induced voltage signal received by the coil, and through the mathematical relationship:

$$\Delta T = \frac{2n \cdot (V_S - V_R) \cdot D}{V_S \cdot V_R}, n \in N^+ \tag{1}$$

the time ΔT between the peak value signal of adjacent S wave and R wave can be calculated. Where, V_S is S wave velocity, V_R is R wave velocity, n is the positive integer, D is the thickness of the specimen.

3. The principle of super-heterodyne phase-sensitive detector

In general, the thickness information of the specimen can be fed back through formula (1), but the high noise and low detection efficiency of electromagnetic ultrasonic hinder the accurate extraction of the time-domain signal. However, the super-heterodyne phase-sensitive detection method can effectively extract the echo signal by improving the signal-to-noise ratio, and obtain more accurate detection signal information. As shown in Figure 2.
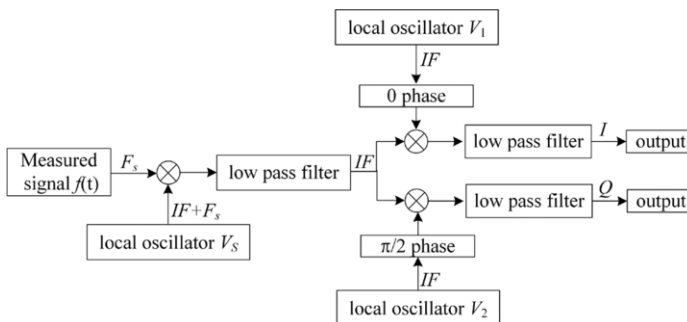
Figure 2. The principle of super-heterodyne phase-sensitive detector

The measured signal is regarded as a sinusoidal pulse signal $f(t)$ with Gaussian window modulation with exciting frequency F_S:

$$f(t) = A_t e^{-\alpha(t-\tau)^2} \sin[2\pi F_s t + \varphi] \tag{2}$$

where A_t is the excitation current amplitude, α is the bandwidth coefficient, τ is the time coefficient, φ is the phase angle of the measured signal.

The local oscillator generates a local oscillation signal V_S with frequency of $IF+F_S$, $f(t)$ is mixed with V_S through the mixer, and the mixed signal contains two frequencies of IF and $IF+2F_S$, when the mixed signal passed through the low-pass filter, intermediate frequency signal with frequency IF is only retained. According to the principle of super-heterodyne phase-sensitive detector, two reference oscillation signals V_1 and V_2 with frequency IF and phase difference $\pi/2$ are generated by the local oscillator. They are multiplied with intermediate frequency signal by multiplier in order to obtain the same phase signal and orthogonal signal. These two signals are respectively filtered through the low-pass filter to remove the high frequency signals, and the differential frequency signals I and Q are retained and output.

$$I = A_g e^{-\alpha(t-\tau)^2}\sin\varphi \tag{3}$$

$$Q = A_g e^{-\alpha(t-\tau)^2}\cos\varphi \tag{4}$$

A_g is constant, including the total gain and conversion coefficient. According to formula (3) and formula (4), the phase φ of the received signal is deduced:

$$\varphi = \arctan\frac{I}{Q} \tag{5}$$

4. Finite element simulation and analysis

Finite element simulation software is used to simulate the ultrasonic field of EMAT, the echo voltage signal is received in the spiral coil as shown in Figure 3(a).
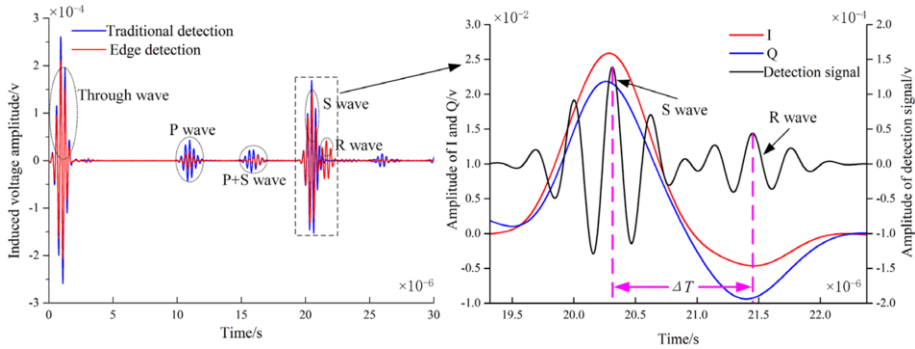
Figure 3. (a).Received time domain signal (b). Super-heterodyne phase-sensitive detection

According to the formulas (2) to (4), the S wave and R wave signals are processed through the super-heterodyne phase-sensitive detection system, and the result is shown in Figure 3(b).

When the thickness of the specimen change slightly, it is difficult to determine thickness change information by pulse-echo method. However, the phase change is very

significant after the phase detection of 0° and 90°, because for every 0.1μs increase in the time, the phase angle increase by 108 degrees after the super-heterodyne phase-sensitive detection. Therefore, the change in phase information can be used to reflect the change in specimen thickness accurately. But the phase angle φ_S of S wave and phase angle φ_R of R wave are both between (-90°, 90°), in order to determine their true phase relationship, the S wave and R wave data are processed, as shown in Figure 4. Where, j is S or R.
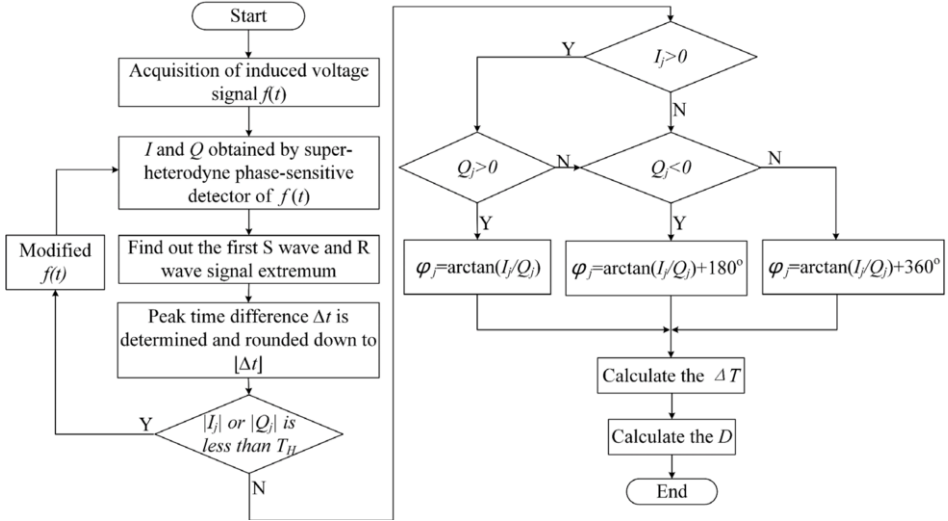
Figure 4. Data processing flow chart

There is the echo noise interference in the output signals I and Q by the super-heterodyne phase-sensitive detection system, which makes the phase extremum of the noise generated in addition to the S wave and R wave. Finally, this will lead to inaccurate extraction of the extremum of the signals I and Q. In order to solve this problem, the threshold T_H is set in this paper, T_H is generally not less than 0.6 times the maximum value of I or Q between (-90°, 90°).It means that when the extreme value of $|I_j|$ or $|Q_j|$ is lower than T_H, the induced voltage signal $f(t)$ needs to be corrected. The specific correction method is to change the initial phase of the excitation signal, because the signal $f(t)$ is affected by the initial phase of the excitation signal. Finally, the extremum of the output signal I and Q will be changed to meet the threshold T_H.

According to the phase signal I or Q of the adjacent S wave and R wave, the peak time Δt is determined and rounded down to $\lfloor \Delta t \rfloor$. From the phase angle relation:

$$\Delta T = \frac{\varphi_R - \varphi_S + 2 \lfloor \Delta t \rfloor \pi}{2\pi F_s} \tag{6}$$

the time ΔT can be obtained, and the thickness D can be calculated accurately.

In order to verify the feasibility of the super-heterodyne phase-sensitive detection method, aluminum material in this paper is taken as the research object, its geometric structure is shown in Figure 5(a), which is used to simulate the tiny change of thickness of material due to uneven friction. Then the phase value φ calculated by sine signal I and cosine signal Q is compared with the theoretical phase value, and its phase error curve is

shown in Figure 5(b). The results show that the maximum relative error of phase value is 0.23%, and the maximum error of aluminum thickness is 0.077mm.
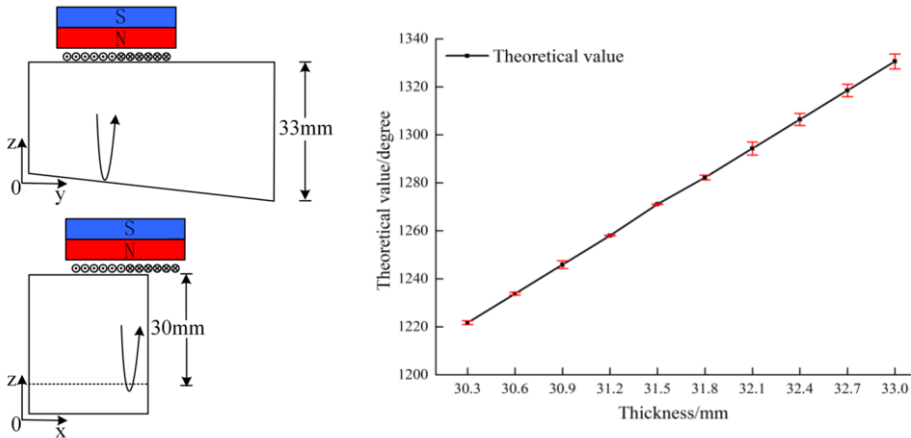
Figure 5. (a) Geometry of specimen, (b) Phase error curve

5. Conclusions

In this paper, a method based on super-heterodyne phase-sensitive detector of edge mode conversion is proposed to measure specimen thickness. The results show that the method has a higher accuracy for the thickness, and a higher resolution for the specimen with slight changes of thickness. This method is superior to the traditional pulse-echo method, and the results prove the potential of this method in thickness measurement. However, the R wave signal is weak in the simulation process. Further research will be conducted on how to optimize the transducer to enhance the detection effect.

References

[1] Putkis O., Dalton R.P., Croxford A.J., The anisotropic propagation of ultrasonic guided waves in composite materials and implications for practical applications, *Ultrasonics* **65** (2016),390–399.

[2] Peng Chen, Delai Han, Qiangfu Cai, Meiquan Liu, Research progress in electromagnetic acoustic testing, *Foreign Electronic Measurement Technology* **31** (2012),18-21.

[3] Shujuan Wang, Riliang Su, Xiaoyang Chen, Lei Kang, Guofu Zhai, Numerical and experimental analysis of unidirectional meander-line coil electromagnetic acoustic transducers, *IEEE Transactions on Ultrasonics, Ferroelectrics, and Frequency Control* **60** (2013),2657-2664.

[4] Peng Chen, Delai Han, Qianfu Cai, Meiquan Liu, Research progress in electromagnetic acoustic testing, *Foreign Electronic Measurement Technology* **31** (2012) ,18-21.

[5] Jingpin Jiao, Zhaoqing Yu, Wenhua Liu, Qiang Zhang, Electromagnetic acoustic thickness measurement method of thin liquid layer based on wavelet transform , *Chinese Journal of Scientific Instrument* **34** (2013),588-595.

[6] Mingxi Deng, Experimental study of evaluation of damage in metallic plates using electromagnetic acoustic resonance techique, *Technical Acoustics* **30** (2011),327-330.

[7] Nian Jiang, Zhaoba Wang, Youxing Chen, Yu Chen, The experiment parameters of the steel-sheet thickness measurement by electromagnetic ultrasonic, *Chinese Journal of Sensors and Actuators* **28** (2015),498–502.

[8] Zhichao Cai,Lan Chen,Zhenyong Zhao,Guiyun Tian, Research on electromagnetic acoustic resonance for plastic deformation in Q235steel, *Chinese Journal of Scientific Instrument* **40** (2019),153-160.

Design and Application of a Magnetoelectric Composite Sensor for Pipeline Defect Detection

Haibo Zhu[a] , Huadong Song[a,1], Xiaoting Guo[a] , Wenqiang Zhang[a] ,
Yunpeng Song[a] , Chunfeng Xu[a] , Yueting Yu[a]
[a] *Shenyang Academy of Instrumentation Science Co., Ltd, Shenyang, 110043, China*

Abstract. Nowadays, there are 160000 kilometers of pipelines in China. How to get more pipeline information in pipeline integrity management is a vitally important research topic. This paper designs a magnetoelectric composite sensor which is suitable for the non-destructive detection of the buried pipeline. according to the defect characteristics. this paper introduces the working principle, structure and characteristics of the composite sensor. Combined with the advantages of the magnetic sensor which is sensitive to the volume defects of the tube wall and the high frequency eddy current sensor which is sensitive to the near-surface defects of the tube wall on the principle of magnetic flux leakage, it realizes the identification and evaluation of the inner and outer wall defects of the tube wall. In this paper, the pipeline in the traction test field is taken as the test object. The test results show that there are 37 defects picked up by the magnetic sensor and 19 defects judged by the eddy current sensor.

Keywords. Sensor, eddy current, defect of pipeline, defect recognition, pull testing

1. Introduction

The pipeline is known as the national energy artery, which vital important to the national energy supply. With the increase of the service life of the pipeline, due to the role of corrosion and stress, various types of defects will appear in the pipeline. Therefore, it is necessary to detect the pipeline regularly and effectively, eliminate the defects in time, and reduce the occurrence of pipeline rupture accidents.

At present, various nondestructive testing systems have been proposed, such as the Conventional ultrasonic testing system, electromagnetic ultrasonic testing system, eddy current testing system and magnetic flux leakage detection systems[1-2]. The existing detection systems and detection probes can not meet the existing detection requirements duo to the complex structural characteristics and various forms of defects of the inner wall of the pipeline. Therefore, how to develop a new detection system to solve the above problems has become an urgent problem. This paper introduces the principle, application conditions and advantages of MFL testing and eddy current testing, and designs a

---

[1] Corresponding Author: Huadong Song, professor of engineering. The main research direction is nondestructive testing. E-mail: huadong_song800713@126.com.

magnetoelectric composite sensor for nondestructive testing of oil and gas pipelines. The probe is used in the dragging test of the detector in the pipeline, and the test data show that it can not only detect the pipeline defects, but also distinguish the inner wall defects and the outer wall defects, which has far-reaching significance for the subsequent engineering application of the probe.

2.Detection principle and characteristics of magnetoelectric composite sensor

The principle of MFL detection is to use the high permeability of ferromagnetic materials to measure the change of permeability in ferromagnetic materials due to the existence of defects [3-4]. The principle of pipeline magnetic flux leakage detection is shown in Figure 1. The two parts of the pipe wall are the longitudinal section view of the pipe. The upper pipe wall has a defective bottom wall. During the detection process, the permanent magnet magnetizes the pipe to be tested. When the tube wall is complete, defect-free and the material of the tube wall is uniform, all the magnetic lines pass through the magnetic circuit composed of the tube wall, permanent magnet, wire brush and soft iron. When the tube wall reaches the saturation magnetization state, if the tube wall is defective, part of the magnetic flux passing through the defect will still pass through the magnetic circuit, but a small amount of magnetic lines will be twisted at the defect, and leak to the outside of the tube wall along the edge of the defect So as to form magnetic flux leakage in the surrounding air. When the sensor passes through the defect free pipe wall, the output voltage does not change, because there is no magnetic flux leakage change. When the defect pipe wall passes, the voltage change achieves the purpose of defect detection [5-6]. The analysis of magnetic flux leakage signal can accurately judge the defect.
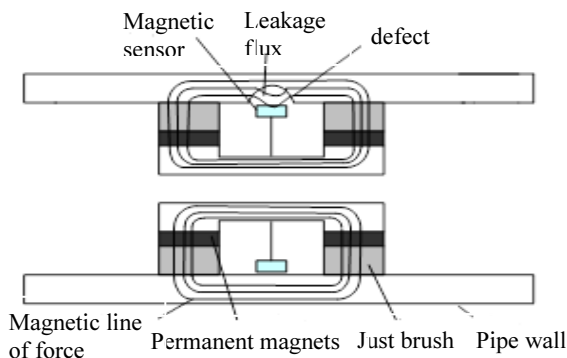
Figure 1. Schematic diagram of pipeline magnetic flux leakage detection

The application of magnetic sensor in magnetic flux leakage detection system has high corrosion sensitivity, which is suitable for high temperature, cold, underwater and other harsh environments. However, the magnetic sensor can only detect the volume defects of axial length, circumferential width and radial depth of the wall of the pipeline. In addition, even if the magnetic sensor can detect the defects in the pipe, it can not distinguish whether the defect locates at the inner wall or the outer wall.

According to the electromagnetic induction law, when the magnetic flux in the closed metal conductor changes, the closed induction eddy current will be generated in the

conductor, which will hinder the change of the magnetic flux [7-8]. The working principle of the eddy current displacement sensor is shown in Figure 2.
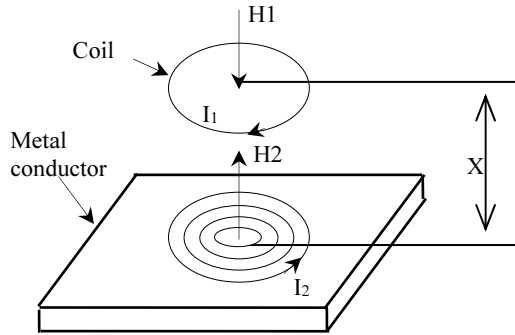
Figure 2. Working principle of eddy current displacement sensor

The induction coil is excited by the alternating current signal, which produces Joule heat and hysteresis loss, which causes the loss of alternating magnetic field energy and changes the equivalent impedance Z of the sensor. The factors affecting the impedance Z include the conductivity of the measured conductor σ, permeability μ, excitation frequency f of the coil, displacement X between the sensor and the measured conductor, as long as these factors only change the displacement X, If other factors do not change, the equivalent impedance Z of the sensor will become a single function Z (x) of displacement x, and the change of Z can reflect the change of X, so as to realize the purpose of measuring displacement X after linearization.

Eddy current testing system is a non-destructive testing method based on the principle of electromagnetic induction. It has the advantages of fast response, high sensitivity, non-contact and no need for coupling medium. Therefore, it is especially suitable for the detection of inner wall defects of metal pipes [9-10]. However, the sensors in the traditional eddy current testing system generally have the problems of poor consistency, easy detection of the signal, hard to achieve high detection efficiency and high resolution simultaneously, and the poor adaptability to the detection object [11-12].

3. System implementation of magnetoelectric composite sensor

The digital three-axis magnetic sensor transmits the collected leakage magnetic field to the ARM-STM32 control system of the probe through the IIC protocol. At the same time, the eddy current sensor will keep generating eddy current signal. The returned signal will be received by the eddy current coil receiving circuit and transmitted to the ARM-STM32 control probe system via the SPI protocol. It is transmitted to the data acquisition system 1.5m away via the data output driver after being collected and stored by the control system.
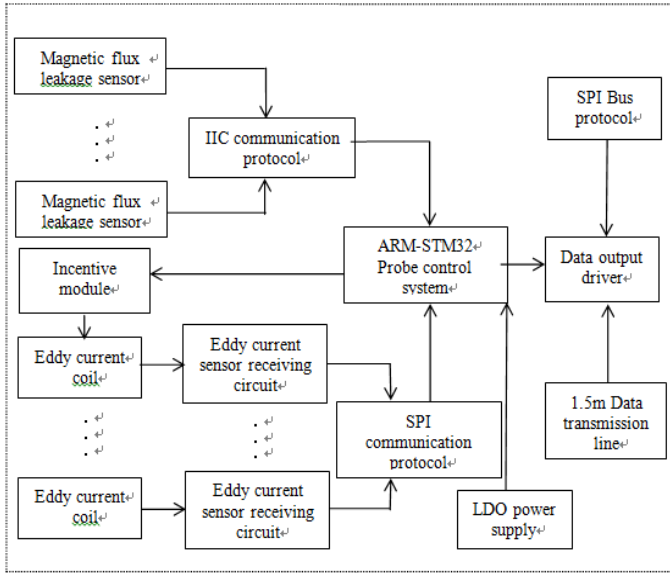
Figure 3. Composite sensor structure block diagram

Using PCB printed eddy current sensor coil instead of the traditional manual winding coil reduces coil volume and improves coil stability and uniformity.

After the eddy current sensor is excited, the eddy current signal generated is collected by the receiving circuit, and the receiving circuit diagram is shown in Figure 4.
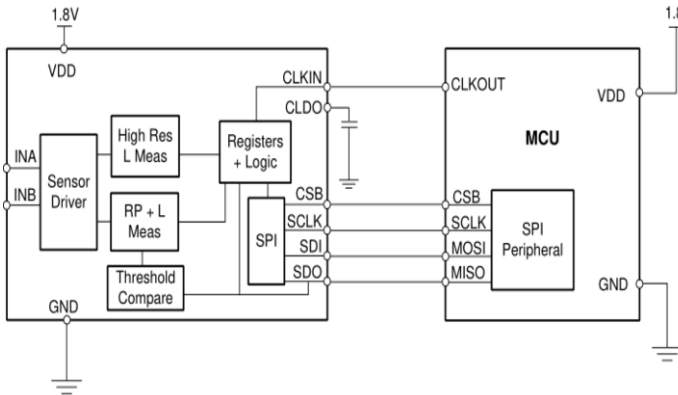
Figure 4. Eddy current sensor coil receiving circuit structure block diagram

The two ends of the eddy current sensor are connected with the signal terminals INA and INB of the LC oscillation circuit. The LC circuit provides excitation voltage, excitation frequency and other relevant parameters during the working process of the eddy current sensor. When the eddy current sensor coil detects a defect in the inner tube wall, its impedance and inductive reactance will change. They are detected by the inductance measurement circuit. Once the inductance value is processed by the register and logic processor, the threshold value is compared and converted into the output signal of the SPI communication protocol to identify the defects of the pipe wall.

As shown in Figure 4, the CSB, SCLK, SDI and SDO signals output by the SPI communication protocol are transmitted to the MCU acquisition system through the

transmission line. The MCU host selects ARM-STM32 series chips, where CLKIN represents the external time base clock input, CLDO connects 15nf capacitor from pin to GND, CSB indicates the start of SPI transmission protocol, SCLK represents the SPI communication protocol clock input, SDI indicates SPI data input Connected to the MOSI of the SPI master, SDO indicates that the SPI data output is connected to the MISO of the SPI master.

Sensor detection data is transmitted to ARM-STM32 control probe system through the SPI protocol. The system includes a high-precision clock module, a stabilized voltage power module, a memory module, a bus protocol module and a FATFS file management module display module for collecting and storing sensor data to display the current output signal.

4. Traction test results and analysis

The magnetoelectric composite sensor is installed on the inner detector of the pipeline, which is used to detect the defects of the pipeline and distinguish whether they are inner wall defects or outer wall defects.
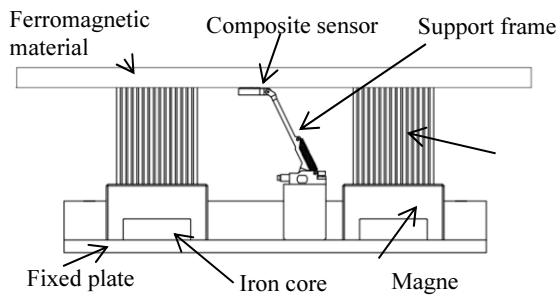
Figure 5. Magnetoelectric composite sensor detection device

In order to verify the reliability and functional integrity of the sensor, the pull test of the corresponding structure is carried out, and the state diagram of the structure before and after the pull test is shown in Figure 6.

Figure 6. State degree of equipment traction test

The detection results of the digital three-axis magnetic sensor of the composite probe are shown in Figure 7.
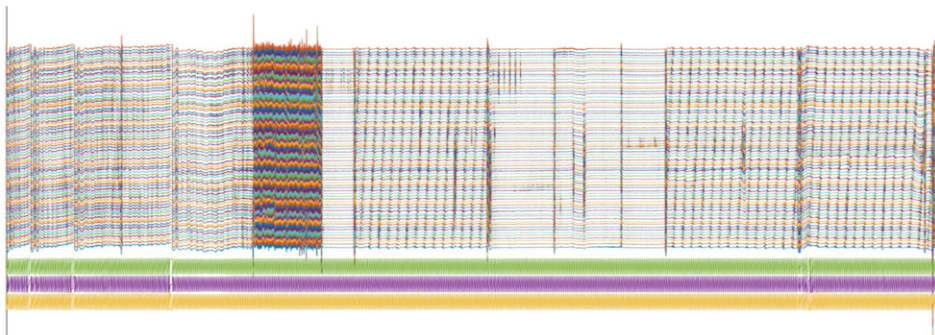
Figure 7a. Z-axis test data of composite probe
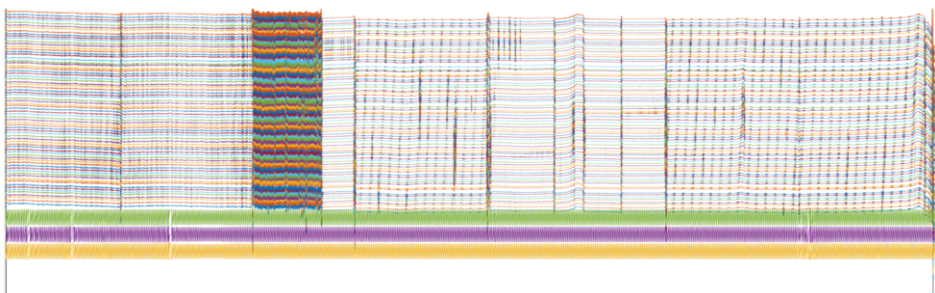
Figure 7b. Y-axis test data of composite probe
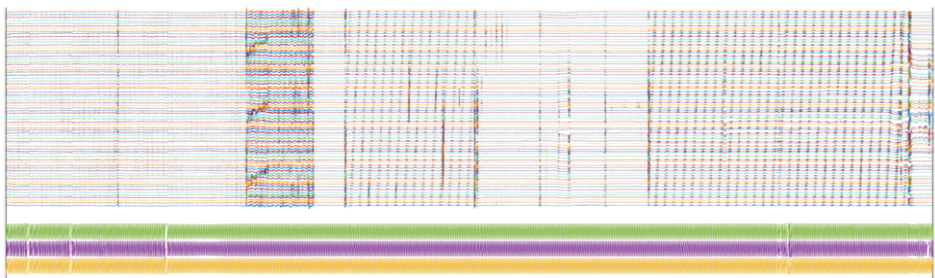
Figure 7c. X-axis test data of composite probe
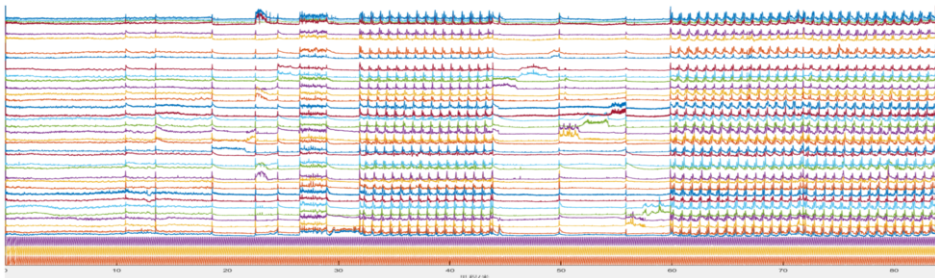
Figure 7d. Composite probe inductive reactance signal
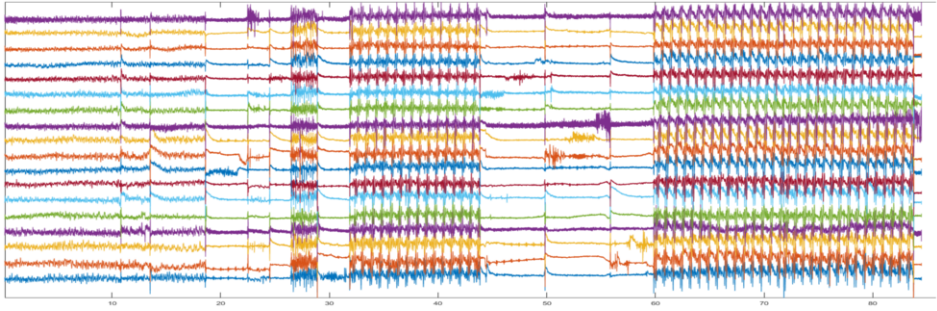
Figure 7f. Composite probe impedance signal

Figure 7. Composite sensor detection defect results

Through Figure 7, it can be seen the signals collected by the composite probe in the traction test pipeline. a, b and c display the data collected by the digital three-axial magnetic sensor, d and f display the impedance and inductive reactance signals collected by the eddy current sensor. Through comparison, it can be seen that the inspection data of Z-axis and Y-axis of composite probe are obvious, and the inspection data of x-axis can only be used as the supplement of the inspection data of other directions; the eddy current sensor is more sensitive to the straight weld and girth weld of pipeline, as well as some defects.

The function of the composite probe is mainly to distinguish the internal and external wall positions of the pipeline defects. According to Figure 7, it can be seen that the data of a certain section of the pipeline is relatively messy. This section is actually a seamless steel pipe laying, and a large number of characteristic defects are artificially designed. The following article mainly analyzes the detection data of the composite probe in this section. The data shown in figure8 (Because there are many defects that can not be pointed out completely, the red circle position is a relatively obvious defect).

It can be seen from Figure.8 that the pipe section with the disorderly signal is laid by two seamless steel pipes. The seamless steel pipe has a certain influence on the detection of the magnetic sensor, and its data fluctuates greatly, but the existence of pipe defects can also be analyzed. According to the construction data, the defects of the front section are all the inner wall, and the defects of the rear section are all the outer wall. According to the detection of the magnetic sensor, the inner and outer walls of defects can not be distinguished in three directions. However, eddy current sensor detection shows that no matter the inductive reactance signal or impedance signal, it will not be affected by the straight seam steel pipe. The front section of the pipe shows defects, and the rear section shows no defects.
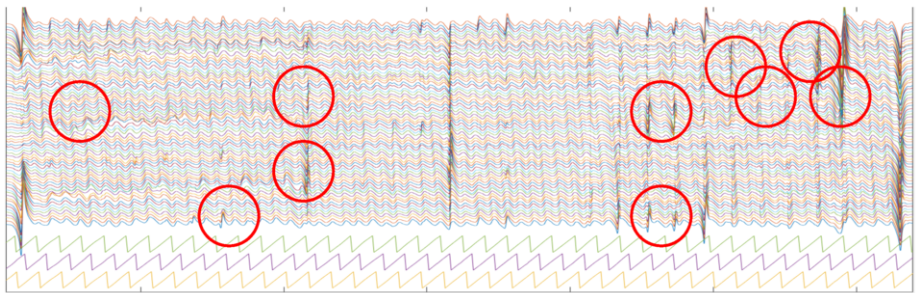
Figure 8a. Z-axis test data of composite probe
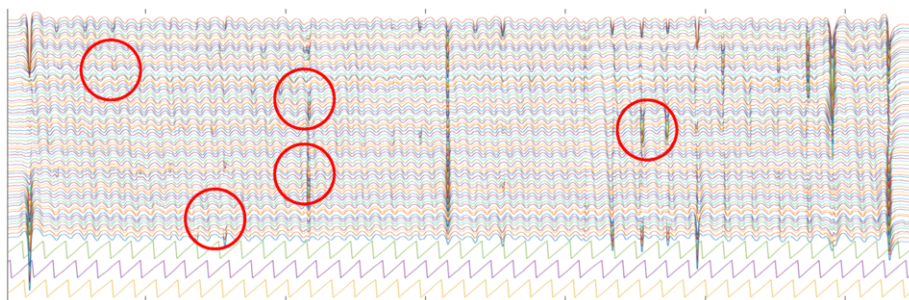
Figure 8b. Y-axis test data of composite probe
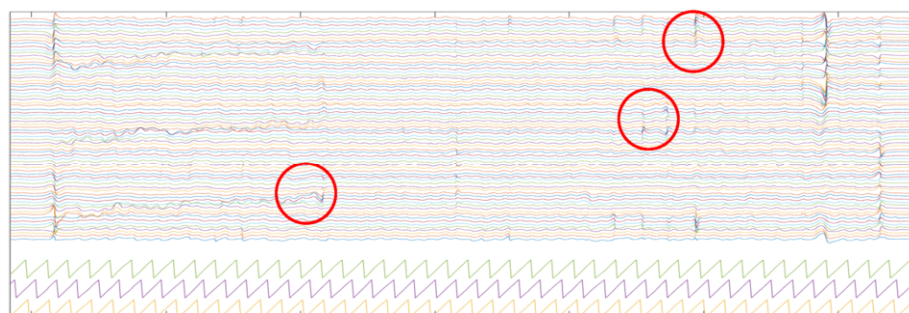
Figure 8c. X-axis test data of composite probe
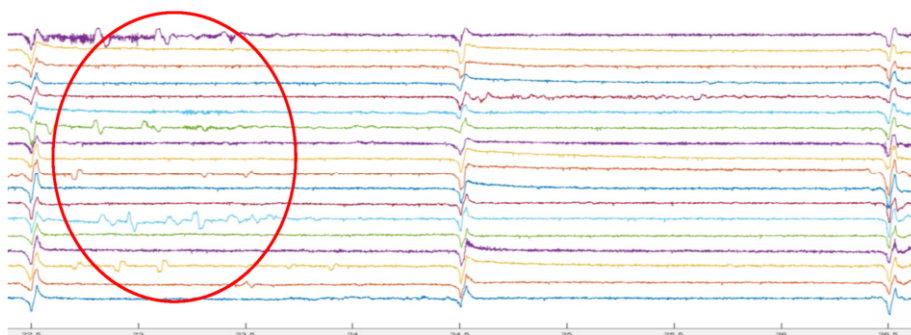
Figure 8d. Composite probe inductive reactance signal
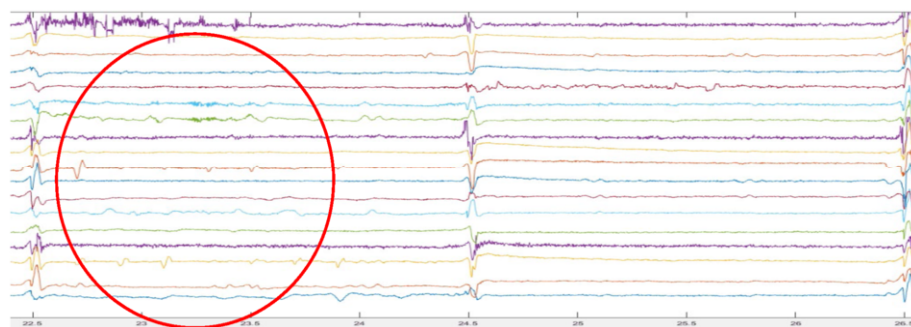
Figure 8f. Composite probe impedance signal

Figure 8. Composite sensor detection defect results

5.Conclusion

In this paper, a composite sensor system for the detector in the pipeline is designed and developed. The principle, structure and function of the system are introduced in detail. The practicability and function of the probe are verified by pull test. Traction test results show that:

1. Both digital three axial magnetic sensor and eddy current sensor can detect the girth weld and spiral weld of pipeline.

2. The composite probe can not only detect the defects of the pipeline, but also distinguish the inner and outer walls of the pipeline defects.

3. For seamless steel pipes, eddy current testing has better stability and can supplement the magnetic signal very well.

References

[1]   Xu Wei, Huang Song-ling, Zhao Wei, Xu Peng, Method and Implementation of Oil and Gas Pipeline Deformation Detection Based on Low Frequency Eddy Current, *Electrical Measurement and Instrumentation* 47 (2010), 10-15.
[2]   Bao Qing-jun, Shuai Jian, Research Progress in Detection Technology of Oil and Gas Pipelines, *Journal of Modern Chemical Industry* 46(2017), 298-301.
[3]   Huang K, *3-D Defect Profile Reconstruction from Magnetic Flux Leakage Signatures Using Wavelet Basis Function Neural Networks*, Ames IA: Iowa State University, 2000.
[4]   Huang Song-ling, et al, *Theory and Application of Magnetic Flux Leakage Detection in Oil and Gas Pipelines*, Beijing: Mechanical Industry Press 9(2013), 25-26.
[5]   Paulsen J.A, Jiles, A Magnetic Imaging System for Evaluation of Material Conditions Using Magnetoresistive Devices, *I-EEE Tansactions on Magnetics* 39(2003), 3453-3455.
[6]   Wang Fu-xiang, Feng Qing-shan, Zhang Hai-liang, Song Han-cheng, Chen Jian, Pipeline Feature Recognition Based on Three-axis Magnetic Flux Leakage Detection Technology, *Non-destructive Testing* 33(2011), 79-84.
[7]   Xu Lin, Wang Heng, Huang Wei, Li Boquan et al, Simulation of Eddy Current Sensor Based on COMSOL Finite Element Method, *Journal of Drainage and Irrigation Machinery Engineering* 12(2015), 1097-1104.
[8]   Yan Yan-chun, Zhu Xiao-zhi, Discussion on Performance Test Requirements of Eddy Current Testing System Based on NB/T47013-2015, *Non-destructive Testing* 39(2017), 69～72.
[9]   Dong Shao-hua, Ji Shou-hong, Zhang Wei-wen, Zhao Xiaoli et al, Development and Industrial Application of G4 High-definition Composite Detector, *Pipeline Protection 1* (2018).
[10] Ding Zhan-wu, He Ren-yang, Liu Zhong, Simulation Analysis and Quantization Model of Defect Signals in Pipeline Magnetic Flux Leakage Detection, *Non-destructive Testing* 35(2013), 30-33.
[11] Ye Ling-wei, Feng Wei. Overview of Eddy Current Testing Research, *Fluid Dynamics* 6(2018), 1-4.
[12] Xiao Chun-yan, Zhu Heng-jun, Qi Hong-yuan et al, Electromagnetic Detection Model of Ferromagnetic Material Hardness, *Journal of Metrology* 23(2002), 294-298.

Analytical and Numerical Modelling

This page intentionally left blank

Modeling of Non-Linear and Hysteretic Magnetization Effects in Transient Potential Drop Measurements

Øyvind PERSVIK [1] and Zhiliang ZHANG

Department of Structural Engineering, Norwegian University of Science and Technology (NTNU), 7491 Trondheim, Norway

Abstract. We have compared transient potential drop measurements on ferromagnetic steel rods with finite difference simulation assuming that the magnetization varies as a quadratic function of the applied field. Good agreement between simulation and experimental measurement is achieved and the results are discussed in terms of the Rayleigh law of magnetization.

Keywords. transient, potential drop, skin effect, non-linear magnetization, Rayleigh law

1. Introduction

Modeling of the response of electromagnetic sensors is a key step in their use for structural health monitoring (SHM) and the evaluation of material properties of ferromagnetic materials such as carbon steel. Commonly, non-linearity in magnetic properties is ignored due to the expediency of assuming linear properties. On the other hand, understanding the implications of non-linear effects can be important when interpreting data. Additionally, non-linear and hysteretic effects are characteristic features of ferromagnetic materials, related to irreversible motion of domain walls in the presence of material defects [1], which may be exploited in non-destructive evaluation (NDE). An example of this principle is the magnetic barkhausen noise (MBN) method [2] where the measured response is due to discontinuous magnetization jumps.

Here we consider the transient potential drop method [3,4] where, by using a pulsed current as the source, sensitivity to varying depths is achieved rapidly and by experimentally simple means. Due to the skin effect the variation of material properties and geometrical features with depth is manifested as a time dependent variation in the transient potential drop analogously to the frequency dependence in alternating current potential drop (ACPD) [5]. Furthermore, recording the transient potential drop due to a pulsed current is analogous to the use of pulsed current in eddy current testing.

The Rayleigh law of magnetization is commonly used as a simple model for the magnetization of ferromagnetic materials at low fields [6]; by including a quadratic term in the field dependence it can be viewed as a first approximation to non-linear magneti-

---

[1]Corresponding Author: Øyvind Persvik; E-mail: oyvind.persvik@ntnu.no.

zation. In a previous similar work [7] ACPD was used to measure the parameters in the Rayleigh law by using the finite difference method to obtain the steady state response due to a sinusoidal drive current. Also, non-constant permeability in steel has been studied in a different approach by interpreting the results of four-point ACPD measurements on steel plates using a linear model and a frequency dependent complex relative permeability [8].

In this paper we report on initial results from modeling of non-linear and hysteretic effects in transient potential drop measurements on ferromagnetic steel. Our approach is similar to that described in [7], notably by using cylindrical rod samples and finite difference simulation, but our main motivation is to compare transient measurements with numerical simulation in the time domain directly. Firstly, this is to validate the approach for predicting transient signals due to pulsed currents when models assuming constant permeability are inadequate. Secondly we discuss the results in view of the Rayleigh law by comparing the reversible and hysteretic responses to unipolar drive current.

2. Transient Potential Drop
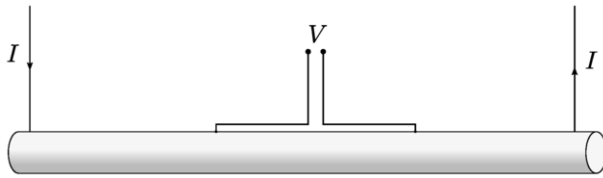
Figure 1. Transient potential drop measurement on a metal rod.

In the transient potential drop method the time domain response due to a pulsed current is measured. Assuming a homogeneous conducting rod (Figure 1), with radius a, conductivity σ and constant relative permeability μ_r, the response to an injected step-like current with exponential rise time τ, $I(t) = I_0 \left(1 - e^{-t/\tau}\right)$, is given by [9]

$$V(t) = V_0 \left(1 - e^{-t/\tau} + \sum_{n=1}^{\infty} \frac{e^{-t/\kappa_n} - e^{-t/\tau}}{1 - \tau/\kappa_n}\right). \tag{1}$$

Here $V(t)$ is the voltage measured between contact probes on the surface separated by a distance l, V_0 is the response in the direct current (DC) limit, $V_0 = l/\pi\sigma a^2$, and $\kappa_n = \mu\sigma a^2/\beta_n^2$ where β_n is the n-th zero of the Bessel function of the first kind of order 1. The parameter $\kappa = \mu\sigma a^2$ is a characteristic decay time of the transient.

Figure 2 shows an example response to a current pulse of width T with exponentially rising and falling edges. The skin-effect voltage represents the summation term in Eq. (1) and is the result of induced eddy currents due to the time-varying injected current.

2.1. Finite difference simulation

In time dependent potential drop problems, quasi-static electromagnetic fields due to a time-varying current source are obtained from Maxwell's equations and are used to cal-
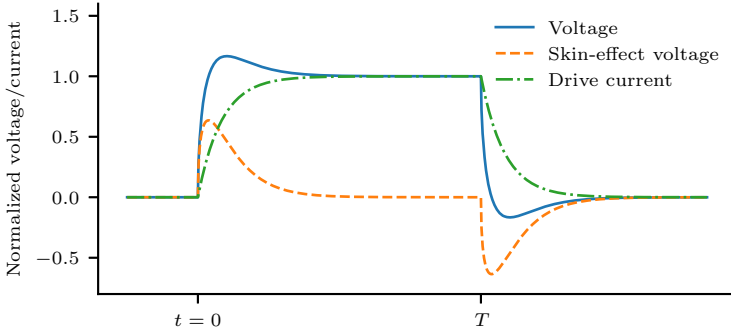
Figure 2. Example of the transient response to a pulsed drive current with rise time $\tau = \kappa/10$ and $T = 1.2\kappa$.

culate the surface potential. An axially symmetric field $\mathbf{H}(\rho,t) = H(\rho,t)\hat{\phi}$ in a cylindrical rod is governed by

$$\nabla^2 H - \frac{H}{\rho^2} = \mu_0 \sigma \left(1 + \frac{\mathrm{d}M}{\mathrm{d}H}\right) \frac{\partial H}{\partial t}. \tag{2}$$

Here M is the magnetization in the material and the right hand side corresponds to the rate of change of the magnetic flux density $\partial B/\partial t$ in Faraday's law.

A first approximation to non-linear magnetization is to assume that the magnetization varies with field strength according to $\mathrm{d}M/\mathrm{d}H = \alpha + \beta H$. To determine the transient potential drop numerically a finite difference scheme is formulated in terms of normalized variables $u = H/\Delta H$, $x = \rho/a$, and $\bar{t} = t/\kappa_\alpha$ with $\kappa_\alpha = (1+\alpha)\sigma a^2$. This gives the non-dimensional equation

$$\nabla^2 u - u = (1+qu) \frac{\partial u}{\partial \bar{t}} \tag{3}$$

where the parameter $q = \beta \Delta H/(1+\alpha)$ reflects the (non-linear) field dependence. For simplicity an explicit scheme is implemented numerically. In Figure 3 a simulated transient is compared with the exact formula, Eq. (1), verifying that the numerical results converge to the expected transient solution in the case of constant μ_r.

The form of $\mathrm{d}M/\mathrm{d}H$ gives a quadratic field dependence corresponding to the Rayleigh law describing the initial magnetization at low fields by $M_i = \chi_i H + \eta H^2$, with initial susceptibility χ_i and the Rayleigh constant η, and the minor hysteresis loop traced out by a a field that varies between $\pm H_0$ by $M_h = (\chi_i + \eta H_0)H \pm \frac{\eta}{2}(H_0^2 - H^2)$.

In the case of unipolar current excitation, typical in pulsed measurements, the magnetic field varies between 0 and $H_0 = I_0/2\pi a$ on the surface and its maximal value decreases linearly with the radial distance to the center of the rod where it is zero in accordance with Ampere's law. The initial response from a demagnetized state follows $dM_i/dH = \chi_i + 2\eta H$ and induces both reversible and irreversible magnetization (indicated in Figure 4) whereas the reversible response to subsequent pulses is assumed to follow $dM_r/dH = \chi_i + \eta H$. In other words the difference between the initial (hysteretic) response and the reversible response is a factor of 2 in the non-linear parameter. This reflects that one half of the quadratic term in the initial magnetization curve is attributed to
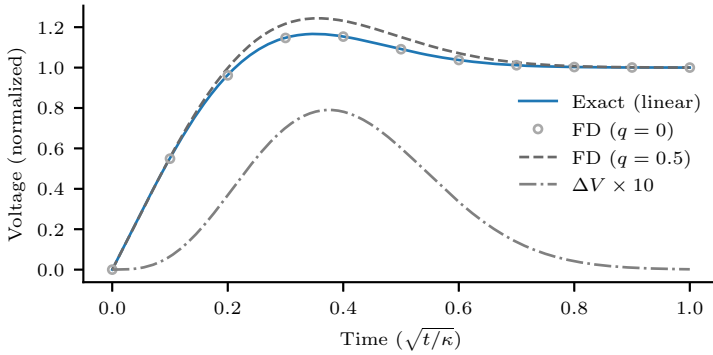
Figure 3. Comparison between theory, Eq. (1), and finite difference simulation ($N_z = 500$) assuming constant μ_r ($q = 0$) and rise time $\tau = \kappa/10$. Also shown is the simulation result for $q = 0.5$ indicating the effect of non-linear magnetization.

irreversible magnetization. This is considered in the following as a guide to interpreting the experimental measurements in terms of the Rayleigh law.
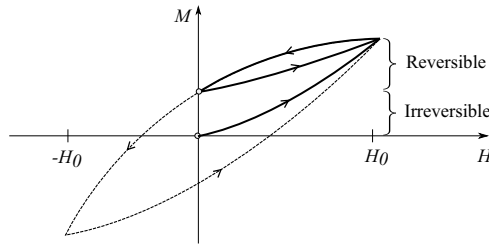
Figure 4. Schematic illustration of minor hysteresis loops. The outer loop is traced out by a field varying between $\pm H_0$. The center point M_0 corresponds to an initial state that may be reached by a demagnetizing cycle where the applied field is reduced gradually to zero.

3. Experiment

The experimental setup consists of an arbitrary waveform generator (AWG), a drive current amplifier, and a PC oscilloscope to record the waveforms of the transient potential drop and the drive current.

Measurements were made on a cylindrical rod sample made of structural steel (grade S235), having a nominal diameter $2a = 10$ mm and length of 150 mm. The sample was initially demagnetized in a solenoid. The current was injected by clamps mounted at the ends and the potential drop was measured using spring-loaded pins separated by a distance $l = 70.6$ mm. In a typical measurement the AWG is programmed with a pulse that rises and falls exponentially. By triggering the AWG the response to a single pulse, or several in succession, is recorded. To achieve a magnetization state corresponding to the center of the minor hysteresis loop for a given magnitude of the drive current (see Figure 4), a low frequency sinusoidal current was injected into the sample with a

magnitude reduced from 1 A to zero over several cycles. The drive current in the potential drop measurements has a rise time of 2 ms and an amplitude of 0.8 A ($H_0 \approx 25$ A/m).

4. Results and Discussion

Figure 5 shows the results of fitting the numerical model to the measurements of the initial response after demagnetization and the reversible response. The model parameters κ and q were estimated by non-linear least squares optimization. The differences between the measured transients and the predicted linear responses are shown to better visually discern the relatively small variation due to non-linear effects. Good agreement between the model calculations and measurements is achieved.
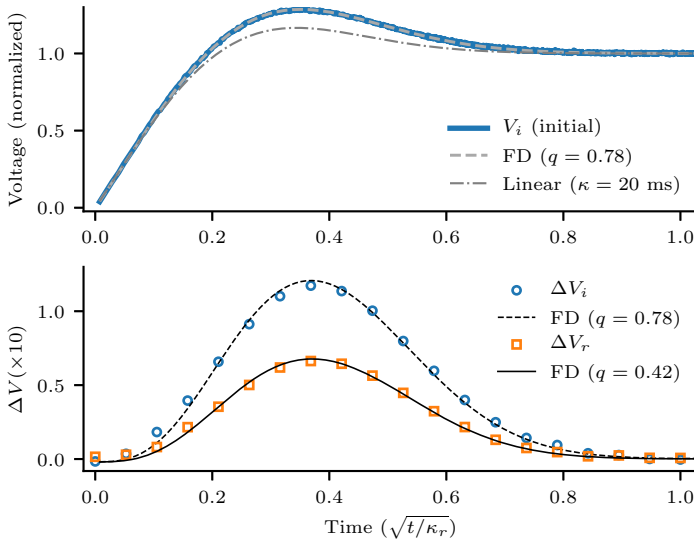
Figure 5. Comparison between measurements and finite difference simulation. The transient response V_i (top) corresponds to the initial response after demagnetization. The estimated non-linear contribution ΔV_i to the initial response is greater than ΔV_r (reversible response) due to irreversible magnetization.

Values of the parameters are $\kappa_i = 20.0$ ms, $q_i = 0.78$ for the initial response and $\kappa_r = 20.7$ ms, $q_r = 0.42$ for the reversible response. In terms of the Rayleigh law, the corresponding values of the relative permeability and the Rayleigh constant η are 103 and 1.59 for the initial response and 107 and 1.76 for the reversible response. The value of q_i is larger than q_r as expected due to the contribution of irreversible magnetization in the initial response. The ratio $q_i/q_r = 1.88$ is less than the factor 2 predicted by the Rayleigh law. Consequently there is a 10% difference in the values of η and there is also a 4% difference in μ_r whereas ideally both parameters would be treated as constants in the Rayleigh regime. In comparison, the standard errors in the parameter estimates are less than 1% meaning the variation is not caused by random measurement error alone. Additional uncertainty derive from potential inhomogeneity of the sample, which could bias the fit results. Also, lacking an independent direct measurement, there is some uncertainty in the accuracy of the Rayleigh law itself for the material.

Table 1 gives some preliminary data for additional samples, obtained as part of a study to quantify effects of treatments such as annealing and work hardening, processes that modify the magnetic properties by changes in stress and microstructure [1]. Clearly, these treatments greatly influence both the linear and non-linear parameters. Indeed, numerous factors are known to affect the magnetic properties of ferromagnetic materials which poses both opportunities and challenges in NDE applications. In this regard the analysis of the non-linearity in the response could provide additional information as an aid in the interpretation of data. In particular the relationship between plastic deformation and the Rayleigh parameters measured using the approach outlined here is the subject of future work.

Sample	σ (MS/m)	μ_r	η	$\eta/\mu_r(\times 100)$
S235 (cold drawn)	6.1	107	1.76	1.6
S235 (annealed)	6.1	237	2.7	1.1
S355	4.5	133	1.15	0.8
S355 (deformed)	4.5	110	0.47	0.4

Table 1. Results for different samples. The deformed S355 sample (yield strength 355 MPa) was plastically deformed in uniaxial tension to 5% strain.

5. Conclusions

We have modeled non-linear effects in transient potential drop measurements using finite difference simulation assuming axial symmetry and a quadratic field dependence of the magnetization. The numerical results are in good agreement with experimental measurements on carbon steel rods. Here we have initially focused on modeling of the response and interpreting the results in view of the Rayleigh law. The approach may prove useful in interpretation of NDE data by providing additional information compared to an analysis of the relative permeability alone.

References

[1] B Cullity and C Graham. *Introduction to Magnetic Materials*. John Wiley & Sons, Inc., 2 edition, 2009.
[2] D C Jiles. Review of magnetic methods for nondestructive evaluation. *NDT Int.*, 21(5):311–319, 1988.
[3] Ø Persvik and J R Bowler. Evaluation of four-point transient potential drop on conductive plates. *Appl. Phys. Lett.*, 110(8):084102, 2017.
[4] H Hognestad and A Honne. Determination of stress in ferromagnetic steel by potential drop measurements. *Mater. Sci. Tech.*, 14(11):1109–1114, 1998.
[5] J R Bowler, Y Huang, H Sun, J Brown, and N Bowler. Alternating current potential-drop measurement of the depth of case hardening in steel rods. *Meas. Sci. Technol.*, 19(7):075204, 2008.
[6] D C Jiles. *Introduction to magnetism and magnetic materials*. CRC Press, 1998.
[7] J I Etcheverry and G A Sánchez. Simple measurement of electromagnetic properties of steel in the rayleigh domain. *AIP Conf. Proc.*, 1511(1):1174–1179, 2013.
[8] N Bowler. Frequency-dependence of relative permeability in steel. *AIP Conf. Proc.*, 820, 2006.
[9] H E Knoepfel. *Magnetic Fields: A Comprehensive Theoretical Treatise for Practical Use*. John Wiley & Sons, 2000.

Numerical Investigation on Faults Diagnosis for AC Induction Machine by Magnetic Flux Distribution

Linfeng Li[1], Yating Yu[1,2]*, Qin Hong[1] and Zhenwei Wang[3]

[1] *School of Mechnical and Electrical Engineering, University of Electronic Science and Technology of China, Chengdu, 611731, China*

[2] *Institute of Electronic and Information Engineering of UESTC in Guangdong, 523808, Dongguan, China*

[3] *School of Aeronautics and Astronautics, University of Electronic Science and Technology of China, Chengdu, 611731, China*

Abstract. AC induction machines are widely used in electric servo drive, information processing, transportation and other fields. However, the unexpected faults cause the serious threat for the normal operation and operator's safety. Therefore, timely faults diagnosis is an effective way to ensure the AC induction machines to work in health condition. In AC induction machines, magnetic field is the basis of energy conversion of motor, and the faults have the directly influence on the electromagnetic field distribution. In this paper, 2D numerical model of the AC squirrel-cage asynchronous induction machine is built by using COMSOL Multiphysics according to finite element method; Then, the magnetic flux distribution of AC induction motor with three different faults which commonly occurs in engineering are simulated. Base on the numerical simulation, the influence of the different faults on the magnetic distribution is discussed in detail. The investigation is beneficial to find a nondestructive fault diagnosis approach to the induction machine.

1. Introduction

Induction machines play an important role in commercial manufacture. It is used in motor drive systems from few watts to several megawatts [1]. To ensure the reliable operation and long lifetime of machines, condition monitoring technologies have been developed to detect the occurred faults and predict impending failures. For the faults diagnosis, L.Siliang proposed a novel fast and online order analysis method, which composed of two algorithms to realize online diagnosis [2]. Rotor eccentricity can be diagnosed by extracting the amplitudes of stator current [3]. By improved motor current signal model can makes the monitoring of rotor bar fault more accurate [4]. The method

---

* Corresponding author:86-13678139939, E-mail address:yuyating-uestc@hotmail.com

of Complete Ensemble Empirical Mode utilize spectrum analysis technology can detect induction motor faults in steady-state operation [5].

Eddy current exists in motor and directly influence magnetic flux density (MFD) distribution. Therefore, the faults can influence the magnetic distribution. To investigate the influence of the rotor eccentricity, rotor bar breakage and shaft crack on the MFD distribution, the FE model is set up, and the relationship of the faults and the MFD are studied in detail. Consequently, the approach to fault diagnosis are proposed.

2. FE modelling

AC induction machine structure is shown in Figure 1. The electrical and geometric parameters of the machine are listed in Table 1. The materials and their parameters of motor parts are listed in Table 2. The revolving speed of the magnetic field is 1500 rpm through calculating. And setting the speed of the rotor as 1485 rpm in simulation.
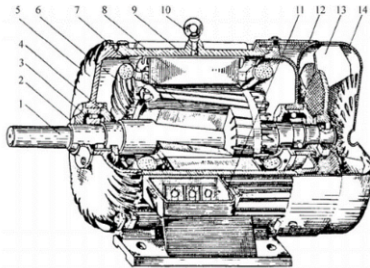
Figure 1. The structure of the AC induction machine. 1-shaft, 2，4-bearing cap；3-bearing; 5,12-frame; 6-stator winding; 7-rotor; 8- stator core; 9-base; 10-ring; 11-outlet box; 13-electric fan; 14-fan housing

Table 1. The electrical parameters and geometric parameters of the machine

Rated power	3KW	Armature slot number	24	Height of air gap	4mm
Rated voltage	380V	Pole number	4	Outer Diameter of stator	130mm
Rated current	6.8A	Phase number	3	Inter Diameter of stator	96mm
Height of core	120mm	Stator slot number	24	Outer Diameter of rotor	88mm
Shaft diameter	24mm	Excitation frequency(Hz)	50		

Table 2. The material and material parameters of the key components in machine

Components / Items	Core	Stator wingding	Rotor winding	Air gap	Shaft
material	Soft steel	Copper	Copper	air	Steel
Ralative magnetic permeability	H-B curve	1	1	1	1
Relative Permittivity	1	1	1	1	1
Electrical conductivity (MS/m)	11.20	59.98	59.98	0	4.03
Area of cross section(mm^2)	/	12.57	21.36	/	/
Turns number	/	30	1	/	/

To simulate the relative motion of the stator and rotor, two independent coordinate systems are set in FE model. One is the stator coordinate system which is fixed on stator, the other is the rotor coordinate system which is fixed on rotor. In simulation, the former is moving and latter is static. The CAD model, mesh model and FE model with the boundary conditions are shown in Figure 2.

According to the FE model in Figure 2, we can obtain the magnetic flux density distribution of the AC machine, and shown in Figure 3. As that can been seen in Figure

3, the most of the magnetic flux form the closed electromagnetic loop by stator core-air gap-rotor core. A few magnetic flux surrounded in the vicinity of the stator core is leakage. Based on the FEM model, the influence of the rotor eccentricity, the rotor bar/ring breakage and shaft crack on the magnetic flux density are investigated.

| (a) | (b) | (c) |
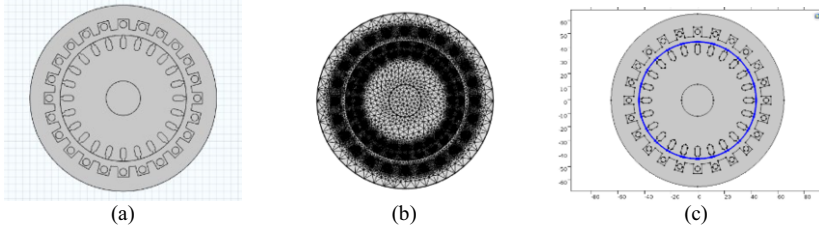
Figure 2. FE model. (a) CAD model (b) mesh model (c) sharing boundary

| (a) | (b) |
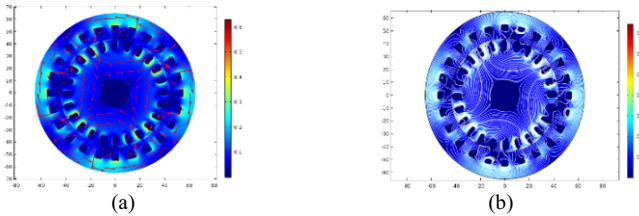
Figure 3. MFD distribution of machine (a) vectorgraph; (b) isogram

3. Study on the influence of different faults on magnetic field distribution of motor

Induction machines typically operate at harsh environment which leads to approximately 6 % failure rate each year [6]. The bear failure rate is 37 %, rotor eccentricity is 12 %, shaft is 5 %-10 % [7]. Among these failure machines, several surveys have investigated and illustrated the detailed failure types and rates [8]. The common failures of induction machines include stator winding faults, bearing faults, rotor bar/ring faults and shaft failures [9]. Therefore, three typical faults: Rotor eccentricity, Rotor bars breakage and crack in shaft are considered in this paper.

3.1. Rotor eccentricity

Eccentricity faults may occur in the squirrel-cage asynchronous induction machine's air gap between the outer side of the rotor and the inner side of the stator due to manufacturing process or operational wear [10]. There are two kinds of air gap eccentric faults: static eccentric and dynamic eccentric [11].

In this paper, the distribution of magnetic field of the AC induction machine (ACIM) with static eccentricity is studied. When no static eccentricity in rotor, the center point of rotor is (0.00 mm, 0.00 mm). In order to investigate the influence of the rotor eccentricity on the magnetic field of ACIM, we set the center point of rotor is (0.50 mm, 0.50 mm), (1.00 mm, 1.00 mm) and (1.50 mm, 1.50 mm), respectively. The distribution of the magnetic field of the ACIM under the different eccentricity are shown in Figure 4.

As the eccentricity distance of the rotor increases, the distribution of the magnetic field lines of the motor become denser when the air gap become narrow. In the contrary, the distribution of magnetic field lines becomes sparser where the air gap become wide.

| (a) | (b) | (c) | (d) |
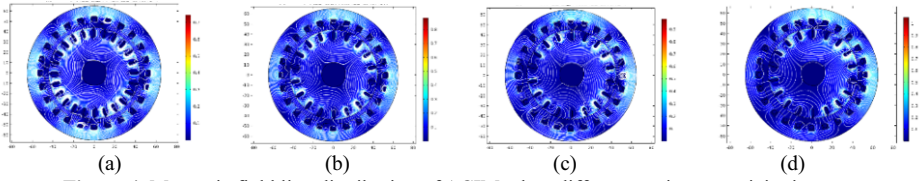
Figure 4. Magnetic field line distribution of ACIM when different static eccentricity in rotor.
(a)rotor center(0.00,0.00); (b)rotor center(0.50,0.50); (c)rotor center(1.00,1.00); (d)rotor center(1.50,1.50)

In order to analyze quantitatively, six reference points shown in Figure 5 (a) are taken to compare the MFD values. The variation tendency of MFD is shown in Figure 5 (b). For the points *a*, *c* and *e*, the MFD increase with the increase of the eccentricity distance of the rotor. For the three points *b*, *d* and *f*, the MFD decrease with the increase of the eccentricity distance. The reason is that the rotor is closer the points *a*, *c* and *e* for the increasing distance of the rotor, while it is farer the points *b*, *d* and *f*.

For making comparison, the difference of the MFD between each set of symmetrical points are grouped. Group 1 includes point *a* and *b*, group 2 includes point *c* and *d*, group 3 includes point *e* and *f*, as well as group 4 includes point *h* and *i*. The variation curve of MFD difference of each symmetrical point with the distance of rotor eccentricity is shown in Figure 5 (c).

| (a) | (b) | (c) |
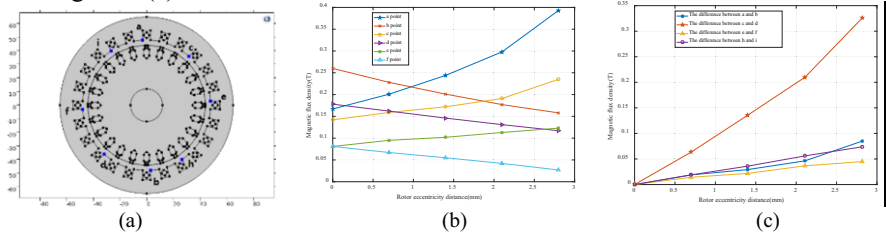
Figure 5. (a) Values points of rotor eccentricity motor; (b) Variation curve of MFD with eccentricity distance at value points; (c) The difference of the MFD of the four groups with the rotor eccentricity

The difference of MFD at the symmetric point of the motor is almost 0 when there is no eccentricity. While, it is linear changing with the increase of the eccentricity distance. Importantly, the difference between point *c* and *d* is most sensitive to the change of the motor eccentricity distance. Therefore, we can not only easily character the rotor eccentricity distance, but also confirm the direction of the rotor eccentricity by detecting the MFD difference in the symmetrical detection points.

3.2. Rotor bars breakage

This section analyzed the electromagnetic field distribution of the ACIM when 4 and 8 rotor bars are broken. The locations of the broken bars are shown in Figure 6.

| (a) | (b) |
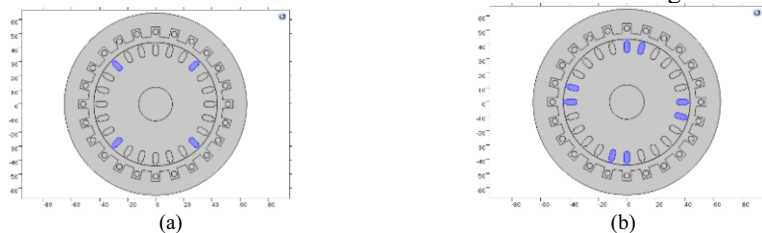
Figure 6. The layout of the broken rotor bars (a) 4 rotor bars are broken; (b) 8 rotor bars are broken

For 4 broken rotor bars, two points near the broken rotor bar are marked as *A* and *B*, and marked *C* and *D* near the normal rotor bar. For 8 broken rotor bars, three points near

the broken bars and marked them as *E*, *F* and *G*. Meanwhile, another three points are taken near the normal rotor bars which is named as *H*, *I* and *J*. The layout of the detection points is shown in Figure 7. The MFD values of each point are listed in Table 3.

(a)   (b)
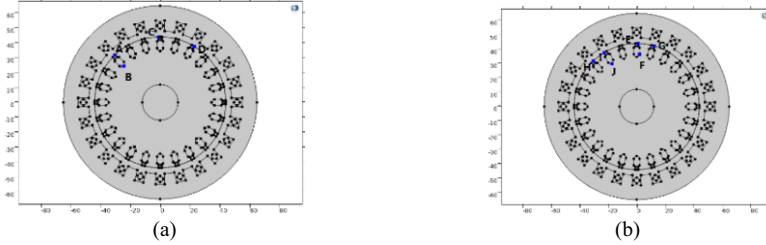
Figure 7. Roken rotor bar points (a)4 rotor bars are broken; (b)8 rotor bars are broken

Table 3. MFD value at different points: (Gs)

Point	4 rotor bars are broken				8 rotor bars are broken					
Status	A	B	C	D	E	F	G	H	I	J
normal	885	2882	279	1342	924	1297	855	885	1677	2868
fault	1041	3002	273	1340	1112	1431	1018	885	1649	2816

From Table 3, we can see that the MFD of the points near the broken bars is obviously higher than the normal condition, while the MFD near the normal bars have little effect by the broken bars. Therefore, we can judge whether the bar breaks or not by detecting the MFD.

3.3. Crack in shaft

For considering the influence of the V shape fatigue crack in the shaft on the MFD. The crack depth along the radial direction is 5.00 mm, and the angle of crack of 6°, 8° and 10° are considered. The magnetic field line distributions are shown in Figure 8.

(a)   (b)   (c)   (d)
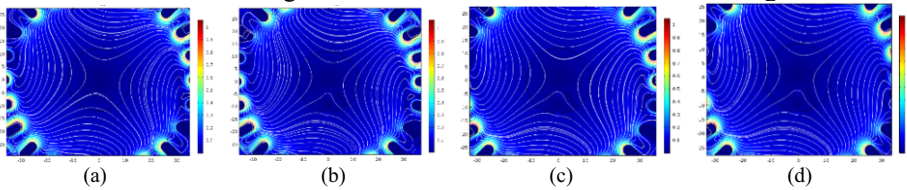
Figure 8. MFD lines with different crack degrees. (a) crack free; (b) spread angle is 6°;
(c) spread angle is 8°;(d) spread angle is 10°

Two reference points are taken to analysis the MFD of different crack degrees. The infulece of the crack in the shaft on the MFD are shown in Figure 9 (a).

(a)   (b)
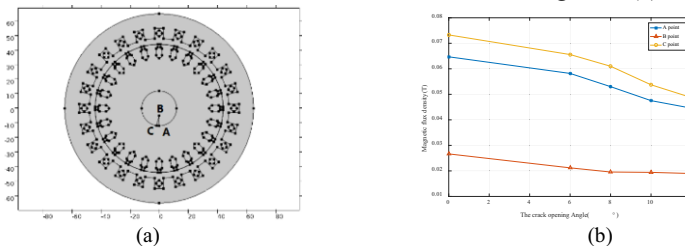
Figure 9. The infulece of the crack in the shaft on the MFD. (a)the layout of the detection points;
(b)the curves of the crfack angle and the magetic flux desnity

Cracks makes the MFD at all detection points decrease compared with the normal condition and the increasing crack angle makes the monotone decreasing of the MFD. However, the influences of the crack on the MFD at point A and point C are greatly

higher than point B. Therefore, we can determine the crack position and crack angle by compare the MFD with that under normal operation of the motor.

4. Conclusion

The variation of MFD of motor under different faults is obtained by numerical simulating, and analyzed in detail. The rotor eccentricity distance as well as the direction of the rotor eccentricity can be diagnosed by detecting the magnitude of the flux density difference in the symmetrical detection points in air gap of the ACIM; the broken bars position can be diagnosed by comparing the MFD distribution near the bars under the fault condition with that under the normal condition; the crack position and crack angle in shaft can be determined by comparing the MFD of the points on the surface of the rotation shaft with that under normal operation of the motor. Therefore, numerical simulations indicate that MFD can be applied to diagnose the three commonly appeared faults in ACIM. In future, a validation by experimental study to the numerical simulation results will be considered.

Acknowledgements

References

[1] W. Cao, K. J. Bradley, Assessing the impacts of rewind and repeated rewinds on induction motors is an opportunity for Re-designing the machine being wasted. IEEE Transactions on Industry Applications 42 (2006), 958-964.

[2] L. Siliang, H. Qingbo, Zh Jiwen, Bearing fault diagnosis of a permanent magnet synchronous motor via a fast and online order analysis method in an embedded system. Mechanical. Systems. and Signal Processing. 113(2018), 36-49.

[3] B.M. Ebrahimi, J. Faiz, et,al. Static-dynamic-and mixed-eccentricity fault diagnoses in permanent magnet synchronous motors, IEEE Transactions on Industry Electronics, 56(2009), 4727-4739.

[4] F. Gu, T. Wang, A.Alwodai, X.Tian, Y. Shao, A. Ball. A new method of accurate broken rotor bar diagnosis based on modulation signal bispectrum analysis of motor current signals. Mechanical. Systems. and Signal Processing 50(2015), 400-414.

[5] P.A. Delgado-Arredondo, D. Morinigo-Sotelo, et al. Methodology for fault detection in induction motors via sound and vibration signals. Mechanical. Systems and Signal Processing 88(2017), 568-589.

[6] A.H. Bonnett, G.C. Soukup, Cause and analysis of stators and rotor failures in 3-phase squirrel-cage induction-motors, IEEE Transactions. on Industry Application 28(1992), 921-937.

[7] A.Sidique, G.S. Yadava, B. Singh. A review of stator fault monitoring techniques of induction motors. IEEE Transactions. Energy Conversion 20(2005), 106-114.

[8] O.V. Thorsen. A survey of faults on induction motors in offshore oil industry, petrochemical industry, gas terminals and oil refineries, IEEE Transactions on Industry Application 31(1994),1186-1196.

[9] Liu Z, Cao W, Huang P H, Non-invasive winding fault detection for induction machines based on stray flux magnetic sensors, IEEE Power and Energy Society General Meeting. JUL 17-21, 2016, Boston, MA.

[10] M. Blodt, P. Granjon, P. Raison, Models for bearing damage detection in induction motors using stator current monitoring. IEEE Transactions on Industrial Electronics, 55(2008), 1813-1822.

[11] Fenger, M, Lloyd, BA, Thomson, WT, Development of a tool to detect faults in induction motors via current signature analysis. 45th Annual Cement Industry Technical Conference, MAY 04-09, 2003, DALLAS, TX.

Simulation and Experimental Study of Closed Crack Detection by Ultrasonic Nonlinearity Under Electromagnetic Loading

Chuang Zhang[a,b,1], Longlong He[a,b], Suzhen Liu[a,b], and Qingxin Yang[a]

[a] *State Key Laboratory of Reliability and Intelligence of Electrical Equipment, Hebei University of Technology, Tianjin, 300130 China*
[b] *Key Laboratory of Electromagnetic Field and Electrical Apparatus Reliability of Hebei Province, Hebei University of Technology, Tianjin, 300387 China*

Abstract. The reliability of micro-damage detection of metal materials plays a crucial role in the safe and reliable operation of large equipment. In recent years, nonlinear ultrasonic nondestructive testing technology has achieved good development in closed cracks detection, but the problem of nonlinear ultrasonic detection of closed cracks is weak response signal and vulnerable to external interference. This paper realizes the modulation of the ultrasonic wave by electromagnetic loading at the closed cracks, which can effectively enrich the frequency components of nonlinear ultrasonic and magnify the amplitude. This lays a foundation for further research on nonlinear ultrasonic detection of closed cracks under electromagnetic loading.

Keywords. Closed crack, electromagnetic loading, nondestructive testing, nonlinear ultrasound

1. Introduction

Metal structure is widely used in various major infrastructures, such as ship shell, train body, aircraft door, tank shell, etc. In service period, these metal structures are subject to the combined action of surroundings, temperature and cyclic load, and are prone to generate plastic damage and closed cracks. Statistical data shows that closed crack is one of the main forms of early fatigue damage in metal structures [1].

The accumulation of early fatigue damage takes up most of the time during the service of the structure, so the detection and evaluation of early fatigue damage is of great importance. Therefore, how to achieve the effective detection of closed cracks is also the focus of research in the field of non-destructive flaw detection [2]. There have been a lot of studies on the detection of macroscopic cracks and defects of metal plates by linear ultrasound [3]-[4]. However, it is difficult to detect the closed cracks by using linear ultrasound because the closed cracks are usually in contact and closed state. In recent years, nonlinear ultrasonic methods have been widely used to detect closed cracks, of which the sensitivity to closed cracks is higher. HJ Lim [5] used nonlinear ultrasonic modulation technology to detect metal plates containing fatigue cracks under different temperature and load conditions, indicating that the nonlinear ultrasonic modulation

---

[1] Corresponding Author Chuang Zhang, Email czhang@hebut.edu.cn.

technology can accurately detect fatigue damage of metal structures under complex environment. H Tohmyoh [6] applied the surface SH wave to detect the fatigue crack on the surface of low carbon steel, and made a quantitative evaluation on the length and depth of the crack. Ikeuchi [7] proposed a method of fundamental wave amplitude difference based on the fundamental wave threshold caused by close cracks contact vibration, which can selectively image closed cracks and eliminate the influence of other linear scatters.

The main problem of closed cracks detection by nonlinear ultrasound is weak response signal. The application of electromagnetic loading technology to the nonlinear ultrasonic detection of closed cracks can not only avoid the additional damage that may be introduced by the mechanical loading to the tested components, but also effectively improve the reliability of the ultrasonic nonlinear detection of closed cracks [8]. In this paper, the closed cracks in metal plates are excited into dynamic fluctuation state through electromagnetic loading to improve the response signal of nonlinear ultrasound. Electromagnetic loading device is compact and portable; therefore, it is easier to operate than mechanical loading. The nonlinear modulation effect of closed cracks in metal plates under electromagnetic loading is verified by simulation and experiments. The influence of different loading frequencies on nonlinear detection of closed cracks is also studied. This provides a basis for the ultrasonic non-linear detection of closed cracks.

The paper is organized as follows. In Section 2, simulation of ultrasonic modulation under electromagnetic loading is discussed. In Section 3, the specimen preparation and experimental setup are described, and the verification experiment of VAM based on electromagnetic loading is elaborated, and Section 4 summarizes the conclusions of the study.

2. Simulation

2.1. Ultrasonic modulating simulation under electromagnetic loading

Fig. 1 is a schematic diagram of the ultrasonic modulating simulation model of an aluminum plate with a closed crack under electromagnetic loading. The COMSOL finite element simulation software is used for finite element analysis. The simulation model includes ultrasonic excitation devices (excitation coils and U-shaped magnets), electromagnetic loading devices (loading coils and rectangular permanent magnets), and an aluminum plate containing a closed crack.
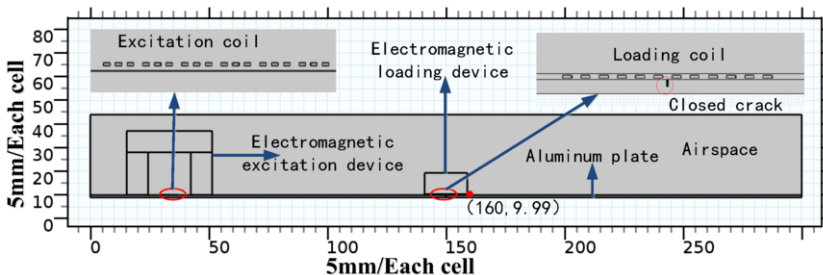
Fig. 1. Ultrasonic modulating model of aluminum plate with a closed crack under electromagnetic loading.

The exciting coil adopts a zigzag-coil, and the loading coil adopts a spiral coil. The closed crack is located at (150, 9.5) of the aluminum plate, of which the depth is 0.5 mm.

The permanent magnet of the electromagnetic loading devices generates a vertical downward magnetic field with a residual magnetic flux density of 1 T. The line spacing of the loading coil is set at 0.5 mm and the number of turns is 12. A sinusoidal current with a peak-to-peak amplitude of 10 A is loaded into the loading coil, of which the frequency is 200 kHz. The magnet of the electromagnetic ultrasonic transducer is a U-shaped magnet, and the residual magnetic flux density is set at 1 T. The excitation coil adopts a three-split wire with a turn of 6, of which the distance between the bundles is set at 1.17 mm and the distance between splitting wires is 0.15 mm. The excitation current is a Gaussian window modulated sine pulse excitation, which has a frequency of 1 MHz, a peak-to-peak amplitude of 10 A, and a circulation of 10. The node B (160, 9.99) on the aluminum plate is used as the signal acquisition point to simulate the ultrasonic modulating effect and analyze the influence of electromagnetic loading parameters on the electromagnetic ultrasonic wave during the propagation in the aluminum plate.
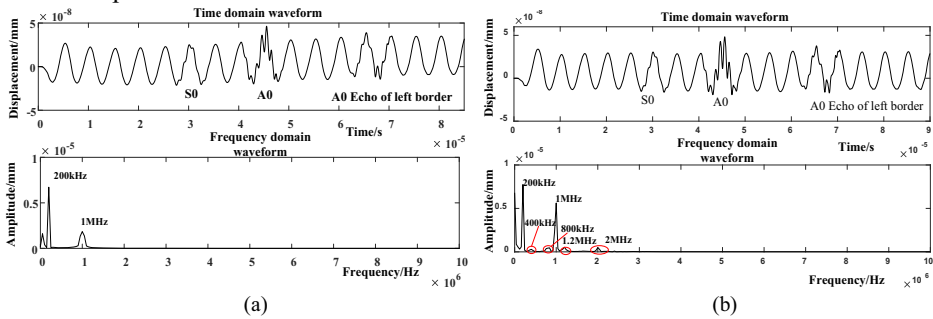
Fig. 2. Time-frequency diagram of intact (a) and defective (b) aluminum plate.

Fig. 2 shows the ultrasonic time-domain waveforms and spectrograms acquired at point B with or without closed cracks and with or without electromagnetic loading. As shown in Fig 2(a), when electromagnetic loading is performed in an intact metal plate, the time domain waveform is a superposition of an electromagnetic loading signal and an ultrasonic signal, and the frequency domain signal contains only a 200 kHz loading frequency and 1 MHz ultrasonic frequency. Fig. 2(b) shows the time-domain waveform and frequency spectrum of the 1 MHz ultrasonic signal propagating in an aluminum plate with a closed crack under 200 kHz electromagnetic loading. It can be clearly seen that the time domain waveform of ultrasonic signal and loading signal has superimposed. Due to the crack fluctuation and electromagnetic loading, the time-domain signal of the received signal is distorted. In addition to the 200 kHz and 1 MHz fundamental signals in the spectrum, there are also the second harmonic components of 400 kHz and 2 MHz and the sum and difference components of 1.2 MHz and 800 kHz.

The analysis above shows that the crack interface undergoes microscopical open-close fluctuation under electromagnetic loading, and the fluctuation will modulate the ultrasonic waves propagating in the aluminum plate. When the ultrasonic wave passes through the closed crack region, it will be strongly modulated. The time domain waveform is distorted, and the modulating frequency components appear in the frequency spectrum. A typical feature is that the sum and difference frequency components appear in the frequency spectrum. By comparing the frequency domain diagrams of the ultrasonic signal with or without electromagnetic loading, it can be seen that the nonlinear components generated by electromagnetic loading are more abundant and have higher amplitude. Therefore, it can be concluded that the detection of closed

cracks can be achieved by detecting the existence of sum frequency and difference frequency components of the ultrasonic response signal of the aluminum plate under electromagnetic loading.

2.2. Influence of electromagnetic loading frequencies on ultrasonic modulation

Changes in electromagnetic loading parameters will affect the eddy current in the aluminum plate. The Lorentz force is determined by the size and distribution of the eddy current. This changes the fluctuating state of the closed crack, which will then affect the ultrasonic waves propagating in it. The following analyze will focus on the influence of electromagnetic loading parameters on nonlinear ultrasonic modulation.
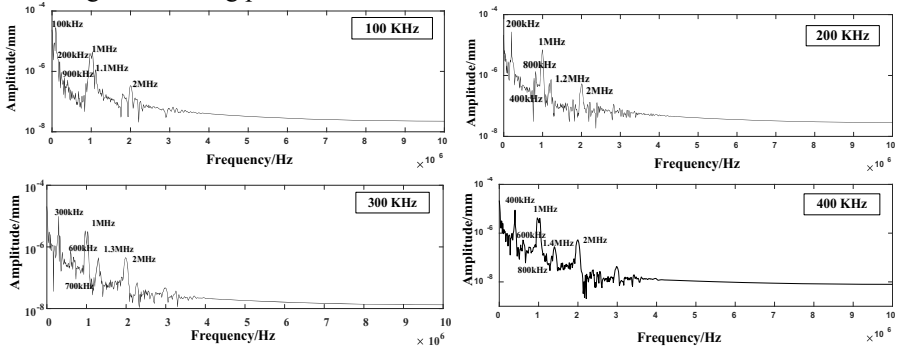
Figure 3. Frequency diagram at different loading frequencies.

The frequency of electromagnetic ultrasonic excitation is 1 MHz. The peak-to-peak amplitude of pulse current is 10 A and the excitation period is 10 cycles. The electromagnetic loading current is kept unchanged at 10 A, and the loading frequency changes. 100 kHz, 200 kHz, 300 kHz, and 400 k Hz are used to simulate and analyze the characteristics of ultrasonic response at different loading frequencies. The results are shown in Fig. 3. When the electromagnetic loading frequency is 100 kHz, the loading frequency is too small compared with the exciting ultrasonic frequency, which leads to the overlap of 1.1 MHz sum frequency component, 900 kHz difference frequency component and 1 MHz ultrasonic frequency. When the loading frequency is 300 kHz, the second harmonic component of 600 kHz is generated due to the closed crack, which cannot be easily distinguished from the difference frequency component of 700 kHz. When the frequency is 200 kHz or 400 kHz, the side-lobe and harmonic components can be easily distinguished. Thus, they can be used as the loading frequency.

3. Experiments and analysis

This section will verify the ultrasonic modulation of closed cracks in aluminum plates under electromagnetic loading through experiments. The tested specimens are an intact aluminum plate and an aluminum plate with a closed crack. As is shown in Fig. 4, the dimension of both is 300 mm×60 mm×1 mm, and the crack is located at 150 mm to the left of the defective plate. The defective piece includes two kinds of defects, namely cutting defects and closed cracks, which are shown in Fig. 4. The manufacturing process of the defective piece is as follows: First, a wire cutting is used to make the cutting defect in the middle of the plate, of which the length is 5mm and the width is 0.5 mm; then it is

fixed in a fatigue tester for cyclic loading. The frequency of cyclic loading is 20 Hz and the force is 5 kN. A closed crack with a length of 15 mm (as shown in Fig. 4) appears in the aluminum plate after loading up to 30,000 times. The experiment is performed on the intact aluminum plate and the defective aluminum plate. The connection of the experimental equipment is shown in Fig. 4. The electromagnetic loading device is placed directly above the closed crack. The vertical magnetic field produced by the permanent magnet of the loading device is approximately 0.3 T. The loading coil adopts a spiral coil. The high-power signal source provides continuous sinusoidal excitation for the electromagnetic loading coil, of which the loading frequency is 200 kHz and the current is 0.75 A.
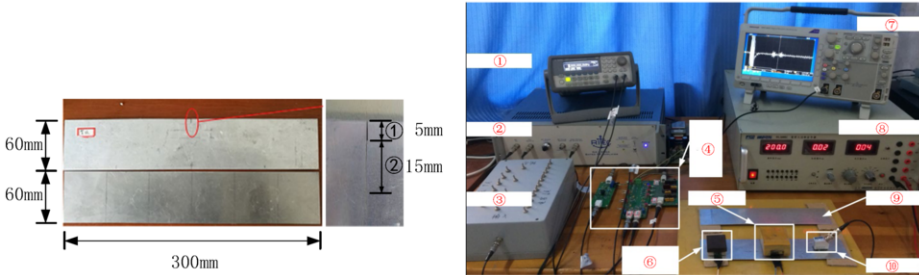
Fig. 4. Tested specimen and experimental equipment wiring diagram.

The electromagnetic ultrasonic exciting device is set 30 mm away from the left side of the aluminum plate. The magnetic field intensity provided by the permanent magnet of the ultrasonic exciting device is 0.4 T. The exciting coil adopts a zigzag-coil. The tone-burst signal generated by the signal generator is amplified by the pulse amplifier and then output to the ultrasonic exciting coil. The impedance matching device matches the internal impedance of the exciting coil and the exciting generator so that the output of the signal reaches the maximum power. The peak-to-peak amplitude of the exciting signal is set at 350 mV, the frequency is 1 MHz, and the number of exciting cycles is 10. The response signal is received using a piezo probe with a central frequency of 2.5 MHz. The probe is put at 200 mm away from the left of the tested aluminum plate. The position of the electromagnetic ultrasonic exciting device and the piezoelectric probe is approximately in line with the top of the closed crack. The received signal is output to the oscilloscope after a preamplifier, a wideband amplifier, and a low-pass filtering one after another.
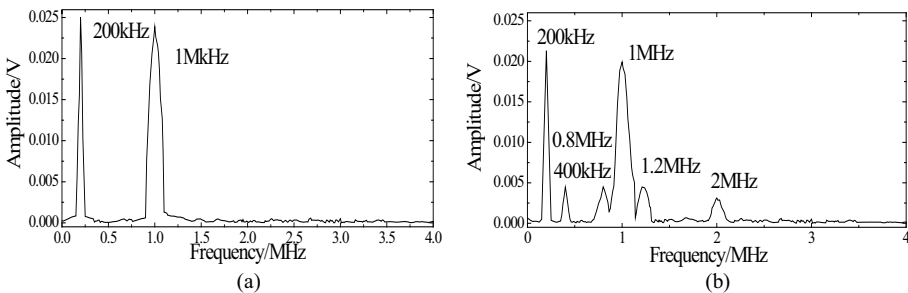
Fig. 5. Frequency domain diagram of the intact and defective aluminum plate.

By analyzing the frequency domain characteristics of the ultrasonic signal of the two specimens shown in Fig. 5, it can be seen that there are only 1 MHz and 200 kHz fundamental frequency components in the spectrum of the signal collected from the

intact aluminum plate, and no significant harmonic components is collected. The spectrum of the signal collected from the defective aluminum plate includes not only the fundamental frequency components but also the second harmonics of 400 kHz and 2 MHz and the sidelobe components of 800 kHz and 1.2 MHz. The Lorentz force generated by electromagnetic loading causes the closed crack to open and close microscopically. The fluctuation of the closed crack will modulate the electromagnetic ultrasonic signal propagating through the crack, which produces a nonlinear modulating effect on the ultrasonic response.

4. Conclusion

To solve the problem of nondestructive detection of the closed cracks, this paper proposes to excite the aluminum plate with closed cracks into dynamic fluctuation by electromagnetic loading. Simulations and experiments show that: (1) Compared with traditional nonlinear ultrasonic testing, ultrasonic modulation under electromagnetic loading can excite richer and higher-amplitude nonlinear components, which increases the reliability of ultrasonic nonlinear detection of closed cracks. (2) The electromagnetic loading frequency should be less than half of the ultrasonic signal frequency, but higher than one tenth of it. This lays a foundation for further research on nonlinear ultrasonic detection of closed cracks under electromagnetic loading. Future work should focus on the elimination of nonlinear effects of equipment, the extraction of modulating signals, and the further optimization of loading parameters. These are very useful for the practical application of the electromagnetic loading ultrasonic modulating method to detect early fatigue damage of metal plates.

References

[1] Staszewski W J, Boller C, Tomlinson G. Health monitoring of aerospace structures: smart sensor technologies and signal processing. Chichester: John Wiley & Sons, 2004.
[2] D. Broda, W. J. Staszewski, A. Martowicz et al., "Modelling of nonlinear crack–wave interactions for damage detection based on ultrasound—A review," J Sound Vib, vol. 333, no. 4, pp. 1097-1118, Feb. 2014.
[3] A. Mirala, R. S. Shirazi, "Detection of surface cracks in metals using time-domain microwave non-destructive testing technique," IET Microwaves Antennas Propag, vol. 11, no. 4, pp. 564-569, Mar. 2017.
[4] X. Xu, L. Zhuang et al., "An Ultrasonic Guided Wave Mode Excitation Method in Rails," IEEE Access, vol. 6, pp. 60414-60428, Oct. 2018.
[5] H. J. Lim, H. Sohn, M. P. Desimio et al., "Reference-free fatigue crack detection using nonlinear ultrasonic modulation under various temperature and loading conditions," Mech Syst Signal Process, vol. 45, no. 2, pp. 468-478, Apr. 2014.
[6] H. Tohmyoh, Y. Ochi, T. Matsumura, "Study on detection and quantitative evaluation of fatigue cracks using surface SH waves (NDE2)," Nihon Kikai Gakkai Ronbunshu, A, vol. 67, no. 661, pp. 1508-1513, Aug. 2017.
[7] M. Ikeuchi, K. Jinno, Y. Ohara et al., "Improvement of closed crack selectivity in nonlinear ultrasonic imaging using fundamental wave amplitude difference," J. Appl. Phys, vol. 52, no. 7 PART 2, pp. 1044-1055, July. 2013.
[8] C. Zhang, W. Pang, S. Liu et al., "Dynamic characteristics analysis of closed cracks in aluminum plate under electromagnetic loading," Zhongguo Dianji Gongcheng Xuebao (Proceedings of The Chinese Society for Electrical Engineering), vol. 38, no. 7, pp. 2171-2178, Apr. 2018. (In Chinese).

Numerical Simulation on Stress Measurement with Eddy Current Thermography

Shuwen DENG[a], Suixian YANG[a,1], Yong YAO[a]
[a]School of Mechanical Engineering, Sichuan University, Chengdu, China

Abstract. Stress in components will lead to the change of material properties and even failure. Therefore, the assessment for the stress state of components is play an important role in testing industry. As a non-contact and multi-physical field nondestructive testing method, eddy current thermography (ECT) can be applied to detect non-homogeneous electromagnetic characteristics parameter distribution in conductive materials. Internal stress and its distribution in a material will affect the value of electromagnetic characteristic parameters. If induction current applied on conductive material, the Joule's heat, which generate in the sample will lead to the temperature rise on the surface of the specimen by induction heating process. The temperature distribution on the specimen surface can be recorded by infra camera and stored as IR images or videos. The feature of the temperature distribution and its variation can be used to express the stress state in the specimen. It is concluded that there is an approximate linear relationship between the surface temperature appreciation and the loading force when the excitation source condition remains unchanged.

Keywords. Numerical simulation, stress measurement, eddy current thermography, conductive material

1. Introduction

The existence of residual stress in the structure is harmful to the safety of the structure in most cases. The detection and elimination of residual stress has always been a focus of industry. Real-time and accurate detection of residual stress in structures is an important means to ensure the safe operation of structures. The commonly used non-destructive testing methods for residual stress mainly include ultrasonic testing[1-3], X-ray diffraction testing[4], neutron diffraction testing[5,6] and magnetic testing[7-9]. Eddy current testing[10-12] and eddy current thermography testing residual stress are also extended based on magnetic measurement. According to the research status of the residual stress nondestructive testing (NDT) in China and abroad, the stress distribution of the structure can be obtained through the existing testing technology. However, the ultrasonic detection process needs coupling agent, the wave velocity is small and the influencing factors are many. X-ray method is harmful to human body and can only measure the stress in one direction at a time. Neutron diffraction measurement has a wide range of average stress, which is difficult to measure the gradient distribution of residual

---

[1] Corresponding Author, Suixian YANG, School of Mechanical Engineering, Sichuan University, Chengdu, China; E-mail: yangsx@163.com.

stress precisely. The magnetic measurement method is limit to ferromagnetic materials with a small measurement range. Eddy current detection method has deficiency in detection range because of eddy current skin effect.

Compared to traditional stress measurement of nondestructive testing methods like ultrasonic etc., eddy current thermography method have abilities to obtain the non-contact testing result of a single large detection area; achieve high detection precision and resolution of complex geometry component; use the distribution of residual stresses for prior detection in a wide range. In recent years, the application of eddy current thermography detection method to stress detection technology are popularity[13-17], many studies are focus on the stress distribution and temperature response curve in thermal image graph with different stress states and various conductive.

In [13], researchers obtained linear coupling relationship between stress and thermal conductivity by applying uniaxial tensile load on conductive material with eddy current thermography. In [14], tensile stress on the surface of specimen was preliminarily quantified by using eddy current thermography as well. In this paper, the influence of electrical conductivity, magnetic conductivity and thermal conductivity caused by different stress states on eddy current thermography testing results will be studied by numerical simulation.

2. Methodology

Electromagnetic parameters of conductive material are the link between ECT and stress detection. Result of stress measurement by using ECT is mainly affected by conductivity, magnetic permeability and thermal conductivity of the sample. The variation of conductivity and magnetic permeability mainly affect the induction heating stage of the testing process, while the variation of thermal conductivity mainly affects the cooling stage. The results depend on the heat propagation process and the eddy current distribution in the sample. Fig.1 is the scheme of the testing principle.
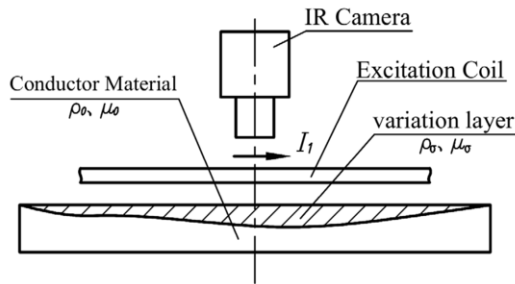
Fig. 1. Principle scheme of stress measurement with ECT.

During the testing process, the heat source of temperature rise is mainly provided by Joule's heating principle due to electromagnetic loss of conductivity material. If an alternating current with certain frequency applies on the excitation coil, there will be an electromagnetic induction phenomenon and eddy current of the same frequency will be generated in the sample[18]. The eddy current field in the sample is governed by Maxwell's equation as Eq.(1):

$$\nabla \times (\frac{1}{\mu} \nabla \times A) + \rho_e \frac{\partial A}{\partial t} + \varepsilon \frac{\partial^2 A}{\partial t^2} = J \tag{1}$$

Where μ is the magnetic permeability of the material, A is the magnetic vector potential, ρ_e is the conductivity of the material, ε is the dielectric constant, and J is the external current density.

2.1. Coupling of solid mechanics and electromagnetic fields

Metal resistance strain effect is the link between solid mechanics and electromagnetic field. The distance between atoms in the material and the dynamic distortion of the lattice will be changed by the internal stress of conductive material, which also lead to the change of the material's resistivity or the material's conductivity [19, 20]. The conductivity is normally negative exponential with the change of stress. When the absolute value of the exponent is far less than 1, the high-order small term could be omitted, and the relationship between conductivity and stress as shown in Eq.(2) is approximately linear[21].

$$\rho_\sigma = \rho_0 \frac{1}{1 + \alpha_r \sigma} \tag{2}$$

Where, ρ_σ is the electrical conductivity of metal with stress, ρ_0 is the electrical conductivity with no stress, σ is the value of stress, and α_r is the stress coefficient.

2.2. Coupling of electromagnetic field and temperature field

The electromagnetic induction heating stage and the heat conduction stage are the connection between electromagnetic field and temperature field. According to Joule's law, part of the eddy current will be converted from electric energy to heat energy in the material. The generated heat Q is proportional to the eddy current density J_s and the electric field intensity E as shown in Eq. (3).

$$Q = J_s \cdot E \xrightarrow{J_s = \rho E} Q = \frac{1}{\rho} |J_s|^2 \tag{3}$$

It can be seen from Eq.(2) that the Joule heat is mainly influenced by conductivity of material and eddy current density. The conductivity and magnetic permeability may also affect the value of eddy current density. The joule heat Q generated in the induction heating stage will be transferred inside the tested piece, and the transfer rule is shown in Eq. (4).

$$\rho C_p \frac{\partial T}{\partial t} - \nabla (\lambda \nabla T) = Q \tag{4}$$

Where, ρ is the material density, C_p is the specific heat capacity of the material, T is the thermodynamic temperature of the material, λ is the thermal conductivity of the material.

3. Methodology

In this paper, a finite element model (FEM) for stress measurement with ECT is established on the COMSOL Multiphysics platform. Solid mechanics, electromagnetic field and temperature field are coupled in the model. The stress of the specimen is loaded with reference to the three-point bending experimental method in the solid mechanics module. During the loading process, compressive stress and tensile stress are respectively generated on the positive and negative surface of the specimen. The relationship between solid mechanics and electromagnetic field is established through the influence of stress on electrical conductivity, and the relationship between temperature field and electromagnetic field is established through joule thermal change. The load is set as a variable, and the law of the surface temperature changing with the load during the induction heating period is investigated. Accordingly, the relationship between the stress of the specimen and the surface temperature during the induction heating process can be derived.
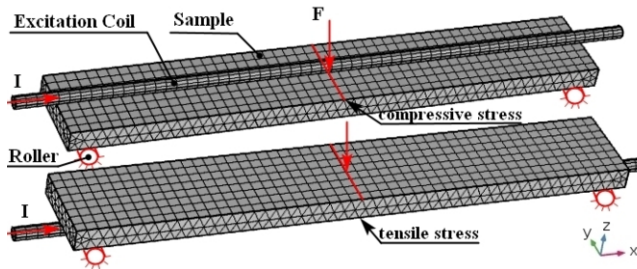
Figure 2. Geometry and parameters of the simulation model.

The simulation model of stress eddy current thermal imaging detection of conductor materials and its grid division are shown in Fig.2. The sample size is *260mm ×40mm × 10mm*. The loading method of three-point bending mechanics experiment is adopted. The excitation coil is arranged 1mm away from the surface of the specimen.

The electromagnetic parameters of the sample and the excitation parameters of the model are shown in Tab.1. The load *F* gradually increases from *0* to *4000N* (the load of reference specimen is *0N*), and the direction of exciting coil is placed in parallel to the stress. The surface temperature of both sides of the three point bending specimens (the longitudinal displacement is negligible) are obtained by induction heating.

Table 1. The excitation parameters and electromagnetic parameters of sample

Parameter of sample	The value
F	0~4000N
Young modulus	2×10^{11}Pa
Poisson's ratio	0.3
I	500A

frequency	250kHZ
heating time	500ms
cooling time	1000ms
conductivity	5×10^6S/m
thermal conductivity	44.5 W/(m•K)
magnetic permeability	1
specific heat capacity	475 J/(kg•K)
temperature coefficient of resistance	1.23×10^{-5}/K
relative dielectric constant	1
density	7850 kg•m^{-3}

4. Results and discussions

After coupling solid mechanics, electromagnetic field, temperature field and other physical fields with COMSOL simulation software, the simulation results are obtained as follows:

The surface plots of stress and surface temperature distribution on the specimens' surface after the three point bending experiment are shown in Fig.3 and Fig.4. It can be found that the specimen surface temperature of the compressive stress area is lower but that of the tensile stress area is higher than the same area of reference specimen. The larger the load is, the greater the temperature difference on the tensile stress side as well as on the compressive stress side is.
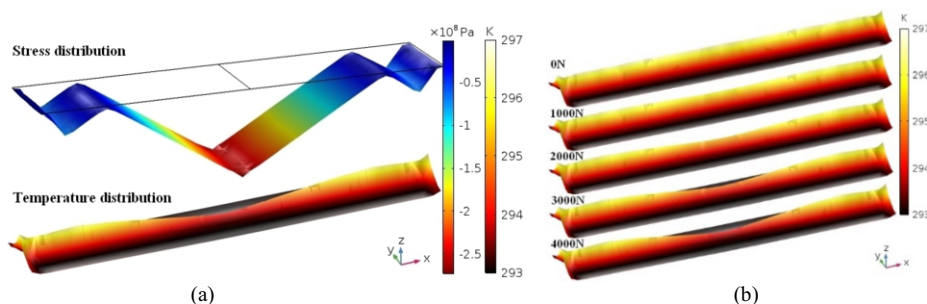
Fig. 3. Influence of load on temperature distribution of compressive stress side, (a) surface plots of stress and temperature distribution; (b) temperature distribution changes with load.
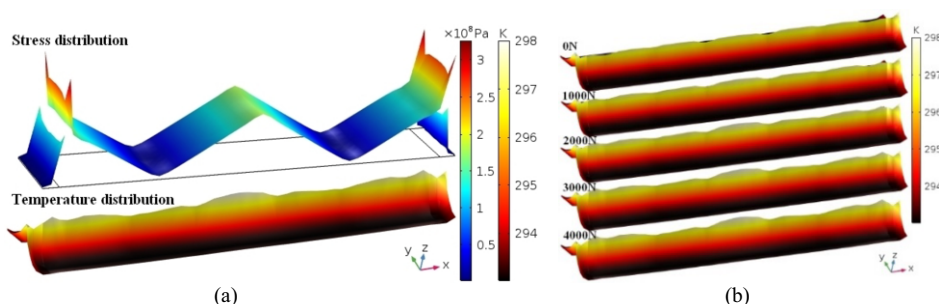
Fig. 4. Influence of load value on temperature distribution of tensile stress side, (a) surface plots of stress and temperature distribution; (b) temperature distribution changes with load.

The curve relation between the load amplitude and the temperature appreciation is obtained by extracting the temperature value at the center of the simulation thermograph of the upper surface of the specimen and subtracting the temperature value of the unloaded specimen.

Fig.5 shows the relationship between temperature difference and load both on the central lines of the tensile stress side and compressive stress side along with X-axis. Lines in Fig.5 indicate that the surface temperature appreciation of the tensile stress side and compressive stress side has a positive and negative linear correlation with the load value respectively. Moreover, the further away the measuring point is from the centerline, the smaller the rate of temperature appreciation corresponding to this point changes with the loading force.

(a) compressive stress

(b) tensile stress
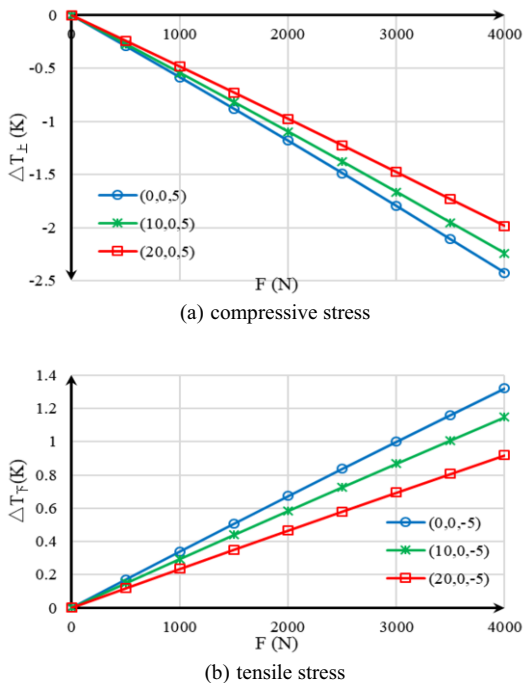
Fig. 5. Effect of load value on temperature rise at different positions on specimen.

5. Conclusions

In this work, a simulation model coupled multi-physical fields has been established and the relationship between stress and temperature rise on the sample surface from the thermal images has been obtained by eddy current thermography. The results show that the stress value of the tested specimen has an approximate linear relationship with the temperature rise on the sample surface, in which the tensile stress is positively correlated with the temperature rise; meanwhile, the compressive stress is negatively correlated with the temperature rise. This result provides a theoretical foundation for the subsequent quantitative experimental study of residual stress.

The residual stress measurement by using eddy current testing based on the correlation between stress and material conductivity has become a popularity subject in the field of nondestructive testing. However, it's still have several scientific problems need to be solved in the future.

- Three-dimensional nondestructive evaluation of stress tensor;
- Based on the electromagnetic non-destructive testing, the influence rule of the material's electromagnetic characteristics on the change of residual stress amplitude needs to be further studied;
- The mapping relationship between stress detection signals, stress amplitude and stress tensor based on eddy current method is needed to be revealed;
- The analysis technology of the corresponding relationship between residual stress state and eddy current thermal imaging test results (thermal imaging image sequence) needs to be further discussed;
- Residual stress detection system based on eddy current testing and the eddy current thermal image processing method have not been fully established.

In the future, we will research quantitative evaluation system for residual stress measurement by setting up the experimental platform by using eddy current thermal imaging test. Based on the theoretical and simulation research in this article, the plan for future experimental research work is as follows:

- The three-point bending experiment on residual stress of prefabricated specimens will be carried out, and the feasibility and accuracy of the experiment will be verified;
- Taking prefabricated sets of quantitative residual stress specimens as the test objects, eddy current thermal imaging experiments will be carried out;
- The eddy current thermographic test results corresponding to different residual stress specimens will be obtained, the data will be analyzed and the characteristic values for quantitative assessment of residual stress will be sought.

References

[1] Chunguang Xu et al. Nondestructive Testing Residual Stress Using Ultrasonic Critical Refracted Longitudinal Wave[J], Physics Procedia 70 (2015)594 – 598.
[2] W. Song, Q. Pan, C. Xu, X. Li and H. Liu, Benchmark of residual stress for ultrasonic nondestructive testing[C], 2013 Far East Forum on Nondestructive Evaluation/Testing: New Technology and Application, Jinan, 2013, pp. 73-76.,doi: 10.1109/FENDT.2013.6635532.
[3] W. Song et al., Residual stress nondestructive testing for pipe component based on ultrasonic method[C], 2014 IEEE Far East Forum on Nondestructive Evaluation/Testing, Chengdu, 2014, pp. 163-167.doi: 10.1109/FENDT.2014.6928254.
[4] GOU Guoqing, HUANG Nan, CHEN Hui et al. Detection of Residual Stress in Aluminum Alloy Carbody of High-Speed Train Using X-ray Diffraction Technology[J], Journal of Southwest Jiaotong University, 2012,47(4):618-622.
[5] Coules H E, Cozzolino L D, Colegrove P, et a1. Neutron diffraction analysis of complete residual stress tensors in conventional and rolled gas metal arc welds[J]. Experimen tal Mechanics, 2013, 53(2):195.
[6] Thibault D, Bocher P, Thomas M，et at Residual stress characterization in Iow transformation temperature 13％Cr-4％Ni stainless steel weld by neutron diffraction and the contour method[J]. Material Sci. Eng. A, 2010, 527(23):6205.
[7] H. Ilker Yelbay et al. , Non-destructive determination of residual stress state in steel weldments by Magnetic Barkhausen Noise technique[J], NDT&E International ,43(2010)29–33.

[8]   ZENG Jiewei SU Lanhai XU Liping et al. Research on the Stress Measurement of Steel Plate Based on Inverse Magnetostrictive Effect [J], Journal of Mechanical Engineering. 2014, 50(8):17-22.

[9]   Blaszkiewicz, M., Albertin, L., & Junker, W. (2009). The Eddy Current Technique for Determining Residual Stresses in Steels. Materials Science Forum, 210–213, 179–186. https://doi.org/10.4028/www.scientific.net/msf.210-213.179.

[10] Y. Shen, C. C. H. Lo, A. M. Frishman, et al., Conductivity profile determination by eddy current for shot-peened superalloy surfaces toward residual stress assessment, *AIP Conference Proceedings* 894, 1229 (2007); https://doi.org/10.1063/1.2718106.

[11] Y. Shen,C.C.H. Lo, N. Nakagawa, A.M. Frishman, Residual Stress Profile Assessment by Eddy Current for Shot Peened Nickel Superalloy[J]. *Nondestruct Eval* (2010) 29: 1–13.

[12] Haihong Huang, Cheng Yang, Zhengchun Qian, et al. Magnetic memory signals variation induced by applied magnetic field and static tensile stress in ferromagnetic steel[J]. *Journal of Magnetism and Magnetic Materials*, Volume 416, 15 October 2016, Pages 213-219.

[13] Xiaodong Zhou. Research and Detection of Residual Stress Based on PEC Thermal Imaging Technology[D]. *University of Electronic Science and Technology of China*, 2016.

[14] LEI Qing, LI Xuan, WANG Yahui. Research on Detection Method of Metal Structural Stress Based on Eddy Current Thermography[J]. *Machine Design & Research*, 2017-(04):103-107.

[15] Urata S, Maeda Y, Nakai H. Classical Eddy Current Loss Evaluation of Electrical Steel Sheet under Compressive Stress[J]. *TRANSACTIONS- INSTITUTE OF ELECTRICAL ENGINEERS OF JAPAN A*, 2017, 137(10):577-583.

[16] Libing Bai, Gui Yun Tian, Stress Measurement Using Pulsed Eddy Current Thermography[C], *51st Annual conference of the British Institute of Non-Destructive Testing* 2012, pp.462-473.

[17] LIU Luye, DENG Shuwen,YANG Suixian. Nondestructive Testing Technique for Residual Stress by Using Eddy Current Thermography and Its Application[J]. *Nondestructive Testing*, 2018, 40(10): 5-9.

[18] Mengchun Pan,Ze He, Dixiang Chen. Eddy Current Thermography Nondestructive Testing[M]. *National Defense Industry Press*, 2013.

[19] Xiaodong Zhou. Research and Detection of Residual Stress Based on PEC Thermal Imaging Technology[D]. *University of Electronic Science and Technology of China*, 2016.

[20] Zou Yu. Study on Eddy Current Nondestructive Testing of Dist-ributed Stress in Conductive Metal[D]. *University of Electronic Science and Technology of China*, 2016.

[21] REN Jilin, LIN Junming, XU Kebei. Eddy Current Testing[M]. *China Mechine Press*, 2013.

Tensor Based Finite Element Model for the Calculation of Leakage Field in Magnetic Flux Leakage Testing

ALIMEY Fred John [a], BAI Libing [a,1] and CHENG Yuhua [a]

[a] *School of Automation Engineering, University of Electronic Science and Technology of China, Chengdu, China*

Abstract. Magnetic flux leakage (MFL) testing is a widely used electromagnetic nondestructive testing (ENDT) method, which has the ability to detect both surface and sub-surface defects in conductive materials. One of its best features is its ability to mathematically model field leakage from the defect area in a magnetized material. In this paper, we propose an optimized FEM model using geometrical weighted tensor (TBFEM), for the calculation of leakage field in MFL. This model using the Einstein's convention eliminates the bulky nature of traditional FEM based on its matrix algebra formation allowing for easy implementation and fast calculations. The proposed model achieves this by reducing the set of matrix equations into a single equation using suffixes which can then be solved with regular mathematical operations.

Keywords. Finite element method (FEM), Einstein's convention, magnetic flux leakage, matrices, weighted tensors

1. Introduction

Over the years, electromagnetic nondestructive testing and evaluation (ENDT&E) has become more and more popular with successful applications (in the aerospace, oil and gas, nuclear and transportation industries) for the determination of the quality and the structural health of components, machineries and equipment. At the core of most electromagnetic techniques that allow for numerical modelling is the finite element method (FEM). This is due to its flexibility and ability to model both linear and nonlinear boundary value problems (BVP). The main purpose of FEM is to determine the approximate solution of a boundary value problem (BVP), which is governed by a partial differential equation (PDE).

In this paper we propose a tensor based finite element model (TBFEM) for the calculation of leakage field in magnetic flux leakage (MFL) testing. MFL testing is a widely used electromagnetic nondestructive evaluation/testing (ENDT&E) method that has the ability to detect both surface and sub-surface defects in ferromagnetic materials. The basic idea is to magnetize a material to saturation using a permanent magnet or yoke as shown in the Figure. 1 below. The presence of defect will cause varying magnetic field distribution in the material which in turn causes flux leakage. These changes in the material can then be detected using magnetic field sensors for further processing.

---

[1] Corresponding author, Bai Libing, School of Automation Engineering, University of electronic science and technology of China (UESTC); (E-mail: libing.bai@uestc.edu.cn).
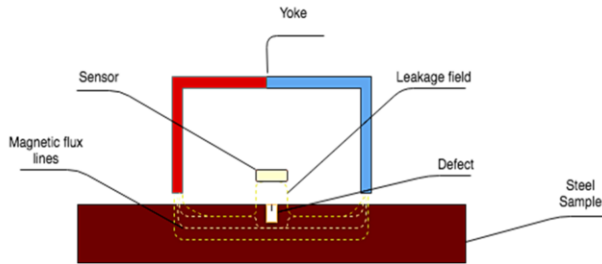
Figure. 1 Principle of magnetic flux leakage (MFL) testing

With MFL testing, two basic models are used for the prediction and visualization of magnetic field interaction with defect region. The analytical model, which was the first theoretical model to relate the shape of defects with the magnetic field strength, material permeability and magnetic field leakage [1], has contributed greatly to the understanding of how the MFL technique works. Even though this model greatly simplifies the difficulties associated with MFL analysis, too many assumptions are made, making it challenging for practical applications. More so, results from this model can only explain simple and regular defects [2] . The second basic model which is widely used is the numerical model. This model has shown more advantages as compared to the analytical model for MFL. According to Lord and Hwang [3], who first introduced the finite element method (FEM) to the calculation of the magnetic leakage field, proved through the study of how different shapes, angles, depth and width influence magnetic field. They then concluded that the only feasible solution for solving complex shape defects problems is through numerical calculation. Since then the finite element method (FEM) has been greatly explored and a lot has been achieved due to its flexibility and robustness. Even with all of its advantages, FEM has its challenges, some of which include excessive need for computing resources and time depending on the number of elements (matrixes) to be processed, as best results are greatly dependent on discretization (meshing) which makes the process time consuming and computationally expensive [4], [5]. In this paper, using the tensor based finite element model (TBFEM) which is derived from the Einstein's convention, we are able to calculate and simulate leakage field more efficiently, with a minimum computer specification, within a shorter time frame as compared to traditional FEM. The implementation is done in MATLAB RB2014 with a windows based computer of 1.4ghz speed, 4GB RAM.

2.   Magnetic leakage calculation using tensor based finite element model (TBFEM)

2.1 Magnetic leakage field calculation

In MFL, calculating the magnetic leakage field means solving the Maxwell's equation under certain boundary conditions. Knowing that $\nabla \cdot B = 0$ in static cases, B can then be expressed in terms of magnetic vector potential V for which $B = \nabla \times V$. Assuming $B = \mu \cdot H$ where μ is the permeability, then combining $B = \nabla \times V$ with $\nabla \times H = J$ where H is the magnetic field intensity, and J is the current density, the partial differential equation (PDE) in the equation (1) below can be obtained.

$$\nabla \times (\nabla \times (\frac{1}{\mu} \cdot B)) = J \tag{1}$$

However, because V is a vector potential, its boundary value problem (BVP) becomes difficult to solve. As shown in the introduction, the basic principle of MFL is to magnetize the sample using a permanent magnet or yoke, which means no conduction current is used within the domain, making $J = 0$. For this reason, a magnetic scalar potential V_m is used, so to describe the magnetic field for which the equations (2) – (4) below are satisfied within the domain.

$$\nabla \times H = 0 \tag{2}$$

$$\nabla \times B = 0 \tag{3}$$

$$B \equiv \mu_0 (H + M) \tag{4}$$

Where M is the magnetization intensity.

Substituting equation (4) into (1) and also $J = 0$ in the same equation (1) we obtain

$$\nabla \times (\nabla \times \frac{1}{\mu} \cdot \mu (H + M) = 0 \tag{5}$$

The equation (5) is further reduced to the generalized form of the magnetic flux continuity law

$$\nabla \cdot \mu_0 H = -\nabla \cdot \mu_0 M \tag{6}$$

Based on the imaginary magnetic charge created with regards to the molecular current from a pair of magnetic dipoles as done in MFL, the density of this magnetic charge can be represented as

$$\rho_m \equiv -\nabla \cdot \mu_0 M \tag{7}$$

In order to represent the magnetic field intensity in terms of scalar magnetic potential V_m the equation (8) below is obtained

$$H = -\nabla V_m \tag{8}$$

For which the MFL governing equation (9), representing the computational domain is obtained and satisfied

$$\nabla^2 V_m = -\rho_m / \mu_0 \tag{9}$$

2.2 Formulation of the tensor based finite element model (TBFEM)

Finite element modelling is the discretization of the computational domain into smaller fine elements called finite elements and the union of these finite elements to form a mesh [6]. The idea is to express unknown functions in terms of a linear combination of certain given functions with unknown coefficients, so that an equation (usually a matrix equation), whose entries are the unknown vectors of the unknown coefficients, are the approximate representation of the functions. In this paper, a test function is used, for which the calculation of dependent variables is done without having to directly solve the PDE. For example $\phi = S_{vi} a^i$ is a simple test function, as used in literature [6][7][8][9], where ϕ is the potential, S_v is the shape vector, a the row vector and $i = 1,2,3,4$......., which is the Einstein's summation convention. According to the Einstein's summation $e_i f^i = e_1 f^1 + e_2 f^2 + e_3 f^3 .....$, where e and f are the functions of i. S_v in the test function can further be defined as $S_{v1} = 1$, $S_{v2} = x$ and $S_{v3} = y$, whiles the values of a^i as $a^1 = a$, $a^2 = b$ and $a^3 = c$, where the values of a, b and c are unknown constants. The equation $\phi = S_{vi} a^i$ requires a system of i equations so as to solve for the unknown constants of a^i. For this reason, 3 different potentials representing the linear variation of $\phi = S_{vi} a^i$ is introduced considering a triangular region of 3 nodes in space. The system of equations is then redefined as $\phi_j = G_{ji} a^i$, where $j = 1,2,3$ the linear variations of nodal potentials as said earlier and G_{ji} is a matrix that contains the coordinate locations of the triangle vertices. The nodal potentials ϕ_j are unknown variables, hence the constant a^i may be defined as functions of these potentials, given by $a^i = g^{ij} \phi_j$ where $g^{ij} = G_{ji}^{-1}$ is the inverse of the matrix G_{ji}, which represents the geometrical weighted tensor. Combining the potentials $\phi = V_i a^i$ and $\phi_j = G_{ji} a^i$ we obtain a linear variation of the potential with the region specified by $j = 1,2,3$ given as

$$\phi = S_{vi} g^{ji} \phi_j \tag{10}$$

Where $S_{vi} g^{ji}$ is a set of linear equations.

2.3 Decomposition of the computational domain using tensor based finite element method (TBFEM)

The main objective of the finite element model (FEM) is to evaluate the approximate solution of a boundary value problem (BVP) that is governed by a linear partial differential equation. Using the proposed FEM model, the governing partial differential equation is solved. Partial differential equations (PDEs), are a function of continuous variables in time domain. A typical boundary value problem (BVP) can be mathematically described in a domain $\Omega \subset R_1, R_2$ or R_3 using the operator notation as shown in Eq. (11) below considering boundary conditions.

$$Lu = f \tag{11}$$

Where L is the partial differential operator, u is the unknown function to be determined and f is the given excitation function. The PDE in (9), considering boundary conditions the equation is rewritten as (11)

$$\nabla^2 V_m = -\rho_m/\mu_0 \qquad \text{in} \qquad \Omega \tag{12}$$

Where Ω is the computational domain, for which the Dirichlet, Neumann and Mixed boundary conditions can be imposed.

$$V_m = \phi \qquad \text{on} \ \ \Gamma_D \tag{13}$$

$$\frac{\partial V_m}{\partial n} = \beta \qquad \text{on} \ \ \Gamma_N \tag{14}$$

$$\frac{\partial V_m}{\partial n} + \alpha V_m = \beta \qquad \text{on} \ \ \Gamma_M \tag{15}$$

Where ϕ , β and α are given functions and Γ_D , Γ_N and Γ_M represent the types of boundary conditions that can be imposed. Representing (12) above as the expression in (11), we obtained (16) below

$$Lu^e = f^e \tag{16}$$

Where u^e represents the potential V_m for each element in the mesh and f^e being the right hand side of the Eq. (12) also representing the excitation function for each element in the mesh. Furthermore, u^e can be expanded, so as to express u^e_j as the

coefficient corresponding to the value of u and N_j^e is the weight function at the j-th node as shown in Eq. (17).

$$u^e = \sum_{j=1}^{n^e} u_j^e N_j^e \tag{17}$$

Using the Galerkin method where $w_i^e = N_i^e$ (where the weight function is identical to the shape functions), Eq. (18) is obtained

$$\int_{\Omega^e} w_i^e L u^e d\Omega^e = \int_{\Omega^e} w_i^e f^e d\Omega^e \tag{18}$$

Now imposing the Neumann boundary conditions, the equation (18) is rewritten as (19)

$$\int_{\Omega^e} w_i^e L u^e d\Omega^e = \int_\Gamma w_i^e L u^e d\Gamma \tag{19}$$

Further expansion of (19) based on the gauss divergence theorem for open surfaces, the equation (20) was obtained

$$\int_\Gamma w_i^e L u^e d\Gamma - \int_{\Omega^e} w_i^e L u^e d\Omega^e = \int_{\Omega^e} w_i^e f^e d\Omega^e \tag{20}$$

Where the first expression in (20) shows the imposition of the Neumann condition over the perimeter Γ. The summation equation for this expression is further given by

$$\int_\Gamma w_i^e L u^e d\Gamma = w^e L u^e \frac{\Gamma}{2} \tag{21}$$

The second expression in Eq. (20) is then computed based on the triangular mesh formation as said in the earlier section, for which its solution is given by (22) below

$$-\int_{\Omega^e} w_i^e L u^e d\Omega^e = -w^e L u^e A_T \tag{22}$$

Where A_T is the area of the triangular element and its obtained by computing the determinate of the matrix (G_{ij}) which contains the coordinate locations of the triangular vertices. Applying the Einstein's convention as stated earlier, with the Eq. (10) using the suffix notation, the Eq. (23) is obtained

$$-w^e L u^e A_T \; = \; -A_T \, g^{lk} \, g^{lj} V_m \tag{23}$$

Next, the solution of the right hand side of the Eq. (20) is obtained based on the area of the triangular element A_T divided by the number of nodes within the triangle as shown in Eq. (24)

$$\int_{\Omega^e} w_i^e \, f^e \, d\,\Omega^e \; = \; f^e \, \frac{A_T}{3} \tag{24}$$

Using the Eqs. (20) – (24), the tensor based FEM for the decomposition of the governing MFL equation is obtained as shown below

$$-A_T \, g^{lk} \, g^{lj} V_m \; = \; f^e \, \frac{A_T}{3} - w^e L u^e \, \frac{\Gamma}{2} \tag{25}$$

3.   Results and discussion

In order to verify the ability of the proposed FEM model, we modelled and simulated the distribution of magnetic field between parallel conductors placed in the XY plane. The field distribution was then computed on the XY direction, with the Z component kept constant (Z = 0). The results of this implementation can be seen in the Figure.2 (a-b) below.

(a)   (b)
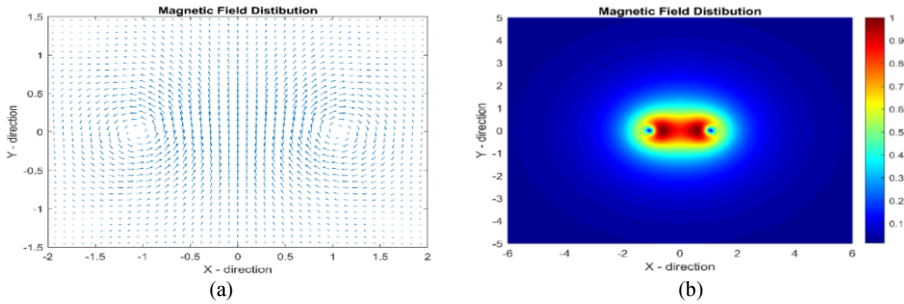
Figure. 2 (a) and (b) Magnetic field distribution between parallel conductors (permanent yokes) simulated using TBFEM implemented in MATLAB

From the Figure. 2 (a-b), the uniformity in the magnetic field distribution between two yokes can be evidently seen, for which the proposed FEM can be verified to yield results that agrees with results from simulations using the traditional FEM models.

Next, we calculated the magnetization of specimen, according to the magnetic field intensity, for which the leakage field is also obtained. Here, the variables for magnetizing the defect material is chosen based on B-H characteristics of a material [10]. The choice of material (low carbon fiber) was based on the common practice in MFL. More so, the magnetization variables were computed, with the traditional FEM model as a standard reference, so as to ensure standard accuracy in MFL signals when material saturation is

achieved. Furthermore, this implementation is done to prove the validity of the proposed model in yielding results, that are consistent with results obtained from traditional FEM in similar conditions. The material size is set to 0.1,0.5 and 0.006m respectively in the x, y and z directions, while the defect size is set to Length (L = 2mm), Width (W = 1mm) and Depth (D = 3mm). Using the both the traditional FEM and the TBFEM, simulation is done. Comparing the Y-components of magnetic field intensity at a liftoff position of 1- 4mm, the results are shown in Figure. 3 (a-d) below, it can be seen that the field distribution calculated by both the traditional FEM and the proposed FEM (TBFEM) greatly agree except for a minimal error of about 0.54%. However, it is also observed that when lift-off is 1mm, there exist a marginable amount of error in peak distribution between the two models. This is due to the fact that when lift-off is relatively small, marginal testing errors can be realized and when liftoff is excessively huge, the peak distribution completely vanishes, resulting to a complete erroneous testing. Therefore, as shown in the Figure. 3 (a-d), varying lift-off from 1 – 4mm is used, so as to verify the effect of lift-off on leakage field signal and to recommend or validate lift-off parameters for best result. Based on the simulation results as shown in Figure 3 (a-d), we can assume that, a standard lift-off of 3-4mm is suitable for achieving best results. As anything above this will or might result to erroneous test. Finally comparing the computation speed between the two models, the traditional FEM uses about 304s for the computation of the above data using a windows based computer of 2.4ghz speed, 8GB RAM, whiles the TBFEM uses about 24s for the same data with the same computer specification. Hence the purpose of the TBFEM is achieved through the reduction of matrixes.
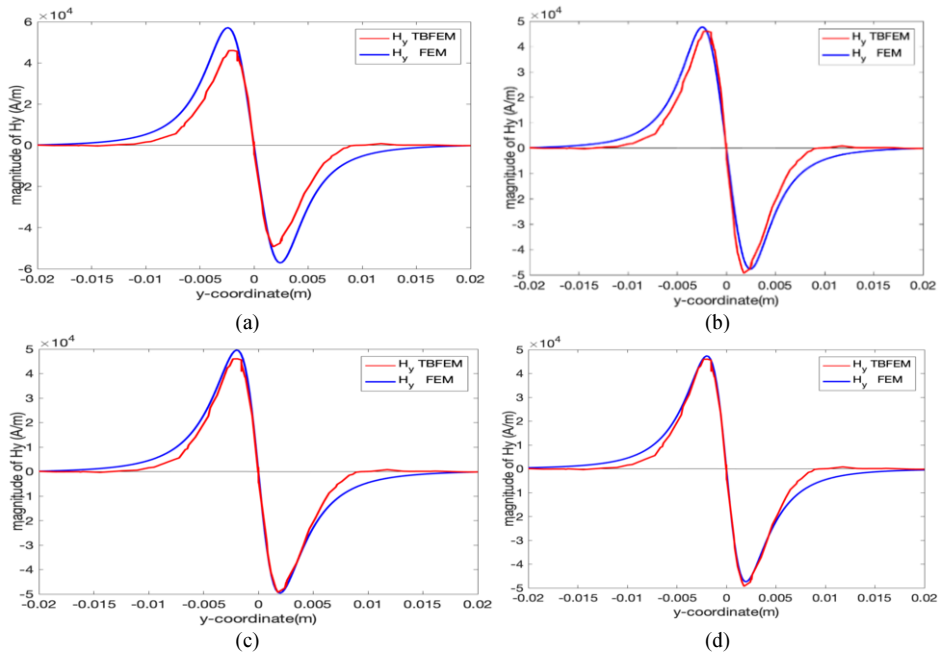
Figure. 3 Magnitude magnetic field intensity (a) when liftoff 1mm (b) when liftoff is 2mm (c) when liftoff is 3mm (d) when liftoff is 4mm respectively

4. Conclusions

This paper presents a tensor based finite element model for the calculation of leakage fields in MFL. This model eliminates the bulky nature of traditional FEM based on matrix formation by reducing the set of matrixes into a single Equation without changing the original meaning. With the proposed method, finer meshes can be generated and calculated within a short period of time with minimum computer resources.

References

[1] V. Suresh and A. Abudhahir, "An Analytical Model for Prediction of Magnetic Flux Leakage from Surface Defects in Ferromagnetic Tubes," *Meas. Sci. Rev.*, vol. 16, no. 1, pp. 8–13, 2016.
[2] S. M. Dutta, F. H. Ghorbel, and R. K. Stanley, "Dipole Modeling of Magnetic Flux Leakage," vol. 45, no. 4, pp. 1959–1965, 2009.
[3] J. H. Hwang, W. Lord, and M. Ieee, "Finite Element Analysis of the Magnetic Field Distribution Inside a Rotating," no. 5, 1974.
[4] S. Nagu, "Finite Element Modeling of Magnetic Flux Leakage Technique in Plates with Defect and without Defect," *Int. J. Mod. Eng. Res.*, vol. 3, pp. 3452–3455, 2013.
[5] Comsol and S. M. FORSCHUNG, "Simulation of Magnetic Flux Leakage Inspection," pp. 8–9.
[6] Ö. Özgün and M. Kuzuoğlu, *MATLAB-based Finite Element programing in Electromagnetic Modeling*, 1st Editio. CRC Press Taylor & Francis, 2019.
[7] Altair university, *Introduction to Nonlinear Finite Element Analysis using Optistruct*, 2nd Editio. Michigan, USA,: Altair HyperWorks Documentation Team, 2018.
[8] C. Hernandez and M. A. Arjona, "Application of tensor analysis to the finite element method," *Appl. Math. Comput.*, vol. 219, no. 9, pp. 4625–4636, 2013.
[9] R. A. Arciniega and J. N. Reddy, "Tensor-based finite element formulation for geometrically nonlinear analysis of shell structures," *Computer Methods in Applied Mechanics and Engineering*, vol. 196, no. 4–6. pp. 1048–1073, 2007.
[10] Y. Shi, C. Zhang, R. Li, M. Cai, and G. Jia, "Theory and application of magnetic flux leakage pipeline detection," *Sensors (Switzerland)*, vol. 15, no. 12, pp. 31036–31055, 2015.

Validation of the Reduced Vector Potential Formulation with the DtN Boundary Condition

Anton EFREMOV [a,1], Lalita UDPA [a] and Antonello TAMBURRINO [b]

[a] *Michigan State University, East Lansing, MI 48824, USA*
[b] *University of Cassino and Southern Lazio, Cassino, Italy*

Abstract. This work describes the validation against experimental data of a Reduced Vector Potential Formulation combined with a boundary condition given by the Dirichlet-to-Neumann operator. One of the classic nondestructive testing problems is investigated: the differential bobbin coil scan inside a tube with a defect. Several defects are simulated, and the results are compared to the experimental data acquired at four frequencies.

Keywords. Boundary Conditions, Eddy Currents, Finite Element Analysis, Nondestructive Testing

1. Introduction

Eddy current systems play an important role in the modern nondestructive testing. An ability to provide an accurate simulation of an eddy current inspection procedure is crucial to multiple applications, including sensor design and optimization, defect characterization, and many others.

A prominent way to set up an eddy current simulation is to utilize one of the differential formulations for the low-frequency approximation of Maxwell's equations and then solve it within a finite element framework ([1], [2]). In this case, the computation domain needs to be truncated and an appropriate boundary condition needs to be set. One way of imposing a boundary condition is to apply a Dirichlet-to-Neumann operator on the truncation boundary, as in [3], [4], [5], [6]. This boundary condition is exact, which means that it does not introduce any error in the physics on the truncation boundary and thus allows to put it close to the investigated object.

The authors previously derived a Reduced Vector Potential formulation with a DtN boundary condition in [7], [8], [9]. This paper contains a brief summary of the proposed formulation and its numerical validation against an experimental data for a typical ECT problem: a coil scan inside a conducting tube that has a volumetric defect in the wall.

---

[1] Corresponding Author: Anton Efremov, Nondestructive Evaluation Laboratory, Michigan State University, College of Engineering, 428 S. Shaw Lane, Room 2580, East Lansing, MI 48824-1226, USA; E-mail: efremova@egr.msu.edu.
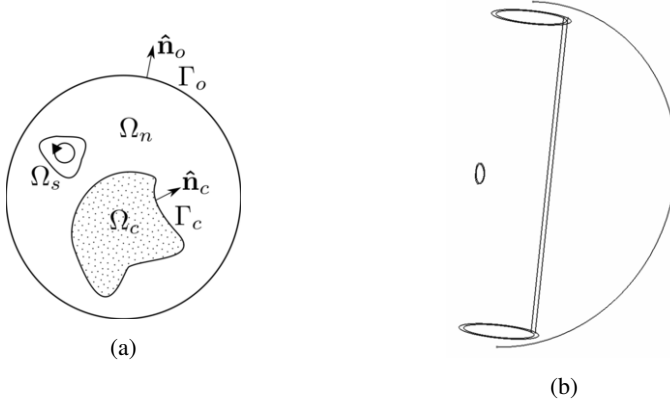
Figure 1. (a) The schematic diagram of the domain Ω , (b) The sketch of the simulated problem geometry: conducting tube with a defect

2. Formulation

2.1. Governing equations

The computational region is defined as $\Omega = \Omega_n \cup \Omega_c$, where Ω_n and Ω_c are the non-conducting and conducting regions respectively (see Figure 1a). The truncation boundary of Ω is denoted as $\Gamma_o = \partial\Omega$, and $\hat{\boldsymbol{n}}_o$ is an outward-looking normal to Γ_o.

In low frequency approximation the displacement current is neglected, and Maxwell's equations, that govern the underlying physics, take the following form ("magneto-quasistatic limit"):

$$\nabla \times \boldsymbol{E} = -j\omega\boldsymbol{B} \qquad\qquad in\ \Omega \qquad\qquad (1)$$

$$\nabla \cdot \boldsymbol{B} = 0 \qquad\qquad in\ \Omega \qquad\qquad (2)$$

$$\nabla \times \boldsymbol{H} = \boldsymbol{J} \qquad\qquad in\ \Omega \qquad\qquad (3)$$

$$\boldsymbol{H} = \nu\boldsymbol{B} \qquad\qquad in\ \Omega \qquad\qquad (4)$$

$$\boldsymbol{J} = \sigma\boldsymbol{E} \qquad\qquad in\ \Omega_c \qquad\qquad (5)$$

Here symbols $\boldsymbol{D}, \boldsymbol{B}, \boldsymbol{E}, \boldsymbol{H}, \boldsymbol{J}$ denote electric and magnetic flux, electric field, magnetic field and current density respectively. Symbols μ, ν, σ represent magnetic permeability, magnetic reluctivity and conductivity, ω is an angular frequency and $j^2 = -1$. The magnetic vector potential $\boldsymbol{A}$ and (modified) electric scalar potential ϕ are defined as follows:

$$\boldsymbol{B} = \nabla \times \boldsymbol{A} \qquad\qquad (6)$$

$$\boldsymbol{E} = -j\omega\boldsymbol{A} - j\omega\nabla\phi \qquad\qquad (7)$$

The source current $\boldsymbol{J}_s$ resides in a source region $\Omega_s \subset \Omega_n$ and generates the source magnetic field $\boldsymbol{H}_s$ and vector potential $\boldsymbol{A}_s$. Now the magnetic vector potential could be represented as $\boldsymbol{A} = \boldsymbol{A}_r + \boldsymbol{A}_s$, where $\boldsymbol{A}_r$ is the reduced vector potential, generated by eddy

currents in the conductor. This decomposition could be utilized to obtain the following system of equations from Eqs.(1)-(5) – the reduced vector potential formulation in weak form ([1], [2]):

$$\int_\Omega (\nabla \times \boldsymbol{N}_n) \cdot (v \nabla \times \boldsymbol{A}_r)\, d\Omega + j\omega \int_\Omega \boldsymbol{N}_n \cdot \sigma \boldsymbol{A}_r\, d\Omega + j\omega \int_\Omega \boldsymbol{N}_n \cdot \sigma \nabla \phi\, d\Omega +$$

$$+ \int_{\Gamma_o} \boldsymbol{N}_n \cdot (\hat{n}_o \times v \nabla \times \boldsymbol{A}_r)\, dS = -\int_\Omega (\nabla \times \boldsymbol{N}_n) \cdot (v_r - 1) \boldsymbol{H}_s\, d\Omega - j\omega \int_\Omega \boldsymbol{N}_n \cdot \sigma \boldsymbol{A}_s\, d\Omega \quad (8)$$

$$- j\omega \int_\Omega \nabla \phi_n \cdot \sigma \boldsymbol{A}_r\, d\Omega - j\omega \int_\Omega \nabla \phi_n \cdot \sigma \nabla \phi\, d\Omega = j\omega \int_\Omega \nabla \phi_n \cdot \sigma \boldsymbol{A}_s\, d\Omega \quad (9)$$

Here N_k and ϕ_k are the test functions. With the use of basis functions $N_k' \in H(curl, \Omega)$ and $\phi_k' \in H(grad, \Omega)$, we can approximate $\boldsymbol{A}_r = \sum\limits_{k=1}^{N_A} \alpha_k N_k'$ and $\phi = \sum\limits_{k=1}^{N_\phi} \beta_k \phi_k'$, where N_A and N_ϕ stand for the number of basis functions, α_k and β_k are unknown coefficients. This expansion is then substituted into the Eqs.(8)-(9), and when we set $N_k = N_k'$ and $\phi_k = \phi_k'$, the square system of linear equations is obtained. An appropriate boundary condition on Γ_o will make this system complete.

2.2. Dirichlet-to-Neumann operator on the sphere

In our case, the Dirichlet-to-Neumann operator Λ could be defined as an operator that acts on the solution of the vector Laplace equation in source free space and maps the tangential part of the reduced vector potential $\boldsymbol{A}_r$ on Γ_o to the tangential part of its curl:

$$\Lambda : (\boldsymbol{A}_r)_t \to (\nabla \times \boldsymbol{A}_r)_t \text{ on } \Gamma_o \quad (10)$$

Within FEM framework, an operator Λ could be utilized to build a boundary condition in a following way. First, we decompose the unknown vector potential on Γ_o into FEM basis N_k and ϕ_k. Then, this decomposition is converted to a tangential curl $(\nabla \times \boldsymbol{A}_r)_t$ with a use of Λ. The obtained expansion is then substituted into Eq.(8).

If the computatinal domain boundary Γ_o is a sphere, analytic form of the operator Λ is available ([7], [8], [9]). If the radius of the sphere is R and $\boldsymbol{U}_{lm}$, $\boldsymbol{V}_{lm}$ denote the tangential vector spherical harmonics (see [10]), the following expansion could be derived:

$$\int_{\Gamma_o} \boldsymbol{N}_n \cdot (\hat{n}_o \times v \nabla \times \boldsymbol{A_r})\, dS = \sum_{k=1}^{N_A} \alpha_k \sum_{lm} \frac{lR}{\mu_0} \left[\frac{\langle \boldsymbol{N}_k, \boldsymbol{U}_{lm} \rangle \langle \boldsymbol{N}_n, \boldsymbol{U}_{lm} \rangle}{||\boldsymbol{U}_{lm}||^2} - \frac{\langle \boldsymbol{N}_k, \boldsymbol{V}_{lm} \rangle \langle \boldsymbol{N}_n, \boldsymbol{V}_{lm} \rangle}{(R^2 ||\boldsymbol{V}_{lm}||)^2} \right]$$

$$(11)$$

The addition of this term completes the system linear equations obtained from Eqs.(8)-(9).

3. Numerical results

3.1. Simulation setup

The investigated problem is a coil scan inside the conductive tube with a volumetric defect inside the wall. The tube is oriented along the z axis. The 3D test geometry of the problem is shown in Figure 1b and the x-z cross-section of the tube is displayed in Figure 2. The tube has an outer diameter of 19.0mm, the wall thickness of 1.1mm and is made of non-magnetic material with $\mu_r = 1$ characterized by its conductivity of $\sigma = 8.71 \times 10^5$ S/m (equivalent resistivity value $\rho = 114.8\ \mu\Omega$-cm).

Four volumetric defects were simulated: the flat bottom holes (FBH) with diameters of 4.8mm, 4.8mm, 2.8mm, 1.3mm and depths of 0.22mm (20% tube wall, TW), 0.44mm (40%TW), 0.66mm (60%TW) and a through-wall hole, correspondingly. The defects were positioned on the outer side of the tube.

The source field was generated by two geometrically identical coils that were carrying the total current of 1A each and a phase difference of 180°. This represents the differential measurement [11]: in the section of the tube away from the defect the induced voltages in the coils have equal magnitude (so that the resulting impedance of the two coil system is zero), whereas in proximity of the defect the induced voltages in the two coils are different, which results in a non-zero signal that could be used to detect the presence of the defect. The simulated coil parameters were the following: outer diameter of 15.2mm and cross-section of 1.5mm by 1.3mm. The spacing between the coils is 1.5mm. The coil lift-off in this case equals to 0.8mm. The simulation of the model result in a one-dimensional array of complex voltages evaluated in every scan position.

The length of the simulated tube segment was 76mm. The computational domain was a sphere of radius 40mm. It was discretized into unstructured non-uniform tetrahedral mesh generated by Gmsh software [12]. Mesh density was set to be approximately 12 elements per wall in the defect area and 6 elements per wall thickness everywhere else.
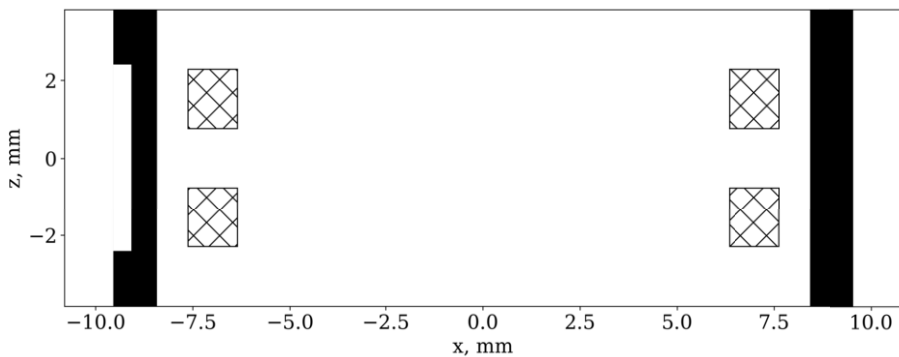
Figure 2. Geometry of the problem: 40%TW defect

Frequency, kHz	Defect Type	Phase difference, deg	Peak voltage error, %
35	20% FBH	4	11.00
35	40% FBH	2	10.00
35	60% FBH	-1	3.00
35	100% FBH	0	0.00
140	20% FBH	-4	8.00
140	40% FBH	-3	7.00
140	60% FBH	5	14.00
140	100% FBH	0	0.00
280	20% FBH	-16	14.00
280	40% FBH	-9	3.00
280	60% FBH	-6	3.00
280	100% FBH	0	0.00
550	20% FBH	-5	3.00
550	40% FBH	-11	9.00
550	60% FBH	-9	20.00
550	100% FBH	0	0.00

Table 1. Error in the simulated voltage and phase versus experimental data

3.2. *Comparison to experimental data*

In order to compare the simulation results to experimental data, the following calibration procedure was applied: the peak magnitude and phase of the signal generated by 100% through-wall defect at each frequency was set to 20V and 140° respectively. This was achieved by multiplying the signal by a constant complex-valued scaling factor, which was further applied to other three signals obtained at the same frequency. Thus, the relative magnitude and phase differences between all defects were preserved. The calibrated signals for two frequencies are demonstrated on Figure 3.

Two metrics were utilized to compare the signals after calibration: the magnitude and phase of the point with the peak magnitude. The results are summarized in Table 1.
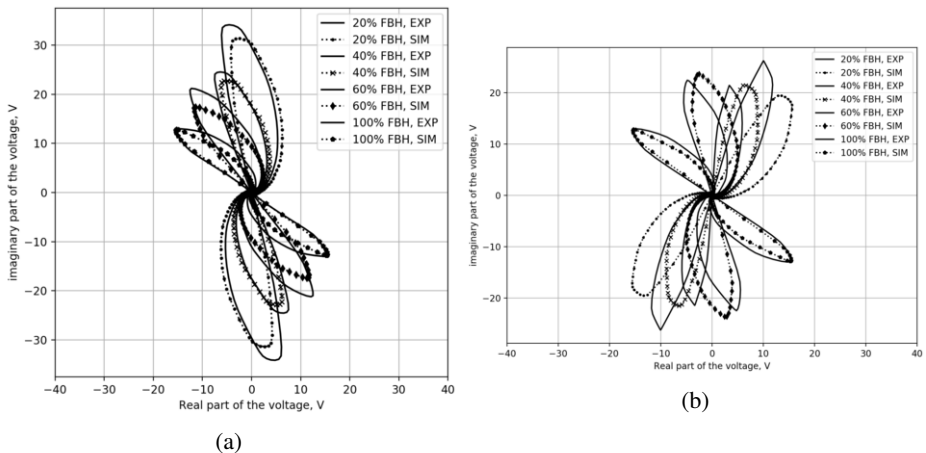
Figure 3. Calibrated differential voltage measurement, real versus imaginary part, (a) 140kHz, (b) 280kHz

4. Conclusions

This paper presents a numerical validation for the Reduced Vector Potential formulation with a DtN boundary condition against an experimental data. This is a differential formulation with an exact non-local boundary condition, which allows an efficient numerical implementation [8], [9].

A typical eddy current inspection problem was simulated: a differential bobbin coil scan inside a conductive tube with a volumetric defect in the wall. The simulation results show a good match with the experimental data, both in magnitude, phase and the overall shape of the signals. As could be seen in Table 1, the results are better for the lower frequency data due to the larger skin depth. Thus, generation of a finer mesh for higher frequency simulations could improve the numbers. However, the perfect match could not be achieved due to discrepancies introduced by the data acquisition system.

The presented analysis allows to conclude that the proposed formulation could be readily applied to simulate the eddy current inspection procedure.

References

[1] O. Bíró, "Edge element formulations of eddy current problems," *Computer Methods in Applied Mechanics and Engineering*, vol. 169, no. 3, pp. 391–405, 1999.

[2] Z. Zeng, L. Udpa, S. S. Udpa, and M. S. C. Chan, "Reduced magnetic vector potential formulation in the finite element analysis of eddy current nondestructive testing," *IEEE Transactions on Magnetics*, vol. 45, no. 3, pp. 964–967, 2009.

[3] A. Bossavit and J. Verite, "The "trifou" code: Solving the 3-d eddy-currents problem by using h as state variable," *IEEE Transactions on Magnetics*, vol. 19, no. 6, pp. 2465–2470, 1983.

[4] J. C. VERITE, "Application of a 3-d eddy current code (trifou) to non-destructive testing," *COMPEL - The international journal for computation and mathematics in electrical and electronic engineering*, vol. 3, no. 3, pp. 167–178, 1984.

[5] D. Givoli and J. B. Keller, "A finite element method for large domains," *Computer Methods in Applied Mechanics and Engineering*, vol. 76, no. 1, pp. 41–66, 1989.

[6] D. Givoli, I. Patlashenko, and J. B. Keller, "Discrete dirichlet-to-neumann maps for unbounded domains," *Computer Methods in Applied Mechanics and Engineering*, vol. 164, no. 1, pp. 173–185, 1998.

[7] A. Efremov, S. Ventre, L. Udpa, and A. Tamburrino, "Reduced vector potential formulation with dtn boundary condition for eddy current problems," *book of abstracts, 23rd Int. Workshop on Electromagnetic Nondestructive Evaluation*, 2018.

[8] A. Efremov, A. Perrotta, S. Ventre, L. Udpa, and A. Tamburrino, "Fem formulation with dirichlet-to-neumann map boundary condition for eddy current problems," *the 22nd International Conference on the Computation of Electromagnetic Fields*, 2019.

[9] A. Efremov, A. Perrotta, S. Ventre, L. Udpa, and A. Tamburrino, "Sparsification of the dtn operator and its applications for eddy current problems," *book of abstracts, 24th Int. Workshop on Electromagnetic Nondestructive Evaluation*, 2019.

[10] J. Jackson, *Classical Electrodynamics*. John Wiley & Sons, 1999.

[11] P. Moore and S. Udpa, *Nondestructive Testing Handbook: Electromagnetic Testing*. Nondestructive testing handbook, Amer Society for Nondestructive, 2004.

[12] C. Geuzaine and J.-F. Remacle, "Gmsh: A 3-D finite element mesh generator with built-in pre- and post-processing facilities," *International Journal for Numerical Methods in Engineering*, vol. 79, pp. 1309 – 1331, 2009.

Investigation of Beam Features of Unidirectional Rayleigh Waves Electromagnetic Acoustic Transducers (EMATs) by a Wholly Analytical Solution

Yuedong XIE[a,] Wuliang YIN [b] and Lijun XU[a,1]

[a] *School of Instrumentation and Optoelectronic Engineering, Beihang University, Beijing, China*
[b] *School of Electric and Electronic Engineering, The University of Manchester, Manchester, UK*

Abstract. Electromagnetic acoustic transducers (EMATs) are widely used in industries due to its non-contact nature. This paper investigates the beam features of unidirectional Rayleigh waves EMATs, especially the effect of the wire length on beam directivity. A wholly analytical model is developed to calculate the Lorentz force distribution and ultrasound displacement distribution. The modelling results indicate that, compared to the coil consists of shorter wires, the coil consists of longer wires results in a narrower bandwidth of main lobe of unidirectional Rayleigh waves, which means the ultrasound are more concentrated. This study can be used for unidirectional Rayleigh waves EMATs design and optimization.

Keywords. Unidirectional Rayleigh waves, EMATs, analytical solutions, beam features

1. Introduction

In industries, such as petrochemical industry and nuclear power area, non-destructive testing (NDT) techniques are commonly used for structural integrity monitoring, and thus NDT is the guarantee for long-term and safe operation [1-3]. Frequently used NDT methods include eddy current testing, ultrasonic testing, magnetic leakage testing, and acoustic emission testing, etc [4-7]. Such technologies can be used for corrosion detection, defect locating and sizing, and material characterization [4-7].

Ultrasonic testing can be implemented via piezoelectric transducers (PZTs) or electromagnetic acoustic transducers (EMATs) based on different ultrasound generation mechanisms [8, 9]. PZTs have the benefits of mechanical flexibility, insensitive to electromagnetic interference, and good penetration depth, but suffer from the need of contact between transducers and samples, which limits them in applications such as detection under high temperature [10]. EMATs, on the other hand, are advantageous due to their non-contact nature and the fact of a variety of waves modes can be generated

---

[1] Corresponding Author, Lijun Xu. School of Instrumentation and Optoelectronic Engineering, Beihang University, Beijing, 100191, China. Email: yuedongxie@buaa.edu.cn; lijunxu@buaa.edu.cn.

[11]. There are two working principles of EMATs, magnetostriction and Lorentz force mechanism, applied for different materials detection [12].

Unidirectional Rayleigh waves EMATs are firstly proposed in [12], from which the beam features of Rayleigh waves are investigated via experiments, and then were optimized based on FEM modelling. This paper focuses on using a wholly analytical solution to analyze unidirectional Rayleigh waves generated by EMATs working on Lorentz force mechanism, especially to analyze the beam features of the Rayleigh waves and investigate the wire length effect on Rayleigh waves' beam directivity. The working principle of unidirectional Rayleigh waves and its analytical model are introduced in Section 2. The beam features analysis and the wire length effect are investigated in Section 3, followed by conclusions and discussions in Section 4.

2. Analytical solutions for Unidirectional Rayleigh waves EMATs

2.1. Working principle of Unidirectional Rayleigh waves EMATs

The EMATs used to generate unidirectional Rayleigh waves consists of a permanent magnet and a double-meander-line (DML) coil. The DML coil, as shown in Figure 1(a), is formed by two separate meander line coils Tx 1 and Tx 2. The DML coil is designed to manufacture via a 4-layer flexible printed circuit board (FPCB), from which Tx 1 occupies the first and second layers while Tx 2 occupies the third and the fourth layers of FPCB. *'L'* denotes the length of the DML coil, *'W'* denotes the center-to-center distance between adjacent wires of each meander line coil, and *'S'* means the spacing between two meander-line coils.

Each meander line coil has a *'W'* equaling to one half of the Rayleigh waves' wavelength to generate Rayleigh waves. *'S'* is set to one quarter of Rayleigh waves' wavelength, and the excitation signals for these two meander line coils have a phase delay of 90^0, so that the generated Rayleigh waves only propagate in one direction based on the wave superposition. In this work, *'L'* is 50mm (the vertical length), *'W'* is 3.033mm, *'S'* is 1.5165mm and the excitation frequency is 483 kHz for aluminum plate detection. The excitation signals used are gaussian modulated sine wave signals as shown in Figure 2(a), and the waves superposition progress is presented in Figure 2(b); the working principle of unidirectional Rayleigh waves EMATs have been illustrated in [13] and are not introduced here.
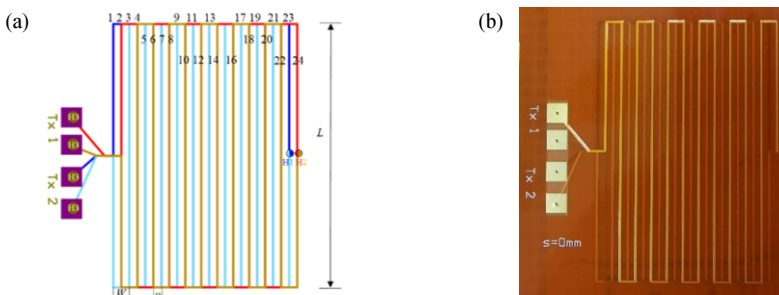
Figure 1. DML coil. (a), the schematic diagram, (b), the manufactured FPCB.

(a)

(b)
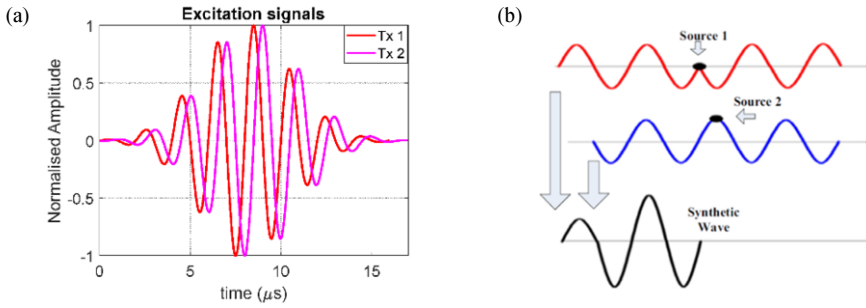
Figure 2. (a), The excitation signals for coil Tx 1 and Tx 2; (b), wave superposition between the source 1 and source 2.

2.2. Analytical solutions to Unidirectional Rayleigh waves EMATs

Since EMATs involve two physical phenomena- electromagnetic (EM) induction and ultrasound (US) propagation, the analytical model for unidirectional Rayleigh waves EMATs can be divided into two parts, EM model and US model. The test piece used was an aluminum plate. For EM model, the classic analytical solution, Dodd and Deeds solution, is employed and adapted to calculate the magnetic vector for the straight wire, and in turn to calculate Lorentz force distribution. Such adaption has been detailed in our previous work [13-14]. The computed Lorentz force from EM model are used as the vibration sources of the US model to excite ultrasound waves; in other words, the calculated Lorentz forces are the link between the EM model and the US model. The combination between the EM model and the US model is shown in Figure 3.
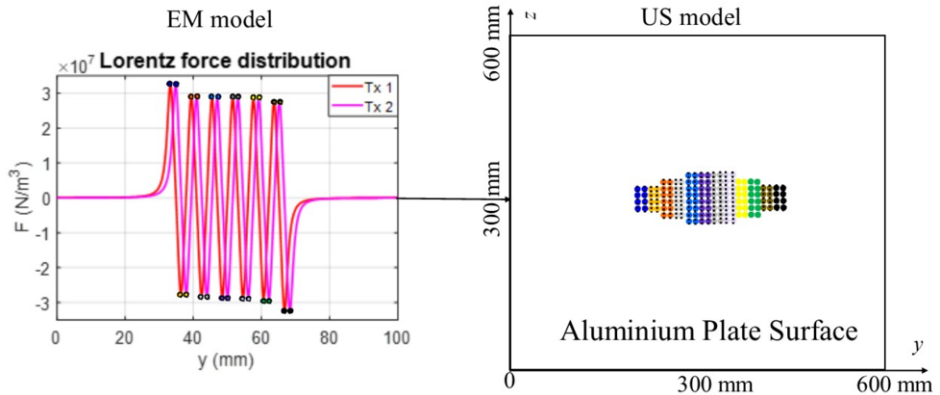
Figure 3. The link between the EM model and the US model.

The analytical solutions for Rayleigh waves radiation have been introduced detailed in our previous work [14]. The modelling parameters are showing in Table 1. Field spatial step means the distance between two adjacent field points on the surface of the aluminum plate; the dimension of the surface of the aluminum plate is $600 \times 600 \times 20$ mm^3 and the field spatial step used is 1 mm, so there are totally 601×601 field points on the surface of the aluminum plate. Source spatial step for each wire means the distance between two adjacent source points on each wire; the length of the wire is 30 mm and

the source spatial step used is 0.2 mm, so there are 151 source points on each wire. The reason we choose dense source points is that lots of source points guarantee the wave interference' integrity.

Table 1. The parameters used for modelling.

Description	Symbol	Value
Length of the sample	Y	600 mm
Width of the sample	Z	600 mm
Field spatial step	Δx_f	1 mm
Length of the meander-line-coil	L	50 mm
Source spatial step for each wire	Δx_s	0.2 mm
Density of the Aluminum plate	ρ	2700 kg/m^3
Frequency	f	483 kHz
Longitudinal waves' velocity	C_L	6.375 mm/µs
Shear waves' velocity	C_s	3.14 mm/µs
Rayleigh waves' velocity	C_R	2.93 mm/µs

The calculated Radiation pattern of the unidirectional Rayleigh waves is shown in Figure 4. From this figure, the Rayleigh waves mainly propagate along one direction with a main lobe and several side lobes. The part circled in the red ellipse should not have a larger intensity compared to that of main / side lobe, which is due to the approximation of the proposed analytical solutions. However, the part included in the red ellipse is not the focus of this work and hence is ignored. The beam features to analyze are the beam directivity of the unidirectional Rayleigh waves, in other words, the displacement field distribution of the main lobe and side lobes.
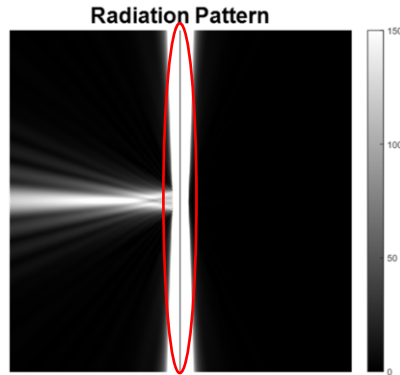
Figure 4. The radiation pattern of the unidirectional Rayleigh waves.

The beam directivity is defined as, at a specific distance away the transducer (which is EMATs in this work), the displacement / velocity fields distribution along different angles. The calculated beam directivity at a distance of 250 mm is shown in Figure 5; only the displacement fields between -30^0 to 30^0 are presented here since most of the acoustic energy are concentrated within such zone. From Figure 5, the unidirectional Rayleigh waves have a main lobe and several side lobes. The main lobe is distributed

from -7.5^0 to 7.5^0, and the bandwidth (also refereed as beam angle) of such main lobe is defined as 15^0.
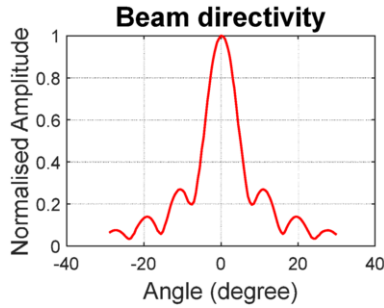
Figure 5. The beam directivity of unidirectional Rayleigh waves for 50mm-long DML.

2.3. The effect of wire length on unidirectional Rayleigh waves' beam features

For a fixed excitation frequency to generate unidirectional Rayleigh waves, the center-to-center distance between adjacent wires of each meander line coil *'W'* and the spacing between two meander-line coils *'S'* are determined. The length of the DML coil *'L'* can be changed and have an effect on beam directivity. In this part, *'L'* is changed from 20mm to 60mm with a step of 10mm, and the beam directivity at different lengths are calculated. The beam directivity comparison between different length DML is shown in Figure 6. From this figure, a longer wire corresponds to a smaller bandwidth of the main lobe; in other words, a longer wire results in a more concentrated unidirectional Rayleigh waves. More specifically, the bandwidth of main lobe are 13^0, 15^0, 19^0, 26^0, and 39^0 at wire length of 20mm, 30mm, 40mm, 50mm and 60mm respectively.
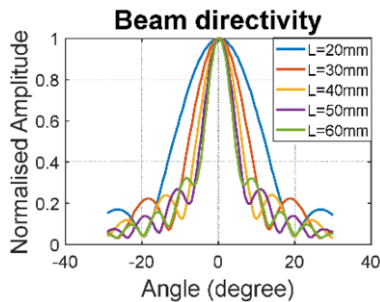
Figure 6. The beam directivity of unidirectional Rayleigh waves for different-length-DML.

3. Conclusions

The beam directivity of unidirectional Rayleigh waves is investigated via a wholly analytical model. Analytical EM model is to calculate Lorentz force distribution while the US model is to calculate the displacement distribution. Results indicate that a longer wire length of the DML coil results in a narrower bandwidth of the main lobe of unidirectional Rayleigh waves. The bandwidth of main lobe with 20mm wire length

DML is three times of that with 60mm wire length DML. This work lays a foundation for unidirectional EMATs design and optimization. Future work will be focused on experimental investigation and focusing Rayleigh waves design and analysis for the small defect detection.

References

[1] Fromme, P., et al., On the development and testing of a guided ultrasonic wave array for structural integrity monitoring. *IEEE Transactions on Ultrasonics, Ferroelectrics, and Frequency Control*, **53** (2006), 777-785.

[2] Lim, S. W. and R.A. Shoureshi. Advanced monitoring system for integrity assessment of electric power transmission lines. in *American Control Conference* (2006), 1-6.

[3] Nakagawa, N., et al. On-line NDE and structural health monitoring for advanced reactors. *Key Engineering Materials*, **321** (2006), 234-239.

[4] Edwards, C. and S. Palmer, The magnetic leakage field of surface-breaking cracks. *Journal of Physics D: Applied Physics*, **19** (1986), 657.

[5] Roberts, T. and M. Talebzadeh, Acoustic emission monitoring of fatigue crack propagation. *Journal of Constructional Steel Research,* **59** (2003), 695-712.

[6] Rose, J.L., W. Zhu, and M. Zaidi, Ultrasonic NDT of titanium diffusion bonding with guided waves, *Materials Evaluation*, **56** (1998), 535-539.

[7] Sophian, A., et al., A feature extraction technique based on principal component analysis for pulsed eddy current NDT. *NDT & E International*, **36** (2003), 37-41.

[8] Benes, E., et al., Sensors based on piezoelectric resonators. *Sensors and Actuators A: Physical*, **8** (1995), 1-21.

[9] Thompson, R.B., Physical principles of measurements with EMAT transducers. *Physical acoustics*, **19** (1990), 157-200.

[10] Colombo, S., et al., Frequency response of different couplant materials for mounting transducers. *NDT & E International*, **38** (2005), 187-193.

[11] Xie, Y., et al., Simulation of ultrasonic and EMAT arrays using FEM and FDTD. *Ultrasonics*, **66** (2016), 154-165.

[12] Wang, S., et al., Numerical and experimental analysis of unidirectional meander-line coil electromagnetic acoustic transducers. *IEEE transactions on Ultrasonics, Ferroelectrics, and Frequency Control*, **60** (2013), 2657-2664.

[13] Xie, Y., et al., A wholly analytical method for the simulation of an electromagnetic acoustic transducer array. *Int. J. Appl. Electromagn. Mech*, 2016 (2016), 1-15.

[14] Xie, Y., et al., A novel variable-length meander-line-coil EMAT for side lobe suppression. *IEEE Sensors Journal*, **16** (2016), 6279-6287.

This page intentionally left blank

Material Characterization

This page intentionally left blank

Study on the Mechanism and Application of Applying Magnetic Barkhausen Noise to Evaluate Dislocation Density and Plastic Deformation

Xueliang Kang[a,b], Shiyun Dong[a], Hongbin Wang[b,1], Xiaoting Liu[a], Shixing Yan[a]

[a] *National Key Laboratory for Remanufacturing, Army Academy of Armored Forces, Beijing 100072, China*
[b] *School of Materials Science and Engineering, Shanghai University, Shanghai 200072, China*

Abstract: Seven specimens of 45 steel with different residual strains were prepared by homogeneous plastic tensile test. The microstructure of the specimens was observed by scanning electron microscopy and the texture characteristics of the specimens were studied by X-ray diffraction. The results showed that plastic deformation mainly leads to dislocation increment in the microstructure rather than obvious deformed grain morphology, texture and residual stress. Then the dislocation density of each sample was calculated by X-ray diffraction method. The MBN signals of the samples were tested by magnetic Barkhausen noise method and the corresponding RMS (root mean square) values were calculated. The results showed that the dislocation density increases and the RMS value decreases with the increase of plastic deformation magnitude, the phenomenon was explained deeply. By establishing the correlation between dislocation density and RMS value, it was found that there was a good linear relationship between dislocation density and RMS value. According to the formula provided by the fitting curve, the dislocation density can be predicted by measuring the RMS value of any degree of plastic deformation.

Keywords: magnetic Barkhausen noise; dislocation density; plastic deformation; quantitative evaluation

1. Introduction

Magnetic Barkhausen noise (MBN) is a nondestructive testing technology that is widely used in detection of thickness of carburization layer[1] and film[2], grain size[3], phase content[4,5], stress[6,7].etc. This phenomenon is due to the interactions of domain walls with defects like grain boundaries, dislocations, inclusions and second phases, so the MBN is sensitive to microstructural changes of ferromagnetic materials. During plastic deformation, microstructure of the material will change significantly, so the MBN method can be used for characterizing plastic deformation.

Pedro P. de C. Antonio et al studied the variation of MBN signal under small plastic deformation, he attributed the change of MBN signal to the influence of many factors[8].

---

[1]Corresponding author: kangxueliangyx@163.com, syd422@sohu.com.

Martin J. Sablik et al tried to model the stress-strain curve with a modified theory, he thought that the $90°$ domain wall would also cause the change of MBN signal, but no further discussion was given[9]. The research in this field is rare, and the experiment is basically carried out under the action of coaxial external force, so the influence of external force is introduced[10,11]. In order to study the influence of dislocation density on MBN signal separately, a special design and demonstration was carried out in this study.

Dislocation is a common type of lattice defect in crystal materials, which is strongly related to mechanical properties of metals, the four theories of strength for materials are all based on dislocation theory. Dislocation has always been a hot topic in the research of metallic materials. The microscopic mechanism of plastic deformation can be explained by dislocation theory[12,13], Dislocation density determines the process of recovery and recrystallization[14-17]. Dislocation density plays a key role in work-hardening of materials[18-20]. In a word, dislocation provides an important characterization method for material science research.

Dislocation density is the main parameter for characterizing dislocation. There are several commonly used methods of calculating dislocation density, among them TEM and X-ray diffraction line profile analysis are the most widely used techniques to quantify the dislocation density. Each analytical method has its characteristics, application range and limitations. TEM technique can give an in-situ observation of dislocation morphology[21,22], however it is time consuming for a TEM sample preparation, and obtained information is from small area. Besides, for a sample with large number of dislocations, it is difficult to distinguish one from another, so TEM is mainly used for low density dislocation research. XRD reveals the average data over a relatively large area and it can be used for high density dislocation research, however, the sample preparation and observation is complex as well.

Detection of dislocation density by non-destructive method is free of the complicated sample preparation process, which is facilitate for life prediction[23] and damage assessment[24]. In this paper, seven specimens of 45 steel with different residual strains were prepared by homogeneous plastic tensile test. The microstructure of the specimens was observed by scanning electron microscopy and the texture characteristics of the specimens were studied by X-ray diffraction. Then the dislocation density of each sample was calculated by X-ray diffraction method. The MBN signals of the samples were tested by magnetic Barkhausen noise method and the corresponding RMS (root mean square) values were calculated.

2. Materials and methods

2.1 Material preparations

Tensile specimens of the same size were prepared with 45 steel. The samples were annealed to eliminate residual stress. In order to obtain different dislocation density, the tensile method was adopted. Three specimens were stretched to break, and the stress-strain curves were obtained. The mean maximum strain was about 21%. Then 7 specimens with different residual strains were obtained by tensile method (Fig.1), the residual strains were 1%, 4%, 8%, 12%, 14%, 16%, and 18% respectively, the specimens were named as #1, #2, #3, #4, #5, #6, #7 correspondingly.
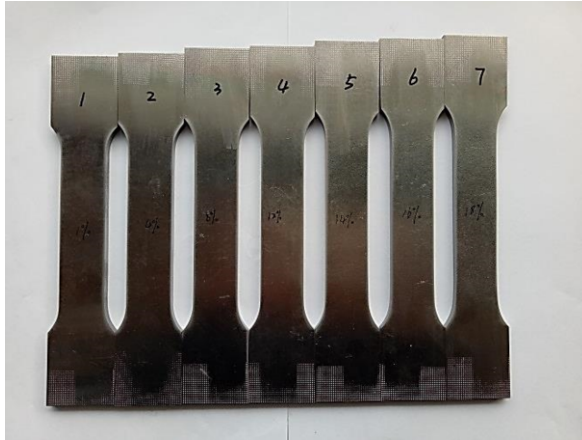
Figure 1. Tensile specimens with different plastic deformation

2.2 MBN measurements

MBN measurement was performed using the experimental system developed in the authors' laboratory. The test system is schematically shown in fig. 2.
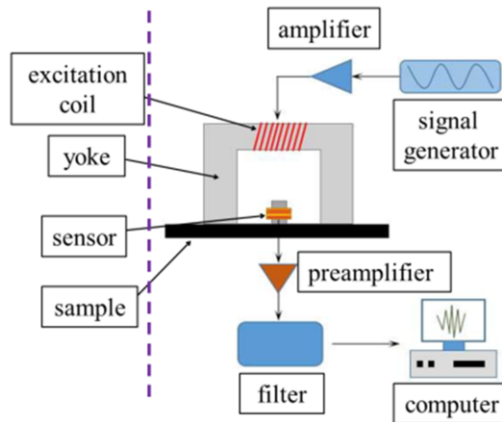
Figure 2. Experimental set-up of MBN

The U-shaped yoke placed on the surface of the sample is used to provide a magnetic field. A sinusoidal signal provided by the function generator is applied to the excitation coil. The pick-up coil used to detect the MBN signals is mounted in the middle between the legs of the U-core. The original signal is amplified and filtered. To minimize undesirable effect of eddy current in the induction process, in the experiment the excitation frequency was set to 10 Hz, the sampling frequency was set to 200 kHz.

The morphology of one MBN signal is shown in figure 3. The MBN signal is composed of many pulses of different intensities. In order to quantitatively describe one MBN signal, the RMS (root mean square) is used as the eigenvalue. The RMS voltage of the MBN signal is computed using the expression

$$V_{RMS} = \sqrt{(\sum_i V_i^2)/n} \qquad (1)$$

Where V_i is voltage intensity and n is the number of voltage pulses.
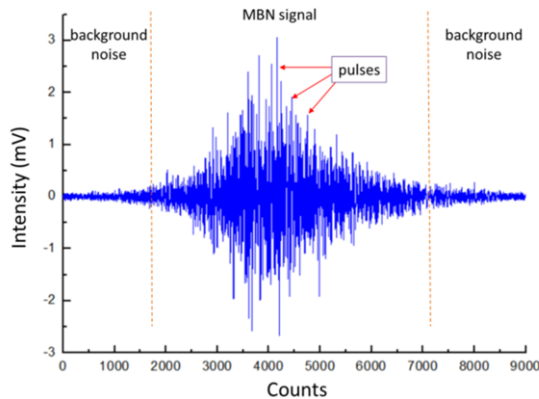
Figure 3. Morphology of one MBN signal

2.3 Microstructure characterization and X-ray Diffraction Measurements

The microstructure of the specimen was characterized by scanning electron microscope (SEM). The specimens were prepared according to the standard procedure, etched with Nitric acid alcohol solution (4% HNO3, 96% alcohol) after grinding and polishing. A PANalytical X-Pert system with $Cu - k_\alpha$ radiation (λ =0.154nm) was used for XRD measurement. The X-ray tube was operated at 40 kV and 40 mA. The diffraction lines were recorded from 2θ =10° to 90° with a step of 0.02° to cover the main diffraction angles of the samples. The (110), (200) and (211) pole figures were measured and the orientation distribution function (ODF) was calculated for texture analysis.

3. Results and discussion

3.1 Microstructure analysis

The samples for MBN and XRD measurement were free from external influences (Force, temperature and magnetic field), the microstructure completely determines the MBN and XRD signals. The influence of microstructure can be divided into different factors, such as dislocation, residual stress, grain size, texture and so on. The external force was uniformly and slowly applied to the cross section of the specimen during tensile test, resulting in uniform plastic deformation in the material, no macroscopic residual stress was generated in the specimens. Texture is another important factor affecting the detection signal. Texture may be formed during plastic deformation, Textural structure with specific orientation distribution results in anisotropy of the detection signals. Plastic deformation can also cause grain shape changes, the size of which depends on the composition of the material, the type of microstructure and the degree of plastic deformation. The morphology and size of the grains will also cause

changes in the detection signals. The microstructure and texture of the specimens were observed.
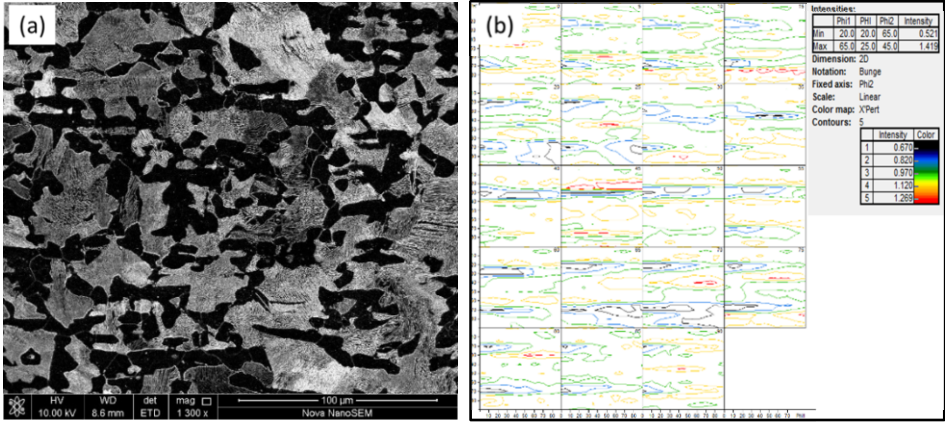
(a)SEM figure; (b) ODF figure

Figure 4. microstructure and texture observation of the #7 specimen

The corresponding result of the #7 specimen was given in figure 4. As shown in Fig.4 (a), the ferrite (black in color) and pearlite (white in color) is uniformly distributed, no obvious deformed structures or bands were observed. Fig.4 (b) shows the orientation density map at different directions. According to the color scale, the orientation density is uniformly distributed in all directions, and there is no orientation concentration in the material. The deformation of the #7 specimen is the largest, and there was no deformed microstructure and texture produced during tensile deformation. The test results of other samples with smaller deformation are similar. In summary, tensile deformation process mainly results in changes of dislocation density of the specimens.

3.2 Dislocation density measured by X-ray diffraction method

The dislocation density was measured according to the XRD profile analysis method. The modified Williamson-Hall method (m-WH) is a widely used method to evaluate the dislocation density[25,26]. The dislocation density measured by X-ray diffraction experiment can be described by the following equation[27]:

$$(\Delta K)^2 = \left(\frac{\alpha}{d}\right)^2 + \beta K^2 C + O(K^2 C^2) \qquad (2)$$

$$\Delta K = \frac{2W\cos\theta}{\lambda} \qquad (3)$$

$$K = \frac{2\sin\theta}{\lambda} \qquad (4)$$

$$\beta = \frac{\pi M^2 b^2}{2}\rho \qquad (5)$$

In which, α is shape factor, d is the average grain size, θ is diffraction angle, W is the full-width-half-maximum (FWHM) of the XRD diffraction peak, ρ is the dislocation density, λ is X-ray wave length, K is the magnitude of diffraction vector,

M is a constant parameter depending on the effective outer cutoff radius of dislocation, in deformed materials M varies in between 1 and 2, for most instance M was selected as 2[28,29], O indicates non-interpreted higher order terms, b is the magnitude of the Burgers vector. C is the so called dislocation contrast factor, which is determined by the elastic anisotropy and the dislocation type of the material

$$C = C'_{h00}(1 - qH^2) \tag{6}$$

C'_{h00} is a constant (0.258). In a similar manner, the q parameter was determined as 1.977. H^2 can be expressed as the fourth–order invariant function of the Miller indices (hkl):

$$H^2 = \frac{h^2k^2+k^2l^2+l^2h^2}{(h^2+k^2+l^2)^2} \tag{7}$$

According to Eq. (2), the ΔK for each (hkl) plane was plotted as a function of K^2C^2, after linear fitting, the slope β was calculated and the dislocation density ρ can be obtained according to Eq. (5).

In this research, b=0.284[31], α is given as 0.9 under assumption of spherical crystals with cubic symmetry[32], the results of X-ray diffraction was given in figure 5.
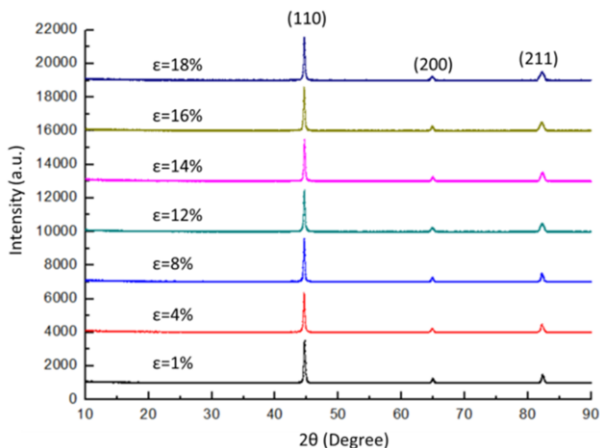
Figure 5. XRD diffraction peaks of the specimens

As shown in figure 5, 3 distinct diffraction peaks ((110), (200) and (211)) were detected in each sample. The diffraction peaks have obvious broadening characteristics. FWHM values of the (110), (200) and (211) X-ray diffraction peaks were obtained from the original diffraction data. However for (h00) plane, the value of H^2 in Eq. (7) is zero. In such a case Eq. (2) cannot be applied[33], so only diffraction data from (110) and (211) was used. The relationship between $(\Delta K)^2$ and K^2C was given in Figure 6. After linear fitting, it can be seen clearly in Figure 6 that with the increase of plastic deformation, the slope of fitting curve is increasing. The β value of each sample was obtained through fitting and the corresponding dislocation density was calculated according to Eq. (4), as shown in table 1, the dislocation density increases with the increase of plastic deformation.
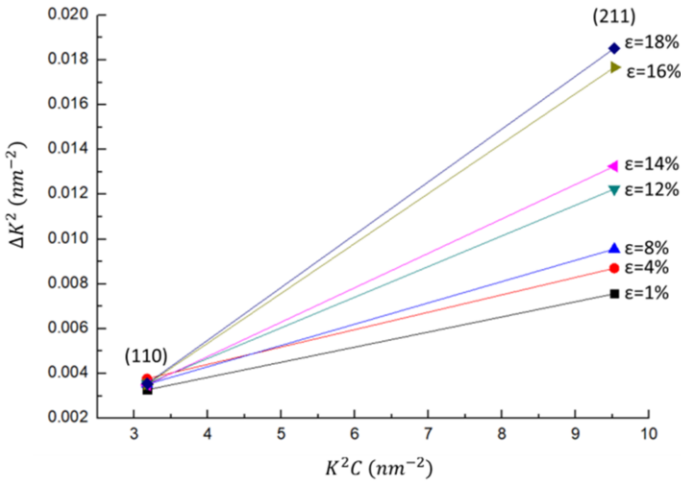
Figure 6. Peak broadening analysis using the modified Williamson–Hall plot

Table 1. Summary of the Coefficient of the Fitting Curve in the Modified Williamson-Hall Plot

specimen	#1	#2	#3	#4	#5	#6	#7
Residual strain (%)	1	4	8	12	14	16	18
β	0.113	0.143	0.172	0.228	0.25	0.328	0.341
ρ ($\times 10^{15}$/m²)	2.2	2.8	3.4	4.5	4.9	6.5	6.7

3.3 Dislocation density evaluated by MBN

After the XRD test，the MBN signals of each sample were tested at the same location. All tests were carried out under the same condition. Figure 7 shows the morphology of 3 MBN signals obtained from each sample. As can be seen clearly, the morphology of each MBN signal is spindle shaped, large in the middle, and small in the two ends. The distribution area of MBN signal corresponding to the plastic deformation of 1% is the largest, indicating that the MBN signal intensity is the strongest of the 7 specimens, whereas the distribution area of MBN signal corresponding to the plastic deformation of 18% is the smallest, indicating the weakest intensity of MBN signals. It looks as if the difference of MBN signal morphology is not obvious between the two specimens with similar degree of plastic deformation, on the whole, the MBN signal morphology of the 7 samples is quite different. The MBN signal intensity of specimens from the smallest plastic deformation to the largest plastic deformation is gradually decreasing. In order to assess this difference quantitatively, RMS of each sample was calculated. Because the overall appearance of MBN signals obtained from the same sample is different. The RMS value of each sample is averaged over ten MBN signals to minimize the effect of signal morphological differences.

From macroscopic view, the difference of MBN signals in different samples is caused by plastic deformation. In fact it is the difference of dislocation density that results in the different intensity of MBN signals. Fig. 8 shows the relationship between

plastic deformation, dislocation density and MBN signal among different specimens. As can be seen clearly, with the increase of plastic deformation degree, the basic rule is the increase of dislocation density and the decrease of MBN signal intensity.
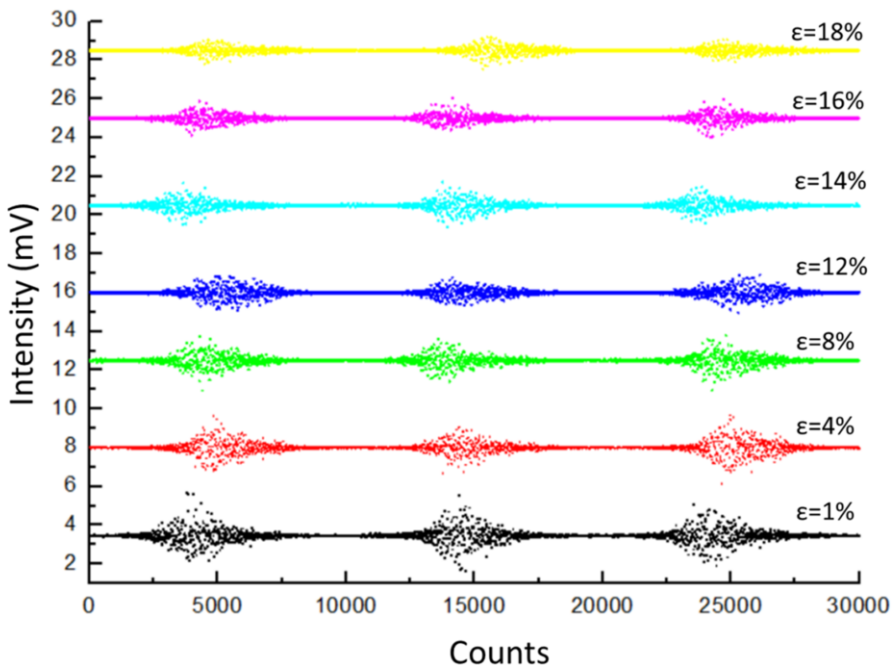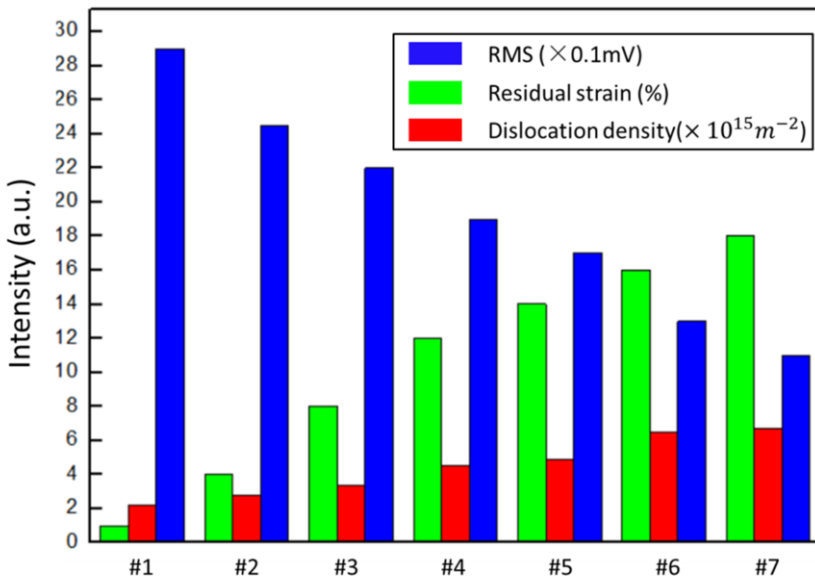

Figure 7. MBN signals of the samples

Figure 8. Variation of RMS and dislocation density with the increase of plastic deformation degree

3.4 Relationship between dislocation density and MBN signal

The value of the dislocation density ρ can be calculated from the average values of the crystallite size D and microstrain ε by relationship[34]

$$\rho = \frac{3\sqrt{2\pi}\langle\varepsilon^2\rangle^{1/2}}{Db} \qquad (8)$$

where b is the Burgers vector.

According to Eq. (8), the dislocation density increases with the increase of plastic strain, the research in this paper has also reached the same conclusion. The dislocation multiplication can be well explained by the Frank-Read source model, which is usually used to characterize dislocation generation in the bulk of a crystalline material[35].

The MBN signal intensity decreases with the increase of dislocation density, this is determined by magnetic domain dynamics. The MBN signal is generated when the magnetic domain moves. Any factor that hinders the movement of magnetic domains will affect the MBN signal. Dislocations hinder the movement of magnetic domain walls. Each dislocation will have a critical value of the pinning force per unite length, the domain wall can move only when the external force is greater than the pinning force provided by all the dislocations. The critical field is defined as[36]

$$H_{crit} = \frac{\gamma \cos\emptyset_{crit}}{\mu_0 M_s L(\cos\Omega_1 - \cos\Omega_2)} \qquad (9)$$

Where L is the distance between two adjacent pinning sites. Under the same test conditions, the other parameters are the same. According to Eq. (9), the critical strength H_{crit} for MBN activity decreases as the spacing L increases. According to the model of Nes and Marthinsen[37,38], the slip length of dislocations reduced due to the formation of cell structures and sub-boundaries during deformation. As the degree of deformation increases, the dislocation density increases, the value of L decreases, the critical field strength required for magnetic domain wall motion increases, and the number of magnetic domains that can be moved decreases, eventually the value of MBN signal decreases.

3.5 Correlation between dislocation density and MBN signal

According to the above analysis, the law that the MBN signal decreases with increasing dislocation density is very clear. This makes it possible to quantitatively evaluate the dislocation density using the magnetic Barkhausen noise method, and the relationship diagram was drawn, in which, dislocation density is abscissa and RMS is ordinate, as shown in figure 9. The seven data points show a good linear relationship. According to the regression analysis, the relationship between RMS and Dislocation density can be expressed as:

$$D = \frac{R - 3.58}{-0.36} \qquad (10)$$

Where R indicates RMS intensity, D indicates dislocation density. In order to verify the reliability of the method, three tensile specimens were prepared using the same material and method. The residual strain of the samples was 15% after tensile deformation. The mean RMS value of the three samples is 1.57, substitute it into Eq. (10), the calculated dislocation density value is $5.58 \times 10^{15}/m^2$. The mean dislocation density of the three specimens tested by the m-WH method was $5.32 \times 10^{15}/m^2$, the

relative error of this method is 4.9%. The results show that the MBN method has high accuracy in measuring dislocation density.
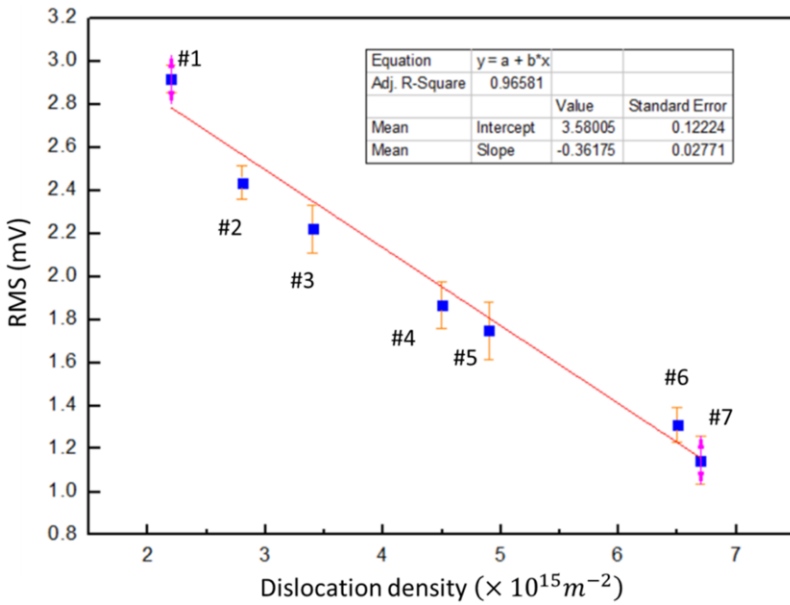

Figure 9. Relationship between RMS and dislocation density

3.6 Correlation between plastic deformation and MBN signal
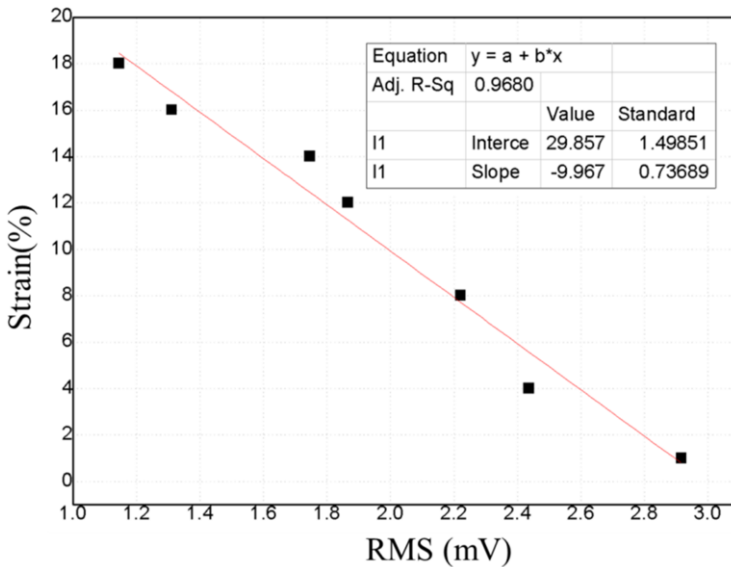

Figure 10. Relationship between RMS and plastic deformation

There is a negative correlation between plastic deformation and MBN signal, as shown in figure 10, in which, RMS is abscissa and plastic deformation is ordinate. Therefore, MBN signal can be used to predict plastic deformation, and the bridge between them is dislocation density, as discussed above.

4. Conclusions

The mainly change of the microstructure of the specimens during tensile deformation is the dislocation multiplication. With the increase of plastic deformation degree, the dislocation density increases and the MBN signal intensity decreases. There are remarkable negative linear relevant relations between RMS and dislocation density as well as plastic deformation. According to the regression function, the dislocation density and plastic deformation can be forecasted, and the prediction value is of high precision. This study confirms that it is feasible to quantitatively evaluate dislocation density and plastic deformation using MBN method.

References

[1] Zhang M L. Study of Magnetic Barkhausen Noise on the evaluation of case depth on carburized steel [J]. Journal of the American College of Cardiology, 2015, 62(11):981–989.

[2] Seemuang N, Slatter T. Using Barkhausen noise to measure coating depth of coated high - speed steel [J]. International Journal of Advanced Manufacturing Technology, 2017(20):1-12.

[3] Ghanei S, Kashefi M, Mazinani M. Comparative study of eddy current and Barkhausen noise nondestructive testing methods in microstructural examination of ferrite–martensite dual-phase steel [J]. Journal of Magnetism & Magnetic Materials, 2014, 356(356):103-110.

[4] Ghanei S, Alam A S, Kashefi M, et al. Nondestructive characterization of microstructure and mechanical properties of intercritically annealed dual-phase steel by magnetic Barkhausen noise technique [J]. Materials Science & Engineering A, 2014, 607(607):253-260.

[5] Vashista M, Moorthy V. On the shape of the magnetic Barkhausen noise profile for better revelation of the effect of microstructures on the magnetisation process in ferritic steels [J]. Journal of Magnetism & Magnetic Materials, 2015, 393:584-592.

[6] Blaow M, Evans J T, B.A. Shaw. Magnetic Barkhausen noise: the influence of microstructure and deformation in bending [J]. Acta Materialia, 2005, 53(2):279-287.

[7] Sheikh Amiri M, Thielen M, Rabung M, et al. On the role of crystal and stress anisotropy in magnetic Barkhausen noise [J]. Journal of Magnetism & Magnetic Materials, 2014, 372(12):16-22.

[8] De C A P P, De Campos M F, S Dias F M D, et al. Sharp Increase of Hysteresis Area Due to Small Plastic Deformation Studied With Magnetic Barkhausen Noise[J]. Magnetics IEEE Transactions on, 2014, 50(4):1-4.

[9] Sablik M J, Augustyniak B, De Campos M F, et al. Modeling of Effect of Plastic Deformation on Barkhausen Noise and Magnetoacoustic Emission in Iron With 2% Silicon[J]. IEEE Transactions on Magnetics, 2008, 44(11):3221-3224.

[10] Dhar A, Clapham L, Atherton D L. Influence of uniaxial plastic deformation on magnetic Barkhausen noise in steel[J]. Ndt & E International, 2001, 34(8):507-514.

[11] Stefanita C G, Atherton D L., Clapham L, et al. Plastic versus elastic deformation effects on magnetic barkhausen noise in steel[J]. Acta Materialia, 2000, 48(13):3545-3551.

[12] Chattopadhyay A K, Aifantis E C. Stochastically forced dislocation density distribution in plastic deformation [J]. Phys.rev.e, 2016, 94(2).

[13] Harjo S, Kawasaki T, Tomota Y, et al. Unusual Plastic Deformation Behavior in Lath Martensitic Steel Containing High Dislocation Density [C]// Materials Science Forum. 2017.

[14] Humphreys F J, Hatherly M. Recrystallization and Related Annealing Phenomena (Second Edition) [M]. Elsevier, 2004.

[15] Momeni A, Dehghani K, Ebrahimi G R. Modeling the initiation of dynamic recrystallization using a dynamic recovery model [J]. Journal of Alloys & Compounds, 2011, 509(39):9387-9393.

[16] Roucoules C, Pietrzyk M, Hodgson P D. Analysis of work hardening and recrystallization during the hot working of steel using a statistically based internal variable model [J]. Materials Science & Engineering A, 2003, 339(1):1-9.

[17] Tian B, Lind C, Schafler E, et al. Evolution of microstructures during dynamic recrystallization and dynamic recovery in hot deformed Nimonic 80a [J]. Materials Science & Engineering A, 2004, 367(1):198-204.

[18] Prasad G V S S, Goerdeler M, Gottstein G. Work hardening model based on multiple dislocation densities [J]. Materials Science & Engineering A, 2005, 400(1):231-233.

[19] Lavrentev F F, Pokhil Y A. Relation of dislocation density in different slip systems to work hardening parameters for magnesium crystals [J]. Materials Science & Engineering, 1975, 18(2):261-270.

[20] Mittra J, Dey G K, Dubey J S, et al. Role of dislocation density in raising the stage II work-hardening rate of Alloy 625 [J]. Materials Science & Engineering A, 2009, 512(1):87-91.

[21] Zielinski W, Lii M J, Gerberich W W. Crack-tip dislocation emission arrangements for equilibrium —I. In situ, TEM observations of Fe, 2wt%Si [J]. Acta Metallurgica Et Materialia, 1992, 40(11):2861–2871.

[22] Li N, Wang J, Huang J Y, et al. In situ TEM observations of room temperature dislocation climb at interfaces in nanolayered Al/Nb composites [J]. Scripta Materialia, 2010, 63(4):363-366.

[23] Huang J H, Qian Y Y, Jiang Y H, et al. A dislocation model of shear fatigue damage and life prediction of SMT solder joints under thermal cycles [J]. IEEE Transactions on Components Hybrids & Manufacturing Technology, 2002, 15(4):553-558.

[24] Pangborn R N, Weissmann S, Kramer I R. Dislocation distribution and prediction of fatigue damage [J]. Metallurgical Transactions A, 1981, 12(1):109-120.

[25] He B B, Hu B, Yen H W, et al. High dislocation density-induced large ductility in deformed and partitioned steels [J] Science, 2017, 357(6355):1029.

[26] Ungár T, Gubicza J, Hanák P, et al. Densities and character of dislocations and size-distribution of subgrains in deformed metals by X-ray diffraction profile analysis [J]. Materials Science & Engineering A, 2001, 319(4):274-278.

[27] Woo W, Ungár T, Feng Z, et al. X-Ray and Neutron Diffraction Measurements of Dislocation Density and Subgrain Size in a Friction-Stir-Welded Aluminum Alloy [J]. Metallurgical & Materials Transactions A, 2010, 41(5):1210-1216.

[28] Renzetti R A, Sandim H R Z, Bolmaro R E, et al. X-ray evaluation of dislocation density in ODS-Eurofer steel [J]. Materials Science & Engineering A, 2012, 534(2):142-146.

[29] Seth P P, Das A, Bar H N, et al. Evolution of Dislocation Density During Tensile Deformation of BH220 Steel at Different Pre-strain Conditions [J]. Journal of Materials Engineering & Performance, 2015, 24(7):2779-2783.

[30] T. Ungár, I. Dragomir, Á. Révész, et al. The contrast factors of dislocations in cubic crystals: the dislocation model of strain anisotropy in practice [J]. Journal of Applied Crystallography, 2010, 32(5):992-1002.

[31] Hajyakbary F, Sietsma J, Böttger A J, et al. An improved X-ray diffraction analysis method to characterize dislocation density in lath martensitic structures [J]. Materials Science & Engineering A, 2015, 639:208-218.

[32] Langford J I, Wilson A J C. Scherrer after sixty years: A survey and some new results in the determination of crystallite size [J]. Journal of Applied Crystallography, 2010, 11(2):102-113.

[33] Ribárik G, Ungár T. Characterization of the microstructure in random and textured polycrystals and single crystals by diffraction line profile analysis [J]. Materials Science & Engineering A, 2010, 528(1):112-121.

[34] Dini G, Ueji R, Najafizadeh A, et al. Flow stress analysis of TWIP steel via the XRD measurement of dislocation density [J]. Materials Science & Engineering A, 2010, 527(10):2759-2763.

[35] Xu S, Xiong L, Chen Y, et al. An analysis of key characteristics of the Frank-Read source process in FCC metals [J]. Journal of the Mechanics & Physics of Solids, 2016, 96:460-476.

[36] Jiles D C. Dynamics of domain magnetization and the Barkhausen effect [J]. Czechoslovak Journal of Physics, 2000, 50(8):893-924.

[37] Marthinsen K, Nes E. A general model for metal plasticity [J]. Materials Science & Engineering A, 1997, 234–236(97):1095-1098.

[38] Erik Nes. Modelling of work hardening and stress saturation in FCC metals [J]. Progress in Materials Science, 1997, 41(3):129-193.

Corrosion Evaluation of Steel Rebar Using Electromagnetic Induction Method

Dongfeng HE[1]

National Institute for Materials Science, Sengen 1-2-1, Tsukuba, Japan

Abstract. Corrosion of steel reinforcing bar (rebar) reduces the strength capacity of concrete, and also causes the crack of concrete due the volume increase of the corrosion products. Detection of corrosion at its early stage is important for the safety evaluation and repairment of the concrete structures. An electromagnetic induction method was developed to evaluate the corrosion of steel rebar. By measuring the electromagnetic response of steel rebar, it was possible to judge the corrosion of steel rebar in concrete. A small compact system, suitable for field experiments was also developed.

Keywords. Steel rebar, corrosion, electromagnetic method.

1. Introduction

Steel reinforcing bar (Rebar) is often used in concrete structure to increase the strength capacity. In case of fresh uncracked concrete, the concrete covering over the rebar is very effective in inhibiting the penetration of corrosive agents to the steel. Also, fresh concrete has a high pH (a unit to measure the acidity of a substance) value which usually inhibits corrosion reactions. However, as time passes the above conditions tend to alter. Water, salt, O_2, CO_2, and industrial gases (if present) slowly begin penetrating the concrete, both the pH value and the protective quality of concrete are decreased. For the concrete used in severe environments where sea water or deicing salts are present. When chloride moves into the concrete, it disrupts the passive layer protecting the steel, causing it to rust and pit. Carbonation of concrete is another cause of steel corrosion. When concrete carbonates to the steel rebar, the normally alkaline environment, protesting steel rebar from corrosion, is replaced by a more neutral environment. Occasionally, a lack of oxygen surrounding the steel rear will cause the metal to dissolve, leaving a low pH liquid. Figure 1 shows the corrosion progress of steel rebar in the service period of concrete structures and the maintenance. In the incubation period, the steel rebar is protected by the oxidic layer of the steel rebar and the high pH value environment in the concrete. Then, after several years, the inner environment of the concrete is altered and the pH value is reduced. The corrosion of steel rebar starts and causes the crack of the concrete due to the volume increase of the corrosion products. Then, water can easily penetrate to the steel rebar through the crack, that accelerates the corrosion of steel rebar. The periodic inspection of the steel rebar in concrete is necessary and important for safety management. Knowing the conditions of

---

[1] Corresponding Author, Dongfeng He, Research Centre of Structural Materials, National Institute for Materials Science, Sengen 1-2-1, Tsukuba, Ibaraki 305-0047; E-mail: he.dongfeng@nims.go.jp.

the steel rebar, such as the location, the diameter, and the corrosion of steel rebar, is important for the safety evaluation of concrete structures.
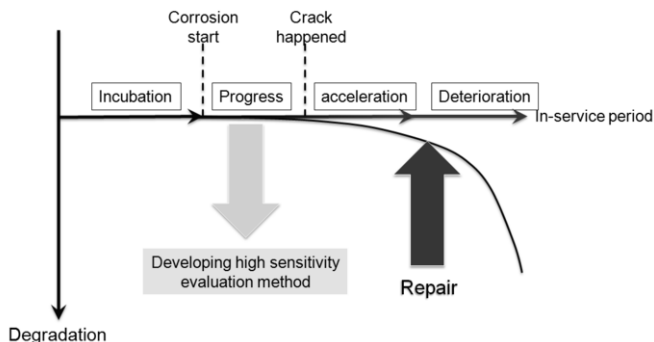

Figure 1. Corrosion progress of steel rebar in concrete and the maintenance of concrete structure.

Electrochemical potential and impedance methods [1,2] are often used to monitor the corrosion of steel rebar in concrete. But it is difficult to locate the corrosion position using these methods. In recent years, ultrasonic waves [3,4] are used for early detection and assessment of localized damage in bare rebars in the form of corrosion pits. Electromagnetic induction (AC field) method [5-9], Microwave radar system [10-12], thermography technology [13, 14], and X-ray method [15] have also been used to evaluate the corrosion of the steel rebar in concrete. For the microwave radar systems, the water or moisture in the concrete structures may have big influence to the detection accuracy. For the X-ray method, the transmitter and the receiver are often on the opposite side. It is not convenient to do field experiments. Pulsed eddy current (PEC) thermography is used to get the image of the steel rebar corrosion. Due to the thermal insulation of the concrete, it is difficult to detect the corrosion of steel rebar with the large depth. Compared with other methods, the low frequency electromagnetic induction method has the advantages of low cost, easy operation, and less moisture influence. In this paper, we will report our experiments of corrosion evaluation of steel rebar using electromagnetic induction evaluation system.

2. Principle of electromagnetic induction method

Table I shows several kinds of corrosion products and their permeabilities and electrical conductivities. The electrical conductivities of all the corrosion products are smaller than that of carbon steel (steel rebar). The permeabilities of FeO and FeOOH are smaller than that of steel rebar, and the permeabilities of Fe_2O_3 and Fe_3O_4 are bigger than that of steel rebar.

Table I. Corrosion products and their permeabilities and conductivities.

	Relative permeability	Electrical conductivity (S/cm)
Carbon steel (steel rebar)	100	7×10^4
FeO	1.0072	300
FeOOH	1.1	5×10^{-9}
Fe_2O_3	Hundreds	10^{-4}
Fe_3O_4	Hundreds	200

The corrosion layer of the steel rebar is often composed of the mixture of above corrosion products. Compared with the steel rebar without corrosion, the corrosion layer has different electrical conductivity and permeability, so it also has different responses to the applied electromagnetic field

Figure 2 shows the principle of low frequency electromagnetic induction method to evaluate the corrosion of steel rebar. The big excitation coil is used to produce the AC magnetic field when AC current flows in the excitation. The small detection coil is used to measure the magnetic field produced by the steel rebar. The lock-in amplifier was used to get the X and Y signal, where the X signal was the same phase signal with the excitation magnetic field, and the Y signal was the signal with 90-degree phase difference with the excitation magnetic field.
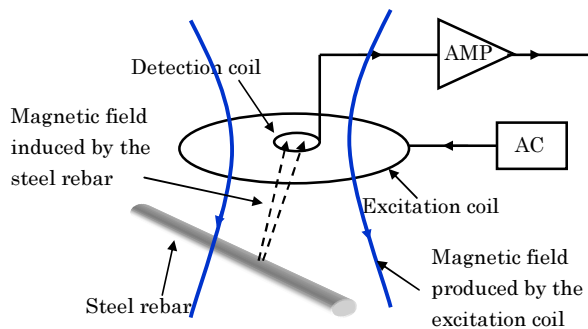

Figure 2. Principle of electromagnetic method to evaluate the corrosion of steel rebar.

There are two effects existing for the steel rebar: magnetization effect and eddy current effect. At very low frequency, the magnetization effect determines the signal; at high frequency, the eddy current effect determines the signal.

3. Experimental system and experimental results

We developed a compact experimental system. Figure 3 shows it. The excitation coil, the detection coil, the amplifier, the lock-in amplifier and the AD converter all were put in a small box of about 9cm×12cm×7cm. Only one USB cable connected with a computer was used for the data transferring and the power supplying. The total power consumption of the system was about 0.5 W. Labview program was developed for data acquisition and data procession. In our experiments, the frequency was about 80 kHz, the diameter of the excitation coil was 3 cm with 100 turns, and the detection coil was 1 cm with 100 turns. When big excitation coil was used, big detection depth could be achieved, but the neighboring steel rebar might also have big influence. The corrosion of the steel rebar normally happens with the depth smaller than 5 cm. Therefore, 3 cm excitation was used in our system. When the excitation frequency was low, the signal difference was small for different corrosion level; when the frequency was high, the stability of the system became less, so the excitation frequency of 80 kHz was chosen according to our experiments.
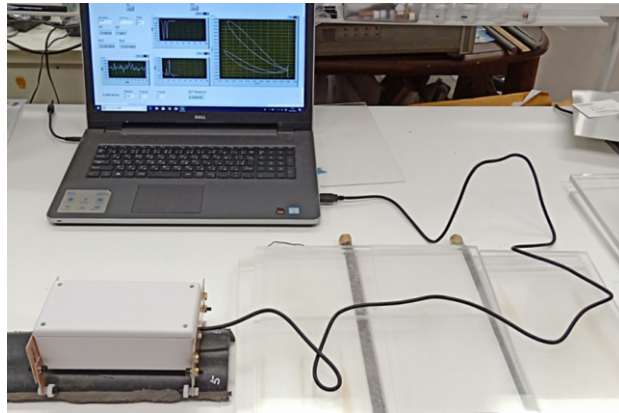
Figure 3. Compact electromagnetic system for the corrosion evaluation of steel rebar.

Figure 4 shows the samples of steel rebar with different corrosion levels. The samples were the deformed steel rebars with the diameter of 16 mm. The steel rebar "a" had no corrosion; steel rebar "b" had a little corrosion, there were some corroded dots on the surface the steel rebar; steel rebar "c" had big corrosion, the thickness of the corroded layer was about 0.1 mm and steel rebar "d" had severe corrosion with the thickness of the corrosion layer of about 1 mm. The steel rebars were from concrete structures, not prepared by artificial corrosion. The corrosion layer was normally the mixture of several kinds of corrosion products.
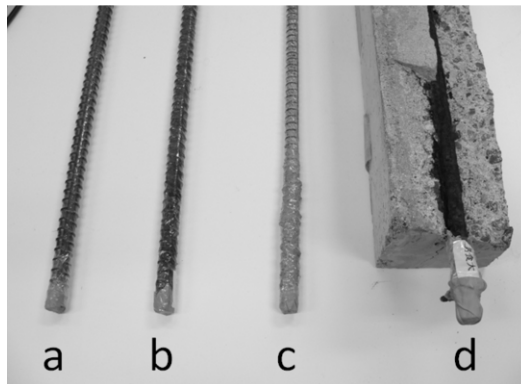
Figure 4. Samples of steel rebar. a: no corrosion. b: a little corrosion with corroded dots on the surface. c: big corrosion with the 0.1 mm corroded layer. d: severe corrosion with 1 mm corroded layer.

We scanned the samples of the steel rebars using the electromagnetic system. The samples were covered by concrete plates with different thicknesses. When 3 cm excitation coil was used, the maximum detection depth was about 7 cm. Figure 5 shows the X-Y graphs of the signals when the covering depth was 2 cm, 3 cm, 4 cm, and 5 cm respectively. The X-Y graphs were plotted using the X and Y output signals of the lock-in amplifier. The slopes were different for the steel rebars with different corrosion levels. For the same steel rebar sample, the slopes were similar for different covering depths.
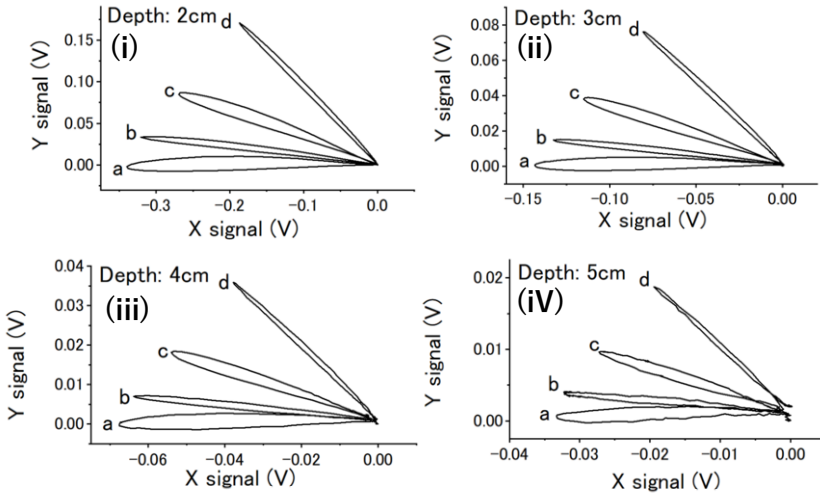
Figure 5. X-Y graphs of the signals when the covering depth was 2 cm, 3 cm, 4 cm, and 5 cm respectively.

We measured the influences of neighbor steel rebar and found that the influence was small when the distance of two steel rebar was bigger than 10 cm. We also measured the influence of the cross steel rabar. Figure 6 shows it. Two steel rebars were put on the top: one had corrosion and another had no corrosion. The other two steel rebars without corrosion were put on the bottom. The steel rebars were covered by the acrylic plate with thickness of 4 cm. In Figure 6(a), the scanning direction was in the middle of the bottom two steel rebars. In Figure 6 (b), the scanning was over one of the bottom steel rebar. Figure 6(c) and Figure 6(d) shows the results respectively. The differences could be observed for the steel rebars with corrosion and without corrosion. The signals were reset to zero as the probe was put on the acrylic plate before the scanning. For the two cases, the bottom steel rebars had less influence to the slopes of the signals.

Figure 6. Measuring the influence of cross steel rebar.

4. Summary

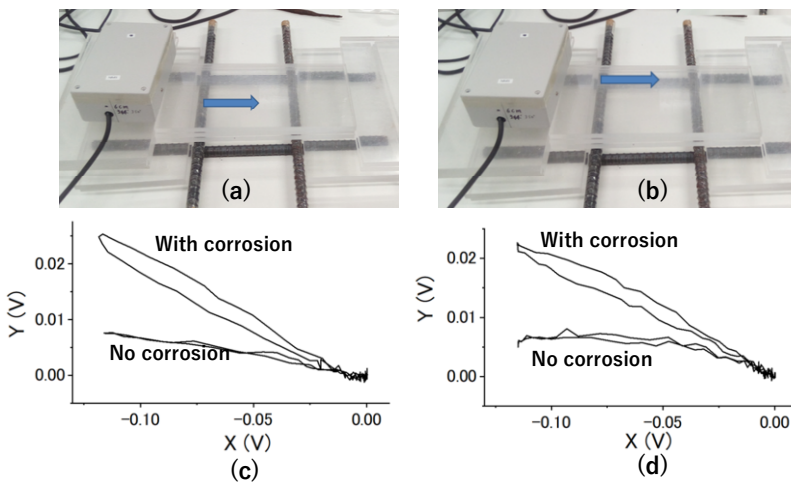We developed electromagnetic induction methods to evaluate the corrosion of steel rebar. Using the frequency about 80 kHz and the X, Y output signals of the lock-in amplifier, the corrosion of steel rebar was evaluated using the slope of the X-Y graph. The slope was determined by the material of the steel rebar and the corrosion level of steel rebar. It had less relation with the depth or distance from the steel rebar. In the future, simulation will be used to optimize the probe.

Acknowledgment

References

[1]   R. Ravi, G.T. Parthiban, "Potential monitoring system for corrosion of steel in concrete," *Advances in Engineering Software*, **37** (2006), 375-381

[2]   Yoshinao Hoshi, Taisuke Koike, Hiroyuki Tokieda, Isao Shitanda, Masayuki Itagaki, Yoshitaka Kato, "Non-contact measurement to detect steel rebar corrosion in reinforced concrete by electrochemical impedance spectroscopy," *Journal of the Electrochemical Society*, **166** (2019), C3316-C3319.

[3]   Rajeshwara Chary Sriramadasuabc, Sauvik Banerjeeb, Ye Lu, "Detection and assessment of pitting corrosion in rebars using scattering of ultrasonic guided waves," *NDT & E International*, **101** (2019), 53-61

[4]   Peng Du, DongyuXu, Shifeng Huang, Xin Cheng, "Assessment of corrosion of reinforcing steel bars in concrete using embedded piezoelectric transducers based on ultrasonic wave," *Construction and Building Materials*, **151** (2017), 925-930.

[5]   P.A. Gaydecki, F.M. Burdekin, "An inductive scanning system for two dimensional imaging of reinforcing components in concrete structures," *Meas. Sci. Techno.*, **5** (1994), 1272-1280.

[6]   Z.Z. Yu, P.A. Gaydecki PA, I. Silva I, B.T. Fernandes, F.M. Burdekin, "Magnetic field imaging of steel reinforcing bars in concrete using portable scanning systems," *Review of Progress in Quantitative Nondestructive Evaluation*, **18** (1999), 2145-2152.

[7]   P. Gaydecki, I. Silva, B.T. Fernandes, Z.Z. Yu, "A portable inductive scanning system for imaging steel-reinforcing bars embedded within concrete," *Sensors and Actuators A, Physical*, **84** (2000), 25-32.

[8]   G. Miller, P. Gaydecki, S. Quek, B. Fernandes, and M. Zaid, "A combined Q and heterodyne sensor incorporating real-time DSP for reinforcement imaging, corrosion detection and material characterization," *Sensors and Actuators A, Physical*, **121** (2005), 339–346.

[9]   G. Miller, P. Gaydecki, S. Quek, B.T. Fernandes, M.A.M. Zaid, "Detection and imaging of surface corrosion on steel reinforcing bars using a phase-sensitive inductive sensor intended for use with concrete," *NDT&E International*, **36** (2003), 19–26.

[10]   J.H. Bungey, and S.G. Millard, "Radar inspection of structures," *Proceedings of the Institution of Civil Engineers - Structures and Buildings*, **99** (1993), 173-178.

[11]   T.C.K. Molyneaux, S.G. Millard, J.H. Bungey, and J.Q. Zhou, "Radar assessment of structural concrete using neural networks," *NDT&E International*, **28** (1995) 281-288.

[12]   M.R. Shaw, S.G. Millard, T.C.K. Molyneaux, M.J. Taylor, J.H. Bungey, "Location of steel reinforcement in concrete using ground penetrating radar and neural networks," *NDT&E International*, **38** (2005), 203–212.

[13]   S.A. Keo, F. Brachelet, F. Breaban, D. Defer, "Steel detection in reinforced concrete wall by microwave infrared thermography," *NDT&E International*, **62** (2014), 172–177.

[14]   Yunze He, Guiyun Tian, Mengchun Pan, Dixiang Chen, "Eddy current pulsed phase thermography and feature extraction," *Appl. Phys. Lett.*, **103** (2013), 084104.

[15]   A. Michel, B.J. Pease, M.R. Geiker, H. Stang, J.F. Olesen, "Monitoring reinforcement corrosion and corrosion-induced cracking using non-destructive x-ray attenuation measurements", *Cement and Concrete Research*, **41** (2011), 1085-1094.

Impact Damages Detection on CFRP Using Eddy Current Pulsed Thermography

Abdoulaye Ba[a], Qiuji Yi[b], Junzhen Zhu[b], Huu-Kien Bui[a], Gui Yun Tian[b],
Gérard Berthiau[a,1], Guillaume Wasselynck[a]

[a] *Institute of Research in Electrical Energy of Nantes-Atlantiques (IREENA),*
University of Nantes, 44602, Saint-Nazaire Cedex, France
gerard.berthiau@univ-nantes.fr

[b] *School of Engineering, Newcastle University, Newcastle Upon Tyne,*
NE1 7RU, United Kingdom
g.y.tian@newcastle.ac.uk

Abstract. Carbon Fiber Reinforced Polymer (CFRP) materials are widely used in aerospace due to their low weigh to strength ratio. Non-destructive Testing (NDT) Techniques becomes a necessity with increasing use of CFRP materials. Induction Thermography is a new NDT technique that can be exploited as a promising fast and global control. However, the detection of typical flaws in carbon composites such as delamination, fibers rupture and impact damages need to be further investigated in order to optimize the technique. Optimization can be done in the test configuration level and by the use an appropriate image technique. In this paper Eddy Current Pulse Compression Thermography (ECPuCT) is used to detect impact damages on CFRP materials. The Principal Component Analysis (PCA) based image processing technique is used to detect and visualize impact damage area from transient thermal images. Flaw detection results using experimental measures will be shown and discussed.

Keywords: Eddy Current Pulsed Thermography (ECPT), Eddy Current Pulse Compression Thermography (ECPuCT), Principal Component Analysis (PCA), Carbon Fiber Reinforced Polymer (CFRP), Non-destructive Testing (NDT).

1. Introduction

Eddy Current Pulsed Thermography (ECPT) [1] and Eddy Current Pulse-Compression Thermography (ECPuCT)[2] are one of the NDT techniques which can be applied for the non-destructive testing of various kind of conductor work piece such as Carbon Fiber Reinforced Polymers (CFRP). Induction Thermography system combines two techniques : Eddy Current and Thermography. The heat is not limited to the sample surface ; it can reach a certain depth according to the penetration depth of the electromagnetic wave into a conductive material. Eddy-Current Thermography focuses the heat on the defect area due to Eddy Current distorsion. This phenomenon increases

---

the thermal contrast between the defective region and defect-free areas.

In this paper, experimental induction thermography testing will be carried out. The Principal Component Analysis is applied for ECPuCT thermal responses for quantitative analysis of a composite plate with impact damages of 9 J, 15 J, 16 J, 16.55 J, 18 J and 21 J. The composite Plate with impact damages was given to us by AIRBUS, as part of the PhD of Huu-Kien Bui [1]. The defects are evaluated by analyzing the heat distribution and patterns in thermal images. This paper will investigate whether impact damages can be detected using ECPuCT and Principal Component Analysis (PCA). Only the impact damage of 18 J will be investigated in this paper.

2. Principal Component Analysis (PCA)

The principal component analysis method is used to reduce data dimensions and extract main features. PCA is a multivariate statistical analysis method which transforms the ECPuCT thermal data into uncorrelated eigenvectors or principal components (PCs) corresponding to the maximum variability within the data. In PCA method, each principal component is a linear combination of the original variables. In general, the first principal components carry most of the information regarding the original data [3]. The detailed steps of Principal Component Analysis are summarized as follows :

- Organization of the dataset;

- Calculation of the mean along each dimension;

- Calculation of the deviation;

- Determination of the covariance matrix;

- Calculation of the eigenvectors and eigenvalues of the covariance matrix;

- Sorting the eigenvectors and eigenvalues;

- Computation of the cumulative energy content for each eigenvector;

- Selection of the first PCs.

3. Application on composite sample

Experimental ECPuCT system in figure 2 is used to investigate impact damage in a CFRP sample. The sample is a 37 plies composite plate with six impact damage defects. The composite plate has dimensions of $300mm \times 300mm \times 37h_{ply}$ where h_{ply} is the thickness of a ply which is equal to $140\mu m$. The defects are numbered from A1 to A6 as shown in fig. 1. The table 1 gives the dimensions of the composite plate.

Table 1. Characteristic of the composite sample

Number of ply	37
Lay-up sequence	$X/0/X_S$
X = [0°/0°/135°/0°/45°/0°/45°/90°/135°/0°/135°/90°/45°/0°/45°/0°/135°/0°]	

X_S denotes the symmetric lay-up sequence of X with respect to 0° ply.

The fig.1 shows the configuration of the composite sample with six impact damages from A1 to A6. In this paper, only the impact damage A3 will be investigated.
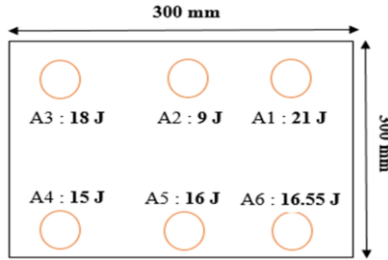

Figure 1. Composite sample with impact damages location.

The fig. 2 shows the schematic diagram of the used Eddy Current Pulsed Thermography for the experimental studies. The schematic diagram contains four units : a signal generator, an excitation module, an infrared camera and a computer.
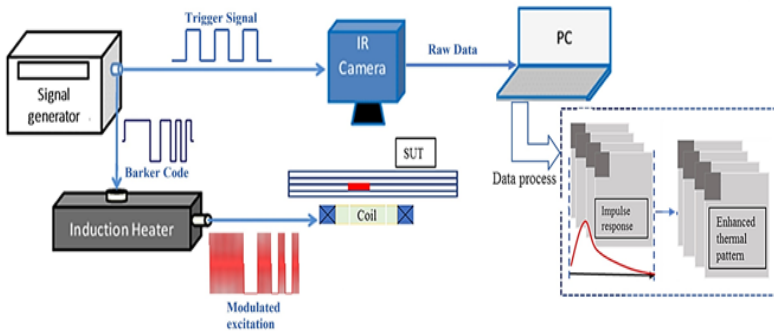
Figure 2. Eddy Current Pulsed Compression Thermography configuration[2].

A high frequency and high power signal generator provides high power currents for induction heating. Signal generator is used to send both the Barker code signal [2] to the induction heating coil and a reference clock trigger signal to the infrared camera to acquire thermograms at 50 frames per second. The induction heater is a Cheltenham EasyHeat 224 with a maximum excitation power of 2.40 kW, a current value of 400 A and an excitation frequency range of 150-400 kHz. An IR camera FLIR SC655 was used to record the thermal responses of the specimen. The camera has a resolution of 640×480 pixels at a frame rate of 50 Hz and a sensitivity of 7.5-14.0μm.

4. Results

In this section, we present the experimental results obtained in our work. After calculating the impulse response of the thermal images, PCA method is used to locate the impact area. Firstly, we plot the thermal response along the line A as shown in fig. 3. The line A crosses the area of the impact damage A3. We can expect that the thermal response on the area A3 be higher than surrounding area.

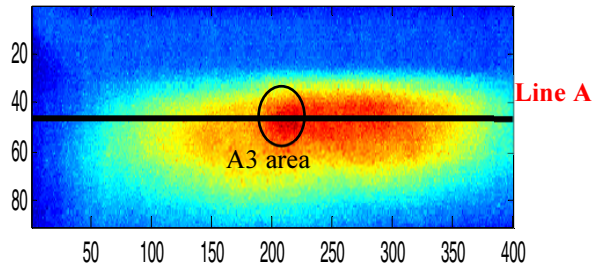**Figure 3.** Thermal distribution along A3 at 1 s

Fig. 4.a shows the thermal response of two pixels. The curve of the pixel in blue is in the area of the impact A3 and for the red curve, the pixel is near to the impact area. We observe in the fig. 4.a three stages. The stage 1 and 2 are the heating stage but in the stage 2 we observe the effects of the Barker code which is a bit length of 13 with a series of 1 or -1. The temperature increases during this two stages. The last stage is the cooling stage. In this stage the temperature decreases gradually. The heating and cooling times are respectively 13 seconds and 30 seconds.

The fig. 4.b shows the thermal responses along the impact damage A3 at recorded time of 1 s, 2 s, 3 s and 4 s respectively. From the thermal responses of fig. 4.b, we can distinguish the area of the impact damage A3. Indeed, the thermal response in the area of the impact damage increases due to fiber breakage in the area of the impact damage. This can be observed by thermal lobes in fig. 4.b.
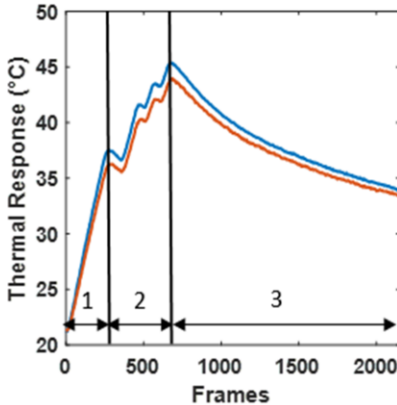
Figure 4.a. Thermal of two pixels   **Figure 4.b.** Thermal response along A3
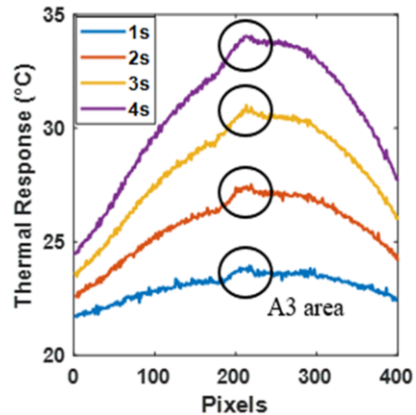
From fig. 5, we can see that by using PCA method, the impact damage A3 is clearly revealed in the image reconstructed by the second principal component. The impact point is like a hot spot because the electrical conductivity is decreased at the impact point, which leads to Eddy Current diversion in the area of A3, increasing the Eddy Current density. The temperature at the impact point is higher than surrounding area. The effect of non-uniform heating is almost eliminated and only the area of the impact damage A3 remains in the second principal component image. The profile of the impact A3 can be precisely obtained using the PCA method. Above the 3rd principal component, the information useful for detecting the impact damage A3 is limited. To sum up, PCA is

effective to enhance the features of impact damage in the IR image sequences by eliminating the effects of non-uniform heating.
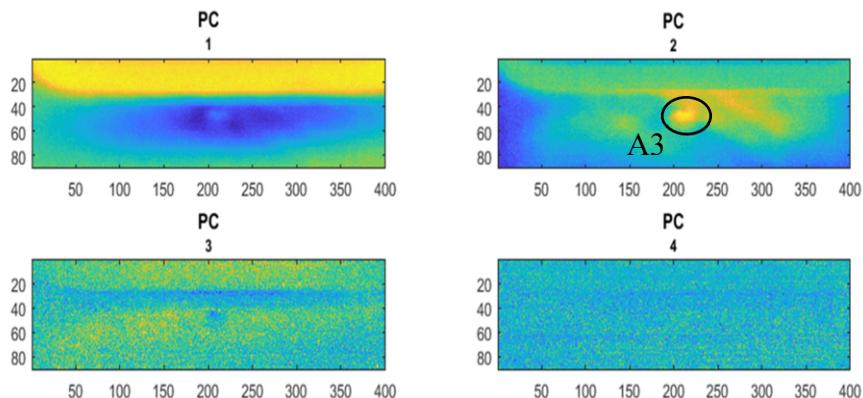
Figure 5. Results of ECPuCT testing. Images reconstructed by the PC 1, 2, 3 and 4

5. Conclusion

The experimental measurements have been conducted to investigate the performances of Eddy Current Pulse Compression Thermography (ECPuCT) applied to the detection of impact damage defects on a CFRP material. The principal component analysis has been applied to the ECPuCT data to identify impact area on the composite plate. The results show that the PCA can be used to eliminate the effect of non-uniform heating and reveal clearly the defect in the image reconstructed by the second principal component

Acknowledgements

References

[1]   H. K. Bui, G. Wasselynck, D. Trichet, and G. Berthiau, "Study on flaw detectability of NDT induction thermography technique for laminated CFRP composites," *Eur. Phys. J. Appl. Phys.*, vol. 73, no. 1, p. 10902, 2016.

[2]   Q. Yi, G. Y. Tian, H. Malekmohammadi, J. Zhu, S. Laureti, and M. Ricci, "New features for delamination depth evaluation in carbon fiber reinforced plastic materials using eddy current pulse-compression thermography," *NDT&E Int.*, vol. 102, pp. 264–273, 2019.

[3]   L. Cheng and G. Y. Tian, "Transient thermal behavior of eddy-current pulsed thermography for nondestructive evaluation of composites," *IEEE Trans. Instrum. Meas.*, vol. 62, no. 5, pp. 1215–1222, 2013.

Research on Stress Detection of DC01 Steel via Barkhausen Noise

Xiang Zhang [a], Jianping Peng[a,1], Xiaorong Gao [a], Jie Bai [a] and Jianqiang Guo [a]

[a] *Photoelectric Engineering Institute, Southwest Jiaotong University, Chengdu, China*

Abstract. The industrial component under loading change its mechanical characteristics by stress. It is very important to make clear the distribution of the applied stress in the component to reduce the failure. In this paper, magnetic Barkhausen noise (MBN) method is used to evaluate the stress of DC01 steel. Combined with theory for both magnetic domain and magnetization, this work analyzed MBN signal from energy point of view. Magnetic strength corresponding to the maximum MBN shows a downward trend with the increase of tensile stress. Plots of energy against stress showed a relationship providing a convenient method for detecting stress levels by MBN.

Keywords. Magnetic Barkhausen noise, magnetic domain, magnetization

1. Introduction

Traditional stress testing methods will cause different damages to the testing materials. Since some components are not allowed to be destroyed, some scholars have proposed a magnetic nondestructive testing method - Barkhausen noise (MBN) to describe the tendency of stress change in materials [1-3]. The Barkhausen effect was found in 1919, while it mainly describes the physical phenomena of a series of electric pulses produced by ferromagnetic materials in an alternating magnetic field [4]. From the microscopic point of view, ferromagnetic materials are composed of domain walls and domains. In the second stage of magnetization, a large number of irreversible emotions are generated in the domain, and MBN signals are generated in the motion between domain walls (Figure 1) [5].
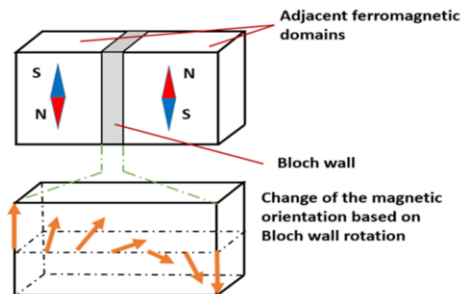

Figure 1. Schematic of domain wall change

---

[1]Corresponding Author, Jianping Peng, Photoelectric Engineering Institute, Southwest Jiaotong University, Chengdu 611756, China; E-mail: peng.jian.ping@126.com.

The method has also been used in many studies for studying the sample's structure. Jiles DC proposed that the strength of the MBN signal is related to the size and distribution of the pinning point of bound domain wall motion in materials [6]. DHAR A pointed out that the external magnetic field will change the distribution of magnetic crystal energy in the domain, breaking the original magneto-static equilibrium state [7]. An external magnetic field may simultaneously affect the internal grains with similar crystal orientation and produce domain wall motion. In the same way, the applied stress breaks the internal crystal structure of the material. The stress effect of single domain crystals was analyzed by Baudouin [8] and Ziman J [9]. Jia L et al. established a correlation model between DW motion and MBN under tensile stress [10]. Also, some scholars extract the peak value, RMS and other characteristics of MBN signal to describe the distributing disciplinarian between MBN and stress [11-13]. J.A. Pérez-Benitéz et al. pointed out that the magnetic strength of peak MBN often appeared near the coercive field [14]. Lo et al. confirmed that the frequency band of MBN signal is almost in the range of 1kHz - 500 kHz [15]. Leonardo et al. [16] clarify the relationship between the microstructure of steels and magnetic measurements, gives the result with MBN and the hysteresis curve.

In this study, an experimental design with different levels of tensile stress was carried out. Barkhausen noise measurements were carried out from the sample's surface, used for stress profiling. The measured stress profiles were characterized by energy while typical BN features such as peak and rms value were used to represent the BN measurements.

2. Methodology

The total energy expression in a unit volume of ferromagnetic material is:

$$E = E_{ex} + E_k + E_{\sigma} + E_d + E_H \tag{1}$$

In Eq. (1), E_{ex} represents material exchange energy, E_k represents material magneto-crystalline anisotropy energy, E_{σ} is the magneto-elastic energy, E_d represents material demagnetizing energy, and E_h represents applied magnetic field energy.

In the absence of a magnetic field, the magneto-static energy of a ferromagnetic body is zero. When atomic spin is not considered, E_{ex}, E_d, and E_h in Eq. (1) do not work, the total energy can be defined as $E_k + E_{\sigma}$.

The magneto-crystalline anisotropy energy E_k in a cubic crystal can be expressed by the following formula:

$$E_k = K_1 \left(\alpha_1^2 \alpha_2^2 + \alpha_2^2 \alpha_3^2 + \alpha_3^2 \alpha_1^2 \right) + K_2 \alpha_1^2 \alpha_2^2 \alpha_3^2 \tag{2}$$

In Eq. (2), K_1 and K_2 are magneto-crystalline anisotropy coupling coefficients α_1, α_2, and α_3 are the cosines of the magnetization vector in three directions of space.

The applied stress can create regional wall motion without applying a magnetic field. With this condition, the magnetic domain structure in the ferromagnetic crystal will undergo a corresponding deformation (Figure. 2). At this time, in addition to the generalized magneto-crystalline anisotropy energy caused by spontaneous deformation, the external energy of the crystal dominant magnetic stress energy.

Let the external stress tensor expression be:

$$\sigma_{ik} = \sigma \gamma_i \gamma_k \tag{3}$$

In Eq. (3), γ_i , γ_k is the direction cosine of external stress intensity of σ .

(a) Primitive morphology of crystals   (b) Domain after Loading Stress
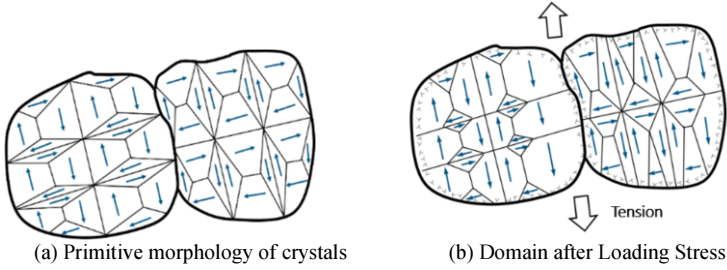
Figure 2. Comparison of Domain Structures before and after Stress Loading

An applied magnetic field may simultaneously affect internal grains with similar crystal orientation and generate domain wall motion. In the elastically deformed region, constant stress can be expressed as an additional magnetic field H_σ , which is a function of magnetoelastic energy E_σ and magnetization M , thereby:

$$H_\sigma = \frac{1}{\mu_0} \frac{\partial E_\sigma}{\partial M} \tag{4}$$

In Eq. (4), where μ_0 is the vacuum permeability, assuming that there is no transverse strain, the magnetostriction is isotropic, the form of the magnetoelastic energy generated by the stress can be simplified as:

$$E_\sigma = -\frac{3}{2} \lambda \sigma \cos^2 \vartheta \tag{5}$$

In Eq. (5), λ is the amount of magnetostriction, and ϑ is the angle of applied stress and magnetization. When the magnetic field has the same direction with stress, Eq. (4) can be expressed as:

$$H_\sigma = \frac{3b\sigma M}{\mu_0} \tag{6}$$

Where in Eq. (6), M is the magnetization, b is the second-order magneto-strictive coefficient, μ_0 represent the vacuum permeability, σ is the strength of applied stress.

$s(t)$ is the original signal, $s_J^1, s_J^2, ..., s_J^i$ is the Jth layer decomposition component of the signal, and $E_J^1, E_J^2, ..., E_J^i$ is the energy of the Jth layer wavelet decomposition amount respectively. Then the energy of each wavelet decomposition can be expressed as:

$$E_J^i(t) = \sum_{\tau=t_0}^{t} \left(s_J^i(\tau) \right)^2 \tag{7}$$

The overall energy of the signal can be expressed as:

$$E_{\text{total}}(t) = \sum_J E_J^i(t) \tag{8}$$

3. Experimental Procedure

DC01 steel is widely used in manufacturing of high-performance and critical components. Both chemical composition and mechanical parameter are given in Table 1 and Table 2, respectively. Non-oriented magnetic steel sheets, DC01, with the 40-mm width × 310-mm length × 1.0-mm thickness were used for the specimens, as shown in Figure 3. During tensile tests, stresses of various amplitudes within the elastic limit were applied using a mechanical testing system (see Figure 4.). MBN measurements were taken for a monotonically increasing load with increments of 16.6 MPa.

The measurement was made by using a sinusoidal magnetic wave of 1 Hz with 12V applied field. The MBN signal was obtained by a pick-up coil after superimposed 10 times and then amplified by an amplifier with a gain of 20dB.
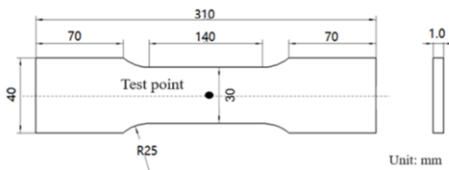

Figure 3. Dimension diagram of DC01 Steel.   **Figure 4.** Mechanical testing system.
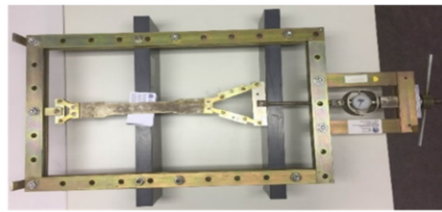
Table 1. Chemical composition % (mass fraction) of the DC01 steel

| Sample name	Standard	C	Mn	P	S
DC01	EN10130:2006	≤0.12	≤0.60	≤0.045	≤0.045

Table 2. Mechanical parameter of the DC01 steel

Sample name	Yield strength No more than	Tensile strength	Elongation after breaking No less than
DC01	280MPa	270-410MPa	28%

The sampling frequency was equal to 100 kHz, conventional signal processing technology based on the Fourier spectrum helps analyze the frequency characteristics. Set the signal divided into eight parts by three-layer wavelet packet decomposition. Through the energy distribution, the energy inside the domain at each stage can be evaluated.

4. Results

The Barkhausen noise measurements were carried out from the DC01 steel after applying a constant loading. The behavior of the Peak and Root Mean Square (RMS) value on samples can be seen in Figure 5. and Figure 6., respectively. It is shown that both Peak and RMS amplitude of MBN was found to correlate with applied stress, showing a clear rising trend for tensile stress under yield strength. It is noteworthy that RMS has a higher coefficient $r^2 = 0.9542$ compared with the Peak coefficient $r^2 = 0.9127$, which means a better correlation can be found with RMS condition.
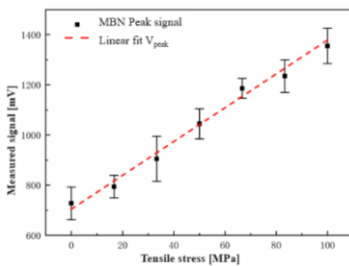
Figure 5. MBN peak amplitude as a function of applied stress.
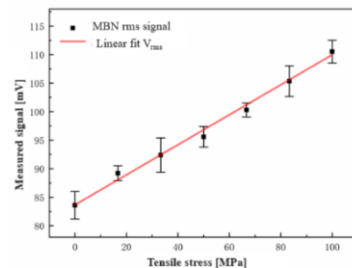
Figure 6. MBN rms amplitude as a function of applied stress.

To further evaluate the effectiveness of the magnetic techniques in determining tensile stresses, energy distribution with different stress levels is presented in Figure 7. It was shown that MBN signal mainly distributes in low-frequency region. Moreover, the energy of each wavelet decomposition shows sensitivity to applied tensile stress, especially at the low-frequency part. Consider using energy to express MBN distribution, Figure 8. presents the distribution between energy and magnetic strength against stress. Increasing stress also increases total energy, but magnetic strength of maximum MBN showing a downward trend. With tensile stress's influences, the shape of hysteresis loop becomes narrower. Therefore, magnetic strength of Peak value decrease.
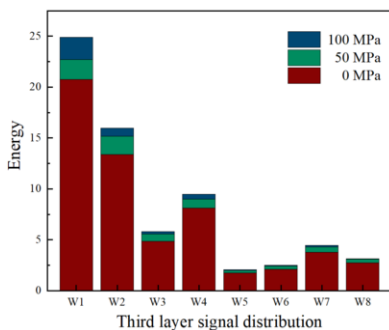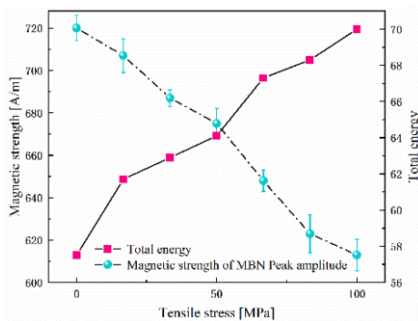
Figure 7. Energy Distribution.

Figure 8. Superposition of total energy and magnetic strength for DC01 steel.

5. Conclusion

This paper describes a method for detecting stress in the surface of magnetic materials based on the measurement of MBN. Both peak and rms amplitude of the MBN has been experimentally shown a vary linearly with stress. Therefore, this result provides a useful calibration curve for determining stress. Then energy was used to evaluate the effectiveness of the MBN. A relationship was found between energy and parabola peak position (magnetic strength), which is associated with the shape of hysteresis loop.

Acknowledgement

References

[1] Samimi A A, Krause T W, Clapham L. Stress Response of Magnetic Barkhausen Noise in Submarine Hull Steel: A Comparative Study[J]. Journal of Nondestructive Evaluation, 2016, 35(2):32.

[2] Kasai N, Koshino H, Sekine K, et al. Study on the Effect of Elastic Stress and Microstructure of Low Carbon Steels on Barkhausen Noise[J]. Journal of Nondestructive Evaluation, 2013, 32(3):277-285.

[3] Tsuchida Y, Enokizono M. Residual stress evaluation by Barkhausen signals with a magnetic field sensor for high efficiency electrical motors[J]. Aip Advances, 2018, 8(4):047608.

[4] Barkhausen H. Two phenomena revealed with the help of new amplifiers[J]. Phys, 1919,20:1-3.

[5] Mierczak L, Jiles D C, Fantoni G. A New Method for Evaluation of Mechanical Stress Using the Reciprocal Amplitude of Magnetic Barkhausen Noise[J]. IEEE Transactions on Magnetics, 2011, 47(2):459-465.

[6] Jiles DC. Dynamics of domain magnetization and the Barkhausen effect[J]. Czechoslovak Journal of Physics, 2000, 50(8):893-924.

[7] Dhar A, Clapham L, Atherton D L. Influence of uniaxial plastic deformation on magnetic Barkhausen noise in steel[J]. NDT&E International, 2001, 34(8):507-514.

[8] Baudouin J B, Monnet G, Perez M, et al. Effect of the applied stress and the friction stress on the dislocation dissociation in face centered cubic metals[J]. Materials Letters, 2013, 97(15):93-96.

[9] Ziman J, Kladivová M, Zagyi B. Influence of a "domain-drag effect" on the movement of a single boundary between circular domains in stress-annealed amorphous CoFeSiB wire[J]. Journal of Magnetism & Magnetic Materials, 2003, 254(254):176-178.

[10] Liu J, Tian G Y, Gao B, et al. Micro-macro characteristics between domain wall motion and magnetic Barkhausen noise under tensile stress[J]. Journal of Magnetism and Magnetic Materials, 2020, 493: 165719.

[11] Ktena A, Hristoforou E, Gerhardt G J L, et al. Barkhausen noise as a microstructure characterization tool[J]. Physica B: Condensed Matter, 2014, 435:109-112.

[12] Sorsa A, Kauko Leiviskä, Santaaho S, et al. Quantitative prediction of residual stress and hardness in case-hardened steel based on the Barkhausen noise measurement[J]. NDT&E International, 2012, 46(1):100-106.

[13] Kypris O. Detection of sub-surface stresses in ferromagnetic materials using a new barkhausen noise method[D]. Ames: Iowa State University, 2015.

[14] J.A.Pérez-Benitéz, Hernandéz-Espina, Ortiz-Martinéz, Unwrapping the influence of multiple parameters on the magnetic Barkhausen noise signal using self-organizing maps[J]. NDT & E International, 2013, 54:166-170.

[15] Lo, C.C.H, Jakubovics J P. Monitoring the microstructure of pearlitic steels by magnetoacoustic emission[J]. Journal of Applied Physics, 1997, 81(8):4069-4071.

[16] Leonardo F. T. Costa, Marcos F. de Campos et al. Hysteresis and Magnetic Barkhausen Noise for SAE 1020 and 1045 Steels With Different Microstructures [J]. IEEE Transactions on Magnetics, 2014.

Dependence of Coercivity and Barkhausen Noise Signal on Martensitic Stainless Steel with and without Quench

Hiroaki KIKUCHI[a,1], Kohei SUGAI[a], Takeshi MURAKAMI[a]
and Keiichi MATSUMURA[b]

[a]*Faculty of Science and Engineering, Iwate University, 4-3-5 Ueda, Morioka, Iwate,*
020-8551, Japan
[b]*INFITECHM Co., Ltd., Yokohama, Japan*

Abstract. We evaluated hysteresis curves and Barkhausen noise properties of the martensitic stainless steel with and without quench, and then investigated the relations between magnetic parameters and hardness based on microstructure changes. The quench introduced to reduce grain size, which relates to an increment of coercivity and Vickers hardness, a decrease in Barkhausen signal. The magnetic property changes reflect the changes in microstructures and mechanical property appeared on the quenched specimen. The obtained results contribute to aim `to develop` a magnetic nondestructive evaluation of residual stress appeared on the ferromagnetic steel combined with and without quench.

Keywords. Hysteresis curve, Barkhausen noise, coercivity, quench, residual stress

1. Introduction

The demands of nondestructive sensing technologies for monitoring degradation and health of infrastructures in power generation plants strongly advance in recent year. The material characterization or nondestructive testing using magnetic measurements such as hysteresis loop [1-6] and Barkhausen noise (MBN) [7-12] have been proposed and it is expected to be a candidate contributes to technologies with rapid diagnosis and low-cost inspection. The steel of turbine components used for a thermal power generation plant is typically quenched to enforce its mechanical performance. On the other hand, quenching induces residual stress into the materials, and also the residual stress is formed during long term operating plants, which sometimes has potential to lead the turbine components to a failure. Therefore, quantitative assessment of the residual stress is important. At present, X-ray diffraction is often used for such request, however, the requirement of pretreatment, time-consuming for measurement, and difficulty of in-situ measurement are disadvantages of the technique. The magnetic measurement may be expected to be an alternative method of X-ray diffraction. Therefore, in this study, as a first step, we investigated the magnetic properties and microstructures of martensitic stainless steel used as turbine component steel for thermal power generation plants when the material includes both non-quenched and

---

[1]Corresponding Author, Hiroaki Kikuchi, Faculty of Science and Engineering, Iwate University, Iwate 020-8550, Japan; E-mail: hkiku@iwate-u.ac.jp.
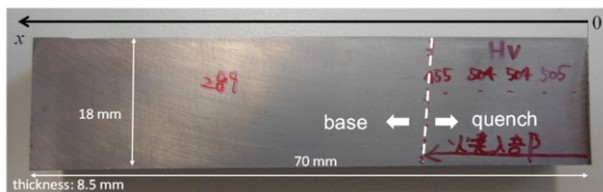
Figure 1 Dimensions and information about specimen used.

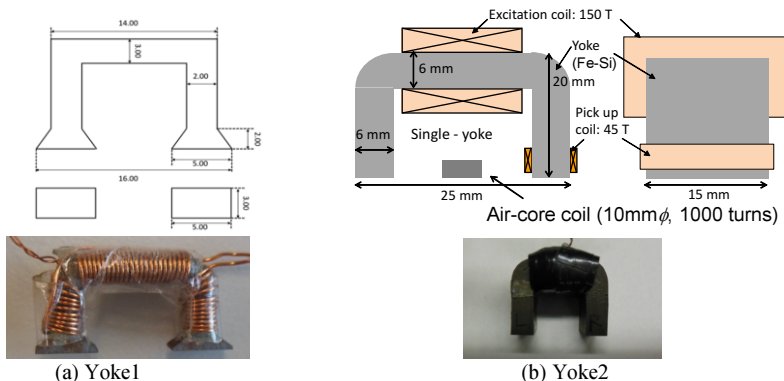(a) Yoke1   (b) Yoke2

Figure 2 Dimensions and configurations of magnetic yokes. (a) small yoke having 46turns for magnetization and 86turns for pick-up (Yoke1). (b) middle yoke having 150turns for magnetization and 45 turns for pick-up (Yoke2).

quenched area. Although our final goal is to evaluate residual stress quantitatively using magnetic measurement, the magnetic properties are very sensitive to not only stress but also microstructure changes. The main purpose of this study, we discuss magnetic characteristics attributed to microstructures changes due to quenching.

2. Experimental procedure

The martensitic stainless steel SUS420J (chemical composition: C 0.17-0.22, Si 0.10-0.50, Mn 0.30-0.80, P < 0.030, S < 0.020, Cr 13.0-14.0, Ni 0.30-0.80, wt.%) was used for the experiments. The specimen size is 70 mm × 18 mm × 8.5 mm. The specimen was quenched over the area from one of edge to 20 mm in length direction (See. Figure 1). The Vickers hardness was about 450 – 500 in quenched area and was 290 in non-quenched (base) area. We prepared two kinds of yoke in this study: small one (Yoke1) made of pure iron and middle (Yoke2) made of Fe-Si steel. Figure 2 shows the details about dimensions and configurations of both yokes. Since Yoke1 is smaller   than Yoke2, its spatial resolution is superior to that of Yoke2. On the other hand, Yoke2 can supply much magnetic flux to the specimen. To investigate these effects, two yokes are used here. The hysteresis curves and MBN properties were measured using magnetic yokes and a pick-up or an air-core coil, respectively. The hysteresis curves were measured using both yokes and MBN signal was measured by Yoke2 only. A triangular current *I* of 0.1 or 1 Hz with an amplitude of 1A is applied to an excitation coil winding around a yoke for magnetizing a specimen, and an induced voltage at the pick-up coil wounded the yoke leg or the air-core coil located at the surface of the specimen was measured. The output at the pick-up coil is used for calculation of flux

(a) quenched and transition area (b) base and transition area
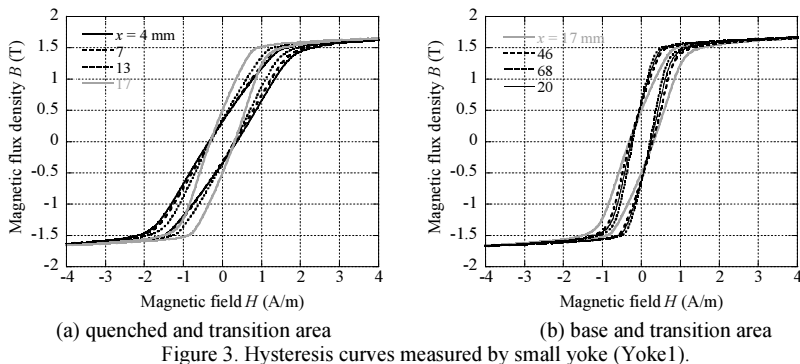
Figure 3. Hysteresis curves measured by small yoke (Yoke1).

(a) Coercivity (b) Remanence
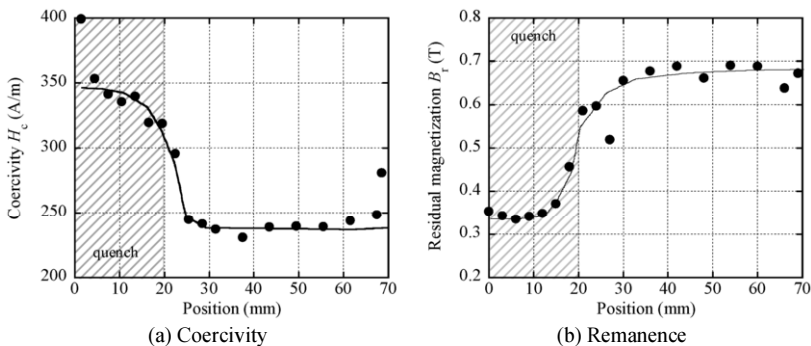
Figure 4. Dependence of coercivity and remanence on measurement point.

density B and the output at the air-core coil was amplified by 1000 times, filtered (100 – 200 kHz) and then captured by a PC as MBN signal. The root mean square value of a half cycle of the output at air-core coil was evaluated as the RMS voltage as following.

$$RMS = \sqrt{\frac{1}{T}\int_0^T V_o^2 dt} \qquad (1)$$

where V_o is the detected signal after amplified and filtered, and T is a half period of magnetizing field. Based on the results of MBN signal, MBN profile in which the moving averaged rms voltage, V_{rms} [13] are plotted against the applied current was obtained at each measurement point. As shown in Figure 1, the quenched edge is defined as $x = 0$ and length direction of the specimen is x -direction. Then the yoke moves along the x -direction and hysteresis curves and MBN signal were measured. The sensor positions are defined as the edge of the yoke leg for hysteresis measurement, and as the center of the air-core coil for MBN measurements.

3. Experiment results

3.1 Changes in magnetic parameters on hysteresis curves

Figure 3 shows the hysteresis curves measured by the small yoke (Yoke 1). The applied magnetic field was parallel to the width direction of the specimen. The curves in the

(a) Hysteresis curves   (b) Coercivity vs. position

Figure 5. Hysteresis curves measured by middle yoke (Yoke2) (a) and dependence coercivity on measurement point.

quenched area (x = 4–17 mm) has a small slope and the slope gradually increases with shifting measuring point to the base area. The coercivity and the residual magnetization were obtained from the hysteresis curves sh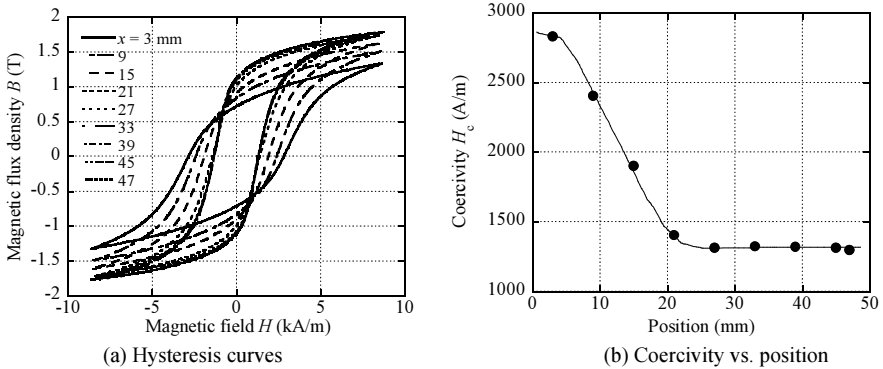own in Figure 3, and they are plotted against a measuring position. The coercivity shows large value in the quenched area, and has a small value in the base area. In the transition area between quench and non-quench, the coercivity rapidly decreases when measurement point moves from the quenched area to the base. On the other hand, the remanence increases with moving measurement point from quenched area to the base area. We also confirmed that the magnetic parameters correlate with Vickers hardness; the coercivity and the hardness are hard magnetically and mechanically, in quenched area respectively, and they become softer with shifting to the base area.

Figure 5 (a) shows the hysteresis curves measured by the middle yoke (Yoke2). Though the changes in the profile are qualitatively same as the case of Yoke1, we can see clearer changes on the hysteresis curves. The curve becomes swollen with a shifting measurement point from the base to the quenched area. Figure 5 (b) plots the coercivity obtained from the curves in Figure 5 (a) against the measurement point. Though the tendency of change is same as the results of Yoke1, the changing ratio becomes milder; the coercivity drops suddenly at the boundary between quenched and base area in case of Yoke1. This depends on the size of the yoke. Since Yoke1 is smaller, thus its spatial resolution is higher than that of Yoke2. However, its volume is smaller, which is attributed to less capability supplying magnetic flux to specimen. Indeed, we can understand in Figure 3 that the magnetic yoke is magnetically saturated.

3.2 MBN profiles

Figure 6 (a) shows the MBN profiles and Figure 6 (b) shows the position dependence of RMS voltage. The profile shows the results with half cycle, from negative to positive field. Opposite profile, from positive to negative, and the profile in Figure 6 (a) are symmetric with respect to the voltage-axis. The peak height is nearly 100 mV at I = 0.2 A in the quenched area while the peak height is above 500 mV at I = 0.05 A on the base area. The profiles show a little bit complicated behavior in the transition area. For example, at x = 6 mm, the profile shows another peak around I = –0.1 A, and peak position at 0.2 A in the quenched area shifts to the lower applied current, and its height becomes higher with moving measurement point to the base area. The latter peak may

(a) MBN profile　　　　　　　(b) RMS voltage vs. position
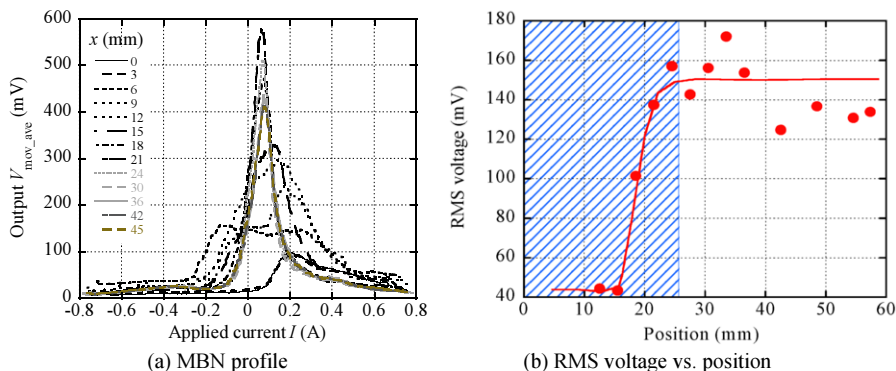
Figure 6. MBN profiles measured at different point (a) and position dependence of RMS voltage (b).
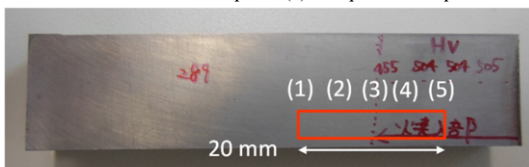
Figure 7. Observation area for EBSD.

(a) (1)　　　　　　　(b) (3)　　　　　　　(c) (5)
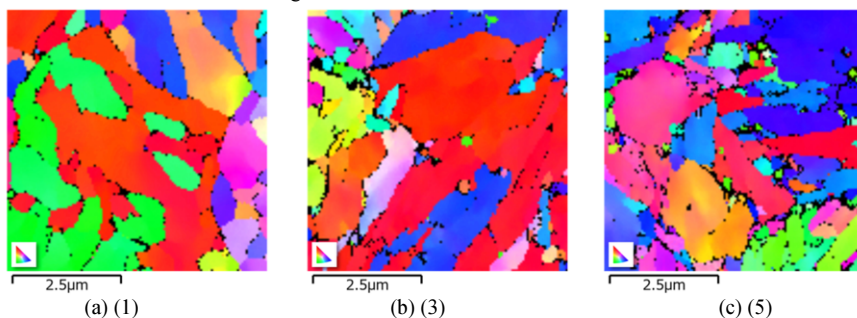
Figure 8. Orientation map obtained by EBSD observation.

be related to the microstructures change due to quenching, while the former may have relation with another factor; one possibility is due to residual stress. RMS voltage in quenched area shows low values and it increases at the base area.

4. Discussion

The obtained results in the previous section indicated that the pinning site for domain wall in the quenched area increases. To investigate the changes in microstructures, microstructure observations using an electron backscatter diffraction (EBSD) have done. The specimen for EBSD was cut from the specimen used for the magnetic measurement. As shown in Figure 7 (a), part (1) and (2) is the base area, (4) and (5) is the quenched area, and (3) is a transition area. Figure 8 shows the orientation map obtained from the EBSD observations. We can see that the grain size in the quenched area becomes fine compared with the base area, which means quench has an effect to reduce grains size, that is, increases grain boundaries.

The magnetic properties and MBN signal originate from the interaction between domain wall and pinning site for domain wall. The grain boundary acts as the

pinning site for domain wall. Since quenching makes grain small, grain boundary increases, which is consistent with that pinning for domain wall increases. Thus, the coercivity increases and MBN signal decrease in quenched area. The grain boundary also acts as a pinning site for dislocations, which contributes to increases hardness.

5. Conclusions.

We evaluated magnetic parameters of martensitic stainless steel with and without quench. The grains become fine due to quench, which introduces the increase in coercivity and the decrease in RMS voltage of MBN. Vickers hardness becomes larger with quench and it has correlations with magnetic parameters. Magnetic properties in a transition area between bases and quench may reflect microstructures change and stress distribution. Though the specimen used here includes residual stress partially, microstructure changes about grain size strongly affect the magnetic properties of hysteresis and RMS voltage. On the other hand, residual stress may be evaluated using analysis based on MBN profiles.

References

[1]   H. Kronmüller, Magnetic Techniques for the Study of Dislocations in Ferromagnetic Materials, *International Journal of Nondestructive Testing* **3** (1972), 315-350.

[2]   D. C. Jiles, *Introduction to Magnetism and Magnetic Materials*, London UK, Chapman & Hail (1991).

[3]   J. Šternberk, E. Kratochvílová, A. Gemperle, V. Faja, and V. Walder, Dependence of characteristics of hysteresis loops on dislocation densities for low-alloy Cr-Mo steel, *Czechoslovak Journal of Physics B* **35** (1985), 1259–1266.

[4]   A. Martínez-de-Guerenu, K. Gurruchaga, and F. Arizti, Nondestructive characterization of recovery and recrystallization in cold rolled low carbon steel by magnetic hysteresis loops, *Journal of Magnetism and Magnetic Materials* **316** (2007), e842–e845.

[5]   S. Takahashi, J. Echigoya, and Z. Motoki, Magnetization curves of plastically deformed Fe metals and alloys, *Journal of Applied Physics* **87** (2003), 805–813.

[6]   H. Kikuchi, Relationship between magnetic properties and hardness and its effect on recovery and recrystallization in cold rolled steel, *IEEE Transactions on Magnetics* **51** (2015), article # 2004804.

[7]   J. Degauque, B. Astie, J. L. Porteseil, and R. Vergne, Influence of the grain size on the magnetic and magnetomechanical properties of highpurity iron, *Journal of Magnetism and Magnetic Materials* **26** (1982), 261–263.

[8]   C. Gatelier-Rothea, J. Chicois, R Fougeres, P. Fleischmann, Characterization of pure iron and (130 p.p.m.) carbon–iron binary alloy by Barkhausen noise measurements: study of the influence of stress and microstructure, *Acta materialia* **46** (1998), 4873-4882.

[9]   C. G. Stefanita, D. L. Atherton and L. Clapham, Plastic versus Elastic Deformation Effects on Magnetic Barkhausen Noise in Steel, *Acta materialia* **48** (2000), 3545-3551.

[10] J. Anglada-Rivera, L. R. Padovese, and J. Capó-Sánchez, Magnetic Barkhausen noise and hysteresis loop in commercial carbon steel: Influence of applied tensile stress and grain size, *Journal of Magnetism and Magnetic Material* **231** (2001), 299–306.

[11] A. Martínez-de-Guerenu, F. Arizti, M. Díaz-Fuentes, and I. Gutiérrez, Recovery during annealing in a cold rolled low carbon steel. Part I: Kinetics and microstructural characterization, *Acta materialia* **52** (2004), 3657–3664.

[12] X. Kleber, A. Vincent, On the role of residual internal stresses and dislocations on Barkhausen noise in plastically deformed steel，*NDT & E International* **37** (2004), 439–445.

[13] H. Kikuchi, K. Ara, Y. Kamada, and S. Kobayashi, Effect of Microstructure Changes on Barkhausen Noise Properties and Hysteresis Loop in Cold-rolled Low Carbon Steel, *IEEE Transactions on Magnetics* **45** (2009), 2744-2747.

An Investigation of Corrosion Progression Using Laser Profilometry

Hong ZHANG [a,1] and Ruikun WU [b]

[a] *Key Laboratory of Nondestructive Testing, Fuqing Branch of Fujian Normal University, Fuqing, P. R. China*

[b] *School of Electronic and Information Engineering, Fuqing Branch of Fujian Normal University, Fuqing, P. R. China*

Abstract. Atmospheric corrosion progression characterisation on metal substrates is a major problem in the field of corrosion science and Non-destructive Evaluation (NDE). A laser profilometry has been used to characterise the corrosion on the mild steel plate at a low cost and high resolution. Four mild steel samples have been measured which exposed to the marine environment from 1 month to 10 months. Two features have been developed to characterise thickness variation in the corrosion layer. These features have been used to characterise corrosion progression through experimental studies. The relationship between these features and corrosion progression has been derived which is useful for corrosion progression measurement, early-stage corrosion prediction, and monitoring areas.

Keywords. Atmospheric corrosion, corrosion progression, feature extraction, laser profilometry.

1. Introduction

Due to its relatively low cost, mechanical strength and ease of manufacture, mild steel is the preferred metal for use in many applications. Its main disadvantage is that it corrodes easily unless adequately protected, and then rapidly loses strength, which will lead to structural failure. Corrosion is the deterioration in material properties due to interaction with the environment [1] and materials which corrode including metals and alloys, non-metals, woods, ceramics, plastics, and composites [2]. Recent studies have estimated that the direct cost of corrosion is between 3% and 4% of the gross domestic product (GDP) in every country [3]. To improve the reliability of these steel components, various non-destructive testing and evaluation (NDT&E) methods have been adopted to detect corrosion without affecting their future performance [4-7], each of which has different capabilities.

The early stages of corrosion should be detected and evaluated, which is important in understanding the progression of corrosion, corrosion protection, lifetime extension, and condition-based maintenance. However, most studies of atmospheric corrosion using mass loss methods are used for long-term corrosion measurement and analysis.

---

[1] Corresponding Author, Hong ZHANG, Key Laboratory of Nondestructive Testing, Fuqing Branch of Fujian Normal University, Fuqing, P. R. China; E-mail: zhhgw@hotmail.com.

Otherwise, electrochemical techniques are usually applied in laboratory investigations to understand corrosion mechanisms [8].

NDT&E is a well-established manual testing and evaluation technique which focuses on the detection and characterisation of corrosion in steel. It has been extended to metal with corrosion. For example, acoustic emission has been used to locate pitting in steel plates [9], ultrasonic [10] and radiography [11] have been adopted to acquire and analyse images to detect corrosion, and fibre optics have been employed for the corrosion monitoring of steel in reinforced concrete [12]. Laser profilometry can provide real-time data concerning the health and operational conditions of steel components. Real corrosion is more complex, within the corrosion layer, the thickness, electrical conductivity, and magnetic permeability are changed [13], rather than being metal loss. In this paper, the thickness variation measured using laser profilometry is also used to characterise corrosion progression over exposure time.

The rest of the paper is organized as follows. Firstly, the corrosion sample design is introduced in Section II. Experimental set-up is described and feature extraction is introduced in Section III. Then, steel corrosion with different exposure times is characterised using laser profilometry in Section IV. Finally, conclusions are outlined in Section V.

2. Sample setup

A set of corrosion progression samples has been created to investigate the capabilities of the proposed system to differentiate between different exposure times. These samples are created by exposing S275 steel plates to marine atmospheric conditions for different lengths of time, as shown in Figure 1, giving more realistic results. Details of these samples used in experimental work are shown in Figure 3. This set of samples provides corrosion occurring after different exposure times, which are known as corrosion progression.

Figure 1. Sample preparation in an outdoor environment.

These samples were created by exposing a small 30 mm × 30 mm section of the plates to the atmosphere for 1, 3, 6, and 10 months. The differences between the stages of corrosion are evaluated to understand the progression of corrosion. Moreover, the proportions of the constituents of corrosion change over time and this has a slight effect on composition [14]. The volume of corroded metal will change because iron oxides and hydroxides have different densities. Therefore, to identify the differences among these corrosion progressions, a laser profilometry experimental system has been adopted to evaluate corrosion progression.

Laser profilometry measurements link physical property variations in steel samples to evaluate present corrosion in the material: corrosion causes a change in the

components of steel material to iron oxides leading to an increase or decrease in thickness of the sample for different exposure times.

3. Evaluation of corrosion progression

To evaluate the variance in the corrosion layer with different exposure time, these samples were then measured using laser profilometry. The thickness of these steel samples is about 3 mm, with sample (a) exposed for 1 month, sample (b) for 3 months, sample (c) for 6 months, and sample (d) for 10 months. Figure 3 shows photographs of typically corroded steel samples, showing that there is a slight increase in the thickness of the corroded area.

As shown in Figure 4, the line scans with laser profilometry for different corrosion stages results in variations in corrosion layer thickness. The lateral resolution of this machine is approximately 1 μm, which is depended on the size of the focused laser beam, and the resolution of the Z-axis is about 0.01 μm.
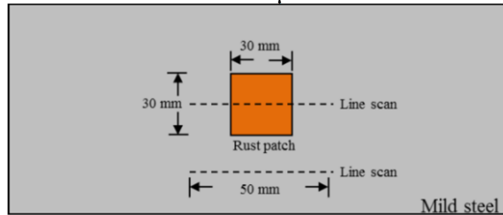
Figure 2. Line scanning position for corrosion measurement.
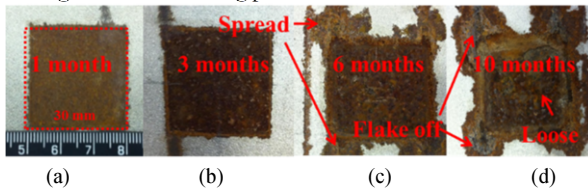
Figure 3. Photographs of corrosion with exposure times of 1, 3, 6 and 10 months.

4. Results

As shown in Figure 2, the line scans with laser profilometer for different corrosion stages results in variations in corrosion layer thickness. The surface measurements of corrosion samples were scanned with a laser profilometer. It is developed by the German UBM. The lateral resolution of this machine is approximately 1 μm, which is depended on the size of the focused laser beam, and the resolution of Z-axis is about 0.01 μm. A length of 50 mm line was scanned for each sample. This standard method is used for the purpose of characterising the microstructure of the four samples employed in this study. The software provided by UBM was used to calculate several parameters. The measurement results are shown in Figure 4.

It is possible to conduct non-contact and non-destructive measurements of corrosion areas with laser profilometry. The scanning length is 50 mm, which is larger than the corrosion area. Hence, the average height is employed to denote the variance of the corrosion layer thickness for each corrosion progression. The measured average heights of corrosion for 1, 3, 6 and 10 months are 43.86 μm, 71.72 μm, 79.09 μm, and 70.99 μm

respectively. From 1 month to 6 months, the height has a positive relationship with exposure time. However, the corrosion height after 10 months shows a decrease than compared to 6 months. This is due to the nature of corrosion [15]. After 6 months exposure corrosion is spreading rather than increasing in height. Besides, the rust layer of corrosion begins to loosen and flake off. It results in the height of the 10 months corrosion sample are lower than those of 3 and 6 months. Moreover, the corrosion layer begins to decrease in mass after 6 months.
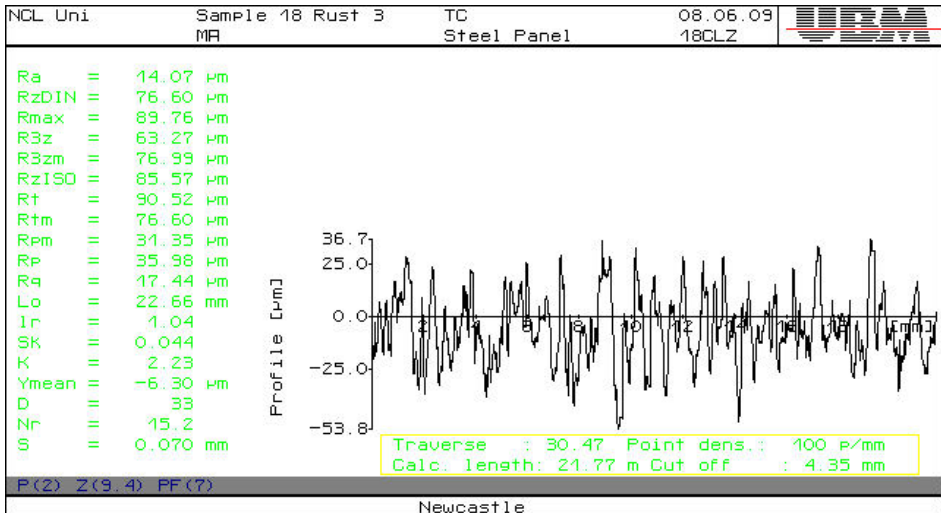
(a) 1 month
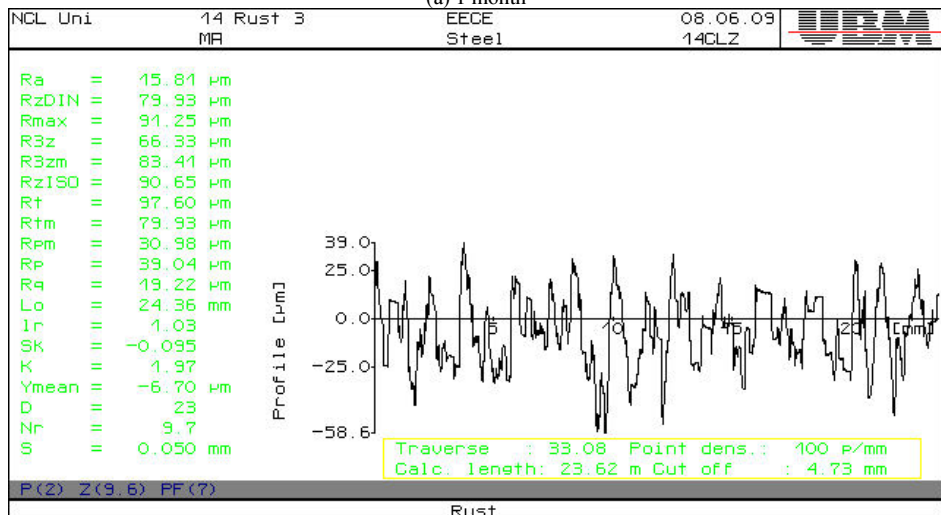
(b) 3 months

(c) 6 months

(d) 10 months
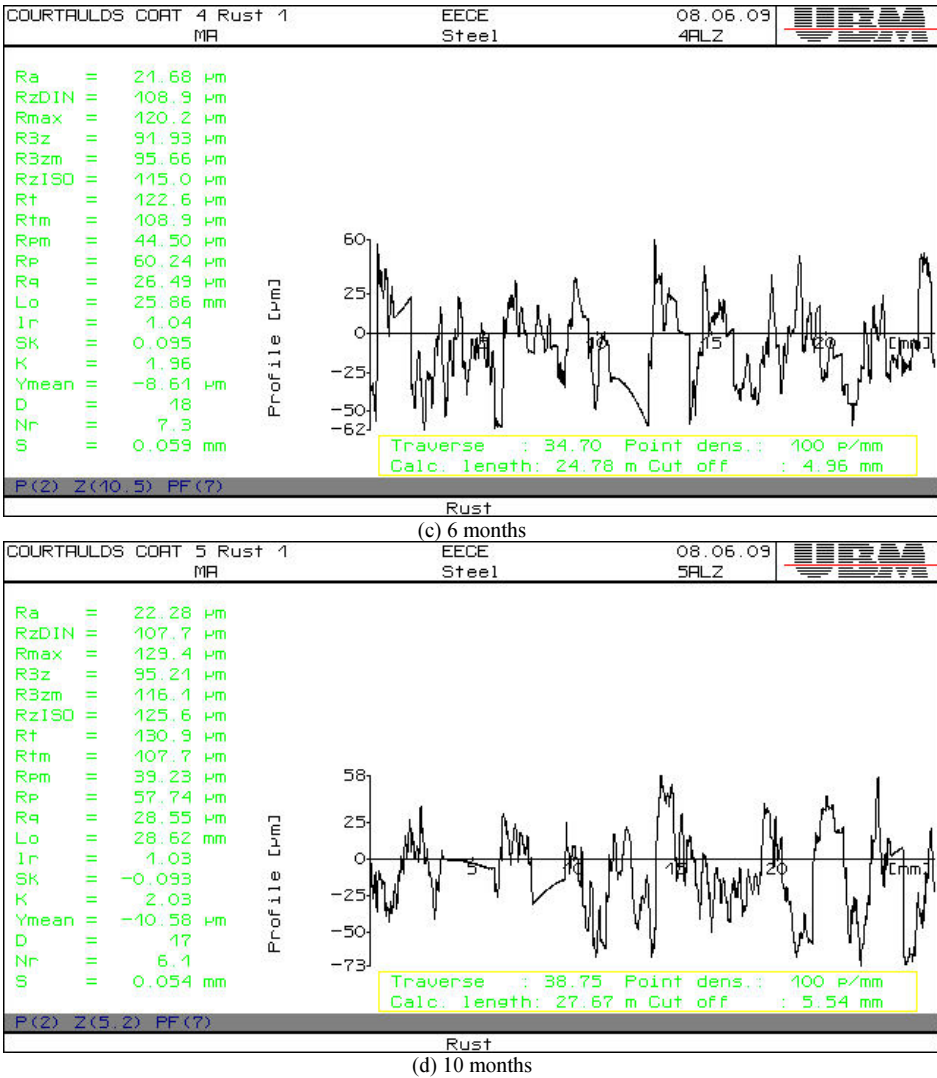
Figure 4. The surface profile of corrosion samples with different exposure times.

Because the thickness of the corrosion layer $d = d_1 + d_2$, d_1 is the corrosion height, d_2 is corrosion depth (as shown in Figure 5). The corrosion height cannot integrally represent variance in the corrosion layer's thickness over exposure time. Furthermore, after 6 months of exposure time, the corrosion layer is going to expand. Therefore, for better understanding, the roughness value is used.
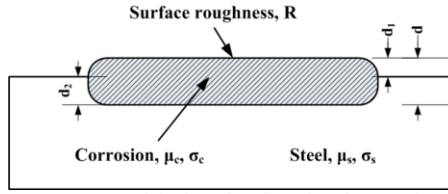
Figure 5. Model of steel and steel with corrosion.

A roughness value can be calculated either on a profile or on a surface. Many different profile parameters can be used. Roughness average R_a is more commonly used among these profile parameters and can be calculated using equation 1:

$$R_a = \frac{1}{n} \sum_{i=1}^{n} |y_i| \tag{1}$$

where yi is the vertical distance from the mean line. For better comparison, values of R_a are also calculated for an un-corroded steel plate. The results of the measurements of corrosion stages show that as exposure time extends from 1 month to 6 months, the thickness of the corrosion layer increases. From 6 to 10 months, the thickness of the corrosion layer increases more slowly, and then even decreases due to the loss of metal.

Table 1. R_a for corrosion progression over exposure time

0 month	1 month	3 months	6 months	10 months
14.21	17.44	19.22	26.49	28.55

Table 2. Measured values for various corrosion specimens.

| Exposure time / Parameters	No corrosion	1 month	3 months	6 months	10 months
Surface Roughness (μm)	14.210	17.440	19.220	26.490	28.550
Conductivity PV(ΔBnorm) (a.u.)	0	0.025	0.034	0.052	0.056
Permeability Max(ΔB) (a.u.)	0	-0.325	-0.422	-0.713	-0.850

These results from laser profilometry are shown in Table 1. Results from pulsed eddy current (PEC) [15] are shown in Table 2. The correlation coefficient of surface roughness average R_a and electrical conductivity from the PEC results is 94.70% ± 1.50%. Moreover, the magnetic permeability and surface roughness average R_a is 90.39% ± 1.60%. The results of the measurements of corrosion stages show that as exposure time extends from 1 month to 6 months, the thickness of the corrosion layer increases. From 6 to 10 months, the thickness of the corrosion layer increases more slowly, and then even decreases due to the loss of metal.

However, laser profilometry has some advantages, due to the fact that the laser can be used without contacting the corrosion layer. Therefore variation in corrosion depth with exposure time can be evaluated in detail with real-time. Meanwhile, these results suggest that electrical conductivity and magnetic permeability are monotonically increasing with increased thickness of the corrosion layer over exposure time.

5. Conclusions

In this paper, laser profilometry has been employed to study the atmospheric corrosion progression over exposure time to determine variations in the physical properties of the corrosion layer. The laser profilometry is sensitive to thickness variations. It has advantage in non-contact and high resolution. Therefore, corrosion progression on mild steel can be characterised in terms of thickness. Taken together these results provide important insight into the physical change of corrosion layer over different exposure time. These results indicate an association between the properties of corrosion and corrosion progression. However, this work has some limitations, due to the fact that the laser cannot penetrate into the corrosion layer. Therefore variation in corrosion depth with exposure time is not evaluated in detail. In the further study, variations in the corrosion layer are investigated using microwave.

Acknowledgement

References

[1] Z. Ahmad, *Principles of Corrosion Engineering and Corrosion Control*, 2006.

[2] R. W. Revie and H. H. Uhlig, *Corrosion and Corrosion Control: An Introduction to Corrosion Science and Engineering: Fourth Edition*, 2008.

[3] R. Baboian, *Corrosion tests and standards : application and interpretation*, 2nd ed. West Conshohocken, PA: ASTM International, 2005.

[4] V. G. M. Annamdas and C. K. Soh, "Application of electromechanical impedance technique for engineering structures: Review and future issues," *Journal of Intelligent Material Systems and Structures,* vol. 21, pp. 41-59, 2010.

[5] P. Priyada, M. Margret, R. Ramar, *et al.*, "Intercomparison of gamma scattering, gammatography, and radiography techniques for mild steel nonuniform corrosion detection," *Review of Scientific Instruments,* vol. 82, pp. 035115-035115-8, 2011.

[6] P. Huthwaite, R. Ribichini, P. Cawley, *et al.*, "Mode selection for corrosion detection in pipes and vessels via guided wave tomography," *Ultrasonics, Ferroelectrics and Frequency Control, IEEE Transactions on,* vol. 60, pp. 1165-1177, 2013.

[7] J. Ou and H. Li, "Structural health monitoring in mainland china: Review and future trends," *Structural Health Monitoring,* vol. 9, pp. 219-231, 2010.

[8] A. Nishikata, Y. Yamashita, H. Katayama, *et al.*, "An electrochemical impedance study on atmospheric corrosion of steels in a cyclic wet-dry condition," *Corrosion Science,* vol. 37, pp. 2059-2069, 1995.

[9] C. K. Lee, J. J. Scholey, S. E. Worthington*, et al.*, "Acoustic emission from pitting corrosion in stressed stainless steel plate," *Corrosion Engineering Science and Technology,* vol. 43, pp. 54-63, 2008.

[10] G. Rannou, D. Thierry, and N. Le Bozec, "Ultrasonic monitoring of steel corrosion during accelerated corrosion testing and outdoor field exposures," ed, 2010.

[11] K. Edalati, N. Rastkhah, A. Kermani*, et al.*, "The use of radiography for thickness measurement and corrosion monitoring in pipes," *International Journal of Pressure Vessels and Piping,* vol. 83, pp. 736-741, 2006.

[12] X. Li, S. Zhang, Z. Huang*, et al.*, "Fiber optics sensing technique for monitoring corrosion of steel in reinforced concrete," *Corrosion Science and Protection Technology,* vol. 11, pp. 172-173, 1999.

[13] Y. Gotoh, H. Hirano, M. Nakano*, et al.*, "Electromagnetic nondestructive testing of rust region in steel," *IEEE Transactions on Magnetics,* vol. 41, pp. 3616-3618, 2005.

[14] D. de la Fuente, I. Díaz, J. Simancas*, et al.*, "Long-term atmospheric corrosion of mild steel," *Corrosion Science,* vol. 53, pp. 604-617, 2011.

[15] Y. He, G. Tian, H. Zhang*, et al.*, "Steel Corrosion Characterization Using Pulsed Eddy Current Systems," *Sensors Journal, IEEE,* vol. 12, pp. 2113-2120, 2012.

Evaluation of Fatigue Damage in 304 Stainless Steel by Measuring Residual Magnetic Field

Yi LIU[a], Xiwang LAN [a] and Bo HU [a,1]

[a] *Key Laboratory of Nondestructive Testing, Ministry of Education, Nanchang Hangkong University, Nanchang, PR China*

Abstract. To demonstrate the feasibility of the passive magnetic NDT method for damage assessment of 304 austenitic stainless steel, the residual magnetic field change of the 304 stainless steel specimens under fatigue loads was investigated. The measurement was carried out using a fluxgate sensor and the magnetic characteristics were extracted for analysis of fatigue state. Then, the XRD test was carried out to investigate the mechanism of magnetic field changes and verify the reliability of the proposed method. The results show that the variation of the maximum gradient is consistent with the process of fatigue crack growth, which indicates that the fatigue damage can be estimated by residual magnetic field measuring. In future stage, how to distinguish the magnetic field changes derived from martensite transformation or stress magnetization effect will be investigated.

Keywords. 304 stainless steel, residual magnetic field, fatigue damage, martensite transformation

1. Introduction

Damage assessment is a significant part of Materials' State Awareness (MSA) and Non-destructive Evaluation (NDE) technologies [1]. At present, several different electromagnetic NDE methods for damage assessment such as Magnetic Barkhausen Noise (MBN), Pulsed Eddy Current (PEC), magnetic properties measurement, and Potential Drop (PD) detection have been proposed. MBA method is an active magnetic technique usually in need of high strength, low–frequency fields to drive the material into saturation [2]. PEC testing has a limited sensitivity in depth owing to skin effect [3]. Passive magnetic NDT methods such as Metal Magnetic Memory (MMM) or Residual Magnetic Field (RMF) measurement, have been widely verified in the damage assessment of ferromagnetic materials [2,4]. However, 304 austenitic stainless steel is a paramagnetic material with low permeability (about 2~3 orders of magnitude lower than ferromagnetic materials), and the induction magnetic field variations caused by stress or fatigue is small. Therefore, they put forward higher requirements for sensor sensitivity compared with ferromagnetic materials. PD method has been exploited for creep monitoring of nonferromagnetic materials such as SUS 304 austenitic stainless steel and aluminum alloy [5]. However, the sensitivity to creep is low in the absence of geometrical effect of deformation [6]. Considering the low permeability of 304 stainless

[1] Corresponding Author, Bo HU, Tel.: +86 13627914320; E-mail: cumthubo@163.com.

steel and high sensitivity of magnetic sensors, it is suggested to have the potential for early damage assessment of some non–ferrous materials by passive magnetic methods. Different types of magnetic sensors can be used for passive measurement, including Hall, AMR, GMR, MI, TMR, RTD fluxgate, SQUID, etc. The fluxgate sensor has a detectable field range of $10^{-6} \sim 10$ Gauss. It performs well in the measurement of weak magnetic field changes owing to its wide range and high accuracy [7].

In this paper, the passive NTD method based on fluxgate sensor was used to detect the induction magnetic field of 304 stainless steel specimens under different fatigue degrees. Before conducting fatigue and magnetic field measurement, the initial magnetism of 304 stainless steel was clarified by the magnetization test. Then, the XRD phase test was carried out on the specimens before and after fatigue. The results indicate that fatigue has caused the martensite transformation and changed the magnetic permeability as well as the residual magnetic field of 304 stainless steel. The maximum magnetic gradient presented an approximately linear relationship with the loading cycles, which were directly related to the fatigue crack growth. In the final section of this paper, the conclusions were drawn and the future research directions were also highlighted.

2. Materials and Methods

Residual magnetic field measurement is a passive NDT method based on the geomagnetic field. When the material in the geomagnetic environment is inhomogeneous owing to the increase of dislocation density, the change of local shape, or the mechanical stress, the induction magnetic lines will bend and pass through intensively in the high permeability areas while thinly in the low permeability parts. As a result, the induction magnetic anomaly is formed, and this disturbance is detectable by a magnetic sensor [2]. This section will present details on the test object and the measuring procedure itself.

2.1. Materials

The test material is austenitic 304 stainless steel, its chemical composition is shown in Table 1. The specimen was processed into a standard rectangular cross–section tensile sample with length, width, the thickness of 190, 40, and 3 mm, respectively according to the Chinese standard of GB / T228.1–2010. Detailed geometry parameters are shown in Figure 1, which values in millimeters (mm).

Table 1. Main chemical composition of 304 stainless steel (mass fraction / %).

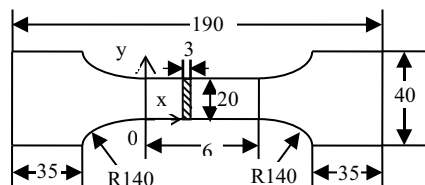| C	Si	Mn	Cr	Ni	S	P
≪ 0.07	≪ 0.75	≪ 2.00	17.5~19.5	8.0~10.5	≪0.03	≪0.045

Figure 1. Schematic diagram of sample geometry.

2.2. Experimental Setup and Procedure

The experiment was carried out in three processes. During the first stage, a magnetization test was performed to determine the initial magnetization state of 304 stainless steel. The base metal was processed into small pieces of 2 mm × 2 mm × 2 mm as test samples by wire–electrode cutting. After being polished, the samples were put into an ultrasonic oscillator and cleaned with distilled water and then being dried. A comprehensive physical property measurement system (SQUID) produced by the Quantum Design company of the United States was used. The test temperature was 300 K, and the maximum applied magnetic field was 2 T.

Then, an Instron8801 electronic universal testing machine was used to perform a tensile–tensile fatigue test of 304 stainless steel. The main parameters load, stress ratio, and the maximum loading frequency were set as 230 MPa, 0.1, and 10 Hz respectively. After every certain loading cycle, the residual magnetic field of the specimen was measured by a magnetic probe composed of a fluxgate sensor. The magnetic core material of the sensor was cobalt-based amorphous alloy, which has high permeability and low coercivity ensuring good anti–interference effect and low loss [7]. The measurement range was 10^{-10} T~10^{-4} T, the resolution was 0.1 nT, the measurement error was $\pm0.25\%$, the measurement frequency and the detection distance was set as 25 Hz and 60 mm respectively. The specimen was detected in a stable magnetic field environment with the probe vertical to the sample surface and without lift–off. The experimental setup is shown in Figure 2.
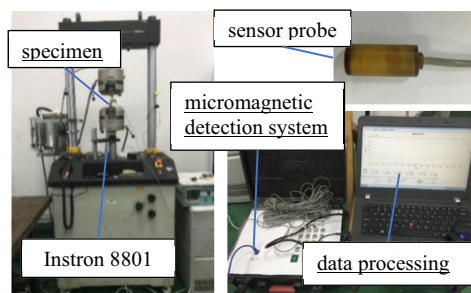
Figure 2. Photo of the experimental setup.

Finally, to verify the martensitic transformation of 304 stainless steel in the fatigue process, the X–ray diffraction test was conducted on the specimens before and after fatigue. The samples were processed into small blocks of 10 mm × 10 mm × 3 mm. As in the first stage, the block samples were mechanically polished and then cleaned before use. A D8 Advance X–ray diffractometer was used to conduct phase analysis in this test. The incident wavelength was 1.5406 Å, the measuring angle range was 20°~80°, the step length was 0.02°, and the measuring temperature was 300 K.

3. Results and Discussion

3.1. Initial Magnetism of 304 Stainless Steel

Figure 3(a) shows the magnetization curve of 304 stainless steel. As can be seen, the magnetization of the material is approximately linear with the increase in the external

magnetic field, and there is no magnetic saturation. Additionally, the magnetization curve has weak hysteresis near the zero magnetic field. The magnetic susceptibility is calculated, which is shown in Figure 3(b). When the external magnetic field is within ± 6000 A/m, the magnetic susceptibility of sample 1 is between 0.022–0.243, and that of sample 2 is between 0.046–0.303. As a result, the average relative magnetic permeability is between 1.034–1.273, which is 2–3 orders of magnitude lower than that of ferromagnetic materials. Therefore, the initial state of 304 stainless steel is paramagnetic.
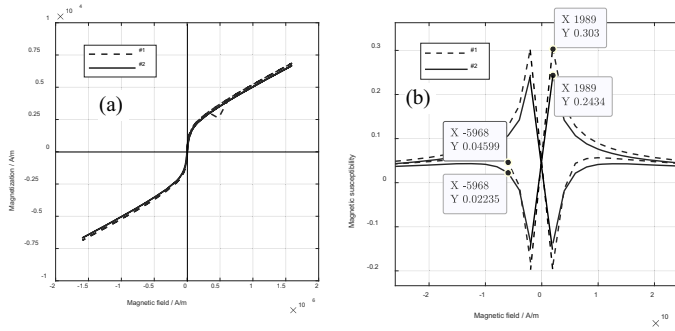

Figure 3. H–M curve (a) and susceptibility curve (b).

3.2. Variations of Magnetic Induction Intensity and Magnetic Gradient

Figure 4 shows the magnetic induction field of 304 stainless steel under different cyclic loads. It can be seen that the initial magnetic induction intensity on both sides is greater than that at the center. With the increase in cycles, the magnetic field curve rotates clockwise and when the cycles reach 42048, the specimen breaks and the curve fluctuates sharply. This indicates that the induction magnetic field is sensitive to component fracture, but it cannot characterize the early fatigue damage as the variations of 100–10,000 cycles are not significant. It is noted that there is no magnetic field data from 10,000 to 42,048 cycles, this is because the effect of residual stress on fatigue life was underestimated in the experiment. Generally, the fatigue cycle of 304 stainless steel in a low-stress area ($< (0.3{\sim}0.45)\sigma_b$) can reach 100,000 times [8]. But in this test, the specimen was taken off from the fatigue machine after a certain cycle to measure the magnetic field, and then reloaded. This resulted in the addition of residual stress to the applied load, and caused low cycle fatigue of the specimen.
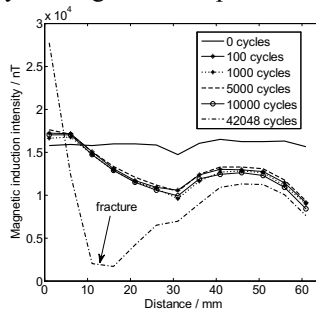

Figure 4. Magnetic induction intensity under different cycles.

To further describe the variations of the residual magnetic field, the gradient was extracted to be investigated. It can be expressed as: $k_B = \dfrac{dB}{dx}$, where k_B is the magnetic

gradient, B represents the induction magnetic field, and x denotes the measurement distance. Figure 5(a) shows the gradient signal without fatigue. The magnetic gradient has a peak value at the center of the sample, which is opposite to the magnetic field change trend showed in Figure 4. Therefore, it is believed that gradient k_B can only qualitatively reflect the stress concentration but cannot quantitatively represent the magnitude of stress or fatigue damage. Multiple methods should be used to further investigate the correlation between gradient k_B and fatigue degree.

The k_{Bmax} is the maximum magnetic gradient in a scanning process, and it usually appears around cracks and is considered to have some correlation with crack depth [9]. The gradient k_{Bmax} under different cycles is calculated, as presented in Figure 5(b). k_{Bmax} increases slowly with the increasing loading cycles in the early and middle stages and increase sharply in late stage. By the least square method, the fitting result can be expressed as $y = 0.0038 \times x + 3.5e^2$. According to the theory of fatigue crack growth [8], it can be seen that the variation trend of k_{Bmax} is the same as that of crack depth with the increase of loading cycles in the fatigue process. From the results, it should be underlined that there is a certain rule between the maximum gradient and fatigue damage. However, further research should be done considering the various factors that affect magnetic such as the material, temperature, and geometry of the specimen.
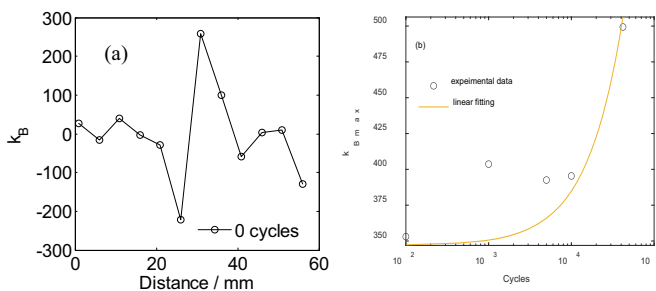

Figure 5. Variations of magnetic characteristic parameters with cycles:

(a) magnetic gradient k_B, (b) maximum gradient k_{Bmax}.

3.3. XRD Analysis

Figure 6 shows the XRD diffraction intensity spectrum of the 304 stainless steel samples before fatigue and after a fracture. For the sample after fatigue, the diffraction peaks of α' martensite phase is superimposed on that of the original γ austenite phase and the highest peak $\gamma(111)$ decreases largely, whereas the $\alpha'(110)$ increases relatively. Therefore, we can conclude that fatigue has caused the martensite transformation and changed the magnetic permeability as well as the residual magnetic field of 304 stainless steel. However, there are several challenges to characterize the fatigue damage of austenitic stainless steel by the residual magnetic field measurement. First, the martensite transformation is strongly temperature-dependent, which increases the uncertainty of sensitivity for components working at high temperature. Second, the transformation is a significant factor affecting magnetism but is not directly related to the life reduction. Furthermore, the magnetic sensor might be sensitive to other factors such as stress magnetization and surface morphology simultaneously, which might cause the lack of selectivity for the particular fatigue damage.
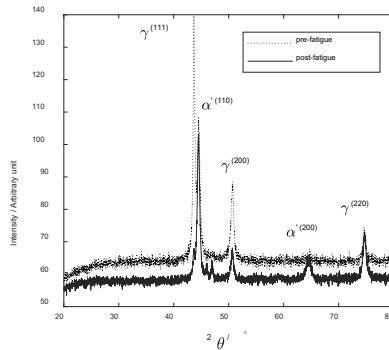
Figure 6. XRD spectrum of 304 stainless steel samples before and after fatigue.

4. Conclusions

This paper presented a residual magnetic field measurement method based on the fluxgate sensor for the evaluation of fatigue damage in paramagnetic 304 stainless steel. It was found that the maximum magnetic gradient increases with the increase in fatigue cycles and the variation rules are consistent with the law of crack growth in the fatigue process. The martensitic transformation caused by fatigue might be the main reason for the change of the residual magnetic field. It is possible to estimate fatigue damage of 304 stainless steel components by the passive magnetic NDT method. Future research will include demonstrating the feasibility of passive magnetic DNT methods in damage assessment of austenitic stainless steel under high temperature. The selectivity of detection methods for particular materials and damage mechanism types will be investigated. Additionally, the multi-modal monitoring in combination with other methods will be developed for comprehensive evaluation of material states in practical engineering situation.

References

[1] P. B. Nagy, Non-destructive methods for materials' state awareness monitoring, *Insight* **52** (2010), 61–71.
[2] J. W. Wilson, G.Y. Tian, S. Barrans, Residual magnetic field sensing for stress measurement, *Sensors and Actuators A: Physical* **135** (2007), 381–387.
[3] M. Morozov, G.Y. Tian, P. J. Withers, Elastic and plastic strain effects on eddy current response of aluminium alloys, Nondestructive Testing and Evaluation **28** (2013), 300–312.
[4] N. Venkatachalapathi, G.J. Raju, P. Raghavulu, Characterization of fatigued steel states with metal magnetic memory method, *Materials Today: Proceedings* **5** (2018): 8645–8654.
[5] G. Spositoa, C. Wardab, P. Cawley, et al, A review of non-destructive techniques for the detection of creep damage in power plant steels, *Ndt & E International* **43** (2010), 555–567.
[6] E. Madhi, P. B. Nagy, Sensitivity analysis of a directional potential drop sensor for creep monitoring, *Ndt & E International* **44** (2011), 708–717.
[7] L.J. Yang, C.B. Tu, S.W. Gao, Detection method of weak magnetic field based on fluxgate sensor, *Instrument Technique and Sensor* **09** (2014), 84–87.
[8] R.T. Liu, W. B. Liu, J.Y. Liu, Mechanical properties of engineering materials, Harbin Institute of Technology, Harbin, 2001.
[9] N. Chen, H. Lin, X.K. Wang, Crack propagation analysis and fatigue life prediction for structural alloy steel based on metal magnetic memory testing, *Journal of Magnetism and Magnetic Materials* **462** (2018), 144–152.

Prediction of the Hardness of X12m Using Barkhausen Noise and Chebyshev Polynomials Regression Methods

Zibo Li[1,2,3*], Shicheng Li[1,2], Donghao Wang[1,2], Guangmin Sun[3], Cunfu He[4], Yu Li[3], Xiucheng Liu[4], Yanchao Cai[4], Chu Wang[1,2]

[1]Beijing JingHang Research institute of computation and communication, Beijing, 100074, China. Email glory0117@163.com

[2]The Classified Information Carrier Safety Management Engineering Technology Research Center of Beijing, 100074, China

[3]Faculty of Information Technology, Beijing University of Technology, Beijing, 100124, China

[4]College of Mechanical Engineering and Applied Electronics Technology, Beijing University of Technology, Beijing, 100124, China

Abstract. Barkhausen noise (BN) is electromagnetic pulse sequence that could be used to nondestructively predict the properties of materials such as hardness, residual stress and carbon content. Current BN signal analysis methods fail to describe the highly variated BN signal and achieve high regression accuracy due to the low interpretability of neural network and limited capacity of mathematical regression tools. In this paper, two multi-variable regression tools, named partial Chebyshev polynomial regression (PCPR) and Mutual Information-based Feature Selection with Class-dependent Redundancy and multi-variable Chebyshev polynomials regression (MIFS-CR+MCPR), are employed for the first time to predict the hardness of Cr12MoV steel (i.e. X12m). Combined with Chebyshev polynomials, our regression tools are designed on the basis of cascaded regression and mutual-information-based feature selection. As represented by the experimental results for predicting the hardness of X12m, the proposed method outperforms other comparative methods including neural network and partial linear square regression method.

Keywords. Non-destructive Evaluation, Hardness Prediction, Chebyshev polynomials regression, Barkhausen Noise

1. Introduction

As one of the famous non-destructive evaluation (NDE)[1,2] methods, Barkhuasen Noise (BN) is generated by the irreversible movements of domain walls and could be analyzed to predict the properties of materials such as hardness, residual stress and carbon content. The biggest challenge in analyzing BN is the pseudo-random nature. Therefore, features directly extracted from BN signal might be largely varied. In the last decade, many studies were carried out for finding stable BN features that could represent changes of material property. In order to measure the residual stress of materials, Aki Sorsa et al.[3-6] assembled the features including peak information, statistical results, bandwidth,

entropy and the parameter in BN profile and then concatenated them to predict the property of materials (e.g. hardness of 18CrNiMo7-6[6]). Liu. et al.[7] compared two models which are multivariable linear regression (MLR) model and BP neural network in applying surface hardness prediction of 12CrMoV steel plate. 6 BN features (such as peak value, mean value of BN profile) and 5 tangential magnetic field (TMF) features (such as amplitude of the 3rd, 5th and 7th harmonics) were extracted as the input to the two regression models. In our previous work,[8] we have focused on the feature extraction methods of BN for hardness prediction. Compared with the conventional BN features (called isolated features in [8]), a stable and unified feature that was generated by signal component analysis (i.e. slow feature analysis and discriminant incoherent component analysis) was proposed to predict the hardness of X12m. It could be observed that these mentioned prediction systems are designed to deal with multiple inputs. Therefore, the multi-variable regression method should be adopted in these prediction systems. However, the regression models (e.g. linear regression[7], neural network[9-11], and partial linear regression method[3-4]) adopted in the previous mentioned methods share the limited capacity. Among different regression tools, the polynomial-based multi-variable regression outperforms other methods in regression accuracy. In NDE research domain, to our best knowledge, it is the first time that the polynomial-based multi-variable regression method is employed to predict the properties of material.

The remainder of this paper is organized as follows: Section II introduces the details of our method. Section III presents experimental setup, results and discussions. Finally, Section IV provides the summary and conclusion.

2. Methods

In this section, the BN features information will be firstly proposed. Then the basic model of multi-variable Chebyshev polynomials regression and two improving algorithms on the polynomial regression will be introduced.

2.1. Data Preprocessing

In this study, for each measurement, the detected BN signal contains 6 complete magnetization loops or 12 BN loops. The first task in the subsection is to remove the incomplete loops and divide the signal into 11 intervals that starts from the same strength of tangential magnetics. Each interval includes one complete magnetization loop. To remove the incomplete loops, the position of the first peak among whole BN signal is detected as the cut-off point from which the 11 analyzed intervals are extracted. Then in each analyzed BN interval, a moving average window is slide on the signal to filter noise and build the profile. Subsequently, 9 features are extracted, as shown by Figure. 1 and Table 1. With the increasing number of hardness, the qualified relationship between hardness and each chosen feature could be shown in Figure.1. Some features such as peak value show a downward trend whereas some are upward trend such as peak position. In contrasts to the conventional features (i.e. peak information, bandwidth and intercept of tangential magnetic field), the information of sub-peak value and frequency domain were adopted in this paper. According to the literature[6], the hardness of materials is link strongly to the main peak of BN signal profile. Therefore, the sub-peak is employed here as an auxiliary feature for the prediction of hardness. The relationship between sub-peaks and main peak are shown in Figure.2. Besides, the harmonic information of BN includes

the value of 3rd, 5th and 7th harmonic points were adopted in this study as mentioned in [7]. All the mentioned features are concatenated as the input of our regression algorithm.

Table 1. The selected features in our study

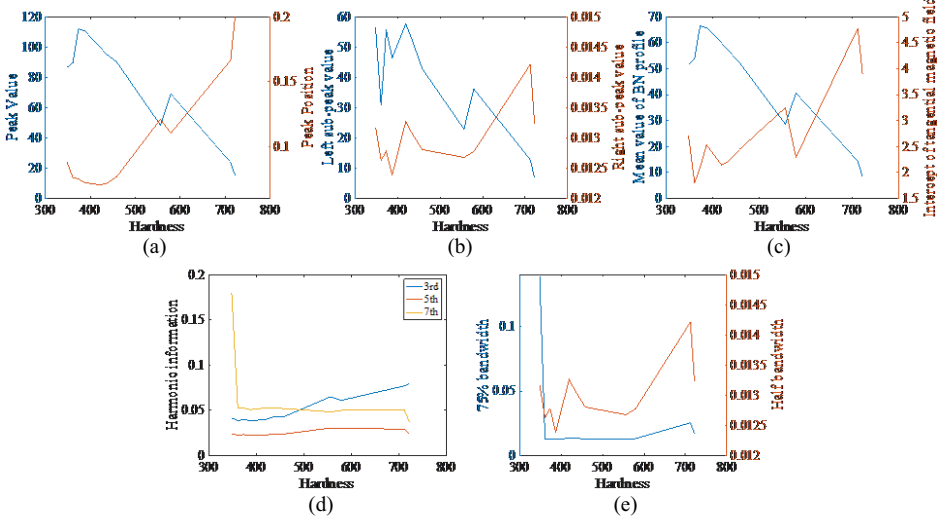|		
Peak value	Peak Position	Mean value of BN profile
Left sub-peak value	Right sub-peak value	Intercept of tangential magnetic field
Harmonic information	75% bandwidth	Half bandwidth

Figure. 1 Features vary as hardness of X12m increased. (a) Peak value and Peak position, (b) Left sub-peak value and Right sub-peak value, (c) Mean value of BN profile and Intercept of tangential magnetic field, (d) 3rd, 5th and 7th Harmonic information, (e) 75% bandwidth and Half bandwidth.
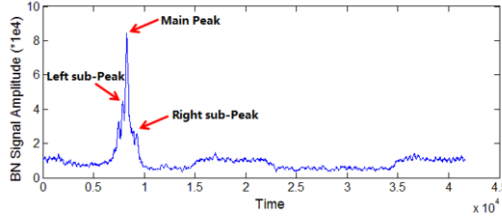

Figure. 2 Two half-period BN samples labeled with Peak information.

2.2. Introduction to Regression Methods

Given a variable $x \in (-1,1)$ and the parameter $n \in Z_0$, the Chebyshev polynomials of class 2 (i.e. CP-2) $U_n(x)$ is defined as:

$$U_n(x) = \frac{\sin((n+1)\arccos x)}{\sin(\arccos x)} \tag{1}$$

And the CP-2 could be rewritten as the second-order recursion [15]:

$$U_{n+2}(x) = 2xU_{n+1}(x) - U_n(x) \text{ with } U_0(x) = 1 \text{ and } U_1(x) = 2x \tag{2}$$

The first eight terms of CP-2 polynomials are listed in Table 2. Based on the single-variable CP-2, Zhang Y. et al. [14] further designed the multi-variable format of CP-2 by adopting Bernstein polynomials, which is called multi-variable Chebyshev polynomials regression (MCPR). However, the number of regressed coefficients of MCPR is exponentially proportion to the number of input variables. To overcome the coefficient

explosion problem, in our work[12], two strategies including feature selection and cascaded regression are designed to alleviate this problem.

Table 2. The first eight CP-2 polynomials

$U_0(x) = 1$	$U_4(x) = 16x^4 - 12x^2 + 1$
$U_1(x) = 2x$	$U_5(x) = 32x^5 - 32x^3 + 6x$
$U_2(x) = 4x^2 - 1$	$U_6(x) = 64x^6 - 80x^4 + 24x^2 - 1$
$U_3(x) = 8x^3 - 4x$	$U_7(x) = 128x^7 - 192x^5 + 80x^3 - 8x$

In terms of feature selection idea, a novel feature selection method[13] named "Mutual Information-based Feature Selection with Class-dependent Redundancy" (MIFS-CR) are combined with MCPR to directly reduce the number of the input variables of MCPR. Inspired by the idea that the potential and selected variable equally contribute to the redundancy of mutual information between selected variable and class set, MIFS-CR achieves better performance than the former feature selection methods and the details of MIFS-CR could be found in the related manuscript[13].

In terms of cascaded regression idea, on the foundation of the cascaded regression and the framework of PLSR[16], our CP-2-based cascaded regression idea could be represented as the following iteration way:

$$E_t = Z_t c_t^T + E_{t+1}$$
$$F_t = Z_t r_t^T + F_{t+1}$$
(3)

where t is the iteration number, E_t, F_t are the residual input and target in the former $t-1$th iteration, c_t, r_t represent the regression coefficients. As the most important element in (3), Z_t is defined as:

$$Z_t = U(u_t) \in R^{N \times n} = \bigcup_{l=1}^{N} \prod_{j=1}^{n} U_{s_j}((u_t)_l)$$
(4)

where n is the number of CP-2 polynomials, N is the sample number, u_t is denoted as the main component of E_t, $\prod$ represents concatenating operator in the column of Z_t and $\bigcup$ represents the concatenating operator in the row. In other words, in tth iteration, the residual target F_t and input E_t is approximated by the single-variable CP-2 regression tool and the variable u_t is the main component of residual input E_t (i.e. $u_t = E_t p_t$, where p_t is the projection vector generated from $E_t^T F_t F_t^T E_t$ [16]). And the errors generated from regression tool is treated as the residual target and input for the next iteration $t+1$.

3. Experiments

3.1. Experiment material and data measurements

Plate samples with the size of 200mm*60mm*3mm manufactured from case-hardened steel Cr12MoV (i.e. x12m) were studied in this paper. In the quenching procedure, all tested samples were carburizing case-hardened at 650℃ for 60 min, 850℃ for 90 min, 1030℃ for 150 min, and then Nitrogen-cooling for 25 min. In the tempering procedure, the tempering temperature varied between 180 and 720℃ and times for 210 min which is related to the hardness label of each sample. The properties of Cr12MoV material and initialization about measurement are shown in Table 3.

As shown by Figure. 3, the MBN sensor are composed of the excitation coil with 2100 turns winding onto the U-shape ferrite core and the hall sensor next to the surface of sample. The excitation signal was the singular wave with 12Hz and 8V and generated by LabVIEW. The sampling rate was chosen as 1MHz. And the BN signal was stored with NIPXle multi-channel acquisition card and LabVIEW software. For each sample, the measurement was repeated for 5 times and the BN signal generated from each repetition contained 12 magnetization loops.

Table 3. The properties of Cr12MoV material and initialization about measurement

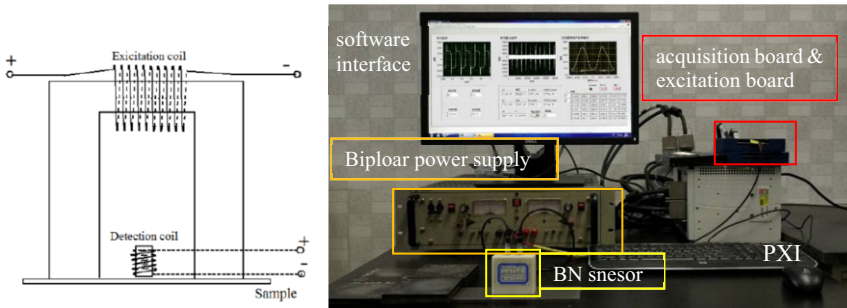| Tempering Temperature (℃)	720	700	680	660	640	590	575	550	525	505	180
Averaged Vickers hardness	348	361	373	387	419	434	458	556	579	712	722

Figre.3 The diagram of sensor settlement.

In terms of hardness prediction experiment, RMSE is used as the criterion for accuracy of prediction, three conventional models and representative methods were compared. These conventional methods include the neural network (i.e. back propagation neural network (BP)), cascaded regression method (i.e. PLSR) and random forests (RF). All algorithms involved in this paper were tested in a 10-cross-validation (CV) way.

3.2. Results

The Vickers hardness prediction results are shown by Figure.4 and the accuracy results about different algorithms are presented by Table 4. According to the Figure. 4(a-c), the scatter points are far away from the base line and imply that the accuracy of the conventional algorithms is unacceptable. This phenomenon could also be found in Table 4. Compared with the results brought by the conventional algorithms, the scatter points of our designed algorithms (shown by Figure.4(d-e)) are closer to the base line and the best performance is achieved by MIFS-CR+CP-2 (i.e. Figure.4(d)). In accordance with Table.4, the RMSE of CP-2-based algorithms is less than other conventional algorithms and the best accuracy (i.e. **0.3629**) is achieved by MIFS-CR+CP-2. This high performance could be ascribed to three aspects: Firstly, given a proper order, any nonlinear model could be approximated by an orthogonal polynomials; Secondly, compared with the NN-based model, a specific mathematical equation could be deducted by the polynomials-based model; Thirdly, according to the theory of PCPR, the basic idea of PCPR is to enhance the efficiency with the cost of accuracy[12] and therefore the prediction error is slightly larger than feature-selection-based MCPR method (i.e. MIFS-CR+CP-2). Therefore, CP-2 could be ascribed as the main reason for this phenomenon and the enhancement of the prediction accuracy by multi-variable CP-2 regression tool is our main contribution.

Table 4. The regression accuracy

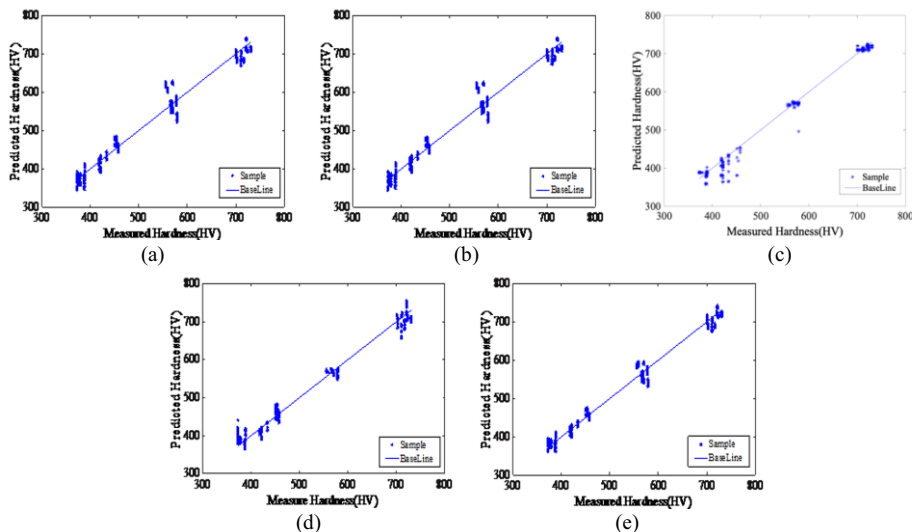| Algorithms	BP	PLSR	RF	MIFS-CR+CP-2	PCPR
RMSE(HV)	0.5548	0.5331	0.5151	**0.3629**	0.4144

Figure. 4 Scatterplot of predicted output and the measured output with different algorithms based on Cr12MoV material. (a) BP (b) PLSR (c) RF (d) MIFS-CR+CP-2 (e) PCPR.

4. Conclusions

In this paper, the feature-selection-based and cascade-based regression algorithms (i.e. MIFS-CR+CP-2 and PCPR) proposed in our previous study are employed for the purpose of accurate hardness prediction of X12m steel by analyzing Barkhausen noise. In the data processing part, conventional and self-designed BN features are generated. All features are proven that the qualified relationship between hardness and selected feature. In experimental part, the Vickers hardness of Cr12MoV steel is predicted using the conventional NDE-applied regression tools and our proposed regression algorithms. As shown in the results, the performance of our feature-selection-based regression tool outperforms the other methods. Due to the wide-applied property of regression tools, it could be inferred that CP-2-based regression tools could be applied to solve the hardness prediction problem and have the potential to solve other NDE problems. Therefore, our algorithms can be expected to be further employed in more NDE applications.

References

[1] Kashefi M, Rafsanjani A, Kahrobaee S, et al. Magnetic nondestructive technology for detection of tempered martensite embrittlement. Journal of Magnetism and Magnetic Materials, 324(2012), 4090-4093.
[2] Bray D E, Stanley R K. *Nondestructive evaluation: a tool in design, manufacturing and service*. CRC press, 1996.
[3] Sorsa A, Isokangas A, Santa-aho S, et al. Prediction of residual stresses using partial least squares regression on Barkhausen noise signals. *Journal of Nondestructive Evaluation*, **33**(2014), 43-50.

[4]   Sorsa A, Santa-aho S, Vippola M, et al. A case study of using radial basis function neural networks for predicting material properties from Barkhausen noise, *signal Proceedings of 18th Nordic Process Control Workshop*, 6p. 2013,3633-3642.

[5]   Sorsa A, Leivisk, K, Santa-aho S, et al. An efficient procedure for identifying the prediction model between residual stress and Barkhausen noise. *Journal of Nondestructive Evaluation*, **32**(2013), 341-349.

[6]   Sorsa A, Leivisk, K, Santa-aho S, et al. Quantitative prediction of residual stress and hardness in case-hardened steel based on the Barkhausen noise measurement. *Ndt & E International*, **46**(2012), 100-106.

[7]   Liu XC, Zhang RH, Wu B, et al. Quantitative Prediction of Surface Hardness in 12CrMoV Steel Plate Based on Magnetic Barkhausen Noise and Tangential Magnetic Field Measurements. *Journal of Nondestructive Evaluation*, (2018) 37:38.

[8]   Li Z, Sun G, He C, et al. Prediction of the hardness of X12m using Barkhausen noise and component T analysis methods. *Journal of Magnetism and Magnetic Materials*, **478**(2019), 59-67.

[9]   Perez-Benitez J A, Espina-Hernandez J H, Martínez-Ortiz P. Unwrapping the influence of multiple parameters on the Magnetic Barkhausen Noise signal using self-organizing maps. *NDT & E International*, **54**(2013): 166-170.

[10]   Perez-Benitez J A, Padovese L R. Feature selection and neural network for analysis of microstructural changes in magnetic materials. *Expert Systems with Applications*, **38**(2011), 10547-10553.

[11]   Perez-Benitez J A, Padovese L R. Study of the influence of simultaneous variation of magnetic material microstructural features on domain wall dynamics. *Journal of Magnetism and Magnetic Materials*, **322**(2010), 3101-3105.

[12]   Z. Li, G. Sun., et al. Multi-variable Regression Methods using Modified Chebyshev Polynomials of Class 2. *Journal of Computational and Applied Mathematics*, **346** (2019), 609-619.

[13]   Zhang Y, Yin Y, Guo D, et al. Cross-validation based weights and structure determination of Chebyshev-polynomial neural networks for pattern classification. *Pattern Recognition*, **47**(2014), 3414-3428.

[14]   Wang Z, Li M, Li J. A multi-objective evolutionary algorithm for feature selection based on mutual information with a new redundancy measure. *Information Sciences*, **307**(2015), 73-88.5-7916.

[15]   Celant G, Broniatowski M. *Interpolation and Extrapolation Optimal Designs V1: Polynomial Regression and Approximation* Theory. John Wiley & Sons, 2016.

[16]   Bastien P, Vinzi V E, Tenenhaus M. PLS generalised linear regression. *Computational Statistics & Data Analysis,* **48**(2005), 17-46.

This page intentionally left blank

Inverse Problem and Signal Processing

This page intentionally left blank

Sensitivity Analysis for the Inverse Problems of Electromagnetic Nondestructive Evaluation

Sándor BILICZ [1]

Budapest University of Technology and Economics, Hungary

Abstract. Sensitivity analysis of the model-based inverse problem associated to electromagnetic nondestructive evaluation is dealt with. Some uncertainty of the arrangement is inevitable present (imprecise host material parameters, sensor mispositioning, etc.), and this induces uncertainty on the reconstructed defect parameters. The aim of this work is to present a methodology for the ranking of the different sources of random error according to their contribution to the reconstruction uncertainty. To this end, state-of-art mathematical tools of sensitivity analysis are applied, including Sobol' indices, and a polynomial chaos expansion surrogate model to reduce the computational burden of the method. A numerical example drawn from magnetic flux leakage nondestructive evaluation is presented to illustrate the proposed methodology.

Keywords. inverse problem, sensitivity analysis, Sobol' index, polynomial chaos, surrogate model

1. Introduction

Inverse problems of electromagnetic nondestructive evaluation (EM NDE) are dealt with in this work. Model-based inversion is to reconstruct defect parameters based on the measured EM field. This problem is usually traced back to an optimization problem for which various efficient global optimization algorithms have been applied for decades. However, beyond the mere reconstruction of defect parameters, the uncertainty of the parameter values obtained by the inversion algorithm is also important. This uncertainty is inevitably present because the setup parameters (e.g., host material, specimen dimensions, sensor position, etc.) are never precisely known.

Uncertainty quantification (UQ) is to assess the uncertainty induced on a quantity of interests due to random inputs: in our case, uncertainty of reconstructed defect parameters due to imprecise setup parameters. Sensitivity analysis aims at ranking the sources of uncertainty with respect to their contribution to the output uncertainty.

In the present contribution, a framework is proposed for the sensitivity analysis of the solution of the entire inverse problem. For certain values of the measured data, optimization-based inversion is performed to obtain the reconstructed defect parameters which obviously depends on the uncertain setup parameters. The quantitative character-

---

[1]Corresponding Author: Sándor Bilicz; E-mail: bilicz@evt.bme.hu

ization of the uncertainty is given by the Sobol' indices [1,2], which quantify not only the contribution of each setup parameter but also of their combinations. The benefit from this sensitivity analysis is that one gains proper knowledge on how the uncertain setup parameters influence the reconstruction capability of an inversion procedure. This may promote the optimal design of NDE arrangements with respect to robustness. Furthermore, it can screen the most important sources of uncertainty, which have to be taken into account in another inversion routines, e.g., the model-free approach in [3]. Finally, the proposed method provides a deeper insight into the importance of different physical phenomena behind the EM NDE method.

2. Problem definition

Let the deterministic vector-vector function $\boldsymbol{y} = \boldsymbol{f}(\boldsymbol{x}|\boldsymbol{w})$ represent the relationship between the observable signal $\boldsymbol{y} \in \mathbb{R}^K$ (e.g., spatial scan of the B-field in flux leakage testing), the vector of the defect parameters $\boldsymbol{x} \in \mathbb{R}^N$ (e.g., crack dimensions) and the setup parameters $\boldsymbol{w} \in \mathbb{R}^M$ (e.g., host material permeability, probe misalignment, etc.). The forward operator $\boldsymbol{f}$ is realized by electromagnetic simulation.

In recent works, the application of sensitivity analysis by means of Sobol' indices of the forward operator $\boldsymbol{f}$ is presented [4]. Such studies can lead to valuable knowledge on (i) how each setup parameter w_i contributes to the output uncertainty and (ii) whether the setup uncertainty hinders the reconstruction of small variations of the defect parameters.

In the present work, the inverse problem is considered as follows. For a certain output signal $\boldsymbol{y}'$ resulted from a measurement, the inverse problem reads as

$$\hat{\boldsymbol{x}} = \boldsymbol{g}(\boldsymbol{w}) \equiv \underset{\boldsymbol{x} \in \mathscr{X}}{\arg\min} \|\boldsymbol{y}' - \boldsymbol{f}(\boldsymbol{x}|\boldsymbol{w})\|^2 \tag{1}$$

where $\mathscr{X}$ is the region of interest of the defect parameters and $\hat{\boldsymbol{x}}$ stands for the reconstructed defect parameter vector. The latter depends on the uncertain setup parameters $\boldsymbol{w}$, which are modelled by the random vector $\boldsymbol{W} \in \mathbb{R}^M$. Hereafter the joint probability density function of $\boldsymbol{W}$ is assumed to be known (e.g., from manufacturing tolerances or based on a statistical estimation from measurements). The reconstructed defect parameters are also considered as a random vector $\hat{\boldsymbol{X}} = \boldsymbol{g}(\boldsymbol{W})$. The goal of the analysis presented below is twofold: (i) characterization of the mean and standard deviation of $\hat{\boldsymbol{X}}$, and (ii) calculation of the Sobol' indices of each component of $\hat{\boldsymbol{X}}$ with respect to the random setup parameters $\boldsymbol{W}$.

3. Uncertainty quantification and sensitivity analysis

To achieve the goals in the previous section, the following scheme is proposed.

1. A defect $\boldsymbol{x}'$ is chosen and the inverse problem of reconstructing $\boldsymbol{x}'$ from the corresponding measured output signal is studied. Note that different defects within $\mathscr{X}$ may yield different outcomes of the sensitivity analysis.
2. The measured output signal is approximated by the synthetic data $\boldsymbol{y}' = \boldsymbol{f}(\boldsymbol{x}'|\boldsymbol{w})$, by using the deterministic forward model $\boldsymbol{f}$.

3. Finally, a heuristic approximation for $g(w)$ is introduced as

$$g(w) \approx \underset{x \in \mathcal{X}}{\arg \min} \| \underbrace{f(x'|w)}_{y'} - \underbrace{f(x|w_0)}_{\tilde{f}(x)} \|^2 \qquad (2)$$

where w_0 stands for the mean of the random setup parameters: $w_0 = \mathbb{E}[W]$. This approximation reduces the computational cost of the optimization: the forward model with $w = w_0$ kept fixed, whereas $f(x|w_0)$ can be approximated by a surrogate model $\tilde{f}(x)$. The latter can be, e.g., a sparse grid [5], a kriging or a radial basis function [6] surrogate model, just to name a few among the common choices.

Sobol' indices. A state-of-art tool of sensitivity analysis is based on the Sobol' indices [2]. Each component (with notation omitted for simplicity) of the function g in Eq. (2) can be decomposed [1] as

$$g(w) = g_0 + \sum_{i=1}^{M} g_i(w_i) + \sum_{1 \leq i < j \leq M}^{M} g_{ij}(w_i, w_j) + \cdots + g_{1,2,\ldots,M}(w_1, w_2, \ldots, w_M), \qquad (3)$$

This decomposition is unique under certain conditions for the sub-functions (see, e.g., in [2]). These conditions ensure that the variance of $g(W)$ can also be partitioned into the sum of sub-variances:

$$D \equiv \mathbb{E}[(g(W) - g_0)^2] = \sum_{i=1}^{M} D_i + \sum_{1 \leq i < j \leq M}^{M} D_{ij} + \cdots + D_{1,2,\ldots,M} \qquad (4)$$

with $D_{i_1,i_2,\ldots,i_S}$ denoting the contribution of the group of parameters $\{w_{i_1}, w_{i_2}, \ldots, w_{i_S}\}$. The Sobol' indices of each possible groups are defined via normalization with D,

$$S_{i_1,i_2,\ldots,i_S} = D_{i_1,i_2,\ldots,i_S} \Big/ D, \qquad (5)$$

that makes the sum of all possible indices equals to 1. Indices corresponding to one setup parameter are called 1st order indices. Higher order indices reflect the effect of the interaction of two or more setup parameters to the reconstruction uncertainty.

Polynomial chaos expansion (PCE). Even if surrogate models of f can effectively reduce the computational burden associated to Eq. (2), sensitivity analysis of $g(w)$ with respect to its input variables remains cumbersome when traditional methods (e.g., Monte Carlo sampling [7]) are used. Therefore, a PCE surrogate model of $g(w)$ is built, which provides robust estimates for the total variance D and the Sobol' indices, respectively, with a moderate resource demand. The PCE approximation of each component of g reads as

$$g(W) \approx \sum_{\alpha \in \mathcal{A}} c_\alpha \Psi_\alpha(W) \qquad (6)$$

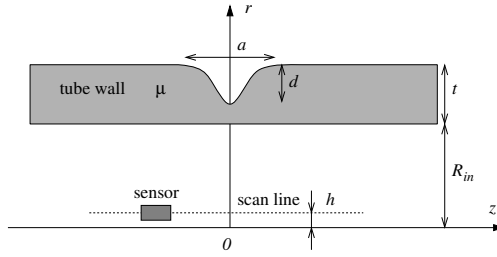where the basis functions $\Psi_\alpha(W)$ are products of univariate functions, i.e.,

Figure 1. Sketch of the configuration: a ferromagnetic tube is affected by a circumferential groove on the exterior surface. A static magnetic field is incident in the axial (z) direction; the z-component of the leaking magnetic field is measured by a sensor scanning near the tube axis.

$$\Psi_{\boldsymbol{\alpha}}(\boldsymbol{W}) = \Phi_{\alpha_1}^{(1)}(W_1)\Phi_{\alpha_2}^{(2)}(W_2)\cdots\Phi_{\alpha_M}^{(M)}(W_M). \tag{7}$$

where each factor $\Phi_{\alpha_m}^{(m)}$ is the α_m-th member of a polynomial family which is orthonormal with respect to the marginal probability density function corresponding to the m-th setup parameter. For example, uniform and normal distributions correspond to Legendre and Hermite polynomials, respectively.

The index set $\mathscr{A}$ in Eq. (6) is chosen as a reasonable subset of $\mathbb{N}^M$, e.g., by a linear truncation $\mathscr{A} = \{\boldsymbol{\alpha} : \boldsymbol{\alpha} \in \mathbb{N}^M, |\boldsymbol{\alpha}|_1 \leq L\}$ where L is a small integer (in our example, around $6\ldots8$). The coefficients $c_{\boldsymbol{\alpha}}$ in Eq. (6) are calculated by means of a least squares fit to a set of training data $\{\boldsymbol{w}^{(q)}, g(\boldsymbol{w}^{(q)})\}$, $q = 1, 2, \ldots, Q$, obtained by Q number of evaluations of Eq. (2). Once the PCE surrogate models for each component of $\boldsymbol{g}$ are built, the variance of $\boldsymbol{g}(\boldsymbol{W})$ and all Sobol' indices can be calculated from the PCE coefficients.

4. Numerical examples

The configuration and the EM model. A magnetic flux leakage NDE arrangement for tube inspection has been chosen as illustration. The configuration is kept simple so that the emphasis is put on the sensitivity analysis. A ferromagnetic tube (Fig. 1) with relative permeability μ, inner radius R_{in}, and wall thickness t is assumed to be affected by a circumferential groove on the exterior surface. An axially directed static magnetic field ($\boldsymbol{H} = \hat{\boldsymbol{z}}H_0$) is incident within the tube wall. Due to the groove, a leaking magnetic field is present. The total field is written as the sum of the incident field and the perturbation field caused by the groove: $\boldsymbol{H} = \boldsymbol{H}_0 + \Delta\boldsymbol{H}$, where $\Delta\boldsymbol{H}$ has both axial and radial components. A sensor is scanning along a straight line parallel with the tube axis, and the z component of the perturbation field (ΔH_z) is measured at 51 equi-spaced sensor positions, yielding the observable signal vector $\boldsymbol{y}$. The grove cross-section is modelled by a parametrized 3rd order spline, with the parameters a (opening) and d (depth), denoted together as defect parameters $\boldsymbol{x} = [a, d]$. The region of interest in terms of defect parameters is defined by the ranges $a \in [0.5, 1.5]$mm and $d \in [0.2, 1.5]$mm, respectively.

As uncertain setup parameters, the probe misalignment h, the tube wall thickness t, and the relative permeability μ are considered. They are modelled by independent random variables, with details on their distribution given in Table 1. The tube inner radius is kept fixed ($R_{\text{in}} = 5$mm), and the length of the line scan is 20 mm.

Due to the axial symmetry of the configuration, a two-dimensional EM model is applied. The perturbation field is calculated by means of the method of moments.

Table 1. Probability distribution of the random setup parameters

parameter	distribution	properties
probe misalignment (h)	uniform	range = $[0, 0.25]$mm
tube wall thickness (t)	normal	mean = 2 mm, standard deviation = 0.1 mm
tube relative permeability (μ)	normal	mean = 20, standard deviation = 1.5 (Test A) or 0.5 (Test B)
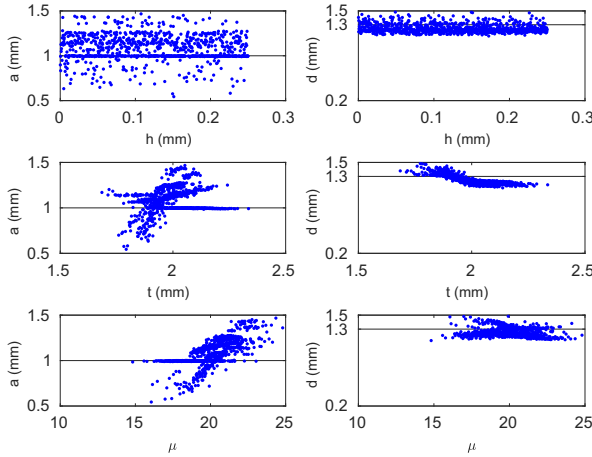
Figure 2. Distribution of the reconstructed defect parameters vs. realizations of the random setup parameters (legend: black line [—] true parameter values; blue dots [·] reconstruction results)

Table 2. Defect parameters in the examples: true values and reconstruction results

	true	reconstructed mean		standard deviation	
		Test A	Test B	Test A	Test B
a (mm)	1.0	1.08	1.07	0.1460	0.1091
d (mm)	1.3	1.25	1.25	0.0611	0.0542

The optimization in Eq. (2) has been performed by the `fmincon` Matlab®function. One call of f and g (as in Eq. (2)) takes ca. 0.25 s and 10 s, respectively, on a standard desktop PC (i7 CPU @3.60GHz, 8 GB RAM). The PCE surrogate models are built with $Q = 900$ training samples in each case. Nevertheless, convergence studies subsequently proved that only 300 samples would have provided almost the same accuracy.

Studies and results. Two slightly different scenarios are studied. According to Table 1, the relative permeability of the tube wall has a higher (Test A) and a lower (Test B) variability. In both cases, the same defect is to be reconstructed: $[a, d] = [1.0, 1.3]$mm.

In Fig. 2, scatter plots present the reconstructed defect parameters wrt. the realization of the random setup parameters for Test A. Note that the uniform and normal distributions of the setup parameters (as defined in Table 1) are clearly seen, as well as that the reconstructed opening a is sensitive to t and μ. Yet, the depth d can be reconstructed with a high accuracy. Uncertainties are quantitatively characterized in Table 2.

The sources of the uncertainties are ranked by means of Sobol' indices (Fig. 3). The bar plots are in harmony with the conclusions of Fig. 2: the probe misalignment h
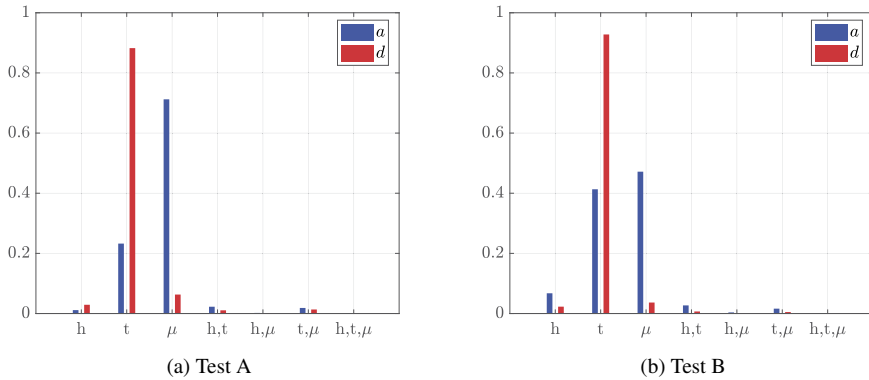
(a) Test A (b) Test B

Figure 3. Sobol' indices.

has little effect to the reconstruction. On the contrary, the effect of the uncertainty of t and μ is significant. When changing from Test A to B (i.e., μ is better controlled), the Sobol' index of μ decreases as expected. Mutual effects (2nd and 3rd order indices) in this example are actually not significant, yet this method is able to reveal such interactions.

5. Conclusion

A framework is presented for the sensitivity analysis of model-based inverse problems of EM NDE with respect to uncertain setup parameters. The computation burden that is commonly associated to inverse problems, can be reduced by surrogate models. The entire inversion scheme is approximated by a polynomial chaos expansion surrogate model, that provides a simple way to calculate Sobol' indices. In so doing, the sources of uncertainty can be ranked based on their importance, which reveals the most efficient ways of improving the accuracy of the NDE arrangement. A simple magnetic flux leakage NDE method has been analysed to demonstrate the capabilities of the framework.

References

[1] Sobol' IM. Sensitivity estimates for nonlinear mathematical models. Mathematical Modelling and Computational Experiments. 1993;1(4):407–414.

[2] Sudret B. Global sensitivity analysis using polynomial chaos expansions. Reliability Engineering & System Safety. 2008;93(7):964–979.

[3] Zhu P, Cheng Y, Banerjee P, Tamburrino A, Deng Y. A novel machine learning model for eddy current testing with uncertainty. NDT & E International. 2019;101:104 – 112.

[4] Bingler A, Bilicz S. Sensitivity Analysis Using a Sparse Grid Surrogate Model in Electromagnetic NDE. In: Lesselier D, Reboud C, editors. Electromagnetic Non-Destructive Evaluation (XXI). vol. 43 of Studies in Applied Electromagnetics and Mechanics. IOS Press; 2018. p. 152–159.

[5] Bilicz S. Sparse grid surrogate models for electromagnetic problems with many parameters. IEEE Transactions on Magnetics. 2016;52(3):1–4.

[6] Douvenot R, Lambert M, Lesselier D. Adaptive Metamodels for Crack Characterization in Eddy-Current Testing. IEEE Transactions on Magnetics. 2011;47(4):746–755.

[7] Fan M, Wu G, Cao B, Sarkodie-Gyan T, Li Z, Tian G. Uncertainty metric in model-based eddy current inversion using the adaptive Monte Carlo method. Measurement. 2019;137:323 – 331.

Data Analysis of Magnetic Flux Leakage Detection Based on Multi-Source Information Fusion

Weilin Shao [a], Ming Sun [a], Yilai Ma [a], Jinzhong Chen [a,1], Xiaowei Kang [a], Tao Meng [a], Renyang He [a]

[a] *China Special Equipment Inspection and Research Institute, China*

Abstract. For the analysis of the magnetic flux leakage detection data in pipelines, a single information source data analysis method is used to determine the pipeline characteristics with uncertainty. A multi-source information fusion data analysis technology is proposed. This paper makes full use of the information collected by the multi-source sensors of the magnetic leakage internal detector, and adopts distributed and centralized multi-source information fusion analysis technology. First, pre-analyze and judge the information data of the auxiliary sensors (speed, pressure, temperature) of the internal magnetic flux leakage detector. Then, the data of the main sensor, ID / OD sensor, axial mileage sensor, and circumferential clock sensor of the magnetic flux leakage detector are analyzed separately. Finally, the RBF neural network + least squares support vector machine (LSSVM)fusion analysis technology is adopted to realize the fusion analysis of multi-source information. The results show that this method can effectively improve the quality and reliability of data analysis compared with traditional single information source data analysis.

Keywords. Magnetic flux leakage, in-line inspection, multi-source, data fusion, data analysis

1. Introduction

Magnetic flux leakage detection is an effective method to detect pipeline defects and identification features. How to improve the quality and reliability of data analysis in magnetic flux leakage is the key issue to ensure the results of pipeline testing [1]. Yang Lijian et al. [2] used the finite element method to analyze the characteristics of the leakage magnetic field signal to make a preliminary judgment on the defect shape parameters. Shao Weilin et al. [1] adopt the principle that the characteristic curves are relatively consistent to judge the special stolen oil hole signal. Wang Fuxiang et al. [3] can identify the pipeline features by using the triaxial leakage magnetic field pseudo color map. The above literatures all use the data analysis of a single information source to judge the results of the leakage magnetic field signals, while the data analysis using single information sources has certain limitations and uncertainties [4].

---

2. Structure and working principle of multi-source information magnetic leakage internal detector
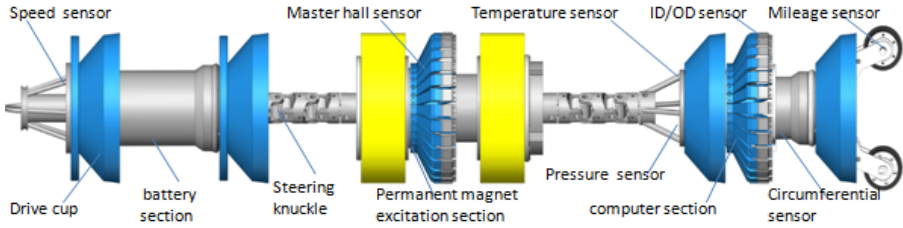

Figure 1. Structure of the magnetic flux leakage detector

The structure of the magnetic flux leakage detector is shown in Figure 1. It is mainly composed of a front-end battery-driven section, an intermediate permanent magnet excitation section, and a rear-end industrial computer section, and each part is connected through a knuckle. The pipeline magnetic flux leakage detecting device is a multi-source information collecting system. Sources of collected information mainly include main sensors, ID/OD sensors, axial mileage sensors, circumferential hour sensors, and auxiliary sensors (speed, pressure, temperature).

The principle of magnetic flux leakage detection is shown in Figure 2. The magnetic field of the leakage magnetic field signal of the wall to be inspected is collected by the main sensor array between the two magnetic poles through the excitation tube body and the permanent magnet thereon, the steel brushes on both sides, and the wall of the tube to be inspected to form a closed loop saturation magnetic circuit. If the material of the wall to be inspected is uniform or the electromagnetic characteristics have not changed, the magnetic field signal of the back is relatively constant; otherwise, the signal of the magnetic flux leakage changes. Through the analysis of the signal signals of each information source, the correlation analysis of the detection data is completed, and the type, shape and size of the relevant features of the pipeline are obtained through the inversion of the signal[1, 3].
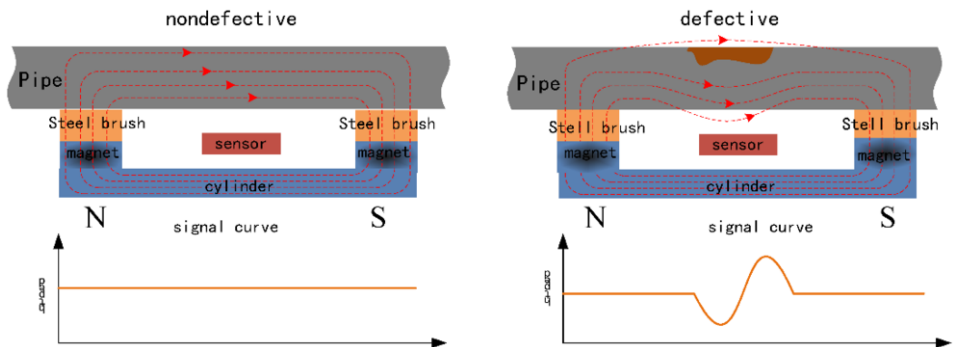

Figure 2. Schematic diagram of magnetic flux leakage detection

3. Data analysis based on single source information

The pipeline magnetic flux leakage detector is a multi-source information acquisition system. By visualizing the detected data, the image of the feature is drawn, and the qualitative analysis of the data is realized by analyzing the signal changes in the image. The following data analysis of signals from different sensor information sources.

3.1. Data analysis of the main sensor information source

The main sensor is located on the permanent magnet excitation section of the detector. The multi-channel three-axis orthogonal Hall sensor array [5] is used to measure the component Bx along the axial direction, the component of the radial direction By and the component Bz of the circumferential direction. Used to identify the type, shape, size, etc. of the feature. The following is a data analysis of the time domain features of the signals in these three directions.

3.1.1. Data analysis of main sensor axial information source

Using the finite element method, the graph of the axial component [6]and the pseudo color map are shown in Figures 3(a) and 3(b). It can be seen from Figure 3(a) that the Bx component is parallel to the axis of the pipe, has a maximum value at the center and is bilaterally symmetric, and has a maximum peak and two valleys. It can be seen from Fig. 3(b) that the contour of the Bx component mainly reflects the inflection point of the bottom contour of the defect, and the valley points are respectively located at the left and right edges of the defect opening, and the peak region is located at the center of the defect opening. The difference between the peak value and the trough value of the Bx component of the feature quantity is defined as the Bx peak-to-valley value [7] (Bxp-p) to evaluate the radial depth of the feature.
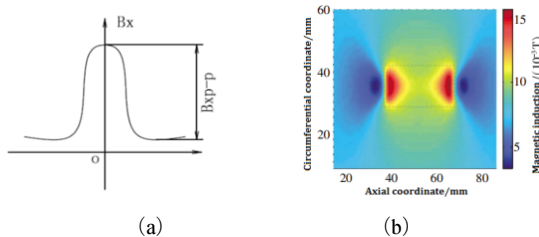

(a)   (b)

Figure 3. Schematic diagram of the axial component of the leakage magnetic field signal

3.1.2. Data analysis of the main sensor radial information source

The finite element method shows that the radial component [6] has a graph and a pseudo color map as shown in Figure 4(a) and 4(b). It can be seen from Figure 4(a) that the By component is perpendicular to the axis of the pipe, which is symmetrical about the center of the defect and zero at the center, and the left and right edges of the defect have a positive value and a negative value, respectively. It can be seen from Figure 4(b) that the contour of the By component mainly reflects the shape of the opening of the defect, and the peak and valley points of By are located at the left and right edges of the defect opening. The difference between the positive peak and the negative peak of the

By component of the feature quantity is defined as the peak value of the By peak [7] (Byp-p) to evaluate the radial depth of the feature. The axial distance between the positive and negative peaks of the By component is defined as the peak-to-peak distance value [7] (Syp-p) to evaluate the axial length of the feature.
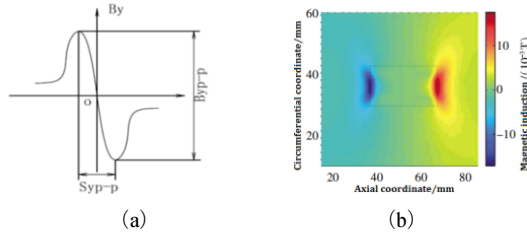

(a)   (b)

Figure 4. shows the radial component of the leakage magnetic field signal

3.1.3. Data analysis of the main sensor's circumferential information source

The finite element method is used to simulate the curve of the circumferential component of the main sensor [6]. From Figure5 (a),it can be seen that the Bz component has two peak points, two valley points, and two antisymmetric planes[13].It can be seen from FIG. 5 (b) that the outline of the Bz component mainly reflects the inflection points of the side boundaries of the defect, the peak points are located at the upper left and upper right edges of the defect opening, and the valley points are located at the lower left and lower right edges of the defect opening. The difference between the peak value and the valley value of the Bz component of the feature amount is defined as the Bz peak and valley value[7] (Bzp-p) to evaluate the circumferential width of the feature[8].
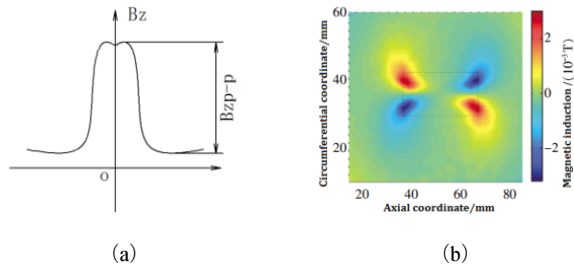

(a)   (b)

Figure 5. Schematic diagram of the circumferential component of the leakage magnetic field signal

3.2. Data analysis of ID / OD sensor information sources

The ID / OD sensor is located in the industrial computer section of the detector. The multi-channel Hall sensor array is used to identify whether the feature is located on the inner or outer wall of the tube. It uses the permanent magnet localized Hall measurement method to magnetize a certain depth using a weak magnetic field. The distance between the inner surface of the pipeline and the absolute magnetic flux leakage vector field in the radial direction follows the principle of magnetic flux leakage. The signal fluctuation is used to determine whether the defect is within the magnetization range to distinguish the features located on the inner and outer walls of the pipeline [9]. First, a certain method is used to extract the characteristics of the curve

data, and then the polarity curve comparison consistency principle [1]is used to judge, which can only evaluate the inner and outer wall distribution of the feature in a limited way.

3.3. Data analysis of axial mileage sensor information source

The axial mileage sensor is located at the end of the detector's industrial control computer section. It uses a multi-channel switch-type Hall sensor for characteristic mileage information positioning. It cooperates with a mileage wheel and a counter to form a redundant mileage positioning system for the detector. The element receives the magnetic signal of the mileage wheel, generates a pulse voltage signal and sends it to the counter to judge the number of revolutions of the mileage wheel, and then calculates the axial mileage based on the circumference of the mileage wheel multiplied by the number of pulses. First, the optimal algorithm is used to extract the features of the triangular wave curve data, and then the time-domain signal alignment analysis is used to locate the feature points. It can only obtain the absolute mileage and relative mileage of the characteristic signal to a limited extent.

3.4. Data analysis of clockwise sensor information source

The circumferential clock sensor is located inside the industrial computer section of the detector. A hammer encoder is used to determine the position of the feature in the circumferential direction of the cross section of the pipeline. The circumferential position adopts the pipe cross-section to align the clock dial to define the clock position. When rotating, the weight always outputs the code disk value to its relatively fixed position to reflect the position of the encoder's circumferential rotation [9]. First, by calculating the two-dimensional curve of the code disk value generated by the initial fixed tip probe, the code disk value corresponding to the characteristic point is selected. Then it is converted into the corresponding hour, and then the hour of the circumferential position of each channel given to the multi-sensor curve is realized. It can only obtain the circumferential clock position of the characteristic signal in a limited manner.

3.5. Data analysis of auxiliary sensor information sources

Auxiliary sensors (speed, pressure, temperature) are located at different positions of the detector, which are used to record the operating parameters and judge the validity of the test data. Each parameter (speed, pressure, temperature) sensor uses the set parameter thresholds to determine whether the operating parameters exceed the working parameters of the detector, thereby realizing the validity of the collected data. When the pressure and temperature parameters exceed the limits, the detection data will be invalid. However, if the speed parameter exceeds the limit within a certain range, a data compensation identification model based on the speed effect must be adopted. First, extract the eigenvalues through the adopted parameter curve, and then use the time domain signal alignment to judge the validity of the data. It can realize the validity of the collected data and the establishment of the recognition model of the compensation model.

4. Data fusion analysis based on multi-source information

4.1. Structure of multi-source information fusion analysis

This paper adopts a distributed and centralized data fusion analysis structure. First, perform independent data analysis on the collected data of each sensor's information source (based on the data analysis method of each sensor), then perform centralized data fusion processing, and finally make a comprehensive data analysis judgment. The data of each single information source sensor is firstly preprocessed by the respective data, and then the local data analysis of each information source sensor is performed according to the respective feature quantities. Before the auxiliary sensor information source data is sent to the fusion center, it needs to be sent to the local data analysis of the main sensor, ID / OD sensor, axial mileage sensor, and circumferential clock sensor information source. First, make a centralized judgment on the effectiveness of the proactiveness of each acquisition system. Then input the results from the local data analysis into the fusion analysis center, make decisions based on the information source sensors and other related information, and make the final comprehensive decision [10].

Figure 6. Fusion analysis structure of magnetic flux leakage detection data

4.2. Multi-source data fusion analysis method

The method of data fusion analysis is critical to the quality and results of data analysis. The comprehensive RBF neural network (RBF ANN) has the characteristics of fast convergence speed, fast network training, strong learning and approximation capabilities, and minimal support vector machine [11] (LSSVM) can solve small sample learning, structure selection, Local extremum, high-dimensional problems [7]. This paper adopts a two-way data fusion analysis model of RBF neural network + minimal support vector machine (Figure 7). That is, the RBF neural network is used to perform pre-data fusion on the auxiliary sensor information source data. Then use LSSVM for feature layer data fusion, the steps are as follows: First, the main sensor axial signal, radial signal, circumferential signal, and ID / OD sensor signal, as well as the time domain characteristic signal data set extracted from the axial mileage signal and circumferential clock signal as the input of magnetic flux leakage detection data LSSVM. Data analysis results as output. Second, normalize the input and output data so that they are between 1 and -1.Finally, determine the kernel function and related

parameters of LSSVM, construct and solve convex quadratic programming, construct the decision function f (x) = sgn [g (x)], and train LSSVM.
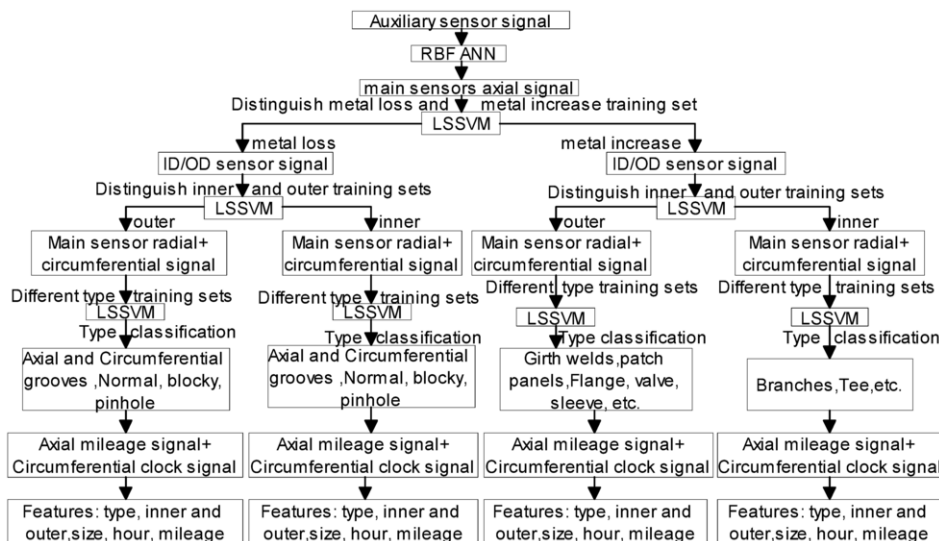

Figure 7. Two-way data fusion model

5. Multi-information source data fusion analysis application

Using multiple information source fusion analysis to analyze the offline data of a certain type of magnetic flux leakage detector, it can be seen that the auxiliary sensor information source signal is judged by RBF neural network fusion, and the data of each collected information source is normal. (A), (B), (C), and (D) of Figure 8 are the graphs of axial signal curve diagram of the main sensor, the graph of radial signal curve of the main sensor, the graph of circumferential signal curve of the main sensor, and the graph of ID / OD sensor signal curve, respectively. Using the LSSVM method to analyze the signals in Figures 8 (A), 8 (B), 8 (C), and 8 (D), it can be seen that this feature is basically directly above the pipe (11:40), and the length and width are basically the same 50mm, and belongs to the metal-addition board and metal loss hole complex. To sum up, it is an external branch pipe, which has been verified as an oil stealing valve after excavation (Figure 9), which shows that the method is feasible.

According to the above-mentioned data fusion analysis, it can be known that the use of multi-source information fusion analysis technology can avoid the limitations and one-sidedness of single-source data analysis when determining features, and can improve the redundancy and superiority of multi-source information systems. Finally, a comprehensive analysis of the detection data is achieved, which can better obtain information such as the type, size, shape, position, and orientation of features.
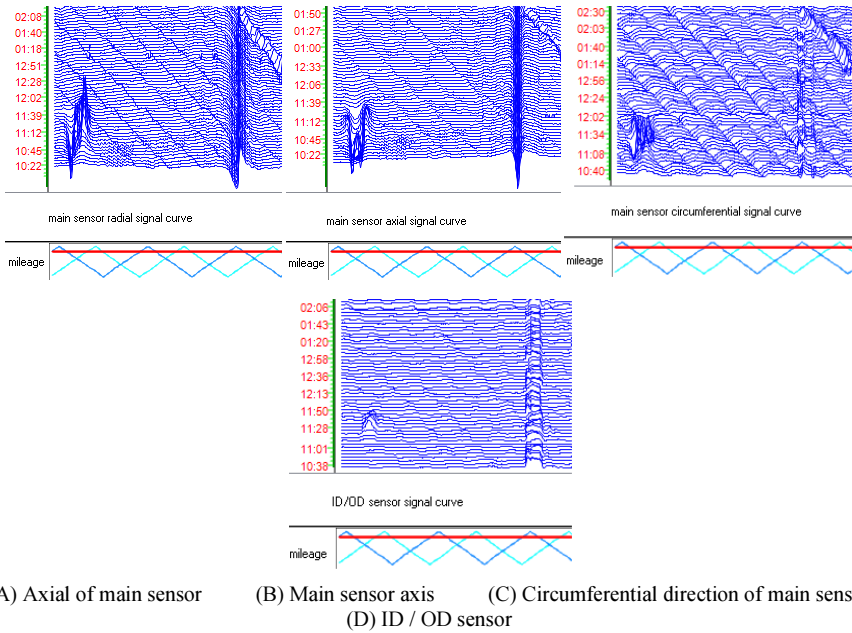
(A) Axial of main sensor   (B) Main sensor axis   (C) Circumferential direction of main sensor
(D) ID / OD sensor

Figure 8. Multi-source information acquisition signal curve

Figure 9. Actual picture of digging verification

6. Conclusion

The pipeline magnetic leakage internal detection equipment is a multi-source information acquisition system, and the sensor is the medium for information source acquisition. The acquisition of pipeline detection information depends on sensors of various information sources with different functions. Multi-source information collection can obtain detection information in all directions, and establishes the basis of complementarity and redundancy of multi-source information.

Multi-source information fusion analysis technology can effectively avoid the limitations and uncertainties of single-source data analysis, and can effectively establish the connection and globality between various sources. Using the RBF neural network + minimum support vector machine data fusion analysis method, compared with the traditional single information source data analysis, it can effectively improve the quality and reliability of the detection data analysis.

7. Acknowledgment

References

[1] W.L.Shao, Identification of the internal magnetic leakage detection signal of oil stealing holes in pipelines, Nondestructive Testing**39**(2017),6-9.

[2] L.J.Yang, Internal magnetic leakage detection technology for long-distance oil and gas pipelines,Journal of Instrumentation**37**(2016),1736-1746.

[3] F.X.Wang, Pipeline feature recognition based on three-axis magnetic flux leakage detection technology, Nondestructive Testing**33**(2011),79-84.

[4] S.Q.An, Research on an improved Bayesian estimation data fusion for tire pressure monitoring system, Journal of Transduction Technology**31**(2018),915-919.

[5] D.Q.Zhou, Pulse magnetic flux leakage detection based on the horizontal component magnetic field analysis of rectangular coils,Journal of Transduction Technology**6**(2017),820-825.

[6] J.J.Chen, Segmental identification method for defect areas in magnetic flux leakage detection of oil and gas pipelines, China Test**11**(2017), 1-7.

[7] S.L.Huang, Theory and Application of Internal Magnetic Flux Leakage Detection for Oil and Gas Pipeline Defects, Machinery Industry Press, Beijing, 2013.

[8] S.Q.Shan, High-resolution triaxial pipeline detector magnetic flux leakage data acquisition system,Sensors and Microsystems**31**(2012),118-121.

[9] L.J.Yang, Internal magnetic leakage detection technology for pipelines, Chemical Industry Press,Beijing,2014.

[10] F.Hu, Research on oil pipeline detection technology based on multi-sensor data fusion, Northeast Petroleum University, Daqing,2011.

[11] H.Y.Yang, Support Vector Machine Identification Method for Magnetic Flux Leakage Detection Signal of Pipeline, Science Technology and Engineering**10**(2010), 6628-6632.

A Signal Processing Method for Steel Plate Thickness Measurement Using EMATs

Chao JIANG[a], and Wencai LIU[b], Youwei LIU[a], Xinjun WU[a,1]

[a] Huazhong University of Science and Technology, Wuhan 430074, China
[b] CNPC Research Institute of Safety and Environment Technology, Beijing, China

Abstract. The time-of-flight (TOF) of the electromagnetic acoustic transducer (EMAT) echo signal can be used to measure the steel plate thickness. There are two ways to obtain the TOF, which are measure the peak to peak time in the time domain and calculate the echo frequency in the frequency domain. In this paper, a simplified signal model is proposed based on the analysis of received signals. Further, the relationship between the echo signal and excitation signal is considered. The echo signal is separated when the asynchronous demodulation method is applied to the received signal, and the thickness of steel plate can be calculated according to the peak spectral frequency in the low frequency band. The simplified model and signal processing method are verified by the experiment, and the results show that the model is reasonable and the accuracy of the signal processing method is high.

Keywords. EMAT, thickness measurement, asynchronous demodulation.

1. Introduction

EMATs can generate different forms of waves by adjusting magnetic circuit and coil structure and don't need coupling agent, so they have been wildly used in the flaw detection, thickness measurement and fatigue detection [1]. For different application, the EMAT signals have different characteristics. Various signal processing methods have been proposed to meet the testing requirement [2].

When EMATs are applied to metal plate thickness measurement, and the time-interval of echo signal is measured to calculate the thickness of steel plate. Typically, the transit time between two consecutive echoes in an ultrasonic waveform are used to be the time-interval value directly [3]. Therefore, the amplitude of the signal and signal-to-noise ratio (SNR) are important indicators of measurement accuracy. In previous studies, many methods had been proposed to improve SNR and improve the measurement accuracy. The timing average and linear filtering method are widely used to reduce the white and grain noise [4], [5]. Stationary wavelet and variational mode decomposition linked wavelet method have been studied in recent years and combined with other method for denoising [6],[7]. These works greatly improve the signal quality in the time domain.

---

[1] Corresponding Author, Xinjun WU, Huazhong University of Science and Technology, Wuhan 430074, China; E-mail: xinjunwu@hust.edu.cn

Frequency component analysis was proposed to gauge the thickness of aluminum sheet by Dixon [8]. Different from those traditional methods, echo frequency is calculated by applying the Fast Fourier transform (FFT) to the signal and then obtain the thickness of aluminum sheet. Therefore, SNR has a small influence on the frequency component analysis. In this paper, the relationship between echo frequency and excitation frequency in the steel plate received signal is studied. Based on the relationship, echo frequency and thickness information are obtained from the received signal by applying asynchronous demodulation to the signal.

2. Signal analysis and processing method

The working process of EMATs includes the coupling between the electric field, magnetic field and sound field. Therefore, the complete mathematical expression of wave is difficult to obtain. Based on the analysis of the received signal, a simplified waveform function is employed to express the relationship between the main component in the signal and then a signal processing method is proposed to obtain the echo frequency based on the waveform function.

2.1. Waveform analysis

The typical received signal of EMATs is analyzed to find an appropriate method and extract the echo frequency in the frequency domain. Figure 1 shows the whole received process of the EMAT. If the paralysis time in the beginning of the signal is ignored, the positive half envelope of the whole signal shows an exponential decay. Then, a segment of the EMAT signal is enlarged in the Figure 2, and it can be seen that the received signal mainly contains two different cycles which are excitation signal cycle and echo signal cycle. The relationship between two signals is that the echo signal is modulated by the excitation signal.
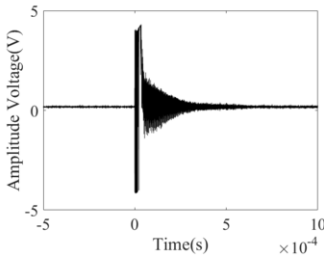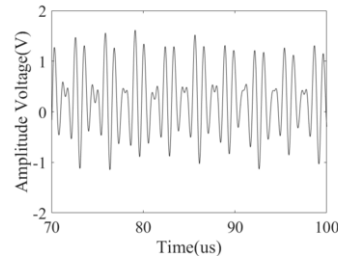

Figure 1. Whole received signal of EMAT.   **Figure 2.** A segment of EMAT signal.

2.2. Signal processing

From the analysis above, the EMAT signal mainly contains the paralysis time, an exponential decay, a sinusoidal excitation signal, and a periodic echo signal. If the paralysis time, harmonic frequency component and noise ignored, a fitting function only contains exponential decay, echo cycle and excitation cycle can be obtained:

$$S(t) = A_0 e^{-\tau t} \sin(2\pi f_0 t) \cdot \left| \sin(\pi f_1 t + \varphi) \right|$$

(1)

Where, A_0 and τ are system dependent coefficients, f_0 is the frequency of the excitation signal and f_1 is the frequency of echo signal, τ is the phase difference between the excitation signal and echo signal. The value of A_0 and τ can be obtained by using two point on the positive envelope of the received signal.

As shown in the Figure 4, the signal amplitude and SNR decrease at the end of the received signal. So, this part of the signal needs to be removed from the analyzed signal. Then a segment of echo signals with a sampling time of T_s can be obtained for analysis.
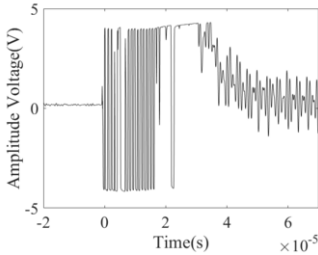
Figure 3. Paralysis time of the EMAT system.   **Figure 4.** The late signal of the EMAT system.
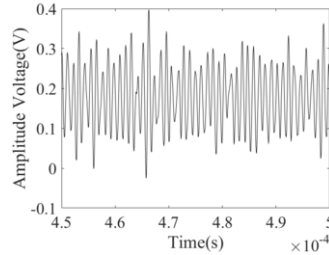
According to the above analysis and the fitting function, the echo signal frequency can be obtained if the received signal is demodulated. Compared with synchronous demodulation, asynchronous demodulation is easy to implement and can avoids the influence of the excitation frequency shift. The first step of the asynchronous demodulation is half-wave rectification, which can be expressed by Eq. (3).

$$S_1(t) = [S(t) + |S(t)|] / 2$$

(2)

The echo signal is demodulated from the received signal when the signal $S_1(t)$ filtered by the low-pass filter and the echo frequency can be obtained after the FFT is applied to the filtered echo signal. According to the relationship between frequency domain resolution and sampling time, the frequency domain resolution of the signal frequency spectrum is the inverse of the sampling time. The low-pass filtering process is omitted and the echo frequency is obtained by reading the peak spectral frequency in the low frequency spectrum after the FFT is applied to $S_1(t)$ directly.

3. Experiment results and discussions

3.1. Experiment setup and procedure

An EMAT experiment platform shown in Fig. 5 is built to study the fitting degree of the fitting function with the actual signal and to verify the correctness of the signal processing method. In the platform, the signal generator and power amplifier circuit generate an oscillating signal about 1MHz and lasts for about 3 cycles. The received signal generated in the probe flow into the preamplifier circuit for processing, and the oscilloscope is used to collect the received signal. The amplification of the signal conditioning circuit is 100db and the oscilloscope used in the experiment is Teledyne

3024 which has a sampling rate of 200MHz. To reduce the impact of noise, the received signal were averaged 128 time by the oscilloscope. All the steel plates used in the experiment are made of 16MnR, in which the propagation velocity of vertical shear wave is 3200 m/s. The thicknesses of the steel plates are 5.20 mm, 7.70 mm and 10.75 mm, and the lift-off between the steel plate and EMAT is 2 mm.
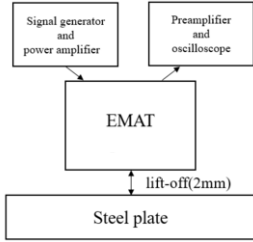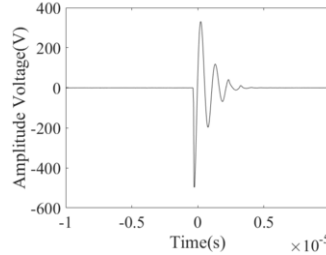

Figure 5. Experiment system diagram.

Figure 6. Exciting signal of the system.

To obtain the fitting degree of the fitting function and actual signal, an important step is to calculate the coefficients of the fitting function. The parameter A_0 and τ can be calculated through the positive half envelope, and fitting function can be obtained if the excitation frequency and the thickness of steel plate already known. In the experiment, using the signal of 7.70 mm steel plate as an example, and the fitting function can be expressed as the Eq. (4):

$$S(t) = 2.2467 \cdot e^{-5504.4286t} \cdot \sin(2\pi \cdot 10^6 \cdot t) \cdot \left| \sin(\pi \cdot 103896 \cdot t + \varphi) \right|$$

(3)

To verify the relationship between the excitation frequency and the echo frequency, the FFT is applied to the 7.70 mm steel plate directly. The frequency spectrum of the fitting function and actual testing signal are shown in Figures 7 and 8, respectively. It can be seen from the spectrum that the fitting function fits the actual signal have a similar frequency component. And as predicted, the echo frequency in the actual signal is modulated by the excitation frequency.
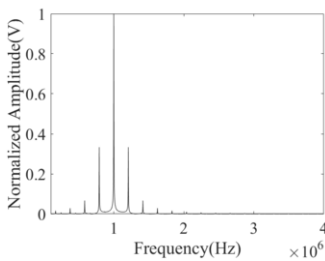

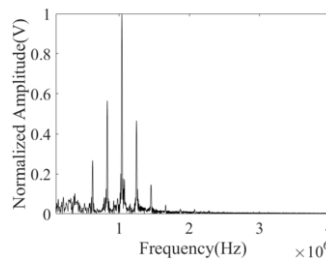**Figure 7.** The spectrum of 7.70 mm steel plate fitting function.

Figure 8. The spectrum of 7.70 mm steel plate testing signal

Obviously, asynchronous demodulation can be applied to obtain echo frequency. The first step of asynchronous demodulation is half-wave rectification, and the spectrums of the fitting function and the actual testing signal after half-wave rectification are obtain in the Figure 9 and Figure 10, respectively.

$$d_s = \frac{V_s}{2f_e}$$

(4)

Compared with the original spectrum, the echo frequency is separated from the excitation frequency in the low frequency band. From the peak spectral frequency (f_e) in the low frequency band, the thickness information can be obtained using the Eq. (5):
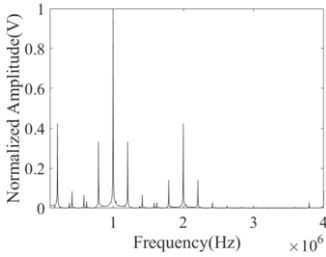

Figure 9. The spectrum of 7.70 mm steel plate fitting function after half-wave rectification
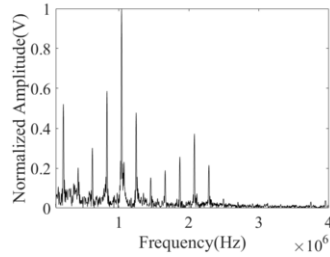

Figure 10. The spectrum of 7.70 mm steel plate actual testing signal after half-wave rectification

3.2. Results and Discussions

By comparing the spectrums of fitting function and actual signal, the correctness of the fitting function and the relationship between the excitation frequency and echo frequency have been verified. And asynchronous demodulation can be used to obtain the echo frequency in the low frequency band. The frequency band can be selected according to the measuring range.
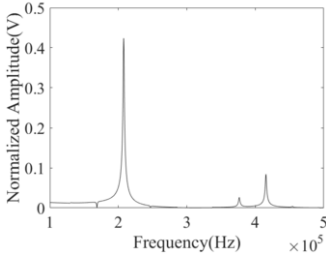

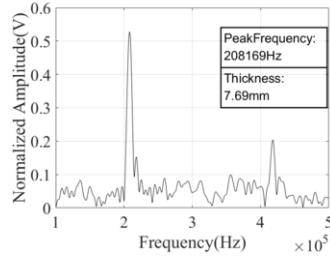**Figure 11.** The 100K~500KHz spectrum of 7.70mm steel plate transformed function

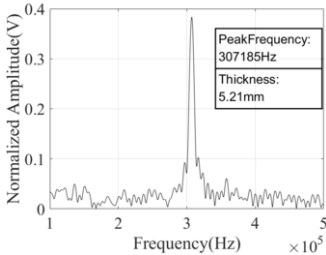**Figure 12.** The 100K~500KHz spectrum of 7.70mm steel plate transformed signal

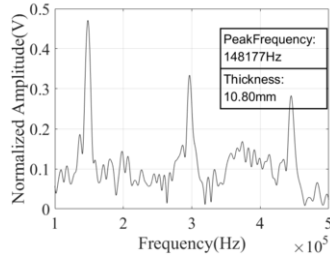**Figure 13.** The 100K~500KHz spectrum of 5.20 mm steel plate transformed function

Figure 14. The 100K~500KHz spectrum of 10.75 mm steel plate transformed function

In the experiment, the frequency band is selected at 100KHz to 500KHz and the measuring range is 3.20 mm to 16.00 mm. Following the processing steps, the thickness can be obtained and the results are shown in Figures 12 to 14. Table 1 show the calculated and actual thickness and the measuring error. In general, the noise coupling into the echo signal will not change the main frequency component of the signal. Compared with transit time measurement, frequency measurement is relatively insensitive to the noise. And the signal processing step is simple and easy to implement by only using hardware.

Table 1. Measurement results and measurement error

Actual thickness	Measured thickness	Absolute error	Relative error
7.70	7.69	0.01	0.1%
5.20	5.21	0.01	0.2%
10.75	10.80	0.05	0.5%

However, as can be seen in Figures 12 to 14, the thickness of the plate should not be too thick, the thicker the plate, the larger amplitude of other frequency component, which may cause mismeasurement.

4. Conclusion

A frequency domain signal processing method for steel plate thickness measurement using EMATs is proposed in this paper. In the first place, simplified waveform function is employed to express the relationship between the main component in the signal and then a signal processing method is proposed to obtain the echo frequency. Then experiment is carried out and results indicate that the simplification of the signal is reasonable. The experiment also verified that the relationship between the excitation frequency and echo frequency is that echo frequency is modulated by the excitation frequency. Most important, the signal processing method obtain a high accuracy in the experiment, and the maximum absolute error of the measured thickness in the frequency is 0.05mm, and the maximum relative error is 0.5%.

Acknowledgement

Reference

[1] Rueter D, Morgenstern TJU. Ultrasound generation with high power and coil only EMAT concepts. 2014;54(8).
[2] Cruz FC, Filho EFS, Albuquerque MCS, Silva IC, Gouvêa LLJU. Efficient Feature Selection for Neural Network Based Detection of Flaws in Steel Welded Joints Using Ultrasound Testing. 2016;73: 1-8.
[3] Hirao M, Ogi HJU. Electromagnetic acoustic resonance and materials characterization. 1997;35(6):413-21.
[4] Kubinyi M, Kreibich O, Neuzil J, Smid RJIToUF, Control F. EMAT noise suppression using information fusion in stationary wavelet packets. 2011;58(5): p.1027-36.
[5] Shankar PMJME. Grain Noise Suppression through Bandpass Filtering. 1988;46.

[6] Kim J, Udpa L, Udpa SJN, International E. Multi-stage adaptive noise cancellation for ultrasonic NDE. 2001;34(5):319-28.

[7] Si D, Gao B, Guo W, Yan Y, NDT YYJ, International E. Variational mode decomposition linked wavelet method for EMAT denoise with large lift-off effect. 2019;107: 102149.

[8] Dixon S, Edwards C, Palmer SBJU. High-accuracy non-contact ultrasonic thickness gauging of aluminium sheet using electromagnetic acoustic transducer. 2001;39(6):445-53.

Fast Localization of Impact Damage on Woven CFRP Based on Sparse Microwave Imaging

Ruslee Sutthaweekul [a,1] and Gui Yun Tian [b]

[a] *Department of Electrical and Computer Engineering, Faculty of Engineering, King Mongkut's University of Technology North Bangkok, Thailand, 10800*
[b] *School of Engineering, Newcastle University, Newcastle, UK, NE1 7RU*

Abstract. Microwave open-ended waveguide scanning has been proved to be a promising NDT technique for imaging of woven carbon fiber reinforced plastic (CFRP) with impact damages. However, it uses a conventional C-scan technique, which is excessively time-consuming and therefore it is not practical for defect detection in a large area. Moreover, without proper feature extraction, the appearance of woven texture within the impact damage area opposes to the localization of the impact. This work proposes a novel framework for fast impact damage localization by means of discrete sparse measurement. Also, the localization accuracy of sparse measurement is improved by mitigating effect of woven texture using principal component analysis (PCA) for feature extraction. The performance of the proposed methods is evaluated by sets of incremental measurements. The performance of the proposed system is and evaluated by localizing the impact damage of 100 non-uniform sparse sampling sequences. Results show that our proposed technique can accurately localize the impact damage with number of samples less than 10% of full measurements, giving approximately 10 times faster than that of the conventional C-scan.

Keywords. open-ended waveguide, CFRP, PCA, sparse measurement, impact damage, localization

1. Introduction

Woven carbon fiber reinforced plastic (CFRP) has been developed and widely used in advanced engineering structures such as aerospace, automobile, and sports equipment. It is due to the superiority in stiffness to weight ratio property. Though CFRP is easily damaged by impact and dropped tools even at very low impact energy [1]. Among electromagnetic NDT techniques for composites, microwave open-ended waveguide is one of the promising techniques for inspection of woven CFRP [2,3]. The ability of this technique has been demonstrated by reconstructing high resolution images of texture and impact damage on woven CFRP [4]. However, this technique requires a traditional full area scan (C-scan) in near-field, which is time consuming and not practical for defect detection in a large area (e.g., aircraft fuselage).

To overcome the challenge of time consuming, the technique of compressed sensing (CS) were introduced [5,6]. Works in [5], we applied a CS technique based on discrete

---

[1] Department of Electrical and Computer Engineering, Faculty of Engineering, King Mongkut's University of Technology North Bangkok, Thailand, 10800; E-mail: ruslee.s@eng.kmutnb.ac.th.

cosine transform (DCT). Results shows that the quality of the reconstructed images is acceptable with the sparse sampling rate of only less than 20% (approximately 5 time quicker than the full measurement). Despite that, the CS requires intensive computation power and therefore it may not suitable for real-time process. Yet, without a proper feature extraction technique, the presence of woven texture within the damage area diminishes detection and localization abilities of impact damage. So far, there no comprehensive research that investigated feature extraction from spectral responses of woven CFRP based on a forward model approach. It is due to the complex of woven CFRP, which involves the weaving structure of inhomogeneous materials with different properties. Alternatively, a statistical approach based on machine learning such as principal component analysis (PCA) has demonstrated ability in solving this type of challenges. In the microwave NDT study, an open-ended rectangular waveguide probe has been employed for characterization of steel corrosion in early stages [7]. The PCA was effectively applied for feature extraction of hidden progressive corrosions with the elimination of the coating layer influence.

In this paper, it is the first time that we investigate feature extraction of impact damage on woven CFRP based on PCA of wideband signal responses (18-26.5 GHz). A principal component exhibiting damage feature with least inference of woven texture will be selected for feature extraction of the impact damage. The performance of proposed PC based feature extraction will be demonstrated by sets of sparse measurement. The rest of this paper is organized as follows. Section 2 describes PCA for feature extraction, procedures for impact damage localization, CFRP sample and measurement setup. Section 3 shows and discusses the results of PCA feature extraction and its localization performance. Section 4 concludes the major findings and the potential future works are discussed.

2. Materials and Methods

The framework of fast localization of impact damage on woven CFRP based on sparse measurement is shown in Figure 1. Prior to the impact damage localization, an offline PC model has to be obtained through PCA. The detailed descriptions of each process are described in the following sub-sections.
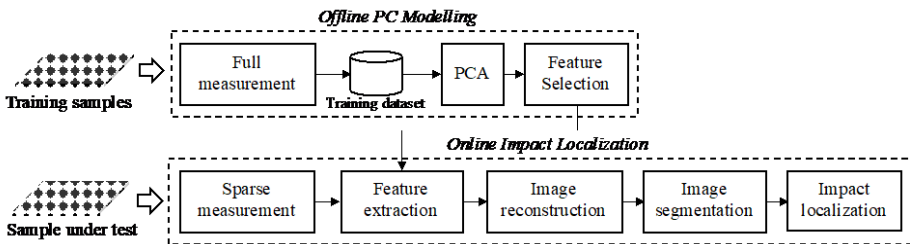

Figure 1. Block diagram for impact damage localization from sparse measurement

2.1. Obtaining a Principal Component Model for Impact Damage Feature Extraction

A principal component (PC) model for impact damage extraction has to be obtained using PCA. PCA has been widely used for feature extraction reducing data dimensions

and preserving prominent features [8,9]. The PCA process for feature extraction consists of two major steps: training and feature selection. In training, covariance matrices of training data sets are formed by subtraction of mean value from each of the data dimensions resulting in a dataset of zero means. The covariance matrix is decomposed to retrieve a matrix of eigenvectors e_i and eigenvalues λ_i. The eigenvectors ranked in descending order of coherent eigenvalues are called principal components (PCs). In feature selection, only high-rank PCs are considered for feature extraction. The projection results of each PC will be visually compared and the PC having the results most correlated to the interesting feature will be selected for feature extraction.

2.2. Fast Localization of Impact Damage

Sparse sampling data are obtained for estimation of the impact location. The processing for each sampling iteration is explained in a flowchart in Figure 2. Initially, the sampling data of four scanning corners are used to fill up the unknown area and form a feature image through Natural-neighbor interpolation technique [10,11]. After that, K-means clustering, with $K = 2$ [12], is used for binary image segmentation and obtains the impact damage area based on the pixel illuminations. Next, the centroid of the impact area is calculated and used to represent the impact center. If the current impact location does not converge to that of the previous iterations and there are more sampling locations, the whole process is repeated with a new sampling data from the next scanning location.
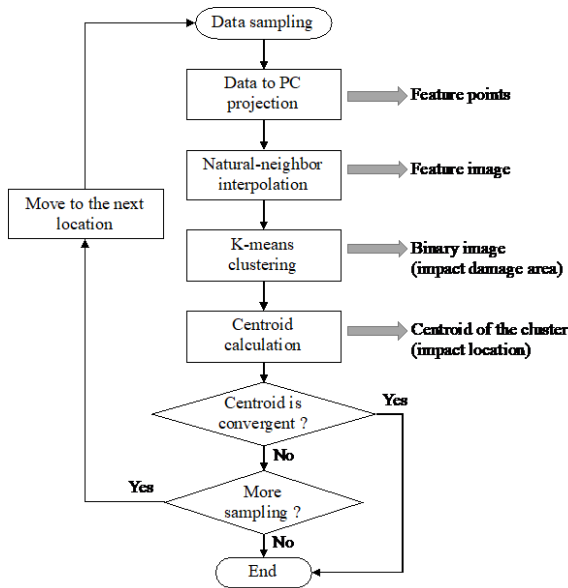

Figure 2. Flowchart of impact localization based on incremental sparse sampling

2.3. Samples and Measurement Setup

The impact damage on CFRP sample is produced by a drop test equipment with a hemispherical bumper head of 20 mm in diameter [4]. It is known that the common defects of low energy impact include surface dent, matrix crack, delamination and fiber

breakage [13]. We choose the 6J impact sample as the training sample because the damage area is large enough for statistical inputs in PC learning process.

The main equipment in the experiment consists of an X-Y scanner (High-Z S-720), a vector network analyzer or VNA (Agilent PNA E8363B) and an open-ended waveguide probe (WR-42). Before the experiment, the tools are calibrated and configured according to the measurement parameters given in Table 1. A computer is used to control the scanning route and store the data for further analysis.

Table 1. Measurement parameters for obtaining training dataset and localization experiments

Measurement Parameter	Value
Operating frequency	18.0 – 26.5 GHz
Number frequency points	1601 (Δf=3.5 MHz)
Probe	Open-ended rectangular waveguide probe No. WR-42
Scanning step size ($\triangle$x and $\triangle$y)	0.5 mm
Probe lift-off	1 mm
Delay between sample	1 second
Scan areas	50x50 mm^2 for training dataset and 30x60 mm^2 for localization experiments

3. Results and Discussions

3.1. Selection of Principal Component for Impact Damage Feature Extraction

A set of principal components are calculated as described in Section 2.1. Only the first six principal components (PC1-PC6) are chosen to be analyzed according to the sufficiency of the cumulative percentage of variance described in Table 2.

Table 2. Percentage and Cumulative Percentage of Variances of PC1-PC6

	PC1	PC2	PC3	PC4	PC5	PC6
Percentage of variance	44.66	23.03	16.46	9.59	3.14	1.67
Cumulative % variance	44.66	67.69	84.15	93.74	96.88	98.55

The reconstructed feature images based on the projection of PC1-PC6 to the training data of full measurement are displayed in Figure 3. Although damages are clearly recognized in both PC1 and PC6, it can be seen that the images from PC1 to PC5 are strongly affected by woven textures, while the PC6 represents an area of impact damage with the least background of woven texture. Hence in this case, only the PC6 is selected as an offline PC model for feature extraction of the impact damage.
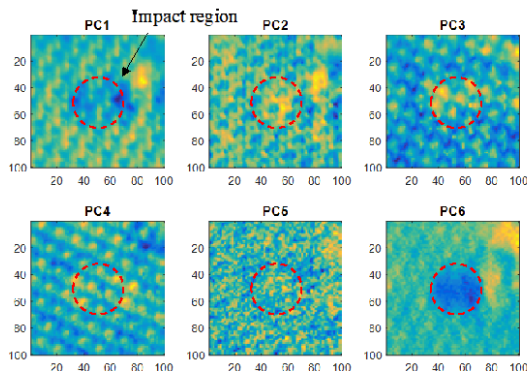

Figure 3. Principal component: PC1-PC6 projected feature images

3.2. Performance of Fast Impact Damage Localization

In each scanning sequence, the data are sampled and processed by the procedures described in Section 2.2. The number of sampling points is in the range from 4 to 720 samples in a sequence. The results of PCA feature is compared with the average magnitude (AM) feature, which is the common feature for microwave and millimeter wave imaging [6]. Figure 4 shows an example of processing results obtained by one scan (out of 100 scans). Only 4 steps (P=4, P=72, P=288, and P=720), with significant changes in the results, are selected to display. At P=4 (0.05% of full measurement): impact damage does not reveal in both AM and PCA feature images. At P=72 (0.98% of full measurement): a small area of impact damage is visible in both AM and PCA feature images. The PCA feature image shows a cleaner impact damage without the edge interference. As result, the calculated centroid of clustered AM is somewhere around the top edge of the sample, whereas the centroid of clustered PCA is confined within the impact area. At P=288 (3.90% of full measurement): The AM feature image shows fragmented impact area because of the presence of woven texture. The centroid of clustered AM is still distant to the actual impact location. The centroid of clustered PCA moves closer to the actual impact location. At P=720 (9.75% of full measurement): the centroid of AM feature moves closer to the actual impact location, whereas the centroid of the PCA feature is convergent as it is already at the location of the actual impact.

The performance of PCA and AM feature for impact damage localization is evaluated by a plot of average distance error over 100 sparse sampling sequences shown in Figure 5. It can be seen that PCA gives higher distance error at the beginning. However, the distance error of PCA goes below that of the AM after around 26 locations are sampled. Then, unlike the AM feature, PCA rapidly approaches zero error at around >720 samples or about 10% of the full measurement.

4. Conclusions

In this work, a novel technique of feature extraction for fast localization of impact damage on woven CFRP is proposed. Our major findings in this work can be summarized as follows.

- PCA demonstrates an ability to characterize impact damage on of woven CFRP with mitigation of the background woven texture.
- Compared to AM feature, the impact location determined from PCA feature is more stable during the progressive area scan.
- Centroid of segmented damage area gives better localization accuracy than the minimum value of feature image.
- The scanning time for the proposed impact damage localization can be shortened by 10 times compared to that of the conventional method.

This work is the first attempt of applying PCA for impact damages on CFRP and we focus only on using a single PC to represent an area of impact damage. With a single PC as a feature, the data dimensions are extensively reduced to a 2-D information, therefore, the types of damages such as matrix cracks or delamination, which may occur within the layers are all flatten and characterized as an impact damage. Hence, the recommended future works include an investigation of using multiple PC features technique that facilitates damage characterization of different types, depth localization of delamination and matrix crack, investigation of Kernel PCA to improve nonlinear classification.
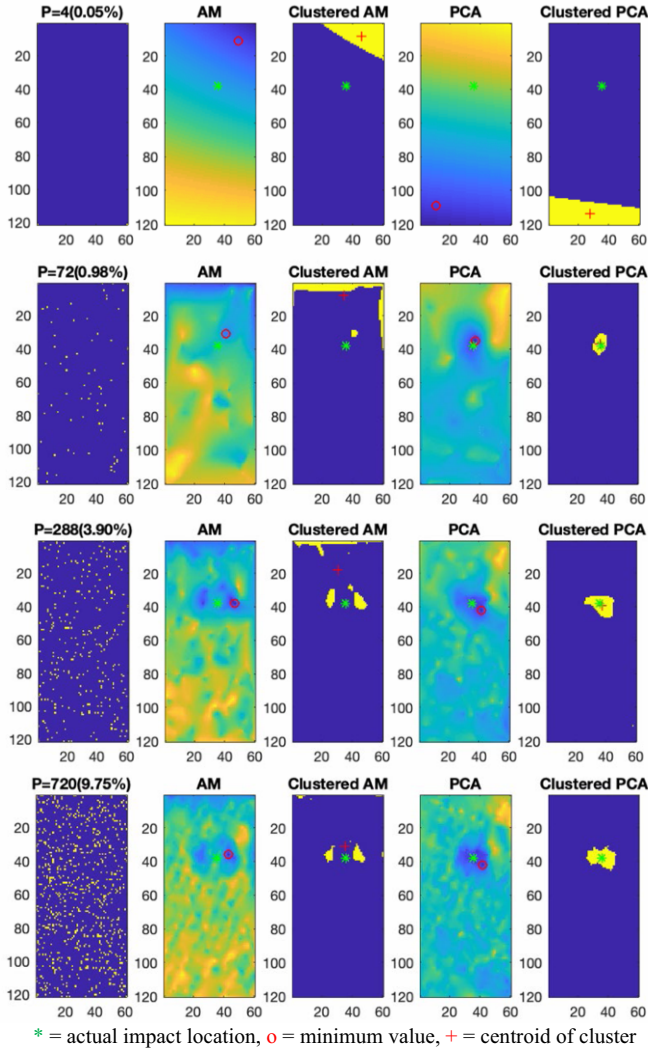
* = actual impact location, o = minimum value, + = centroid of cluster

Figure 4. Image reconstruction and locations of impact damage based on average magnitude (AM) and PCA feature with the number of sampling point P=4 (first row), 72, 288 and 720 (last row).
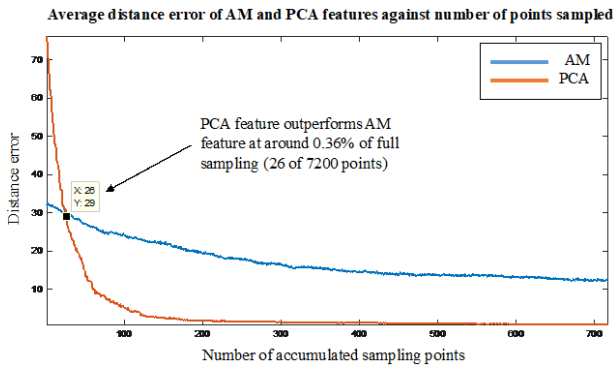

Figure 5. Average distance error of AM and PCA features

Acknowledgement

References

[1]   G. a. O. Davies, and R. Olsson, Impact on composite structures, *The Aeronautical Journal*. **108** (2004) 541–563. doi:10.1017/S0001924000000385.

[2]   R. Zoughi, J.R. Gallion, and M.T. Ghasr, Accurate Microwave Measurement of Coating Thickness on Carbon Composite Substrates, *IEEE Transactions on Instrumentation and Measurement*. **65** (2016) 951–953. doi:10.1109/TIM.2016.2526698.

[3]   R. Sutthaweekul, G. Tian, Z. Wang, and F. Ciampa, Microwave open-ended waveguide for detection and characterisation of FBHs in coated GFRP pipes, *Composite Structures*. **225** (2019) 111080. doi:10.1016/j.compstruct.2019.111080.

[4]   R. Sutthaweekul, G.Y. Tian, and M.D. Buhari, Detection of impact damage and fibre texture on CFRP using open-ended waveguide probe, in: 2016 13th International Conference on Electrical Engineering/Electronics, Computer, Telecommunications and Information Technology (ECTI-CON), 2016: pp. 1–6. doi:10.1109/ECTICon.2016.7561307.

[5]   C. Tang, G.Y. Tian, K. Li, R. Sutthaweekul, and J. Wu, Smart Compressed Sensing for Online Evaluation of CFRP Structure Integrity, *IEEE Transactions on Industrial Electronics*. **PP** (2017) 1–1. doi:10.1109/TIE.2017.2698406.

[6]   X. Yang, Y.R. Zheng, M.T. Ghasr, and K.M. Donnell, Microwave Imaging From Sparse Measurements for Near-Field Synthetic Aperture Radar, *IEEE Transactions on Instrumentation and Measurement*. **PP** (2017) 1–13. doi:10.1109/TIM.2017.2708379.

[7]   R. Sutthaweekul, and G.Y. Tian, Steel Corrosion Stages Characterization Using Open-Ended Rectangular Waveguide Probe, *IEEE Sensors Journal*. **18** (2018) 1054–1062. doi:10.1109/JSEN.2017.2775521.

[8]   A. Sophian, G.Y. Tian, D. Taylor, and J. Rudlin, A feature extraction technique based on principal component analysis for pulsed Eddy current NDT, *NDT & E International*. **36** (2003) 37–41. doi:10.1016/S0963-8695(02)00069-5.

[9]   L.I. Kuncheva, and W.J. Faithfull, PCA Feature Extraction for Change Detection in Multidimensional Unlabeled Data, *IEEE Transactions on Neural Networks and Learning Systems*. **25** (2014) 69–80. doi:10.1109/TNNLS.2013.2248094.

[10] H. Ledoux, and C. Gold, An Efficient Natural Neighbour Interpolation Algorithm for Geoscientific Modelling, in: P.F. Fisher (Ed.), Developments in Spatial Data Handling, Springer, Berlin, Heidelberg, 2005: pp. 97–108. doi:10.1007/3-540-26772-7_8.

[11] H. Ledoux, and C.M. Gold, Modelling three-dimensional geoscientific fields with the Voronoi diagram and its dual, *International Journal of Geographical Information Science*. **22** (2008) 547–574. doi:10.1080/13658810701517120.

[12] T. Celik, Unsupervised Change Detection in Satellite Images Using Principal Component Analysis and k-Means Clustering, *IEEE Geoscience and Remote Sensing Letters*. **6** (2009) 772–776. doi:10.1109/LGRS.2009.2025059.

[13] V. Lopresto, and G. Caprino, Damage Mechanisms and Energy Absorption in Composite Laminates Under Low Velocity Impact Loads, in: S. Abrate, B. Castanié, and Y.D.S. Rajapakse (Eds.), Dynamic Failure of Composite and Sandwich Structures, Springer Netherlands, 2013: pp. 209–289. doi:10.1007/978-94-007-5329-7_6.

Characterization and Imaging of Localized Thickness Loss in GFRP with *Ka*-Band Microwave Open-Ended Waveguides

Jinhua HU[a], Yong LI[a,1], Jianguo TAN[a], Wenjia LI[a] and Zhenmao CHEN[a]

[a]State Key Laboratory for Strength and Vibration of Mechanical Structures,
Shaanxi Engineering Research Centre of NDT and Structural Integrity Evaluation,
School of Aerospace Engineering, Xi'an Jiaotong University, Xi'an 710049, China

Abstract. Glass Fibre Reinforcement Plastic (GFRP) is widely used in engineering fields including aerospace, marine and construction, etc. During practical service, it is prone to the impact damage leading to the Localized Thickness Loss (LTL) which severely influences the integrity and safety of GFRP. To detect and evaluate LTL in GFRP, common Non-Destructive Testing (NDT) techniques such as ultrasonic testing and thermography are usually applied. Complementary to these methods, microwave NDT has been found to be one of the promising techniques in quantitative evaluation of GFRP. In this paper, the characterization and imaging of LTL in GFRP by microwave NDT are intensively investigated. A 2D Finite Element Model (FEM) with the *Ka*-band open-ended waveguide and GFRP sample subject to LTL has been set up and adopted for analysis of field characteristics and testing signals. Following that, an experimental investigation is conducted to further study the feasibility of LTL imaging by microwave NDT with the *Ka*-band open-ended waveguide. The results from simulations and experiments indicate the applicability of *Ka*-band microwave open-ended waveguide for detection and evaluation of LTL in GFRP.

Keywords. Microwave non-destructive testing, localized thickness loss, open-ended waveguide, finite element modelling, average magnitude

1. Introduction

In hash and severe environments, the in-service Glass Fibre Reinforcement Plastic (GFRP) is prone to exterior impact which essentially brings about Localized Thickness Loss (LTL), resulting in structural failure of GFRP [1]. In an effort to secure structural integrity and safety, various Non-destructive Testing (NDT) techniques in GFRP have been developed. However, each of them has drawbacks. Ultrasonic testing requires contact to the testing surface and the detecting range is limited due to the rapid ultrasonic attenuation caused by variation of composite properties [2]. Acoustic emission is costly and needs other NDT methods for re-inspection [3]. X-ray technique is expensive, time consuming and physically damaging [4]. Thermography is limited by insulation property and low thermal conductivity of GFRP composites [5].

Possessed with advantages such as non-contact, low attenuation in non-conductive materials, microwave NDT has been found to be one of the promising complementary to aforementioned NDT methods for evaluation of such dielectric materials as GFRP. Hosoi

---

[1] Corresponding Author, Yong Li, State Key Laboratory for Strength and Vibration of Mechanical Structures, Shaanxi Engineering Research Centre of NDT and Structural Integrity Evaluation, School of Aerospace Engineering, Xi'an Jiaotong University, Xi'an 710049, China; E-mail: yong.li@mail.xjtu.edu.cn.

et al. utilized focusing mirror sensor, detected the 100-μm-thick delamination in 3-mm-thick GFRP laminate [6]. Moreover, by measuring the variation in the amplitude of the microwave reflectivity, a 7.5-μm-thick film was detected in a 3-mm-thick GFRP laminate [7]. Ryu et al. successfully detected and revealed hidden multi-delamination in GFRP laminates using reflection method with THz-TDS imaging system [8]. Sutthaweekul et al. adopted principle component analysis and synthetic aperture radar tomography to evaluate the depth of flat-bottom holes in coated GFRP pipes [9].

Following the research of microwave NDT for GFRP evaluation, in this paper the feasibility of *Ka*-band microwave open-ended waveguide for characterization and detection of LTL in GFRP is investigated through simulations and experiments. A 2D Finite Element Model (FEM) is established to investigate the relations between the reflection parameters i.e., S_{11} and the LTL size. Meanwhile, experimental investigation with the *Ka*-band microwave open-ended waveguides is performed to explore the imaging of LTL in GFRP plates. An image processing algorithm based on the high-pass filtering and normalization is proposed to mitigate the influence of background noise and enhance the detectability of LTL in GFRP.

2. Numerical Simulations via FEM

For the transverse electric (*TE*$_{mn}$) wave in a microwave waveguide, the component of electric field in the direction of propagation vanishes. Further, for the transmission of the *TE*$_{10}$-mode microwave in rectangular waveguide, the electric-field component in the direction along the long side (*m*=1) of rectangular waveguide is zero, and the one along the short side (*n*=0) is independent of the coordinate in the corresponding direction [10]. Hence, the 3D model of microwave NDT is thus simplified into 2D.
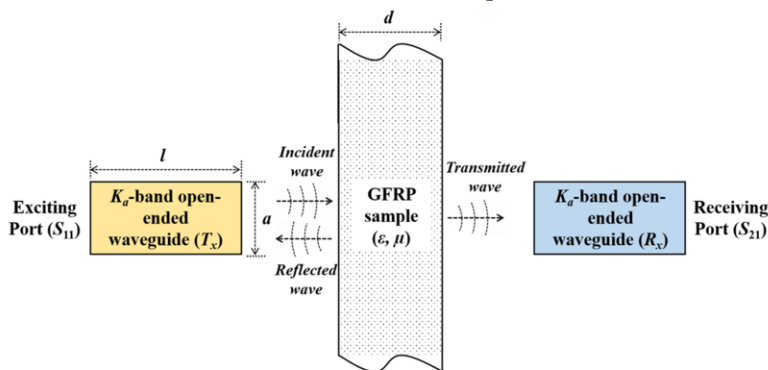

Figure 1. 2D model for inspection of a GFRP sample with *Ka*-band open-ended waveguides

The schematic of the 2D model is presented in Figure 1. Considering the aperture size (7.11mm×3.56mm) and length (*l*=214mm) of the waveguide, in the 2D FEM *a*=7.11mm. The thickness of the GFRP plate is 6mm. The parameters for LTL defects are set with the diameters (*D*) from 5mm to 13mm and depths (*d*) from 2mm to 6mm. The lift-off distance between the waveguide aperture and surface of the GFRP plate is 3mm. The excitation frequency of the waveguide is set as *Ka*-band (30GHz-40GHz). During simulations, the waveguide scans over the GFRP sample with the spatial interval of 0.3mm. At each scanning position, S_{11} against the excitation frequency is acquired. The Average Magnitude (AM) [9] of S_{11} in different scanning positions (X position) is obtained, which eventually gives the scanning curve of LTL. The simulated scanning

curves are shown in Figure 2. It can be observed from Figure 2 that: (1) S_{11} AM varies with the scanning positions, indicating the presence of LTL; and (2) the scanning curve changes with the LTL size. This implies that S_{11} AM could be applicable for LTL detection and quantitative evaluation of LTL size.
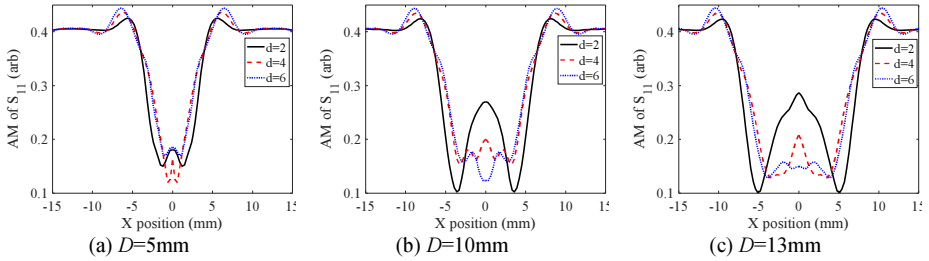

(a) *D*=5mm   (b) *D*=10mm   (c) *D*=13mm

Figure 2. Simulated scanning curves for different LTLs

From the scanning curves, the S_{11} AM at X=0 (corresponding to the LTL centre) is extracted and used for the measurement of LTL depth. The relationship between S_{11} AM and LTL depth is shown in Figure 3. It can be seen from Figure 3 that the S_{11} AM tends to monotonically decrease with the LTL depth. The reasoning could be due to the fact that larger LTL depth diminishes the equivalent relative permittivity [11] of the GFRP sample, which directly results in the decrease of microwave reflection from interfaces and thus the smaller magnitude of S_{11}. As for the evaluation of LTL diameter, the spatial span of minimum values of S_{11} AM in each curve is chosen as the signal feature to estimate the diameter for each LTL. The correlation relation between the spatial span and LTL diameter is presented in Figure 4. It can be seen from Figure 4 that the spatial span is directly proportional to the LTL diameter. Since the minimum S_{11} AM manifests at the edge of LTL due to the large microwave scattering at the LTL edge, as the diameter of LTL increases, the spatial span of minimum values of the scanning curve consequently rises, giving the increasing tendency.
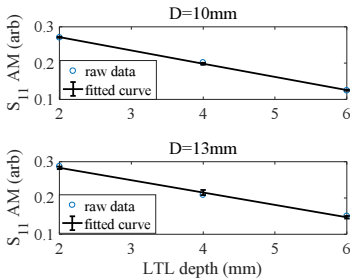
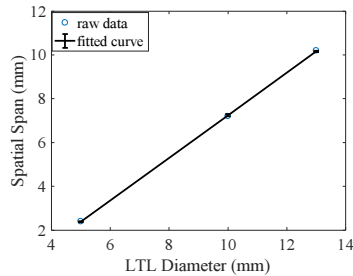

Figure 3. S_{11} AM *vs.* LTL depths

Figure 4. Spatial span *vs.* LTL diameters

3. Experimental investigation

In order to further investigate the feasibility of quantitatively evaluating LTL size by *Ka*-band microwave NDT, a microwave testing system has been set up. The system schematic is shown in Figure 5. The system consists of a Vector Network Analyser (VNA) for excitation of the incident wave and measurement of S_{11}, *Ka*-band open-ended waveguide for transmitting and receiving the *TE$_{10}$* mode electromagnetic wave, and scanning stage for the automatic 2D scanning of a GFRP sample with LTL in different sizes (*D*=5~13mm, *d*=2~6mm). The experimental parameters are listed in Table 1.

Table1. Experimental parameters

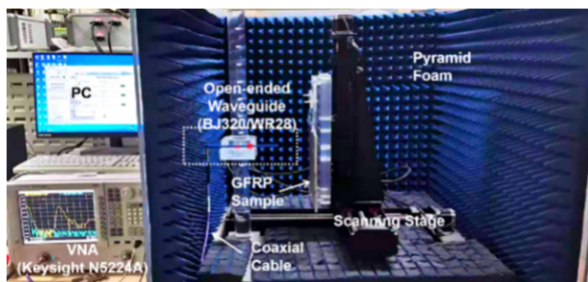|	
Waveguide aperture size	7.11mm×3.56mm
Scanning area	220mm×40mm (2D scanning)
Frequency range	30-40GHz (*Ka*-band)
Number of sampling frequency	201 (Δf=50MHz)
Lift-off	5mm
Scanning step sizes	Δx=Δy=1mm

Figure 5. Experimental set-up

3.1. LTL imaging results and processing

The 2D scanning of the waveguide over the sample is carried out along with acquisition of the S_{11} AM at every scanning position. Figure 6 shows the imaging results. The detected LTLs are 5mm, 10mm and 13mm in diameter in the three subgraphs from top to bottom, while the depths of LTLs in each subgraph are 2mm, 4mm and 6mm from left to right. It can be found from Figure 6 that all the LTL defects are successfully detected. However, the imaging results are severely influenced by the strong background noise which could be due to extraneous wave reflections in the testing region. This gives rise to much difficulty in LTL evaluation.
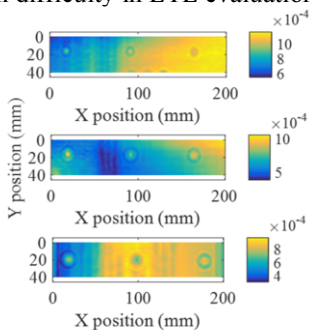

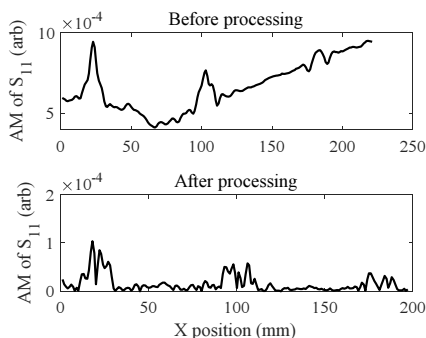**Figure 6.** Raw imaging results

Figure 7. Scanning curves along the centre of LTLs

Considering the fact that the background noise is mostly low-frequency, a processing algorithm based on the high-pass filtering together with normalization is proposed and utilized to mitigate the influence from the background noise. Normalization was conducted by obtaining the ratio between the S_{11} AM in each scanning position and the largest S_{11} AM of all the scanning areas. Figure 7 presents the comparison of the scanning curves along the centre of LTLs with and without processing. It is noticeable from Figure 7 that without processing, the background noise is rather strong. In contrast, after processing, S_{11} AM in flawless area is suppressed to a certain

extent, resulting in higher indication regarding the LTL presence. Figure 8 illustrates the processed LTL images. From Figure 8, it can be observed that the processed S_{11} AM changes with the LTL depth, the larger of the depth, the smaller of the S_{11} AM. The comparison between Figure 6 and Figure 8 indicates that the imaging processing method benefits the detection and sizing of LTL.
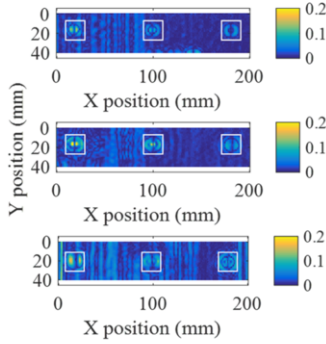

Figure 8. Processed imaging results

3.2. LTL characterization

After being detected via *Ka*-band microwave imaging, the LTLs are subsequently characterized by analysing the correlations between the image feature and LTL size. The sum of normalized S_{11} AMs i.e., $\Sigma S^{N}_{11}(AM)$ in a 20mm×20mm observation window (indicated by the square in Figure 8) whose centre coincides with the LTL centre is computed and taken as the image feature for analysis. Thereafter, for LTLs with the same diameter/depth, linear fitting method was adopted to explore the correlations of $\Sigma S^{N}_{11}(AM)$ with the depth/diameter of LTL. Figures 9 and 10 exhibit the results. It is noted that in calculating the maximum relative errors between experimental $\Sigma S^{N}_{11}(AM)$ and fitted ones are 14.07% (D=13mm) as LTL depth changes, and 16.83% (d=2) as LTL diameter changes, respectively.
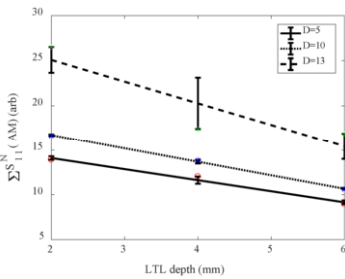

Figure 9 $\Sigma S^{N}_{11}(AM)$ *vs.* LTL depths   **Figure 10** $\Sigma S^{N}_{11}(AM)$ *vs.* LTL diameters
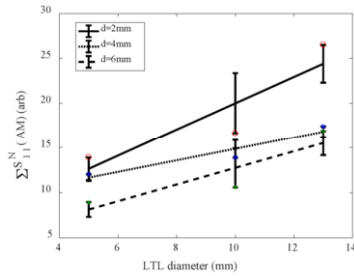
From Figures 9 and 10, it can be seen that $\Sigma S^{N}_{11}(AM)$ has a monotonic relation with the LTL depth/diameter. It decreases as the LTL depth enlarges. In contrast, when LTL diameter rises, $\Sigma S^{N}_{11}(AM)$ increases. This is supportive of the derived correlation from numerical simulations. As mentioned in Section 2, the larger of the depth, the smaller of the equivalent relative permittivity of the GFRP sample and the smaller of the S_{11}

magnitude. Meanwhile, the larger of the LTL diameter, the larger of $\Sigma S^N_{11}(AM)$ because of the broader interface (air and GFRP).

4. Conclusions

In the paper, the detection and characterization of LTL in GFRP plates via *Ka*-band microwave open-ended waveguide is intensively investigated through simulations experiments. It can be concluded from the results that: (1) with the *Ka*-band microwave open-ended waveguide, LTL in GFRP can be localized and evaluated; (2) the processing algorithm proposed based on the high-pass filtering and normalization is applicable for the background removal and LTL sizing; and (3) $\Sigma S^N_{11}(AM)$ has monotonic correlations with the LTL depth and diameter, which benefits the quantitative evaluation of LTL in GFRP. Following the current work, further study will involve: (1) investigation with small-sized/pitting LTL; and (2) detection and characterization of LTL in the back side of GFRP plates.

Acknowledgments

References

[1] Na WS. Possibility of detecting wall thickness loss using a PZT based structural health monitoring method for metal based pipeline facilities. *NDT & E International*. 2017 Jun;88:42-50.

[2] Castellano A, Fraddosio A, Piccioni MD. Quantitative analysis of QSI and LVI damage in GFRP unidirectional composite laminates by a new ultrasonic approach. *Composites Part B: Engineering*. 2018 Oct;151:106-117.

[3] Kumar PK, Kuppan P. Online monitoring of delamination mechanisms in drilling of Mwcnts reinforced Gfrp nanocomposites by acoustic emission. *Materials Today*: Proceedings. 2018;5(5):13036-13047.

[4] Humer K, Spieβberger S, Weber HW, Tschegg EK, Gerstenberg H. Low-temperature interlaminar shear strength of reactor irradiated glass-fibre-reinforced laminates. *Cryogenics*. 1996 Aug;36(8):611-617.

[5] Palumbo D, Cavallo P, Galietti U. An investigation of the stepped thermography technique for defects evaluation in GFRP materials. *NDT & E International*. 2019 Mar;102:254-263.

[6] Hosoi A, Yamaguchi Y, Ju Y, Sato Y. Detection of delamination in GFRP and CFRP by microwaves with focusing mirror sensor. *Material Science Forum*. 2013 Mar;750:142-146.

[7] Hosoi A, Yamaguchi Y, Ju Y, Sato Y, Kitayama T. Detection and quantitative evaluation of defects in glass fiber reinforced plastic laminates by microwaves. *Composite Structures*. 2015 Sep;128:134-144.

[8] Ryu CH, Park SH, Kim DH, Jhang KY, Kim HS. Nondestructive evaluation of hidden multi-delamination in a glass-fiber-reinforced plastic composite using terahertz spectroscopy. *Composite Structures*. 2016 Nov;156:338-347.

[9] Sutthaweekul R, Tian GY, Wang Z, Ciampa F. Microwave open-ended waveguide for detection and characterization of FBHs in coated GFRP pipes. *Composite Structures*. 2019 Oct;225, Article No. 111080.

[10] Ida N. Microwave NDT. London: Springer; 1992. p.75-77.

[11] Ghodgaonkar DK, Varadan VV, Varadan VK. Free-Space measurement of complex permittivity and complex permeability of magnetic materials at microwave frequencies. *Transactions on Instrumentation and Measurement*. 1990 Apr;39(2):387-394.

Multi-Channel IoT-Based Ensemble-Features Fault Diagnosis for Machine Condition Monitoring

Shang Gao[1], Cuicui Du

Nanjing University of Science and Technology, the school of mechanical engineer, 210094, Nanjing

Abstract. This paper proposes a multi-channel internet of things (IoT)-based industrial wireless sensor network (IWSN) with ensemble-features fault diagnosis for machine condition monitoring and fault diagnosis. In this paper, the rolling bearing is taken as an example of monitored industrial equipment due to its wide use in industrial processes. The rolling bearing vibration signals are measured for further processing and analysis. On-sensor node ensemble feature extraction and fault diagnosis using Back Propagation network are then investigated to address the tension between the higher system requirements of IWSNs and the resource-constrained characteristics of sensor nodes. A two-step classifier fusion approach using Dempster-Shafer theory is also explored to increase diagnosis result quality. Four rolling bearing operating in cage fracture, rolling ball spalling, inner ring spalling and outer ring spalling are monitored to evaluate the proposed system. The final fault diagnosis results using the proposed classifier fusion approach give a result certainty of at least **94.21%**, proving the feasibility of the proposed method to identify the bearing-fault patterns. This paper is conducted to provide new insights into how a high-accuracy IoT-based ensemble-features fault diagnosis algorithm is designed and further giving advisable reference to more IWSNs scenarios.

Keywords. IoT, wireless sensor networks (WSNs), fault diagnosis, BP network, Dempster-Shafer theory

1. Introduction

Machine fault diagnosis is becoming increasingly important to meet the higher demand of safety, reliablity and efficiency in many industrial areas. [1, 2]. As the key components of machinery, the rolling bearings have been widely applied in most industrial sectors, [3]. Due to artificial errors, material defects, and inadequate operations of the bearing, various incipient defects of rolling bearings may occur, and potentially lead to a series of unforeseen damages [4]. Hence, bearing-fault diagnosis is of paramount significance to improve the availability, increase the operating efficiency, and ensure the safe operation of the mechanical system [5].

Generally, bearing fault diagnosis depending on on-line monitoring vibration signal of critical devices includes three stages: signal processing, feature extraction,

---

[1] Shang Gao, Corresponding author, the school of mechanical engineer, Nanjing University of Science and Technology, E-mail: shang.gao@njust.edu.cn.

and classification recognition [6]. Currently, in many industrial fields, bearing fault diagnosis relies on the wired systems, which features as high reliability, but expensive maintenance cost, time-consuming [7]. Alternately, the wireless sensor networks (WSNs) have many inherent advantages including less weight, distributed operation, ease installation and relatively low-cost manufacturing, which make them as a promising approach for fault diagnosis [8]. As a new technology, the WSN has drawn more attentions in structural health monitoring (SHM) and NDT&E areas and numerous researchers have yielded some achievements [9-11]. Our previous work demonstrated a new multi-channel MEMS-based Low-Power Wide-Area Network (LPWAN) incorporating LoRa with NB-IoT for machine vibration monitoring [12]. Due to the constrained resources including limited computational ability, communication bandwidth and battery energy in WSN monitoring systems, the on-line feature extraction[13] and fault diagnosis is a promising approach to reduce the quantity of transmitted data, save energy and prolong node lifetime.

In WSN, the single sensor cannot capture more useful data for device fault diagnosis. In this case, the quality of IWSNs and the diagnosis uncertainty are impacted in noise and interference environment. However, if different sensors are adopted, the measurement accuracy of data fusion can be enhanced. Data fusion based on multiple sensors can effectively reduce the amount of data information which saves the resources and energy of the measuring data. The data fusion techniques such as the Bayesian method [14] and fuzzy data fusion [15] have been reported. As a new promising data fusion technique, the Dempster–Shafer theory does not require the knowledge of the prior probability and conditional probability relationships of data. This method based on wired sensor systems for fault diagnosis has been applied on induction motor [16], diesel engine cooling system [17], and railway track circuit [18]. The method has been proved as an efficient classifier fusion approach to increase diagnosis result quality[19].

In this paper, the following design strategies have been adopted to explore the applicability of data fusion for fault diagnosis in WSNs.

1) We propose a new IoT-based Ensemble-Features IWSN for machine fault diagnosis. A local-processing distinct ensemble -extraction algorithm in time-domain and frequency-domain is presented, which contributes to the low power consumption, low cost, and covering all the typical characteristics of vibration signals and current signals.

2) We also extends the previous WSN data fusion by applying Dempster–Shafer theory to for industrial condition monitoring and fault diagnosis.

The remainder of this paper is organized as follows. The system architecture and implementation methodology is briefly introduced in Section 2. The experimental evaluation of the proposed system is given in Section 3. Finally, Section 4 presents the overall conclusions.

2. System Architecture and Implementation

The rolling bearing condition fault diagnosis system with two-classifier data fusion is illustrated in Fig. 1. This IWSN consists of multi-channel sink node and multiple sensor nodes. Some sensor nodes measure the vibration on the head of the motor while other sensor nodes acquire the stator current signal. End node can achieve the signal conditioning, data acquisition, feature extraction (vibration and current

signal), while the multi-channel sink node makes data fusion decision and local fault classification. The diagnosis results are displayed on the centralized computer.
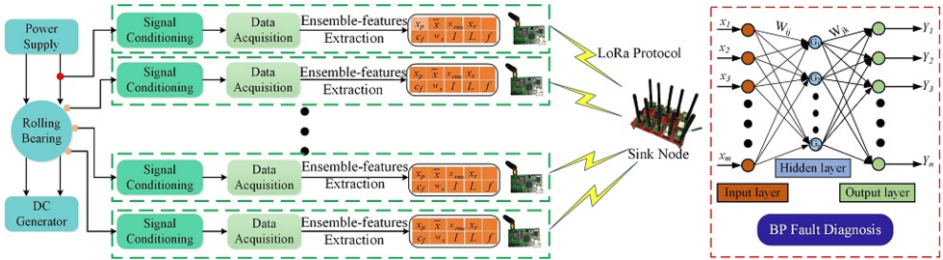

Fig.1 Schematic diagram of the proposed system

2.1. The LoRa-based Multi-Features Extraction Sensor Node (LMESN) and sink node

As is shown in Fig.1, the LMESN is mainly consisted of data acquisition unit, wireless communication unit, wireless unit, power module. The core of data acquisition unit is TI ADS8688AT chip having 16-bit resolution Analog-to-Digital Converter (ADC) and conversion rate of up to 100 kHz. With regard to the data sensing unit, the ADXL345 micro-electromechanical systems (MEMS) accelerometer with 12-bit resolution of measurement ranging from $\pm 2\,g$ to $\pm 16\,g$ and $3.9\,mg\,/\,LSB$ sensitivity is integrated into the LMESN. The collected data are sent to the local-processing feature extraction unit for performing the feature extraction of vibration signal. As for the wireless communication, a low-power RF chip Silicon SX1278 based on LoRa protocol, which can offer a theoretical maximum transfer speed of 500 $kbps$. The SX1278 in wireless unit is connected to STM32F407 processor through SPI ports for exchanging commands and transmitting wireless data. Our previous work has proposed a multi-channel sink node integrated multiple LoRa modules and NB-IoT modules for machine vibration monitoring[12].
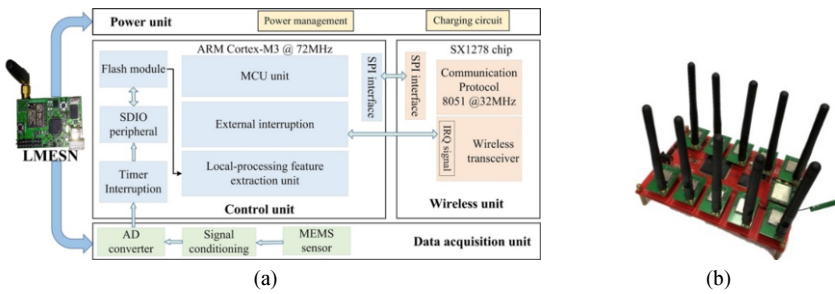

Figure 2. The architecture of (a)LMESN and (b)multi-channel sink node

2.2. Feature-extraction Design

As shown in Fig.3, the architecture of the rolling bearing is consisted of the rolling ball, cage, inner ring and outer ring. In this respect, D is the bearing pitch, d is the diameter of rolling ball and α is the angle between the forced direction of rolling ball and the inner and outer vertical lines. Four common faults of the rolling bearing are

F1="cage fracture," F2="rolling ball spalling," F3="inner ring spalling," and F4="outer ring spalling" respectively.
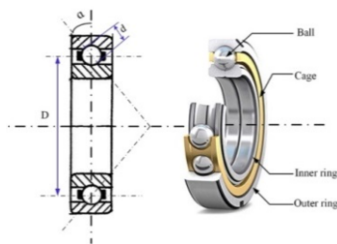

Figure 3. Structure of a rolling bearing

This sensor node extracts the time-domain data features for fault diagnosis from the raw digital data stream. The time-domain characteristic parameters mainly include dimensional parameters (mean value, peak value, root mean square value, square root amplitude) and non-dimensional parameters (tolerance index). Ten frequently occurring frequency components (20480 samples within one fast Fourier transform) were counted and selected as the fault features in the frequency domain. These fault features will be used to classify the healthy rolling bearing. The definition of these parameters is shown in Table 1.

Continuous amplitude monitoring of the stator current signal is used to identify motor load changes and find the abrupt change of load. In addition, periodic load torque changes with the rotational speed can affect the stator current signal spectrum and produce the current harmonics. In this paper, the load changes are tested by the modulation of a resistor connected to a generator used as a load, which is not a cyclic load variation, and do not give other current harmonics. As for the stator current signal, peak-to-peak amplitude and variance value in the time domain are selected as features for fault diagnosis. The selected fault features in this experiment are summarized in Table I.

Table 1. Dimensional and non-dimensional parameters of vibration and current signal

Signal		Time Domain	Frequency Domain
Vibration		Peak value $x_{pv} = max(|x_i|)$	(2,3) f_b, (5,6) f_b,
	Dimensional parameters	Mean value $\overline{x} = (\sum_{i=1}^{N} |x_i|) / N$	(7,9) f_b, (11,13) f_b, (15,17) f_b, (18,20) f_b,
		Root mean square value $x_{rms} = \sqrt{(\sum_{i=1}^{N} x_i^2) / N}$	(21,23) f_b, (26,62) f_b, (68,93) f_b, >93 f_b
		Square root amplitude $x_r = \left| (\sum_{i=1}^{N} \sqrt{|x_i|}) / N \right|^2$	
	Non-dimensional parameters	Kurtosis index $\beta = (\sum_{i=1}^{N} x_i^4) / N$	
Current	Dimensional parameters	Peak value $x_{pc} = max(|x_i|)$	n/a

* $\{x_i\}(i = 1 \sim N)$ is a series of discrete signals (N is data points), the frequency component is about 100Hz, twice of the line frequency. f_b is the resolution of FFT, $f_b = 5Hz$

2.3. Neural Network Classifier

In this paper, a BP neural network is used to achieve local fault classification. It includes several hidden layers and output layers corresponding to five rolling bearing working condition. The log-sigmoid function is selected as the hidden layer and output layer neuron activation function which is defined as:

$$\log sig(n) = \frac{1}{(1 + \exp(-n))} \tag{1}$$

The input vibration or current signals of the neural network are 16 fault features including 10 frequency features, and 6 time-domain features (x_1, x_2,..., x_{16}). In the classifier, the output range of the neural network classifier was (0, 1) which indicates the diagnosis probability. The training error of the neural network was set at 0.01which can be embedded in the local classifier on the sensor node for online primary fault diagnosis. The corresponding ideal output {1, 0, 0, 0, 0} of the neural network classifier if the motor is a healthy.

Dempster–Shafer theory assigns a belief mass to each element of the power set. Shown as (2), a basic belief assignment (BBA), called m in the following, is a function mapping from 2Θ to [0, 1], provided that the sum of all basic belief masses is equal to one and the mass of null set is zero:

$$m : 2^{\theta} \to [0,1] \text{ if } \sum_{A \subseteq \Theta} m(A) = 1 \quad \text{and} \quad m(\varnothing) = 0 . \tag{2}$$

According to (2), the sum of all basic belief masses is equal to one. Therefore, the outputs of neural network classifier $y(B_i)$ need to be normalized as follows:

$$m(B_i) = \frac{y(B_i)}{\sum_{i=1}^{4} y(B_i)} \tag{3}$$

where B_i, i = 1, 2, 3, 4, denotes the four previously described operating conditions of the rolling bearing. The results of the normalized $m(B_i)$ can be used for further decision level classifier fusion.

2.4. Decision Level Fusion

Data level fusion processes are often categorized as data level fusion, feature level fusion, or decision level fusion. Decision level fusion combines the primary recognition data from each sensor and makes an accurate decision. It utilizes the computing capability of individual low-level sensors and reduces the communication throughput. Therefore, in this paper, decision level fusion by Dempster–Shafer theory was selected to combine the outputs of the local neural network classifiers.

3. Experimental Verification

To evaluate the performance of the proposed bearing fault diagnosis method, a series of experiments are conducted. The experimental setup is shown in Fig.4. Four LMESNs nodes are installed on a Drivetrain Diagnostics Simulator (DDS) for implementing to acquire vibration signal of rolling bearing. Then, the processed

vibration signals are sent to the sink node.   Additionally, the sampling frequency of the system is configured to the value of 10.24 kHz, coupling with sampling length set to 20480. The rotating speed of the testing bearing is set to around 1310 r/min.
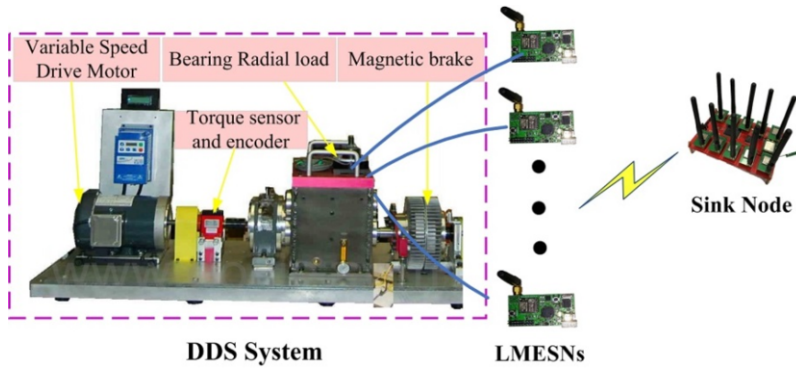

Fig.4 Wireless experimental test for rolling bearings based on DDS system

In this section, to investigate the influence of the number of hidden layer nodes, vibration parameters, current parameter on the fault classification accuracy, we make a detailed comparative analysis under vibration parameters(x_{pv} , $\bar{x}$, x_{rms} , x_r , β),the vibration and current parameters(x_{pv} , $\bar{x}$, x_{rms} , x_r , β and x_{pc}) and the time-frequency-domain parameters (x_{pv} , $\bar{x}$, x_{rms} , x_r , x_{pc} , β and f) respectively, as hidden layer nodes are set to 5, 6, 7, 8, 9, 10. As is shown in Fig. 5 (a), the average classification accuracies under the vibration parameters are below 70%, due to the indistinct differences between 5 vibration parameters for 5 bearing states. In contrast, it is seen from Fig.5 (b) that all average fault classification accuracies under the vibration and current parameters are above 75%. Due to the vibration parameter and current parameter are two types of parameters, so the fault classification accuracy indicates that the combination of vibration features and current parameter could better reflect the actual information of bearings.

As is shown in Fig.5(c), it is noted that the average fault classification accuracies under the combination of the vibration or current time-domain parameters and vibration frequency-domain parameter are nearly close to 95%, proving that this combination for fault classification accuracy outperforms the time-domain parameters or frequency-domain parameters. Additionally, we can see from the three figures that the classification accuracy can reach the highest level as the number of hidden layer nodes reaches 7. It's also worth mentioning from Fig.5 (c) that the classification accuracies of five bearing state degree recognition are achieved with 95.48% (Normal), 97.84% (F_1), 96.28% (F_2), 96.12% (F_3) and 94.21% (F_4), respectively. Nevertheless, it cannot continuously guarantee a high and stable accuracy rate when the number of hidden layer nodes exceeds 7. The reason is the few hidden layer nodes (P.5 and P.6) contributes to inadequate training, while the excessive hidden layer nodes (P.8, P.9 and P.10) result in too long learning time, larger training error and worse generalization ability. In conclusion, the hidden layer node P.7 is the optimal node for the proposed BPNN, which can reach the highest classification accuracies.

In short, the above comparison analysis results have proved that the selected 6 time-domain parameters and 10 frequency-domain parameters with representative ability of extracted features can provide a more reliable and stable fault classification

accuracy for bearings. In addition, the fault classification accuracies can attain the best performance as the hidden layer node of BPNN is 7.
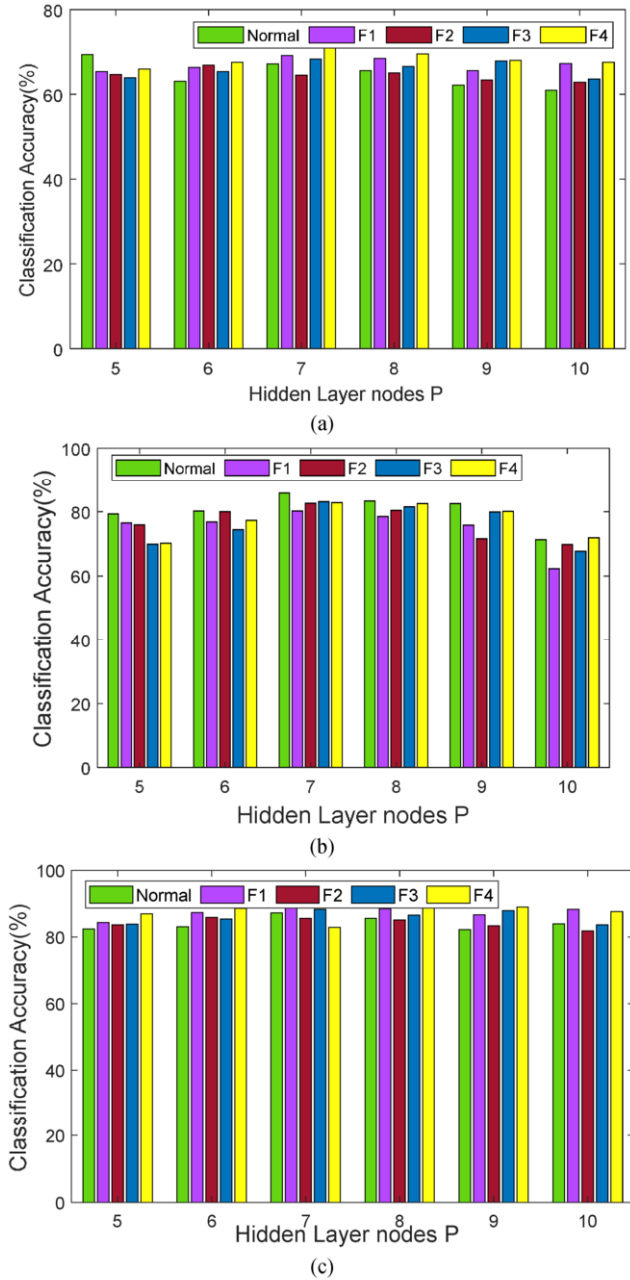

(a)

(b)

(c)

Fig.5. Average fault classification accuracies with different hidden layer nodes of BPNN under different parameters (a) under vibration parameters(x_{pv} , $\bar{x}$, x_{rms} , x_r , β); (b) under the vibration and current parameters (x_{pv} , $\bar{x}$, x_{rms} , x_r , β and x_{pc}); (c) under the time-frequency-domain parameters(x_{pv} , $\bar{x}$, x_{rms} , x_r , x_{pc} , β and f);

4. Conclusion and Discussion

In this paper, we proposed a local-processing ensemble-features fault diagnosis algorithm based on the BP neural network (BPNN) and Dempster–Shafer theory for machine condition monitoring is proposed in this paper. We actualize the LMESN for acquiring vibration and current signals of bearings. In addition, time-domain and frequency-domain vibration signals and time-domain parameters of current signals are extracted as the input vector of the designed BPNN. The feasibility and performance of the proposed method has been verified by a set of comparison experiments on a bearing. Furthermore, considering the key importance of the hidden layer nodes and different number of characteristics to the fault classification accuracy, we conduct many experiments with different hidden layer nodes under different number of characteristics and prove that the average classification accuracies of five bearing state degree recognition under vibration and current parameters reach the highest level as the hidden layer nodes of BPNN P is 7. The proposed strategy is expected to apply in SHM, NDT&E or other multi-sensor monitoring scenarios.

References

[1] R. N. Bell, D. W. McWilliams, P. O'Donnell, C. Singh, and S. J. Wells, "Report of large motor reliability survey of industrial and commercial installation, part I and part II," *IEEE Trans. Ind. Appl.*, vol. 21, no. 4, pp. 853–872, Jul. 1985.

[2] Z. Y. Jiang, Z. W. Li, N. Q. Wu, and M. C. Zhou, "A Petri Net Approach to Fault Diagnosis and Restoration for Power Transmission Systems to Avoid the Output Interruption of Substations," *IEEE Syst J.,* vol. 12, no. 3, pp. 2566-2576, 2018.

[3] Z. Gao, C. Cecati, and S. X. Ding, "A survey of fault diagnosis and fault-tolerant techniques—Part I: Fault diagnosis with model-based and signal-based approaches," *IEEE Trans. Ind. Electron.*, vol. 62, no. 3, pp. 3757–3767, Jun. 2015.

[4] Z. Gao, C. Cecati, and S. X. Ding, "A survey of fault diagnosis and fault-tolerant techniques—Part II: Fault diagnosis with knowledge-based and hybrid/active approaches," *IEEE Trans. Ind. Electron.*, vol. 62, no. 6, pp. 3768–3774, Jun. 2015

[5] Z. W. Wang, Q. H. Zhang, and J. B. Xiong, "Fault Diagnosis of a Rolling Bearing Using Wavelet Packet Denoising and Random Forests," *IEEE Sensors J.*, vol. 17, no. 17, pp.5581-5588, September, 2017.

[6] X. Xue and J. Zhou, "A hybrid fault diagnosis approach based on mixed-domain state features for rotating machinery," *ISA Trans.*, vol. 66, pp. 284–295, Jan. 2017.

[7] A. J. Torabi, M. J. Er, X. Li, B. S. Lim, and G. O. Peen, "Application of Clustering Methods for Online Tool Condition Monitoring and Fault Diagnosis in High-Speed Milling Processes," *IEEE Syst J.,* vol. 10, no. 2, pp. 721-732, 2016.

[8] Y. S. Zhang, Q.W. Gao, Y.X. Lu, D. Sun, Y. Xia, and X. M. Peng, "A Novel Intelligent Method for Bearing Fault Diagnosis Based on Hermitian Scale-Energy Spectrum," *IEEE Sensors J.,* vol.18, no.16, pp. 6743-6755, 2018.

[9] Y. Y. Peng, W. Qiao, L. Y. Qu, and J. Wang, "Sensor Fault Detection and Isolation for a Wireless Sensor Network-Based Remote Wind Turbine Condition Monitoring System," *IEEE TRANSACTIONS ON INDUSTRY APPLICATIONS*, vol. 54, no. 2, pp. 1072-1079, 2018.

[10] L. Hou, N. W. Bergmann, "Novel Industrial Wireless Sensor Networks for Machine Condition Monitoring and Fault Diagnosis," *IEEE Transactions on Instrumentation and Measurement*, vol. 61, no. 10, pp. 2787-2798, 2012.

[11] Lee H C , Chang Y C , Huang Y S, "A Reliable Wireless Sensor System for Monitoring Mechanical Wear-Out of Parts," *IEEE Transactions on Instrumentation and Measurement*, vol. 63, no.10, pp.2488-2497, 2014

[12] S. Gao, X. H. Zhang, C. C. Du, and Q. Ji, "A Multi-Channel Low-Power Wide-Area Network with High-Accuracy Synchronization Ability for Machine Vibration Monitoring," *IEEE INTERNET OF THINGS*, 2019 (Early Access) Available Online: DOI: 10.1109/JIOT.2019.2895158

[13] R. D. Jesus, and R. Troncoso, "Multirate Signal Processing to Improve FFT-Based Analysis for Detecting Faults in Induction Motors," *IEEE Transactions on Industrial Informatics*, vol.13, no. 3, pp. 1291-1300, 2017.

[14] Kia, S.H., Henao, H., Capolino, G.A.: 'Diagnosis of broken-bar fault in induction machines using discrete wavelet transform without slip estimation', *IEEE Trans. Ind. Appl.*, vol. 45, no. 4, pp. 1395-1404, 2009.

[15] S. Mohanty, K. Gupta, K. S. Raju, "Adaptive fault identification of bearing using empirical mode decomposition–principal component analysis-based average kurtosis technique," IET Science, Measurement & Technology, vol. 11, no. 1, pp. 30-40, 2017.

[16] Sandeep S. Udmale, and Sanjay Kumar Singh, "Application of Spectral Kurtosis and Improved Extreme Learning Machine for Bearing Fault Classification", *IEEE TRANSACTIONS ON INSTRUMENTATION AND MEASUREMENT.*, pp. 1-12, 2019. (Early Access)

[17] Q. Fu, B. Jing, P. He, S. Si, and Y. Wang, "Fault feature selection and diagnosis of rolling bearings based on eemd and optimized Elman_AdaBoost algorithm," *IEEE Sensors J.*, vol. 18, no. 12, pp. 5024–5034, Jun. 2018.

[18] He, D., Li, R., Zhu, J., Zada, M.: 'Data mining based full ceramic bearing fault diagnostic system using AE sensors', *IEEE Trans. Neural Netw.*, vol. 22, no. 12, pp. 2202-2031, 2011.

[19] Hou L, Bergmann N W. Novel Industrial Wireless Sensor Networks for Machine Condition Monitoring and Fault Diagnosis[J]. IEEE Transactions on Instrumentation & Measurement, vol. 10, no. 61, pp.2787-2798, 2012.

Application of Compressed Sensing in NB-IoT-Based Structural Health Monitoring of Rail Tracks

Xin Li[a], Yan Yan[b,1], Pan Hu[a], Qing Zhang[a], Haitao Wang[a], Chao Wang[c], Yifan Chen[d], Guiyun Tian[b]

[a] *College of Automation Engineering, Nanjing University of Aeronautics and Astronautics, Nanjing, China*

[b] *School of Automation Engineering, University of Electronic Science and Technology of China, Chengdu, China*

[c] *School of Electronic Science and Engineering, University of Electronic Science and Technology of China, Chao Wang*

[d] *School of Life Science and Technology, University of Electronic Science and Technology of China, Yifan Chen*

Abstract. Ultrasonic guided-wave testing is one of the most widely used technology for Structural Health Monitoring (SHM) of rail tracks. Currently, cable is the main tool of signal transmission for guided wave-based track monitoring systems. The installation of cables can significantly increase the system cost and restrict the flexibility of system deployment. In recent years, the NB-IoT technology has been gradually applied to the field of SHM, it offers long-range wireless communication among a large-scale sensor networks at the cost of minimum construction and maintenance. One primary obstacle hindering the integration of NB-IoT and guided wave-based track monitoring system is that the limited channel bandwidth of NB-IoT leads to significant transmission delay when transmitting the ultrasonic guided-wave signal sampled at Nyquist rate. In this paper, a Compressed Sensing (CS) framework for NB-IoT based rail-track monitoring system is proposed. The proposed CS framework utilizes the sparsity feature of the ultrasonic lamb-wave signal to enable sub-Nyquist sampling and maintain the feature of the measured signal at a low compression rate. To validate the proposed CS framework, the propagation time of lamb-wave is selected as the performance metrics. The experimental results show that compared with the traditional sampling method, the propagation time of lamb wave in rail track can be accurately extracted when the sampling rate is set to 100kHz, therefore, the channel bandwidth of NB-IoT can meet the delay-free data transmission of a single ultrasonic sensor.

Keywords. NB-IoT, compressed sensing, structural health monitoring, rail-track inspection

1. Introduction

The structural integrity of rail tracks has always been paid an extra attention by railway operators. When the track operates under high load for a long time, cracks are easy to appear at the rail tracks. Ultrasonic guided-wave testing has been widely used for Structural Health Monitoring (SHM) of rail tracks [1~2] mainly due to its ability to inspect a long-range of continuously welded rail tracks from a single transducer location[3]. Currently, the cable is the main tool of signal transmission for guided wave-based rail track monitoring systems. The installation of cables can significantly increase the system cost and restrict the flexibility of system deployment. In recent

Corresponding Author, Yan Yan; Email: yan.y@uestc.edu.cn

years, the NB-IoT technology has been gradually applied to the field of SHM, it offers long-range wireless communication among a large-scale sensor networks at the cost of minimum construction and maintenance. For example, Hu et al[4]. applied ZigBee technology to guide wave monitoring of rail. The integration of IoT and the ultrasonic guided-wave testing is expected to provide a promising solution for efficient, fast, and low-cost ultrasonic monitoring system [5]. Because Lamb Wave can detect both internal damage and surface damage, it is often used as an ultrasonic guided wave for structural damage detection. The frequency of the Lamb-wave signal generally ranges from 60kHz to 200 kHz [6]. To minimize the signal distortion, combining the Nyquist sampling theorem[7] with engineering practice, the sampling frequency is usually set to ten times of the frequency of lamb-wave signal. Many wireless standards can be used in IoT scenarios, such as WiFi, Bluetooth, GSM, etc. Among these standards, the NB-IoT plays a leading role by providing long-distance and robust communication to large-scaled, small, low-cost, and battery-powered sensors. Compared to WiFi, Bluetooth, NB-IoT provides a longer communication distance. Compared to GSM, it allows the sensor to achieve the same communication distance while consuming less power. Therefore, NB-IoT is considered as a promising wireless technology for the application of structural health monitoring [8~9]. However, the channel bandwidth of NB-IoT is significantly limited, which ranges from 160 Kbps to 250 Kbps [10], leading to significant transmission delay when transmitting the ultrasonic guided-wave signal sampled at Nyquist rate [11].

In recent years, a novel signal acquisition and compression theory named Compressed Sensing (CS) has been widely used in the application scenarios that require data compression. Unlike conventional data compression methods, CS allow the signal to be sampled at a sub-Nyquist rate, thereby reducing the amount of data to be transmitted, and then reconstructing the compressively sampled signal into a complete raw signal. Yuequan Bao et al. [12] used the acceleration data collected by the SHM system of the Yellow River Road Bridge in Binzhou, Shandong to study the data compression capability of CS. T Di Ianni et al. [13] studied the recovery of guided wave fields of aluminum plates and composite plates under different sparse substrates, and determined that sparse substrates were an important factor affecting the CS reconstruction performance. Yong Huang et al. [14] proposed a Bayesian Compressive Sensing(BCS) algorithm suitable for civil structural health monitoring (SHM) system, which can achieve perfect lossless compression performance at a high compression ratio. Jayawardhana M. et al. [15] studied SHM data acquisition based on CS, especially the application of CS in damage detection and location.

This paper proposes a CS framework for NB-IoT based rail-track monitoring system is proposed. The proposed CS framework utilizes the sparsity feature of the ultrasonic lamb-wave signal to enable sub-Nyquist sampling and maintain the feature of the measured signal at a low compression rate. The proposed CS framework is validated by a set of experiments for measuring the lamb-wave propagation time in a rail-track specimen. Corresponding results show that the minimum compression rate that can maintain the characteristic quantity of lamb wave propagation time is obtained. that under the condition of no loss of lamb wave signal characteristics, the compressed sensing algorithm based on wavelet sparse basis can reduce the sampling frequency of lamb wave signal in the ultrasonic structural health monitoring system for rail-tracks to 10% of the traditional sampling frequency, satisfying the communication requirements of NB-IoT. The remainder of this article is organized as follows: In section 2, the CS theory in the lamb wave monitoring system is briefly introduced, and how to select a

sparse basis to maintain the eigenvalue of lamb and the workflow of CS technology are described. In the third part, a verification test is designed to verify the proposed CS framework, the fourth part evaluates the performance of the proposed CS framework under different compression rates and discusses the minimum compression rate that can maintain the characteristic quantity of lamb. Finally, conclusion and future work are given.

2. Compressed sensing for lamb monitoring system

2.1. Basic Principle of Compressed Sensing

The core idea of CS is that the original signal can be linearly measured by the measurement matrix during signal acquisition and a small number of measurements can be recorded. The nonlinear algorithm is used to recover the exact approximation of the original signal from a small number of measured value [16].

An important premise of compressed sensing is that the signal can be represented by the linear combination of a set of non-zero elements in certain sparse basis. Suppose the expression of signal x(n) on the sparse basis Φ is:

$$\mathbf{x}=\varphi \times \alpha \text{ , or } \mathbf{x}=\sum_{i=1}^{N} \varphi_i \times \alpha_i \tag{1}$$

There are k non-zero elements in $\boldsymbol{\alpha}$, k $\ll$ N, then signal x (N) is k sparse on a sparse basis Φ. Formula (1) is called sparse representation, that is, in a sparse domain, only K elements are useful, and other elements will not affect the original signal even if they are discarded. The sparsity of a time-domain signal could be found by performing some orthonormal transformation [17].

The essence of compression is to project the signal X from the high dimensional space of N × 1 to the low dimensional space of M × 1 through the matrix ϕ independent of φ and obtain the linear measurement value y of M × 1 to realize the signal compression sampling. Its mathematical process can be described as follows:

$$y=\phi \times x \tag{2}$$

By substituting formula (1) into formula (2), we can get:

$$y=\phi \times \varphi \times \alpha = \Theta \times \alpha \tag{3}$$

Where, ϕ is an M×N matrix, called the measurement matrix, and $\Theta = \phi \times \varphi$ is an M×N matrix, called the observation matrix. Signal reconstruction means that y is known to invert x through formula (3). Due to the sparsity of X, namely M$\ll$ N, which ensures that formula (3) has a solution, but also that formula (3) has an infinite number of solutions. There are many methods to find the optimal solution in formula (3), and

this paper adopted Orthogonal Matching Pursuit (OMP) to reconstruct the lamb signals in ultrasonic guided wave-based structural health monitoring system for rail-tracks.

2.2. Investigation of Sparse Representation of Lamb-wave Signal

The sparsity of a signal in a sparse domain is the prerequisite for signal compression sampling. Signal sparsity also affects the accuracy of signal reconstruction. In general, the better the sparsity of the signal under a sparse basis, the higher the accuracy of the reconstructed signal after compression[18~19].
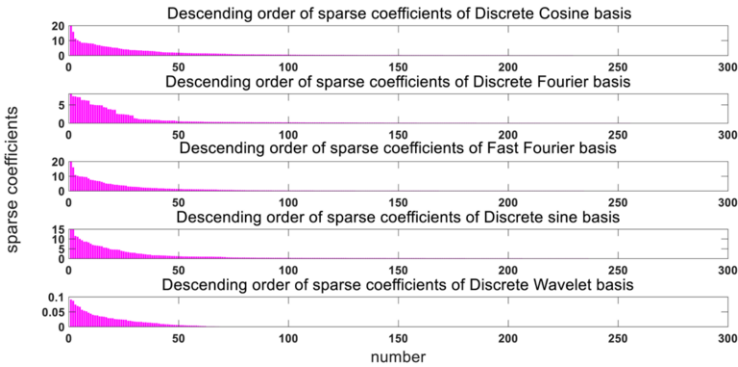
Figure 1. The sparse distribution of lamb signal in different sparse domains

To minimize the compression ratio, we investigate the sparse representation of the lamb-wave signal using various widely used sparse transform basis, which including Discrete Fourier Transform (DFT), Discrete Wavelet Transform (DWT), Discrete Cosine Transform (DCT), and Fast Fourier Transform (FFT), Discrete Sine Transform (DST). As shown in Figure 1, the sparse coefficients of lamb wave signals in the sparse domain such as DCT, DFT, DST, FFT, and DWT are compared. The sparsity coefficients refer to a set of non-zero elements of the signal in the sparse domain, it represents the sparseness of the signal. For a sparse transform basis, the fewer the non-zero element can be used to represent the signal, the higher the sparseness and the higher accuracy of the reconstructed signal[19]. As can be seen from Figure 1, in the sparse domain such as DCT, DFT, DST and FFT, the number of sparse coefficients of lamb signal is greater than 140, and the number of sparse coefficients is the highest in the DST sparse domain. However, in the wavelet sparse domain, the number of sparse coefficients of lamb signal is 60, and its sparsity is the best. The better the signal sparsity, the less the characteristic loss of reconstructed signal. In the ultrasonic rail structure health monitoring system, the flight time of a0 and s0 modal lamb waves is often used as an important characteristic quantity of structural damage[2]. In order to verify the above theory, the flight time of a0 and s0 modal lamb waves of reconstructed signals and original signals under different sparse bases is compared based on the peak time of the wave. The comparison results are shown in Table 1, in which the flight time of a0 and s0 modal lamb waves of reconstructed signals under wavelet sparse basis has the minimum error with the original signal.

Table 1. Preservation of feature quantities of lamb under different sparse basis

Sparse matrix	Peak arrival time of Lamb s0 wave(us)	the peak arrival time (us) of the Lamb s0 wave extracted from reconstructed signals	Peak arrival time of Lamb a0 wave(us)	the peak arrival time (us) of the Lamb a0 wave extracted from reconstructed signals
dwt	88.9	88.8	113.3	113.3
dft	88.9	88.6	113.3	113.3
dct	88.9	94.2	113.3	114.2
dst	88.9	89.2	113.3	112.8
fft	88.9	88.5	113.3	113.2

3. Experimental set-up and Performance Evaluation

3.1. Experimental set-up

The peak arrival times of a0 and s0 modes of lamb-wave is often used as the characteristic quantity of damage detection in lamb wave monitoring. To evaluate the effect of the CS framework on lamb wave characteristics, a series of experiments were carried out. The raw signal is collected by the UT monitoring system shown in Figure 2 (a). Excitation and receiving sensors are shown in Figure 2 (b). The system consists of an excitation signal source, excitation piezoelectric sensor, receiving piezoelectric sensor, conditioning circuit, and oscilloscope responsible for signal acquisition. The specific experimental parameters are shown in Table 2. This system is aimed at the half - moon crack at bottom of the rail[20], and the size of target damage is tens mm order[21].

(a)   (b)
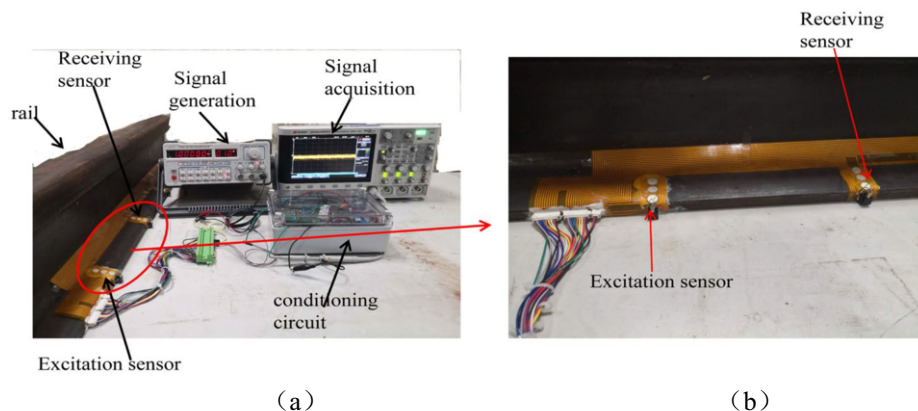
Figure 2. Lamb monitoring system for rail-track

Table 2. Experimental parameters

Monitoring Distance	Frequency of lamb-wave signal	Conditioning circuit amplification factor	Sampling Frequency
200 mm	140KHz	300	1MHz

3.2. The workflow of CS in ultrasonic guided wave-based structural monitoring system for rail-tracks

As shown in Figure 3, the frame diagram of compressed sensing technology is proposed for this paper. In this framework, for lamb signals in ultrasonic-based structural health monitoring system for rail-tracks, the sparse coefficient of lamb signals in the wavelet sparse domain is obtained by using the wavelet sparse bases selected in Section 2.2. Then, Gaussian random matrix is adopted as the measurement matrix and the OMP algorithm is adopted to solve the signal reconstruction problem.
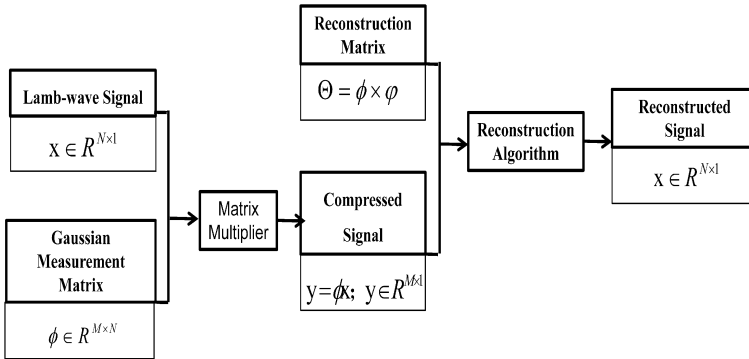
Figure 3. The workflow of CS in UT monitoring system for rail-tracks

3.3. Performance Evaluation

In the experiment, the raw signal sampled at 1MHz contains 2000 individual values, When the compression ratio was 0.3, 600 samples were measured for 2000 samples When comparing the raw signal and the compressive measured signal, it can be seen clearly that the peak arrival time of the two signals is almost the same, which means that the characteristic quantity of the original signal is maintained accurately in the recovered signal. Figure 4 depicts the raw signal sampled at 1MHz, sparse domain, reconstructed signal, and compressive measured signal, respectively.

According to CS theory, according to the compression ratio theory, although low compression ratio is conducive to the collection and storage of data in the ultrasonic testing system of the Internet of Things, it is not conducive to the maintenance of lamb feature quantity. Figure 5 shows the evaluation of the reconstruction accuracy of the above CS framework under different sampling scores. It includes an absolute error, root mean square error, signal to noise ratio (dB), and peak signal to noise ratio (dB). The experimental results show that when the sampling fraction is greater than 0.1, the proposed CS framework achieves better reconstruction performance and remains within a relatively stable range.
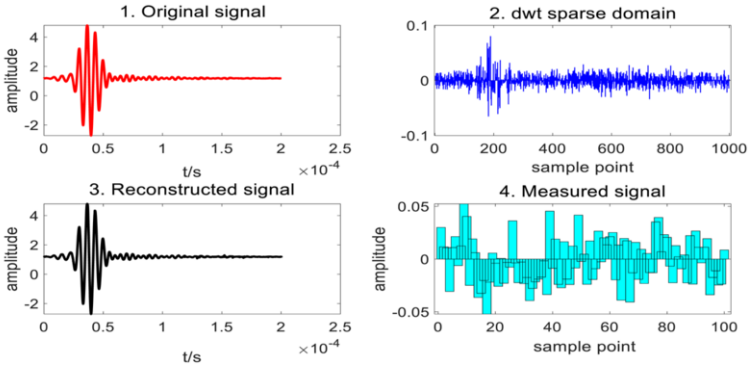
Figure 4. Performance of CS framework
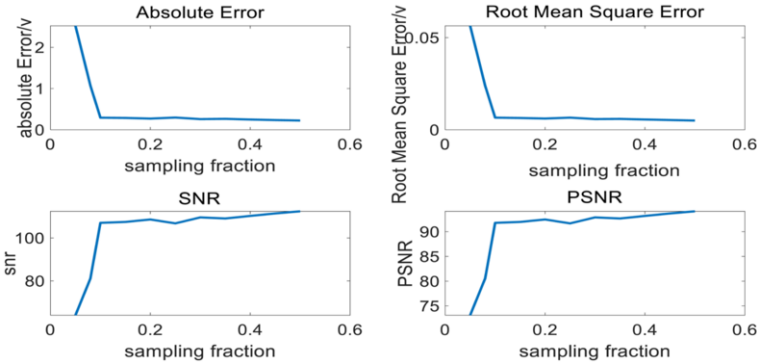
Figure 5. Performance Comparison of the CS method under different compression ratio

As described in Section 2.2, the flight time of the a0 and s0 lamb waves is an important feature of the rail-based ultrasonic structural health monitoring system. This section discusses the lower bound of compression rate of CS algorithm based on wavelet sparse basis when the lamb feature loss is the smallest in ultrasonic structure health monitoring system for rail tracks. Figure 6 shows the original signal and the reconstructed signal when the compression ratios are set to 0.3, 0.1, 0.08, and 0.05 respectively. Table 3 shows the peak arrival time of a0 mode and s0 mode of the original signal and the compression reconstruction signal under different compression rates. As shown in Table 3, when compression ratio > 0.1, the reconstructed signal retains the basic characteristics of the original lamb signal when compression ratio < 0.1, the reconstructed signal cannot maintain the basic characteristics of the original lamb signal, resulting in a large error. Therefore, when the lamb signal in the rail is compressed, the compression rate should not be lower than 0.1. When the compression rate is set to 0.1, the corresponding sampling rate is 100kHz. The bandwidth of NB-IoT can be expressed as:

$$W = D \times F \times N \tag{4}$$

Where W refers to the bandwidth in bits per second, D stands for the sampling resolution (bits/sample), F represents the sampling frequency (sample/second), and N denotes the number of channels. Since the bandwidth of NB-IoT is 250 Kbps, and D≥1,

it can be deduced that the upper bound of sampling frequency is 250kHz per channel. Given that the minimum sampling frequency is 100kHz when applying the proposed CS framework, therefore, the data generated by a single transducer can be transmitted using NB-IoT without delay.
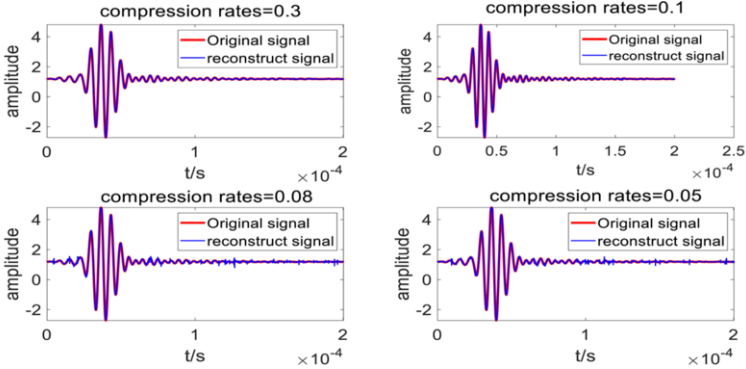
Figure 6. Original signal and reconstructed signal at different compression rates

Table 3. Peak arrival time of original signal and reconstructed signal under different compression rates

Compress rate	Peak arrival time of Lamb s0 wave (us)	Peak arrival time of the Lamb s0 wave (us) extracted from reconstructed signals	Peak arrival time of Lamb a0 wave (us)	Peak arrival time (us) of the Lamb a0 wave extracted from reconstructed signals
0.3	88.9	88.8	113.3	113.3
0.1	88.9	88.8	113.3	114.2
0.08	88.9	88.2	113.3	116.5
0.05	88.9	92.9	113.3	117.1

4. Conclusion and future works

This paper provides a theoretical and experimental basis for realizing the integration of NB-IoT and ultrasonic guided wave-based structure health monitoring system for rail tracks. The experimental results show that under the condition of no loss of lamb wave signal characteristics, the compressed sensing algorithm based on wavelet sparse basis can reduce the sampling frequency of lamb wave signal in the ultrasonic structural health monitoring system for rail-tracks to 10% of the traditional sampling frequency, satisfying the communication requirements of NB-IoT.

In future stage, on the one hand, it is necessary to further verify the influence of the compressed sensing framework proposed in this paper on the characteristics of lamb wave reflected by the damage; on the other hand, sparse dictionary with optimal sparsity estimation can be developed to further reduce the minimum sampling frequency, and a more efficient measurement matrix and reconstruction algorithm should be designed to achieve a lower compression rate on the premise of maintaining the signal characteristics of reconstructed lamb signal.

5. Acknowledgement

Reference

[1] D. Barke, W.K. Chiu, Structural health monitoring in the railway industry: a review, *Structural Health Monitoring* **4** (2005), 81-93.

[2] J.L. Rose, M.J. Avioli, P. Mudge, et al. Guided wave inspection potential of defects in rail, *Ndt & E International* **37** (2004), 153-161.

[3] P.W. Loveday, C.S. Long, Influence of resonant transducer variations on long range guided wave monitoring of rail track, *AIP Conference Proceedings. AIP Publishing LLC* **1706** (2016), 150004.

[4] P. Hu, et al. Wireless localization of spalling in switch-rails with guided waves based on a time–frequency method, *IEEE Sensors Journal* **23** (2019), 11050-11062.

[5] A. Ahmed, Y. Kumar, Internet of things (IoT) platform for structure health monitoring, *Wireless Communications and Mobile Computing* **2017** (2017), 1-10.

[6] B.C. Lee, W.J. Staszewski, Modelling of lamb waves for damage detection in metallic structures: Part I. Wave propagation, *Smart Materials and Structures* **12** (2003), 804.

[7] Wikipedia. 2020. "Nyquist-Shannon sampling theorem" Last modified July 17 2020. https://en.wikipedia.org/wiki/Nyquist-Shannon sampling theorem

[8] Y. Yan, et al. A study on data loss compensation of WiFi-based wireless sensor networks for structural health monitoring, *IEEE Sensors Journal* **16** (2015), 3811-3818.

[9] C. Hemalatha, M.V. Rajkumar, M. Gayathri. IOT based building monitoring system using GSM technique, *IOSR-Journal of Electronics and Communication Engineering* **12** (2017), 68-75.

[10] R. Ratasuk, B. Vejlgaard, N. Mangalvedhe, et al. NB-IoT system for M2M communication, *2016 IEEE Wireless Communications and Networking Conference* (2016), 1-5.

[11] A. Perelli, T. Di Ianni, A. Marzani, et al. Model-based compressive sensing for damage localization in lamb wave inspection, *IEEE Transactions on Ultrasonics Ferroelectrics and Frequency Control* **60** (2013), 2089-2097.

[12] Y. Bao, J.L. Beck, H. Li. Compressive sampling for accelerometer signals in structural health monitoring, *Structural Health Monitoring* **10** (2011), 235-246.

[13] T. Di Ianni, L. De Marchi, A. Perelli, et al. Compressive sensing of full wave field data for structural health monitoring applications, *IEEE Transactions on Ultrasonics Ferroelectrics and Frequency Control* **62** (2015), 1373-1383.

[14] Y. Huang, J.L. Beck, S. Wu, et al. Robust bayesian compressive sensing for signals in structural health monitoring, *Computer-Aided Civil and Infrastructure Engineering* **29** (2014), 160-179.

[15] M. Jayawardhana, X. Zhu, R. Liyanapathirana, et al. Compressive sensing for efficient health monitoring and effective damage detection of structures, *Mechanical Systems and Signal Processing* **84** (2017), 414-430.

[16] D.L. Donoho, Compressed sensing, *IEEE Transactions on Information theory* **52** (2006), 1289-1306

[17] M. Rani, S.B. Dhok, R.B. Deshmukh, A systematic review of compressive sensing: Concepts, implementations and applications, *IEEE Access* **6** (2018), 4875-4894.

[18] I. rović, V. Papić, C. Ioana, et al. Compressive sensing in signal processing: algorithms and transform domain formulations, *Mathematical Problems in Engineering* (2016), 1-16.

[19] Z. Zhang, Y. Xu, J. Yang, et al. A survey of sparse representation: algorithms and applications, *IEEE Access* **3** (2015), 490-530.

[20] D.F. Cannon, K.O. Edel, S.L. Grassie, et al. Rail defects: an overview, *Fatigue & Fracture of Engineering Materials & Structures* **26** (2003), 865-886.

[21] C. Ramadas, M. Janardhan Padiyar, K. Balasubramaniam et al. Delamination size detection using time of flight of anti-symmetric (A0) and mode converted A0 mode of guided Lamb waves, *Journal of Intelligent Material Systems and Structures* **21** (2010), 817-825.

This page intentionally left blank

Artificial Intelligence in ENDE

This page intentionally left blank

245

Data Augmentation and Artificial Neural Networks for Eddy Currents Testing

Romain CORMERAIS [a,b,c], Roberto LONGO [a,b], Aroune DUCLOS [b],
Guillaume WASSELYNCK [c] and Gérard BERTHIAU [c]

[a] *Groupe Signal Image et Instrumentation, ESEO, Angers, France*
[b] *Laboratoire d'Acoustique de l'Université du Mans, Le Mans, France*
[c] *Institut de Recherche en Énergie Électrique de Nantes Atlantique, Saint-Nazaire, France*

Abstract. Eddy Currents (ECs) Non Destructive Testing (NDT) is widely used to determine the position and size of flaws in metal materials. Due to difficulties in estimating these parameters via inverse algorithms based on physical models, approaches focused on Artificial Neural Network (ANN) are nowadays of great interest. The main drawbacks of these techniques still reside in the complexity of the numerical models and the large number of simulated data needed to train and test the ANN, leading to a considerable amount of calculation time and resources. To overcome these limitations, this article proposes a new approach based on a data augmentation procedure via Principal Component Analysis (PCA) applied to numerical simulations.

Keywords. Eddy Currents Testing, Machine Learning, Artificial Neural Networks, Data Augmentation, Principal component analysis

1. Introduction

The goal of Non Destructive Testing (NDT) is to determine the position and size of structural flaws, in order to measure the quality and evaluate the safety of materials [1]. Various techniques, presenting different advantages and drawbacks, are used in NDT, including Ultrasonic Testing (UT), Eddy Currents (ECs), radiography, penetrating testing and thermography [2, 3]. Generally NDT make use of ECs to test metal materials [4–6], but these methods are limited to surface or sub-surface flaws because of the so called "skin effect". Other techniques based on UT are instead affected by the presence of "blind zones" in the ultrasonic beam, which could impair the detection of flaws too close to the surface of the material under test, if not specific coupling is used (i.e. wedges). Hence, this article represents a first step for a combined use of ECs and UT, with the ultimate goal to exploit the complementary between these two approaches. The present work focuses on the ECs part, while the combination with UT is still object of current study.

More in detail, ECs are generated by an electromagnetic field induced into the material under test. Variations on the coil impedance are eventually monitored to detect and characterize defects [7]. Physical models describing ECs can be quite complex, and estimations of flaw parameters like length and depth is not always possible [8]. As alternative, many approaches rely on Machine Learning (ML) methods, employing Artificial

Neural Networks (ANNs) [9–19], as they can perform any function if enough training data are provided [20–22], without requiring a physical model. Moreover, due to the flexibility of these algorithms, ANNs represent an interesting candidate for future integration with UT data. Because building an exhaustive experimental data-set can be difficult, numerical simulations are often used to obtain a training data-set. Among the different possible ways to build a simulated data-set, Finite Element Method (FEM) have been employed here. In detail, the ECs signals, expressed by the coil complex impedance, are derived following the electric vector potential and magnetic scalar potential $T-\Omega$ formulation [23]. This approach, detailed in Section 2.1, focuses on ECs propagation through Aluminum blocks with a large variety of Side Drill Holes (SDHs). Unlikely, the entire procedure needs a significant amount of calculation time and resources.

To overcome this limitation, this article presents a new approach based on data augmentation algorithms via Principal Component Analysis (PCA). The aim is to reduce the number of simulated flaws needed to build the ANN training data-set, significantly reducing computing time and resources. The PCA factorization, presented in Section 2.2, aims to concentrate useful information in a small data-set [24]. The data augmentation procedure based on 3D interpolations over the Principal Components (PCs) is also presented in Section 2.2. The collected original and augmented data-sets are employed to train an ANN whose architecture is presented in Section 2.3. Results are reported in Section 3, showing that data augmentation allows to reduce the simulated training data-set without deteriorating the ANN estimations.

2. Method

2.1. Eddy Currents Simulations in Presence of Side Drill Holes

In this paragraph, the FEM $\vec{T}-\Omega$ formulation [23] is used to obtain signals from homogeneous Aluminum blocks containing SDH. The electrical conductivity and magnetic permeability are respectively set to $\sigma = 37.7$ MS.m^{-1} and $\mu_r = 1$. This formulation allows to compute the induced currents $\vec{J}$, the electric field $\vec{E}$, the magnetic induction $\vec{B}$ and the magnetic field $\vec{H}$. The resistance and reactance of the simulated inductor are respectively calculated through the active and reactive dissipated power, referring to Eq. (1) and Eq. (2). Eventually, the impedance variation of the probe due to the presence of the flaw is calculated. The dimensions of different cylindrical flaws vary with a radius from 0.6 to 8 mm and depth from 0.1 to 4 mm (see **Figure 1**), building a data-set of 3000 different cases. The simulated ECs probe is composed by a 2.25 mm height coil with inner and outer radius of 2.22 and 2.48 mm, driven by a sinusoidal signal at 1 kHz. Air gap is set to 0.18 mm. The probe response is recorded every millimeter along the inspection direction. Examples of simulated signals interacting with SDH from 1 to 5 mm radius at 1 mm depth are depicted in **Figure 2**. A workstation equipped with Intel I7 Processors, NVIDIA Quadro P3000 Graphic Computing Units (GPUs) and 16 Go of RAM has been employed to build the data-set, requiring a calculation time of approximately 2000 hours.

$$RI_{source}^2 = \int_{D_c} \vec{E} \cdot \vec{J} dD_c = \int_{D_c} \sigma^{-1} \vec{J} \cdot \vec{J} dD_c, \tag{1}$$

$$XI_{source}^2 = \int_D \frac{\partial \vec{B}}{\partial t} \cdot \vec{H} dD = w \int_D \mu^{-1} \vec{B} \cdot \vec{B} dD. \tag{2}$$
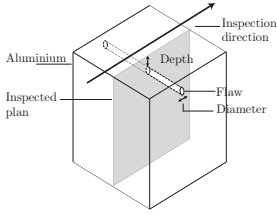
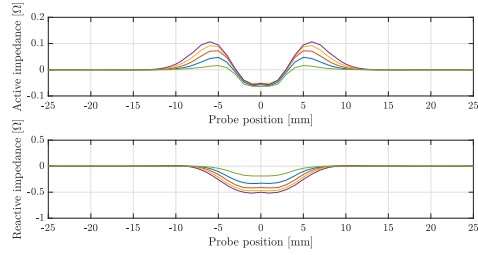**Figure 1.** Example of simulated Aluminum block containing a Side Drill Hole (SDH).

Figure 2. Examples of resistance and reactance obtained simulating five Side Drill Holes (SDHs), with radius from 1 to 5 mm at depth of 1 mm.

2.2. Data Augmentation Based on Principal Component Analysis

This section shows the data augmentation procedure used to process the previous simulated signals. As mentioned in the Introduction, this method is based on Principal Component Analysis (PCA) factorization. In detail, PCA is a statistical method that uses an orthogonal transformation to translate potentially correlated observations into linearly uncorrelated variables called PCs. This transformation is defined in a way that the first PCs present the largest possible variance, and each succeeding component in turn has the highest variance possible in the orthogonal basis [24]. As example, **Figure 3** depicts the radius (top graph) and depth (bottom graph) evolution in function of the two PCs. From this representation, a data augmentation algorithm is developed in order to create additional artificial data at given depth and radius. To start the process, a user-defined depth is selected among the simulated ones. Afterwards, the first PC for a new augmented data point at the desired radius and selected depth is computed with cubic one dimensional interpolation [25]. This interpolation is conducted over the first PCs of the simulated radius at the selected depth. Subsequently, the second PC of the new augmented data point is calculated through linear two dimensional interpolation between the two PCs of the simulated radius at the selected depth and the already interpolated first PC belonging to the new point. Following this procedure, the amount of data composing the augmented data-set can be multiplied by a user-defined factor. As example, **Figure 4** shows the new data-set augmented by a factor of five.

2.3. Artificial Neural Network Architecture and Performance Evaluation

Artificial Neural Networks (ANNs) are proposed in this article to estimate radius and depths from ECs signals, offering an alternative to inverse problems procedures based on physical models. Generally speaking, an ANN is composed by basic interconnected computing units trained to perform a given function. An example is given in **Figure 5**, which shows an ANN composed by N_E inputs, an hidden layer of N neurons and N_S outputs. Each neuron returns the inputs weighted sum $S_v(k)$ or $S_w(k)$, according to the predefined activation functions f_v or f_w, as indicated in Eq. (3). Weights v_{ij} and w_{ij}, firstly randomly initialized, are calculated by minizing an error function defined as the difference between the network outputs S_W and the desired ones T. To do so, a strategy based on error back-propagation has been implemented through the Levenberg-Marquardt algorithm [20, 21, 26]. Eventually, the ANN performance is calculated in function of the
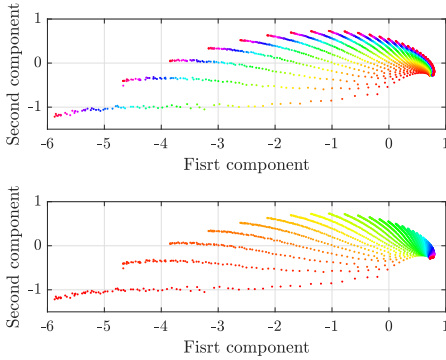
Figure 3. Simulated flaws radius (top graph) and depths (bottom graph) represented in function of the two Principal Components (PCs).
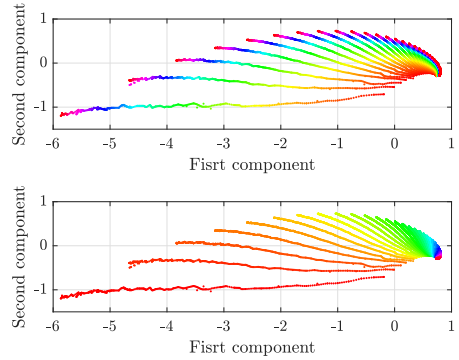
Figure 4. Augmented data for flaws radius (top graph) and depths (bottom graph) represented in function of the two Principal Components (PCs).

Mean Squared Error (MSE) between estimated and real SDHs parameters, following a 10-fold cross validation approach. For that purpose, the simulated data-set has been split into ten groups evenly distributed through the SDHs parameters space, with validation samples evenly distributed inside each training data-set.

In the present study, the ANN is composed by two inputs corresponding to the two first PCs extracted from the simulated signals, as the cumulative sum of eigenvalues shows that they cover 99% of the PCA space information. This choice also reduce the number of weights composing the ANN, and consequently the number of training samples necessary for the optimization process. The ANN inputs are connected to an hidden layer of 20 neurons. This value has been set empirically. The final layer is composed by two outputs neurons leading to radius and depth estimations. The ANN inner and output activation functions, respectively f_v and f_w, are reported in Eq. (4), in order to form a universal function estimator [20, 22].

Eventually, each training data-set of the 10-fold cross validation is progressively decimated until a factor of five in order to evaluate the proposed data augmentation procedure. For each decimation factor, a first ANN is trained with the decimated training data-set and a second one with augmented data. For both, the corresponding test data did not change. As last step, the MSE is monitored in function of the decimation factor. The main results are reported in the next section.

$$\mathbf{S_v}(k) = f_v \left(\sum_{n=1}^{N_E} v_{nk} \times \mathbf{E}(n) \right) \quad \text{and} \quad \mathbf{S_w}(k) = f_w \left(\sum_{m=1}^{N} w_{mk} \times \mathbf{S_v}(m) \right), \qquad (3)$$

$$f_v(x) = \frac{2}{1+e^{-2x}} - 1 \quad \text{and} \quad f_w(x) = ax + b. \qquad (4)$$
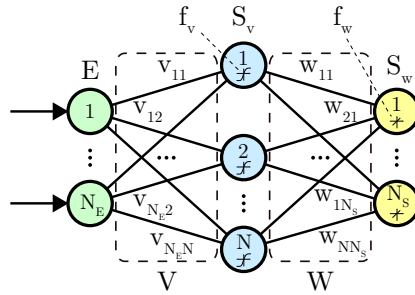
Figure 5. Scheme of an ANN composed by N_E inputs, an hidden layer of N neurons and N_S outputs.

3. Results and Discussion

This section presents the different radius and depth estimations obtained using the proposed data augmentation procedure presented in Section 2.2 applied to the ANNs. In detail, the simulated training data-set is decimated by a factor varying from two to five. Radius and depth estimations accuracy is monitored over the test data-sets through 10-fold cross validation while each training data-set is progressively decimated, as shown in **Figure 6**. The ANN error evolution using the augmented data-set, where decimated data are replaced by augmented ones, is reported in **Figure 7**. Using the decimated data-set, for a decimation factor of five an average error of 50% is recorded over the fifty training. This high error value was expected as the ANN has been trained with a reduced data-set and tested on the original test data. The best performance was reached at the error of 7.5% (see **Figure 6**). Always referring to a decimation factor of five, using the augmented data-set an average error of 3% and minimum error of 2% are recorded (see **Figure 7**). Moreover, the estimations error variance is drastically reduced using the augmented data-set. Eventually, more complex ANN architectures have been tested, without registering significant improvements in the estimations accuracy. To complete this section, it is important to mention that the creation of the augmented data-set employed only 400 hours of calculation time, instead of the 2000 hours needed to build the original one.

4. Conclusion

Artificial Neural Networks (ANNs) are efficient tools largely used for Eddy Currents (ECs) Non Destructive Testing (NDT). One of their drawbacks still resides in the amount of training data needed, often leading to significant calculation time and resources. To overcome this limitation, a data augmentation method based on Principal Component Analysis (PCA) has been presented in this article. The proposed procedure allows to reduce the time needed to build the training data-set by replacing simulated flaws by artificial ones, without deteriorating ANNs performances. Promising results for Side Drill Hole (SDH) radius and depth estimations are compared in terms of Mean Squared Error (MSE). The proposed method also reduces the ANN estimations error variance, facilitating the training procedure. As future goal, the authors count on validating the ANN performances with experimental data. The ultimate goal will be to couple ECs and ultrasonic pulse-echo signals, exploiting the advantages given by the ANNs.
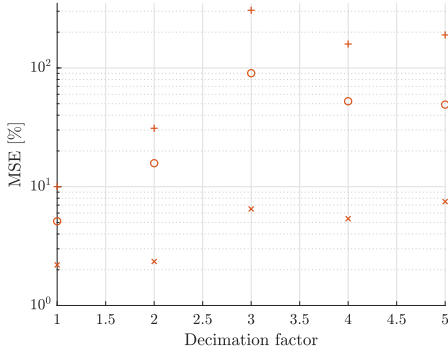
Figure 6. Maximum (+), mean (o) and minimum (x) MSE **obtained decimating the training data-set**. For a decimation factor of five, the radius and depth estimations present an average error of 50%, within a minimum value of 7.5% and a maximum of 190%.
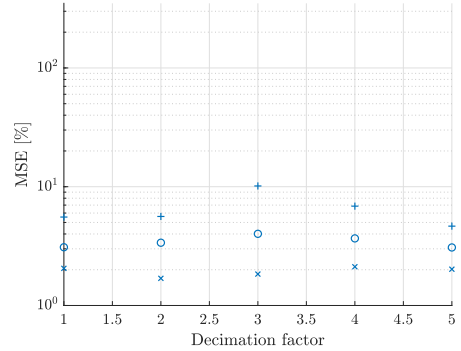

Figure 7. Maximum (+), mean (o) and minimum (x) MSE **obtained using data augmentation**. For a decimation factor of five, the radius and depth estimations present an average error of 3%, within a minimum value of 2% and a maximum of 4.6%.

5. Acknowledgment

References

[1] Chuck Hellier. *Handbook of Non Destructive Evaluation*. McGraw-Hill Professional, 2001.

[2] Jacques Dumont-Fillon. Contrôle non destructif. *Techniques de l'Ingénieur*, 1(0):1–42, 1996.

[3] R Heideklang and P Shokouhi. Application of data fusion in nondestructive testing (NDT). In *Proceedings of the 16th International Conference on Information Fusion, FUSION 2013*, pages 835–841. IEEE, 2013.

[4] Yunze He, Bin Gao, Ali Sophian, and Ruizhen Yang. *Transient electromagnetic-thermal nondestructive testing*. Elsevier, 1st editio edition, 2017.

[5] Cyril Ravat. *Conception de multicapteurs à courants de Foucault et inversion des signaux associés pour le contrôle non destructif.* phdthesis, Université Paris Sud-Paris XI, 2008.

[6] Harold A Sabbagh, R. Kim Murphy, Elias H. Sabbagh, John C. Aldrin, and Jeremy S Knopp. *Computational Electromagnetics and Model-Based Inversion*. Scientific Computation. Springer New York, 2013.

[7] Jain Nikhil. The rebirth of eddy current nondestructive testing: advanced techniques such as ACFM and Eddy Current Array are making rapid strides. *Quality*, 53(8):S19+, feb 2014.

[8] R L Stoll. *The Analysis of Eddy Currents*. Monographs in electrical and electronic engineering. Clarendon Press, 1974.

[9] L. Udpa and S S Udpa. Application of Neural Networks for Classification of Eddy Current NDT Data. In *Review of Progress in Quantitative Nondestructive Evaluation*, pages 673–680. Springer US, Boston, MA, 1990.

[10] Salvatore Caorsi and Paolo Gamba. Electromagnetic detection of dielectric cylinders by a neural network approach. *IEEE Transactions on Geoscience and Remote Sensing*, 37(2 I):820–827, 1999.

[11] Andrea Bernieri, Luigi Ferrigno, Marco Laracca, and Mario Molinara. Crack shape reconstruction in Eddy current testing using machine learning systems for regression. *IEEE Transactions on Instrumentation and Measurement*, 57(9):1958–1968, 2008.

[12] Y L Bihan, J Pavo, and C Marchand. Characterization of small cracks in eddy current testing. *European Physical JournalApplied Physics*, 43:231–237, 2008.

[13] A. Babaei, A. A. Suratgar, and A. H. Salemi. Dimension estimation of rectangular cracks using impedance changes of the eddy current probe with a neural network. *Journal of Applied Research and Technology*, 11(3):397–401, 2013.

[14] Luis S. Rosado, Fernando M. Janeiro, Pedro M. Ramos, and Moises Piedade. Defect characterization with eddy current testing using nonlinear-regression feature extraction and artificial neural networks. *IEEE Transactions on Instrumentation and Measurement*, 62(5):1207–1214, 2013.

[15] B. Helifa, M. Féliachi, I. K. Lefkaier, F. Boubenider, A. Zaoui, and N. Lagraa. Characterization of surface cracks using eddy current NDT simulation by 3D-FEM and inversion by neural network. *Applied Computational Electromagnetics Society Journal*, 31(2):187–194, 2016.

[16] S. Harzallah, R. Rebhi, M. Chabaat, and A. Rabehi. Eddy current modelling using multi-layer perceptron neural networks for detecting surface cracks. *Frattura ed Integrita Strutturale*, 12(45):147–155, 2018.

[17] Lianshuang Dai, Hao Feng, Ting Wang, Wenbo Xuan, Ziqian Liang, and Xinqi Yang. Pipe crack recognition based on eddy current NDT and 2D impedance characteristics. *Applied Sciences (Switzerland)*, 9(4), 2019.

[18] Peipei Zhu, Yuhua Cheng, Portia Banerjee, Antonello Tamburrino, and Yiming Deng. A novel machine learning model for eddy current testing with uncertainty. *NDT and E International*, 101(October):104–112, 2019.

[19] Jinhyun Park, Seong Jin Han, Nauman Munir, Yun Taek Yeom, Sung Jin Song, Hak Joon Kim, and Se Gon Kwon. MRPC eddy current flaw classification in tubes using deep neural networks. *Nuclear Engineering and Technology*, 51(7):1784–1790, 2019.

[20] Yann LeCun. Connectionist Learning Models. *Intellectica, special issue apprentissage et machine*, 1987.

[21] Martin T. Hagan, Howard B. Demuth, and Mark Hudson Beale. Neural Network Design. *Boston Massachusetts PWS*, 2:734, 1995.

[22] Christopher M. Bishop. *Pattern Recognition and Machine Learning*. Springer, 2006.

[23] Thomas Henneron. *Contribution à la prise en compte des Grandeurs Globales dans les Problèmes d'Electromagnétisme résolus avec la Méthode des Eléments Finis*. phdthesis, Université Lille1 - Sciences et Technologies, 2004.

[24] I T Jolliffe. *Principal Component Analysis*. Springer Series in Statistics. Springer-Verlag, New York, 2002.

[25] Hiroshi Akima. A New Method of Interpolation and Smooth Curve Fitting Based on Local Procedures. *Journal of the ACM (JACM)*, 17(4):589–602, 1970.

[26] Martin T. Hagan and Mohammad B. Menhaj. Training Feedforward Networks with the Marquardt Algorithm. *IEEE Transactions on Neural Networks*, 5(6):989–993, 1994.

Corrosion Evaluation Using Clustering Method Based on Eddy Current Pulsed Thermography

Peizhen SHI [a], Song DING [a,1], Yuming CHEN [a], Yiqing WANG [a], Guiyun TIAN [b], Fangjun ZHU[a]

[a] *School of Electrical Engineering and Control Science, Nanjing Tech University, Nanjing, Jiangsu, 211816, China*

[b] *School of Engineering, Newcastle University, Newcastle upon Tyne, NE1 7RU, UK*

Abstract. As a popular defect of steel, corrosion had been a big challenge to industry safe and structural health. For atmosphere corrosion characterization and evaluation, a clustering by fast search and find of density peaks (CFSFDP) algorithm, combined with gap statistic (GS) method is utilized to corroded Q235 carbon steel tubes. With the proposed method, three natural atmosphere corroded samples are investigated and classified. The proposed method successfully identifies the samples with different service periods. The temperature gradient, which indicates the heat generation and conductivity, is used to analyze cluster center selection. The matching rate is presented as a feature to reflect the corrosion state difference.

Keywords. Eddy current pulsed thermography, corrosion evaluation, clustering method.

1. Introduction

As the most widely used material, metal has been applied to social and industrial infrastructures. But corrosion induced fatigue and failures cause fatal disasters which cost billions of dollars per year in the U.S. alone [1], and 40% mechanical failure due to corrosion in the world. To ensure safety, corrosion evaluation which helps re-protecting the material, avoiding accidents and saving lives and money, is expected. To understand corrosion behavior, many chemical and physical methods, such as electrochemical impedance spectroscopy (EIS), scanning Kelvin probe (SKP), scanning acoustic microscopy (SAM) and scanning electrochemical microscopy (SECM), were employed [2]. On the other hand, corrosion state monitoring is more meaningful for in-service equipment and structures. Therefore, many nondestructive testing and evaluation (NDT&E) technologies were applied, such as ultrasonic testing (UT), eddy-current testing (ECT)[3], radiographic testing (RT) and electromagnetic methods[1-8]. Compared to other technologies, eddy current pulsed thermography (ECPT), a novel NDT&E technology that provides an opportunity for efficient nondestructive scanning, has been applied to defect detection and characterization for conductive material [9-11].

---

[1] Corresponding author, School of Electrical Engineering and Control Science, Nanjing Tech University, Nanjing, Jiangsu, 211816, China; E-mail: dingsong@njtech.edu.cn

Aijun Yin et al.[12] interpreted the time responses of ECPT image sequences for two physical processes, accumulation of Joule heating and heat diffusion, from general behavior of ECPT and developed feature extraction and pattern recognition for defect characterization. Yunze He et al.[2] employed ECPT to detect blister and ruptured blister areas. Signal processing algorithms, such as PCA, independent component analysis (ICA) and fast Fourier transform (FFT), are applied for feature extraction to distinguish the ruptured blister. Phase thermography analysis method was proposed by Ruizhen Yang et al. [13] for in-situ early marine corrosion detection, sizing, and monitoring. However, the complex corrosion process and oxide layers [14] bring out fuzzy effects on material properties, such as resistance, electrical conductivity, thermal conductivity, permeability and surface emissivity, which makes it difficult to evaluate the corrosion state based on the ECPT technology.

Previous work of the ECPT technology mostly focused on the transient response and lost sight of the relationship between pixels, which indicates the metallic properties, such as thermal conductivity, electrical conductivity, and permeability. Hence, the general objective of this letter is to characterize the corrosion state by clustering the temperature gradient distribution without any model training.

2. Experimental System and methodology

2.1. Corrosion Samples

For industry enterprises, Q235 carbon steel is widely used to carry dry gas under atmospheric pressure. In this study, three Q235 carbon steel tubes with different atmosphere corrosion, which have exposed to the damp atmosphere for 3 (sample 1), 10 (sample 2) and 14 months (sample 3) as shown in Fig. 1., are selected for investigation. All of these samples have the same diameter of 50mm. The wall thickness of sample 1 is 3mm and the other two are less than 3mm due to corrosion.

(a) 3 months (b) 10 months (c)14 months

Figure 1. Corrosion samples of Q235 steel with different service periods

Obviously, sample 1 has different apparent conditions to sample 2 and sample 3. But for surface visual inspection, it is hard to estimate the corrosion state of sample 2 and sample 3. In this study, all three samples are measured by ECPT system, and the IR images sequence is analyzed to evaluate the corrosion states which are compared with service period of the samples.

2.2. Experiment System

The diagram of ECPT system is shown in Fig. 2. A function generator provides synchronizing pulse which starts the infrared (IR) camera when the induction heater driving the coil. The eddy current supplier, induction heater, drives excitation coil which

generates high-frequency eddy current on the surface of conductive samples. Then, Joule heat is generated by the inductive eddy current and resistance of the material. An infrared camera is employed for capturing the thermal radiation from the samples surface. In order to understand the thermal distribution and heat conductivity process in the sample, infrared image sequence is collected and stored by special software for further analysis.
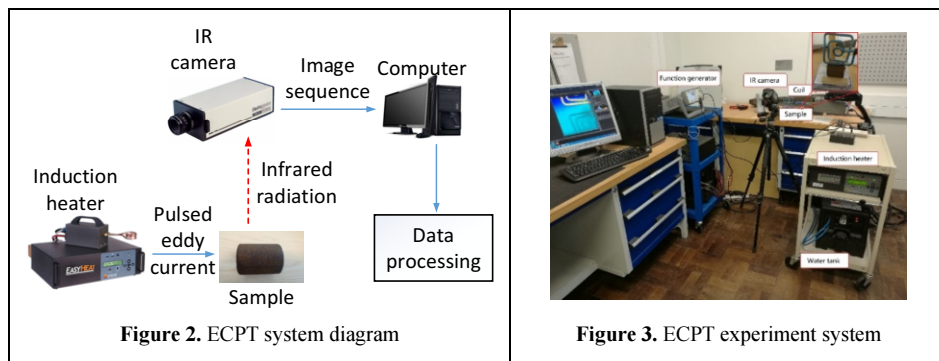

Figure 2. ECPT system diagram

Figure 3. ECPT experiment system

Fig. 3 shows the experimental system for corrosion samples testing which was performed at Newcastle University. The eddy current supplier, EasyHeat 224 from Cheltenham Induction Heating, provides $380A_{rms}$ alternative excitation current (the maximum current is 400 A_{rms}), and excitation frequency from 150kHz to 400kHz. In order to limit the inductive eddy current on samples' surface, which contributes to a shallow heat resource, 260 kHz excitation frequency is selected based on skin depth effect. The rectangular excitation coil is made of 6.35mm high-conductivity hollow copper tube which connected to a pump for water-cooling. FLIR SC655, an uncooled infrared camera with a 640×120 array of 7.5μm InSb detector, is applied to acquire the IR image sequence. IR images are acquired with a 200Hz sampling rate and 30mK temperature sensitivity. For synchronizing the excitation current and IR camera acquisition, a square pulse is generated by a function generator, Keysight 33621A, to start EasyHeat 224 and FLIR SC655.

2.3. Framework

For understanding the characterization of the corrosion state, Fig.4 proposes an overall framework for the study process. It can be divided into three parts. The first part is data acquisition. As shown in Fig.4 part 1, ECPT technology is applied for obtaining thermal images sequence.

Because the raw thermal image data contains large information and some redundant data, it is not suitable for data analysis directly [15]. Generally, feature extraction can be performed on the original thermal images for reducing data and facilitating subsequent analysis. Thus, the second part is feature extraction, which contains area selection, data normalization, polynomial fitting and principal component analysis (PCA). The reasons why the four feature extraction methods are down for the raw thermal images are as follows. During thermal image analyzing, it is necessary to take into account the non-uniform heating of the ECPT technology. At the same time, the area far from the coil is not suitable for analysis because of weak eddy current and low Joule heat generation. The area around the coil was used for analysis due to the heat generation and dissipation
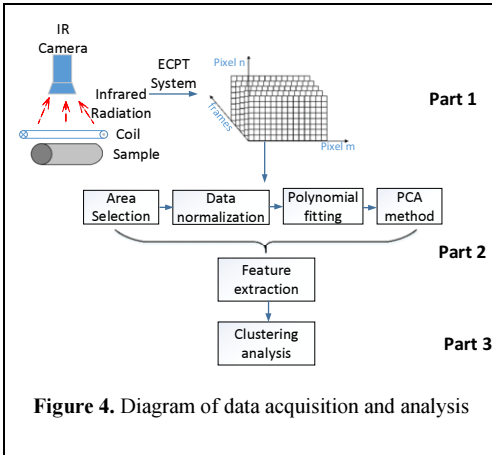
Figure 4. Diagram of data acquisition and analysis
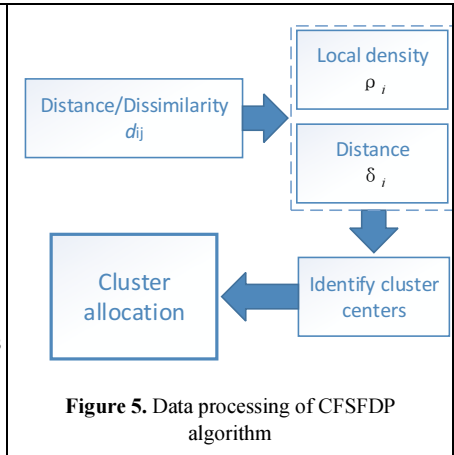
Figure 5. Data processing of CFSFDP algorithm

reflect the material properties. After the area selection, data normalization can observably reduce the lift-off and bias light effect and is helpful to compare the trend of temperature increase and decrease. Since the data acquired from the ECPT system is always discrete and along with noise, the polynomial fitting method can effectively overcome these two problems. Meanwhile, the parameters of the polynomial fitting function can be used to represent the discrete temperature points, and data are greatly compressed. After the polynomial fitting, there is still a lot of redundant information. Therefore, PCA method is applied to reduce the data dimensions. After that, the temperature sequence are normalized between 0 and 1. Finally, the clustering by fast search and find of density peaks is employed for data analysis.

2.4. Clustering by fast search and find of density peaks algorithm

Clustering is the basic composition in data analysis pipelines. Among these algorithms, Clustering by fast search and find of density peaks (CFSFDP) [16] is a novel density-based clustering algorithm that can detect non-spherical data sets with few parameters. The algorithm is based on two assumptions about the cluster centers, which must both have a higher density than their neighbors and a relatively large distance from points with higher local density [16].

In this study, CFSFDP is utilized to analyze the global information of the material surface temperature with different corrosion stage, as shown in Fig.5. For every point on the surface of the material, two parameters need to be calculated by the dissimilarity/distance d_{ij} between data point i and point j. The calculation of the local density of ρ_i of point i is given by equation 1.

$$\rho_i = \sum_{j=1}^{m} \chi(d_{ij} - d_c) \tag{1}$$

Where $\begin{cases} \chi(x) = 1 & x < 0 \\ \chi(x) = 0 & x \geq 0 \end{cases}$, d_c is a cutoff distance. The distance δ_i of point i is defined as:

$$\delta_i = \min_{j:\rho_j > \rho_i} d_{ij} \tag{2}$$

By convention, for the point with the highest density, it is defined as $\delta_i = max_j(d_{ij})$.

3. Result and discussion

As clarified above, the IR images are analyzed by Matlab 2010 software. One typical IR image is shown in Fig. 6, which is the infrared distribution at 200ms after excitation eddy current application.

| Sample 1 | Sample 2 | Sample 3 |
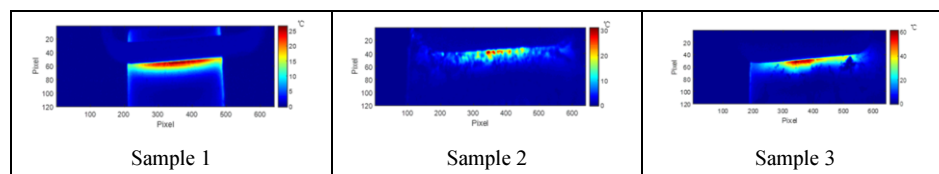
Figure 6. 40th frame of IR image sequence for three samples

Firstly, all three samples are clustered using the CFSFDP algorithm. As shown in Fig. 7(a), obviously, there are three points that are more outstanding, which have larger δ and ρ. Thus, these three points are selected as cluster centers. Fig. 7(e) shows the clustering results. Referring to Fig. 7, the clustering algorithm can basically identify the areas in the data sets.

To verify the clustering algorithm, the clustering results are compared with the actual distribution. As shown in Table 1, the matching rate, correct clustering percentage, of the algorithm is 85.24%, which represents the confidence of the CFSFDP algorithm for characterizing the three corrosion samples. For each sample, 1452 points are selected from the infrared image while only 53 points of sample 1 and 140 points of sample 3 are in the error cluster, respectively. On the contrary, sample 2 shows the lowest matching rate due to 457 error clustered points.

Table 1. The matching matrix of clustering with actual distribution for stage 1, stage2 and stage3

	Cluster 1	Cluster 2	Cluster 3	Total matching rate
Stage 1	1399	0	53	
Stage 2	10	995	447	85.24%
Stage 3	30	110	1312	

To further explore the effectiveness of the algorithm for only two corrosion states, different two samples are selected, clustered and compared. Fig. 7 shows the decision graphs and corresponding clustering results. As shown in this figure, the cluster centers can be easily chosen, and the corresponding clustering results divide data points into two categories for each clustering. In the same way, the matching matrix of clustering groups for different two samples are calculated for comparison.
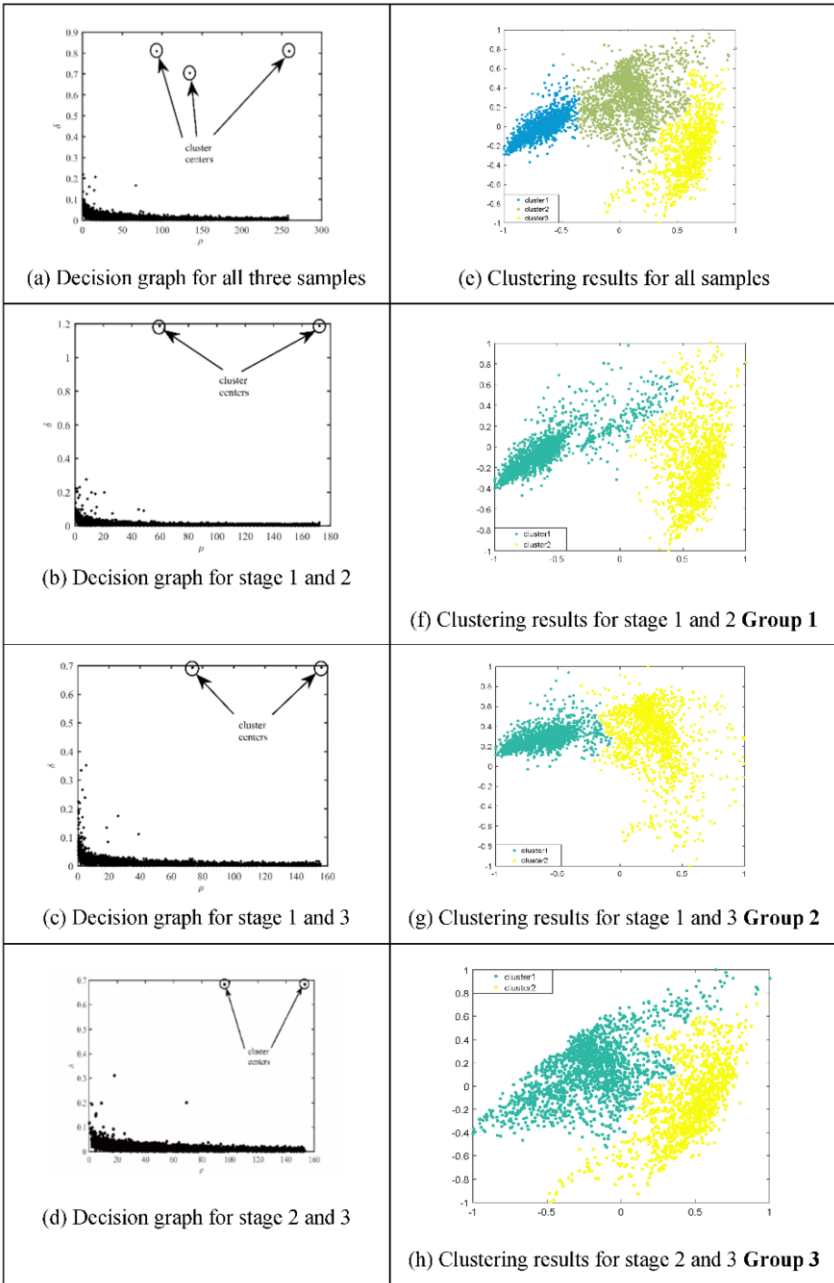
Figure 7. Decision graphs and Clustering results for different clustering groups

From fig. 7 (b)~(d), the distance between cluster centers of clustering 3 significantly smaller than that of group 1 and 2. Accordingly, group 3 has the lowest matching rate, 81.71%. Longer service means bigger variation in the mechanical properties, such as conductivity and emissivity, which makes the feature points distributed more discretely.

As shown in figs. 7 (f)~(h), sample 1 provides obviously concentrated distribution, while sample 2 distributes as discrete as sample 3 due to their similar service periods.

4.　Conclusion and future work

As corrosion affects the material properties, this paper investigates the CFSFDP clustering method based on ECPT technology for inspecting Q235 steel tubes' corrosion state. Temperature gradient distribution is applied for cluster centers selection. After that, CFSFDP algorithm is used to recognize the corrosion state based on the PCA features. All the points in the inductive region are treated indistinguishably and without any training model. Furthermore, matching rates are calculated for different clustering groups, which is proposed as a new feature to characterize the corrosion state after different service periods.

CFSFDP algorithm shows its contributions to corrosion state characterization and evaluation. Moreover, the results show this approach is more credible for two corrosion state recognition than three or more samples distinction. Thus, detailed researches for understanding and quantitative analyzing are expected to improve this clustering approach in future work.

Acknowledgment

References

[1] Fangxin Zou, Frederic B. Cegla. On quantitative corrosion rate monitoring with ultrasound. Journal of Electroanalytical Chemistry. 2018; 812: 115–121.
[2] Yunze H, Guiyun Tian and Mengchun Pan et al. An investigation into eddy current pulsed thermography for detection for corrosion blister. Corrosion Science. 2014; 78: 1–6.
[3] Yunze He, Guiyun Tian and Hong Zhang et al. Steel Corrosion Characterization Using Pulsed Eddy Current Systems. IEEE Sensors Journal. 2012; 12(6): 2113-2120.
[4] M. Yasri, B. Lescop and E. Diler et al. Fundamental basis of electromagnetic wave propagation in a Zinc microstrip lines during its corrosion. Sensors and Actuators B: Chemical. 2016; 223: 352-258.
[5] Keiji Tsukada, Yuta Haga and Koji Morita et al. Detection of Inner Corrosion of Steel Construction Using Magnetic Resistance Sensor and Magnetic Spectroscopy Analysis. IEEE Transaction on Magnetics. 2016; 52(7), 6201504.
[6] Jenifer Alcántara, Daniel de la Fuente and Belén Chico et al. Marine Atmospheric Corrosion of Carbon Steel: A Review. Materials. 2017; 10, 406.
[7] Ivan S. Cole. Recent Progress and Required Developments in Atmospheric Corrosion of Galvanised Steel and Zinc. Materials. 2017; 10, 1288.
[8] Hong Zhang, Leng Liao and Jianting Zhou et al. The Non-Destructive Test of Steel Corrosion in Reinforced Concrete Bridges Using a Micro-Magnetic Sensor. Sensors. 2016; 16, 1439.
[9] Yunze He, Mengchun Pan and Guiyun Tian et al. Eddy current pulsed phase thermography for subsurface defect quantitatively evaluation. Appl. Phys. Lett. 2013; 103,144108.
[10] Kongjing Li, Guiyun Tian and Liang Cheng et al. State Detection of Bond Wires in IGBT Modules Using Eddy Current Pulsed Thermography. IEEE Trans. on Power Electronics. 2014; 29(9): 5000-5009.
[11] Libing Bai, Bin Gao and Guiyun Tian et al. Spatial and Time Patterns Extraction of Eddy Current Pulsed Thermography Using Blind Source Separation. IEEE Sensors Journal. 2013; 13 (6): 2094-2101.

[12] Aijun Yin, Bin Gao and Guiyun Tian et al. Physical interpretation and separation of eddy current pulsed thermography. Journal of Applied Physics. 2013; 113, 064101.

[13] Ruizhen Yang et al. Through coating imaging and nondestructive visualization evaluation of early marine corrosion using electromagnetic induction thermography. Ocean Engineering. 2018; 147: 277–288.

[14] U.S. Department of Energy. DOE Fundamentals Handbook, Chemistry Module 2 Corrosion. Washington, D. C. 1993. 140p.

[15] Bin Gao, Xiaoqing Li and W.L. Woo et al. Quantitative validation of Eddy current stimulated thermal features on surface crack. NDT & E International. 2017; 85: 1-12.

[16] A. Rodriguez and A. Laio, Clustering by fast search and find of density peaks. Science. 2014; 334(6191): 1492–1496.

Industrial Applications of ENDE

This page intentionally left blank

A Parallel Wire Cable Tension Testing Method Based on a Permanent Magnetizer

Youwei LIU and Xinjun WU [1]

School of Mechanical Science & Engineering, Huazhong University of Science and Technology, Wuhan 430074, China

Abstract. Obtaining the cable tension accurately is important to the structural safety. Among different cable tension testing methods, the method of testing stress under the excitation of constant magnetic field is not affected by the boundary condition of the cable and avoids the affection of eddy current. Through analyzing the structural features of parallel wire cable, a cable tension testing method is presented based on the principle of testing stress under the excitation of constant magnetic field. An experiment setup is carried out to verify the feasibility of the method.

Keywords. Parallel wire cable, cable tension, constant magnetic field

1. Introduction

The cable is one of the commonly used components on bridges, dome structures and so on. The tension of the cable can affect the safety of the structures, so measuring the cable tension is of great significance. Presently, there are four often-used cable tension testing methods: the lift-off method, the pressure sensor method, the vibration method and the magnetic method. The lift-off method is low in efficiency and hard to be used in the built bridge. For the pressure sensor method, the tension information can be obtained directly, while it is necessary to embed pressure sensors inside the cable which increases the cost. For the vibration method, the natural frequency is used to characterize tension. A linear theory of free vibration of suspended cables is presented [1]. However, the result of vibration method can be easily influenced by the boundary conditions of the cable. The magnetic method is based on the effect of stress on magnetic parameters. It has unique advantages such as low cost, no pollution and free from the influence of the boundary conditions. The metal magnetic memory (MMM) technique is the most representative passive magnetic method. Doubov uses the normal and tangential magnet flux density to judge the stress distribution and find the stress concentration [2]. Magnetizing windings and sensing coils are used in several magnetoelastic methods to monitor the steel forces [3-4]. Coils are usually employed to excite and receive magnet signals in above research, which brings the influence of eddy current. In order to overcome this shortage, the principle of testing stress under the excitation of constant magnetic field was proposed. Permanent magnets are employed to magnetize steel wire and Hall elements are used to measure the magnetic flux density at different lift-offs [5]. According to the measured data, the inner magnetic flux density and magnetic field intensity are obtained by using

---

[1] Corresponding Author, Xinjun WU, Huazhong University of Science and Technology, Wuhan 430074, China; E-mail: xinjunwu@hust.edu.cn

the interpolation method and magnetic boundary conditions, and then the steel wire stress can be deduced. For the parallel wire cable (PWC), because there's high density polyethylene (HDPE) layer surrounding the steel wires, it is difficult to magnetize the PWC and measure the magnetic field for magnetic testing.

In this paper, a cable tension testing method based on the theory of testing stress under the excitation of constant magnetic field is carried out. In the method, Gauss' law is applied to establish the relationship between stress and a feature parameter at a large lift-off from the cable surface. Finally, an experiment is carried out to verify this method.

2. Principle

The principle of the PWC tension testing method proposed in this paper is shown in Figure 1. First of all, when an axial stress is applied to the cable, it can be assumed that the axial stress in the steel is uniformly distributed. Then, circumferentially uniform constant magnetic excitation is employed to the cable to produce an axially-varying magnetic field. The axial magnetic flux density B_{fer}^z inside the steel is uniformly distributed in a cross section. Also, since the axial component B_{fer}^z is far higher than the radial component B_{fer}^r in the steel, B_{fer}^z equals to the magnetic flux density B_{fer} in the cable. Based on these conditions, further derivation is developed.
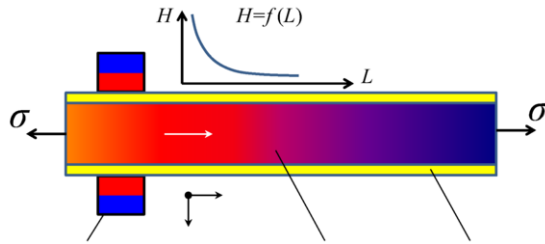
Figure 1. The principle of testing parallel wire cable tension based on a permanent magnetizer

According to the J-A-M model[6], B_{fer} is function of H and σ, which can be written as

$$B_{fer} = F_1(H, \sigma) \tag{1}$$

Under the excitation of the constant magnetic field, H is only the function of the axial position L. So,

$$B_{fer} = F_2(L, \sigma) \tag{2}$$

when L is determined, B_{fer} is only relative to σ, which means it can characterize σ. However, it is unable to measure B_{fer} inside the cable. Also, because of the HDPE layer surrounding the steel wires, the lift-off is large and previous extrapolating method may not be feasible any more. Thus, it is necessary to find a new feature parameter for the cable tension testing under constant magnetic field excitation at large lift-off.

Figure 2 shows how Gauss's law is applied for analyzing. The bundle composing all steel wires in the cable is simplified into a cylinder of diameter d. The axial position of the cylinder is L away from the permanent magnet and the height of the cylinder is ΔL.
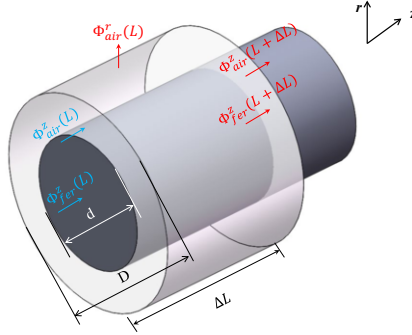
Figure 2. Gauss' law for magnetism at the unit length ΔL

As is shown in Figure 2, the magnetic flux passing through the base of the cylinder consists of the magnetic flux inside the ferromagnetic area denoted as Φ_{fer}^z and outside the ferromagnetic area denoted as Φ_{air}^z. The magnetic flux passing through the side of the cylinder is denoted as Φ_{air}^r. According to Gauss' law for magnetism, the net magnetic flux passing through the cylinder surface is always zero. Then the derivation can be:

$$\Phi_{fer}^z(L) + \Phi_{air}^z(L) = \Phi_{air}^r(L) + \Phi_{fer}^z(L + \Delta L) + \Phi_{air}^z(L + \Delta L) \tag{3}$$

Since $\Delta L \rightarrow 0$, B_{fer}^z is uniformly distributed in the cross section and B_{air}^z and B_{air}^r varies with the radial and axial position, these flux expressions can be written as:

$$\Phi_{fer}^z(L) = B_{fer}^z(L) \cdot \pi d^2/4 \tag{4}$$

$$\Phi_{air}^z(L) = \int_{d/2}^{D/2} B_{air}^z(L, r) \cdot 2\pi r dr \tag{5}$$

$$\Phi_{air}^r(L) = B_{air}^r(L, D/2) \cdot \pi D \cdot \Delta L \tag{6}$$

$$\Phi_{fer}^z(L + \Delta L) = B_{fer}^z(L + \Delta L) \cdot \pi d^2/4 \tag{7}$$

$$\Phi_{air}^z(L + \Delta L) = \int_{d/2}^{D/2} B_{air}^z(L + \Delta L, r) \cdot 2\pi r dr \tag{8}$$

So, Eq. (3) can be rewritten as

$$B_{air}^r(L, D/2) \cdot \pi D \cdot \Delta L = [B_{fer}^z(L) - B_{fer}^z(L + \Delta L)] \cdot \pi d^2/4$$
$$+ \int_{d/2}^{D/2} [B_{air}^z(L, r) - B_{air}^z(L + \Delta L, r)] \cdot 2\pi r dr \tag{9}$$

Since B_{air}^z and its gradient is far smaller than these of B_{fer}^z, the second term on the right side of Eq. (9) can be ignored, then there is

$$B_{air}^r(L, D/2) = (d^2/4D) \cdot [B_{fer}^z(L) - B_{fer}^z(L+\Delta L)]/\Delta L = (d^2/4D)\partial B_{fer}^z/\partial L \tag{10}$$

It is obvious in Eq. (10) that the radial magnetic flux density B_{air}^r at certain axial position and D is proportional to the derivative of B_{fer}^z on L at that axial position. A certain D is equivalent to a certain lift-off from the outer surface of HDPE layer. Combined with the approximation that $B_{fer} = B_{fer}^z$ and Eq. (2), if the lift-off is fixed to l_0, for example, there is

$$B_{air}^r(L, lift-off = l_0) = F_4(L, \sigma) \tag{11}$$

It means that B_{air}^r at certain lift-off l_0 is function of axial position L and stress σ. Different L determined different linearity between B_{air}^r and σ. If we find proper L and lift-off, it can be feasible to use B_{air}^r to characterize σ. Therefore, it is possible to get the stress information by measuring B_{air}^r at a large lift-off.

3. Experiment verification

3.1. Experiment setup

In order to verify the above cable tension testing method, a PWC tension testing experiment setup is built as is shown in Figure 3.

(a)   Diagram of the experiment setup   (b) the experiment setup site photo
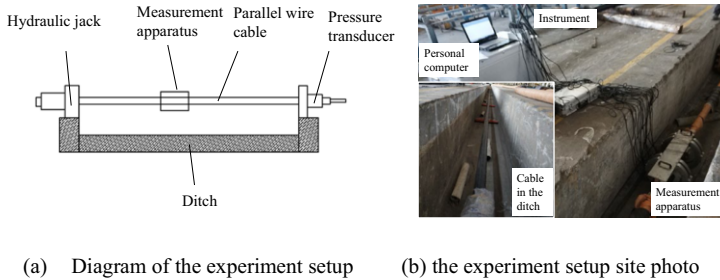
Figure 3. Diagram and photo of the experiment setup

The whole experiment is carried out on one PWC of type LZM7-85 with an external diameter of 87 mm. It consists of 85 steel wires and HDPE layer surrounding them. Steel wire diameter is 7 mm. The cable is put in a ditch and is tensioned by hydraulic jack at one end. At the other end, a pressure transducer is installed to measure the axial tension of the cable. A measurement apparatus based on the above principle is set up on the PWC.

The measurement apparatus includes the permanent magnetizer and the magnetic field measuring element is shown in Figure 4. The material of permanent magnet is NdFeB and its grade is N52. Five permanent magnetizers are attached circumferentially uniformly on the cable. 16 rows of Hall element sensors distribute from 55 mm to 580 mm away from the magnetizer to measure the field. The Hall element sensors' model is HAL1823 from Micronas. A row of sensors measure B_{air}^r at 4 different lift-offs, which are 1.5 mm, 3 mm, 4.5 mm, and 6 mm away from the outer surface of the cable.

The breaking load of the cable is 5460.11 kN, and during the experiment, the biggest tension applied to the cable is 50% of the breaking load. Six different tensions are applied

to the cable in the experiment, which are 34%, 36%, 38%, 40%, 42% and 46% of the breaking load.
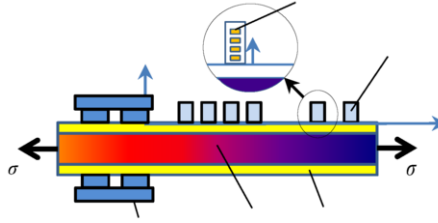
Figure 4. Diagram of the permanent magnetizer and the magnetic field measuring element

3.2. Experiment result

Since the cable's cross-sectional area can be seen as the same at any axial position, the cable tension is always proportional to the stress. Also, the tension of the cable can be seen as the same along the whole cable as well as the stress. Thus, the relationship between B_{air}^r and the cable stress can be extended to that between B_{air}^r and the cable tension. What is analyzed below is the B_{air}^r-tension relationship.
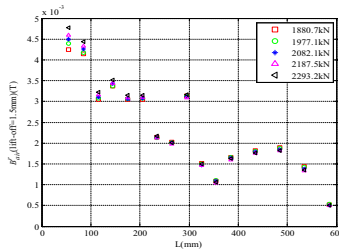
Figure 5. B_{air}^r(lift-ff=1.5mm)-L relationship

(a) L=55 mm, lift-off=1.5 mm (b) L=55 mm, lift-off=6 mm

(c) L=145 mm, lift-off=1.5 mm (d) L=145 mm, lift-off=6 mm
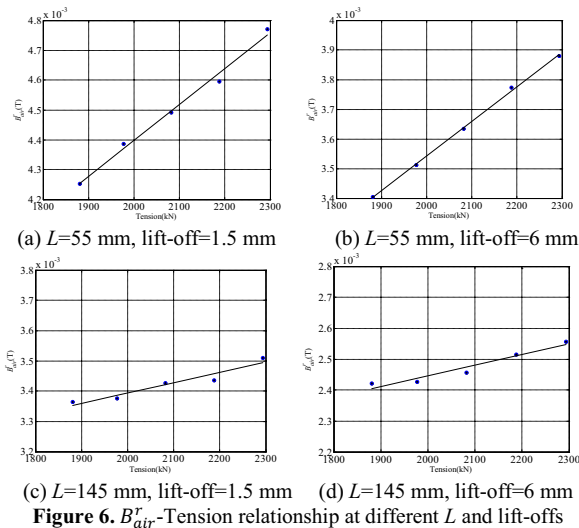
Figure 6. B_{air}^r-Tension relationship at different L and lift-offs

Figure 5 shows the B_{air}^r-L distribution at 1.5 mm lift-off from the surface of the HDPE layer under different tensions. It can be found that B_{air}^r varies with cable tension and the variation trend is different at different L. Use the data under the first 5 tension to do the linear regression analysis. The goodness of fit of the four conditions in Figure 6 are respectively R_a^2=0.9903, R_b^2=0.9987, R_c^2=0.9306 and R_d^2=0.9451. It shows that B_{air}^r (L=55mm) has a better linearity with cable tension than B_{air}^r (L=145mm). The linearity varies notably with the axial position L, which agrees with the above derivation.

From the above analysis, B_{air}^r (L=55mm,lift-off=6mm),which has the best linear relationship with cable tension T, can be used to fit the cable tension and the equation of linear regression is B_{air}^r=1.2×10^{-6}T+0.00199. Use the function to extrapolate another tension on the cable being experimented. The extrapolation result is 2547.9kN while the true value is 2498.6kN. The relative error of linear regression is 1.97%.

4. Conclusion

A parallel wire cable tension testing method based on a permanent magnetizer is studied. Permanent magnetizer is used to produce an axial-varying magnetic field on the cable and a principle is presented to characterize cable stress. Based on the J-A-M model and the field spatial distribution feature, a stress-characterizing parameter B_{air}^r is derived using Gauss's law. To verify the method, an experiment setup is built. The experiment result shows that B_{air}^r(L=55mm,lift-off=6mm) has the best linearity with cable tension. The best goodness of fit can be 0.9987, and the best error of linear regression analysis is less than 2%. The result indicates that the cable tension testing method is correct and it is feasible to use B_{air}^r to characterize cable tension.

5. Acknowledgement

References

[1] Caughey H M I K . The Linear Theory of Free Vibrations of a Suspended Cable[J]. Proceedings of the Royal Society of London. Series A, Mathematical and Physical Sciences, 1974, 341(1626):299-315.

[2] Doubov A A , Demin E A , Milyaev A I , et al. The Experience of Gas Pipeline Stress-Strain State Control With Usage of the Metal Magnetic Memory Method as Compared With Conventional Methods and Stress Control Means[J]. Welding in the World, 2002, 46(9-10):29-33.

[3] Jarosevic, A. "Magnetoelastic method of stress measurement in steel." Smart Structures. Springer, Dordrecht, 1999. 107-114.

[4] Ru Z, Yuanfeng D, Siu Wing O, et al. Smart elasto-magneto-electric (EME) sensors for stress monitoring of steel cables: design theory and experimental validation [J]. Sensors, 2014, 14(8): 13644-60.

[5] Dongge D , Xinjun W , Su Z . A Steel Wire Stress Measuring Sensor Based on the Static Magnetization by Permanent Magnets[J]. Sensors, 2016, 16(10):1650-.

[6] Sablik M J , Jiles D C . Coupled magnetoelastic theory of magnetic and magnetostrictive hysteresis[J]. IEEE Transactions on Magnetics, 1993, 29(4):P.2113-2123.

Passive Method for Monitoring Atmospheric Phenomena by Evaluating the Cellular Network Signals

Michal KUBA [a], Peter FABO [b,1], Dušan PODHORSKÝ [c], Dagmar FAKTOROVÁ [a] and Adriana SAVIN [d]

[a] *Faculty of Electrical Engineering and Information Technology, University of Žilina, Žilina, Slovak Republic*
[b] *Research Centre, University of Žilina, Žilina, Slovak Republic*
[c] *Slovak Academy of Sciences, Department of Atmospheric Physics, Bratislava, Slovak Republic*
[d] *Nondestructive Testing Department, National Institute of R&D for Technical Physics, Iasi, Romania*

Abstract. An integral part of our environment in addition to the surface of the Earth is the adjacent part of the atmosphere, the lower layer of the troposphere. This part of the troposphere has essential influence on weather evolution and information on its condition is an important part of the weather forecasting models. Standard methods of the data acquisition such as radars, satellites and weather stations do not provide information with sufficiently high temporal and spatial resolution. The subject of the article is a method of monitoring the condition of lower layers of the troposphere by passive monitoring and evaluation the parameters of cellular network signals. The elementary theory of an virtual sensor for the atmospheric radio refractive index monitoring and the preliminary results of experimental monitoring of the selected meteorological situation are presented.

Keywords. Index of refraction, radio refractive index, refractivity, radar, satellite, Euler–Lagrange equation

1. Introduction

An integral part of our environment is the biosphere which in addition comprise not only of the Earth's surface, but also of the adjacent part of it, the low layers of the troposphere. It is known that about 85% of the solar energy at the boundary of the atmosphere will hit the Earth's surface at ideal conditions, transforming it to other forms of energy and ultimately to heat. Therefore the condition in the ground layer of the atmosphere has a major influence on the global parameters determining the weather evolution.

The basic parameters for describing the condition of the atmosphere are pressure, temperature, air humidity and the presence of hydrometeors. Because all of these factors affect the propagation of electromagnetic waves, radar measurements from ground stations and satellites have become a standard part of atmospheric monitoring. Because of fundamental reasons, however, they do not affect the ground layers of the atmosphere and do not have sufficient temporal and spatial resolution especially in populated areas where the need for detailed information is highest.

---

[1] Corresponding Author, Peter Fabo, Research Centre, University of Žilina, Žilina 010 26, Slovak Republic; E-mail: peter.fabo@rc.uniza.sk.

The subject of the paper is a description and realization of a passive virtual sensor using specific properties of electromagnetic energy propagation in the atmosphere to describe its refractive index in the radio frequency domain. The determination of refractivity value from temporal parameters of the signal propagating in the atmosphere is described, e.g. in the literature [1], [2]. The basic principle is that the propagation velocity of radio signals depends on the refractive index of the air, which is a function of pressure, temperature, humidity, water vapour density and presence of hydrometeors. Changes in the water vapour density and changes in presence of hydrometeors along the propagation path lead to changes in the propagation velocity. These changes in turn manifests itself in the propagagation delay changes which can finnaly be observed by measuring the changes in the relative phase of the signal between the transmitter and receiver. In contrast to the methods mentioned in the literature [1], [2], the method presented here does not require knowledge of the signal structure, nor autocorrelation parameters of the signals. Also it does not require exact knowledge the value of the time instant at which the signal left the signal source. The determination of the refractive index is based on the measurement of the time parameters in the 1 GHz radio frequency band and advantageously utilizes mobile operators' Base Transceiver Stations (BTS) as energy sources.

In [2] the procedure for continuous tracking the phase of DAB (Digital Audio Bradcasting) signal by pilot symbol tracking is indicated. This algorithm requires some demodulation of the signals to recover the in-built synchronisation (pilot) symbols. The authors had to used a low phase-noise signal generator phase-locked to a GPS disciplined rubidium oscillator to provide a low-jitter ADC sample clock. The DAB signal contains a ≈1 ms synchronisation symbol in every ≈96 ms data frame. From this a carrier burst can be extracted and the changes in phase can be tracked using a phase-locked-loop or some other form of phase estimator. The carrier burst is recovered from the synchronization symbol by mixing the synchronization symbol with a conjugated replica of the constant-amplitude zero auto-correlation (CAZAC) sequence. The null symbol, which precedes synchronization symbol, consists of repeated CAZAC sequence.

In [1] a roundtrip propagation delay between the receiver and the reflector in form of the phase delay using the phase in the side peak of the delay profile is determined. Delay profiles are defined as the impulse responses of system whose inputs are signals from transmitters and whose outputs are signals received by a receiver. The authors derived the delay profiles by inverse Fourier transform of OFDM (Orthogonal Frequency Division Multiplexing) synchronization symbol in received signals from ISBD-T – the digital terrestrial TV broadcasting standard used in Japan so the algorithm requires some demodulation of the signals as well. By using this method it is possible to measure the variation of propagation delay between the receiver and the reflector in millimeter order.

Unlike the methods described in [1] and [2] the proposed method determines the propagation delay changes in form of the phase delay changes as the time difference in propagation delay between two not very different propagation paths in Line-of-Sight (LOS) toward the BTS in the area between the transmitter/BTS and the receiver without the need of using the reflector. The real-time phase measurement system adopts a software defined radio (SDR) technique. The main components are LimeSDR, which is two channel SDR device supplied by Lime Microsystems, a PC and two commercial Yagi type antennas. The two-channel coherent SDR is essentially two SDRs on a common local oscillator so there is the precise phase synchronisation between the two channels/receivers. Two similar but steel different propagation paths are selected using two directional antennas. These antennas are located in the same place or there may be a

small distance between them. More about this is discussed in the section 3. In this study only the synchronisation signal of mobile operators in GSM standard which is transmitted by each BTS was utilized because of high penetration of mobile operator's BTSs in the territory of the Slovak Republic. The signals received by the antennas are sampled to produce in-phase and quadrature phase (IQ) time series in each of the two channels. From these two complex time series the phase delay between the two propagation paths is determined without the need for signal demodulation. The advantages of the proposed method are that there is no need to use neither antenna reflector nor high precision external local oscillator and signal demodulation is not required as well. So it is no necessary to use a priori information about time structure of the signal. The disadvantage is the use of two-channel SDR which is more expensive then the single-channel SDR. By using SDR with a high sampling rate (in this case 25 Msps), it was possible to monitor the entire radio spectrum (from 935 MHz to 960 MHz) in which the downlink (BTS to mobile) of GSM-900 standard occurs. Because the frequencies of the pilot signals among neighboring BTSs are different from each other, it was possible to measure changes in propagation delay simultaneously from different directions from all BTSs which are surrounding the receiver. In the longer term it is possible using a network of more such receivers deployed over a larger area as a network of passive sensors receiving cellular network signals to measure path-averaged refractivity from different directions and after some processing that information (by using e.g. the tomographic techniques) there might be the possibility to derive two-dimensional, time-evolving boundary-layer moisture fields and spatially strongly bounded meteorological situations related to humidity, rainfall, turbulence etc. in the given area.

2.   Atmospheric refractivity

The standard methods for monitoring the atmospheric condition focus on monitoring the movement and properties of air masses with the primary goal of obtaining the information which is needed to produce weather forecasts.

The standard methods include the radar measurements, multispectral monitoring of the atmosphere and the Earth's surface by satellites, ground station networks and additional sources of information such as balloon measurements, aircraft and ship crew reports. However, these methods are not suitable for determination the atmospheric condition in the ground layer for height up to the level of 100 m which significantly affects the environment. The lowest height level of observability by standard meteorological radar usually does not drop below 600 m in flat areas, satellites usually are not able to observe relatively small local atmospheric changes and the ground station network is relatively sparse and usually covers only critical infrastructure such as airports and ports.

Atmospheric monitoring usually uses the SHF (3-30 GHz) frequency bands and higher, where the attenuation properties of the atmosphere are already present and the wavelength allows monitoring of hydrometeors and their manifestations (Doppler effects, polarization and others). In the frequency band below 3 GHz the attenuation effects of hydrometeors is practically negligible [3] therefore these frequency bands are not suitable for use by standard methods. However the parameter that affects the propagation of electromagnetic energy in the atmosphere over the whole frequency range is the refractive index of the atmosphere which determines the propagation velocity of

electromagnetic waves. The typical value of refractive index for a standard atmosphere is typically of $n = 1.000320$ which slightly differs from the value of 1. However, for practical reasons the index of refractivity is defined as follows:

$$N = (n - 1) * 10^6$$

For average value of refractivity as a function of height h [km] (long-term average value for the globe, $h_0 = 7.35$ km) according to [4], [5] the following relationship holds:

$$N = N_0 \cdot \exp\left(-\frac{h}{h_0}\right) = 315 \cdot \exp\left(-\frac{h}{7.35}\right)$$

According to [6] for low altitudes the approximate value of -39 N/km of vertical gradient of refractivity usually is used.

3.   Principle of refractivity measurement

The principle of a virtual sensor operation is shown on elementary theory in the simplest case of a linear vertical dependence of refractive index, which can be defined in this form:

$$n(y) = n_0 \left(1 + \alpha y\right)$$

where n_0 is the refractive index on the Earth's surface, α is the gradient value. For such a refractive index profile we look for a trajectory $y(x)$ along which electromagnetic energy is propagated in the environment between the source and the detector. The optical length of the trajectory (terminology from the optics) is given as:

$$f(x, y, y') = \int n \, \mathrm{dl} = \int n(y) \sqrt{1 + (y')^2} \, \mathrm{dx}$$

The trajectory $y(x)$ is obtained by solving the Euler-Lagrange differential equation:

$$\frac{\mathrm{d}}{\mathrm{dx}} \left(\frac{\partial f}{\partial y'}\right) - \frac{\partial f}{\partial y} = 0$$

in form of:

$$y(x) = -\frac{1}{\alpha} + \left(y_0 + \frac{1}{\alpha}\right) \cosh\left(\frac{x}{y_0 + \dfrac{1}{\alpha}}\right)$$

where y_0 is the value determined from the initial conditions as the highest point of the trajectory. For example, in Fig. 1 the calculated trajectories for a vertical gradient of -40 N/km are depicted. The trajectory endpoints are 900 and 1000 m away from the signal source.

The goal is to determine the time difference between the propagation times of the signal from the source to the destination points A and B for the different refractivity gradient values. The optical length of the SA trajectory is given as

$$L_{SA} = \int_{x_S}^{x_A} n(y)\, \mathrm{d}s = \int_{x_S}^{x_A} n_0 \left(1 + \alpha\, y(x)\right) \sqrt{1 + y'(x)}\, \mathrm{d}x$$

Similarly the optical length of the SB trajectory can be obtained. Let λ is the wavelength of the source of the electromagnetic energy. Because it seems that the time variations will be very small it is reasonable rather to work with phase delay ϕ instead of using the time difference between signals at points A and B.
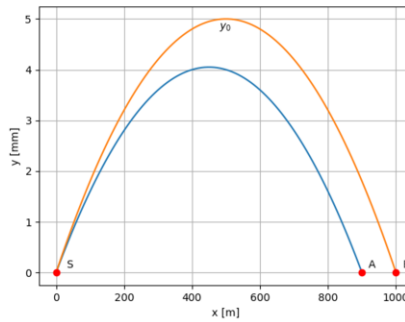
Figure 1. The trajectory between the source and the two destination points A and B.

The L_{SA} and L_{SB} optical lengths are functions of refractivity and its gradient. The L_{AB} distance between the points A and B does not depend on the refractivity and gives a constant offset to the result. Therefore it can be subtracted from the difference of optical lengths:

$$\phi = \frac{L_{SB} - L_{SA} - L_{AB}}{\lambda} \cdot 2\pi$$

After all numerical calculations of integrals which define the values of L_{SA} and L_{SB} optical lengths and the signal phase delay value, the distance between antennas in meters was selected when the refractive index value varies approximately in the range from 290 to 400.

4.   Experimental results

It is clear that by measurement of the phase delay between signals at points A and B it is possible to obtain values which are proportional to the atmospheric refractivity. There is obvious relationship among physical parameters of the atmosphere and its refractivity. Therefore, it is possible to obtain a virtual sensor for monitoring the condition of the atmosphere on the SAB line in a such relatively simple manner.

A direct comparison of the phase delay and refractivity determined from standard meteorological sensors (pressure, temperature, humidity) is, for obvious reasons,

however, only possible for specific meteorological situations in which the atmosphere is homogeneous along the path of propagation which includes the position of the sensors. On Fig. 2 the measured signal phase delay together with the refractivity values, which were calculated from the values obtained from the local measurement of temperature, pressure and humidity is depicted.
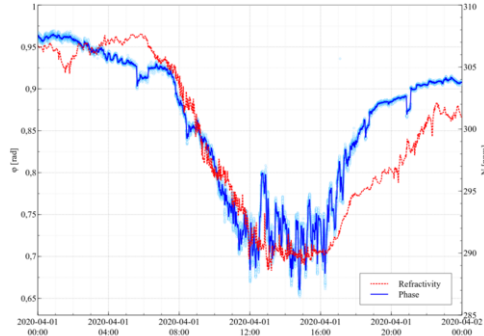
Figure 2. The comparison of the phase delay and the refractivity.

Fig. 3 shows the results obtained by monitoring of cold front passage over a region of western Slovakia along with radar measurements at indicated times and areas. The measurements were taken in Trenčín city, the distance to the BTS was 400 m, the distance between the antennas at points A and B was approximately 2 m. Several BTS were monitored simultaneously in receiver bandwidth of 25 MHz.
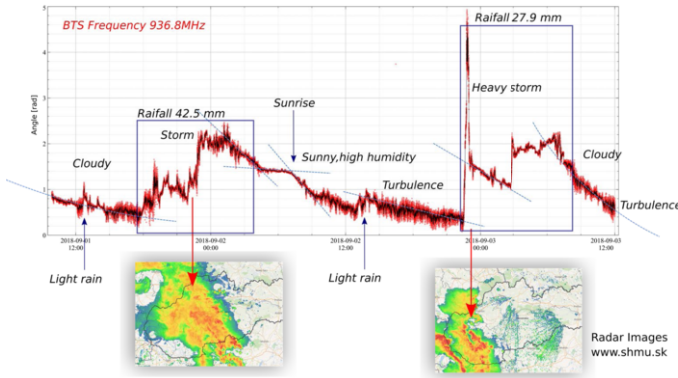
Figure 3. Cold front passage monitoring

The monitored BTS is operated at a frequency of 936.8 MHz. The GSM G2 mobile network pilot signal was being received. The total bit rate from the dual channel SDR was 320 MB/s, the total amount of processed data in the figure was approximately 20 TB at a recording time of approximately 2 days.

The data show the effect of atmospheric phenomena on the phase angle – rainfall and storms, the relaxation of atmospheric humidity after rainfall, the influence of the sun, humidity changes during the day, the origin and extinction of thermal turbulence as well as the extinction of vertical atmospheric movements at night.

5. Conclusion

From the practical point of view the measurement requires using an arbitrary two-channel coherent SDR receiver with sufficiently fast enough communication interface and a computer for evaluation of the phase shift between IQ signals from both channels of the receiver. As a signal sources the BTS of mobile operators in the LOS were used. At the same time a more signals can be received if the sufficiently powerful SDR receiver will be used and therefore it is possible to monitor the condition of the atmosphere from different directions. From mentioned above the following features of the technology result:

- passive method – no self-radiation – utilizes radiation from another sources
- without legislative restrictions – no data streams decoding
- creates virtual sensors among power sources and receiving antennas
- possibility of measurements from more directions simultaneously
- independence on modulation formats, type of service, etc.

Description and implementation of the above mentioned virtual sensor is one of the many possibilities of monitoring the condition of the lower layers of the troposphere by passive monitoring and evaluation of the sources of electromagnetic radiation on the Earth's surface. Another method that have been successfully tested in the project utilizes the correlation properties of the power characteristics of spatial and diversity reception. The monitoring of signal sources can be extended to multiple receiving systems. This way can be obtained the system of many intersecting LOS and by using of the suitable algorithms there is the possibility to obtain the information about spatial localization of the selected meteorological phenomena such as local rainstorms and downpours, ground fog areas and others.

References

[1] S. Kawamura et al., Water vapor estimation using digital terrestrial broadcasting waves, Radio Science, Volume **52**, Issue 3, March 2017, Pages: 283-427.
[2] R.J. Watson and Chris Coleman, The use of signals of opportunity for the measurement of atmospheric refractivity, Conference: *Antennas and Propagation (EuCAP)*, 2010, Proceedings of the Fourth European Conference on, Pages: 1-5.
[3] C.C. Chen, Attenuation of Electromagnetic Radiation by Haze, Fog, Clouds and Rain, *United States Air Force Project RAND*, 1975.

[4]   B.R. Bean, E. Dutton, *Radio Meteorology*, Central Radio Propagation Laboratory, National Bureau of Standards, Boulder, Colorado, 1966.

[5]   ITU-R, The radio refractive index: its formula and refractivity data, ITU 2016.

[6]   A.R. Webster, Raypath Parameters in Tropospheric Multipath Propagation, *IEEE Transactions on Antennas and Propagation*, vol. AP-30, no. 4, Jul. 1982, pp. 796-800.

Developments in GPR Based NDT for Ballastless Track of High-Speed Railways

Xiaoting XIAO[a,1], Guiyun TIAN [b], Dong LIU[a], Mark ROBINSON [b] and Anthony GALLAGHER [b]

[a] *School of Automation Engineering, University of Electronic Science and Technology of China*
[b] *School of Engineering, Newcastle University, UK*

Abstract. For the past decades, ballastless track has been developed and used successfully throughout the world. Due to the multi-layer concrete structure of a ballastless track, timely detection of problems becomes a significant challenge. Ground Penetrating Radar (GPR), as an effective nondestructive method, has been applied to ballastless track in the last ten years. This paper reviews the state-of-the-art of GPR for the ballastless track. The challenges and problems are highlighted and discussed. A Vector Network Analyser (VNA) based stepped-frequency GPR system is considered for the problems and detection requirements. The experimental results show that the proposed system can detect narrow cracks in the depth up to 50cm.

Keywords. Ballastless track, high-speed railway, ground penetrating radar, non-destructive testing, Vector Network Analyser (VNA)

1. Introduction

Railways currently in service can be divided into two categories: ballast and ballastless [1]. The latter is also known as slab track [2]. With the rapid development of the high-speed railway, ballastless track has been widely used. The high-speed railway construction mileage of China is expected to reach 39,000 kilometers by the end of 2020 [3]. The advantages of ballastless track include the improvement in smoothness, stability, and safety; reduction of structure height and maintenance, etc. [4-5]. The disadvantages are the requirement for very high stability for the subgrade and higher construction costs. Different problems, such as inner cracks and interlayer gaps, may occur due to the construction quality, subgrade sinking, drastic weather changes, etc. However, as a ballastless track is composed of a multi-layer concrete structure, timely detection of problems and planning of maintenance is a significant challenge for ballastless railways [6].

The common inspection methods for ballast track such as digging trenches and taking core samples are not applicable for ballastless track, since they are expensive, destructive, time-consuming [7] and have low spatial sampling density. Ground Penetrating Radar (GPR), a commonly used non-destructive testing (NDT) equipment, has a great potential in ballastless track inspection since it is efficient and effective for

---

[1] Corresponding Author Xiaoting Xiao, E-mail: xt_xiao@foxmail.com.

both qualitative and quantitative evaluations of different defects [8]. In this paper, we focus on the applications of GPR for defects of ballastless track. A newly developed stepped-frequency GPR system is presented with some promising experimental results.

2. Review of Ground Penetrating Radar

For ballastless track, there is less research on inspection methods than for ballast track. However, we can refer to the successful use of GPR on traditional ballast track and other concrete structures.

2.1. Basic principles of GPR

Radar systems can be divided into two types: pulse and continuous wave (CW). Pulse GPR systems either transmit very short impulses (on the order of nanoseconds) or longer pulses (such as linear FM chirps) where pulse compression is employed when the received data is processed. Impulse GPR is the most used as it is relatively easy to implement and requires minimal processing to obtain useful data. However, the penetration depth is limited by the required resolution.

Continuous-Wave (CW) systems are less common and require more complex transceiver circuitry. To obtain ranging information the wave is FM modulated, either continuously (FMCW: Frequency-modulated continuous wave) or discretely (SFCW: Stepped-frequency continuous wave). The radial resolution of FMCW and SFCW systems is dependent on their frequency discrimination capabilities, whereas for pulse systems it is dependent on the full width at half maximum (FWHM) of the transmitted waveform or the result of a matched filter applied to the transmitted waveform.

Regardless of the modulation technique used, RF energy is injected into the subsurface by the transmitting antenna and collected by the receiving antenna, which is usually collocated. For pulsed systems, the received signal is amplified by a variable gain amplifier and then digitized by an ADC. For CW systems the output of the variable gain amplifier is input to a mixer where it is multiplied by the signal from the transmitter, and the lower frequency output is digitized by the ADC. Each pulse or modulation period produces a one-dimensional graph, known as an A-scan. As the radar moves over the surface, numerous collected A-scans are then used to form a two-dimensional image or B-scan, as illustrated in Figure 1.
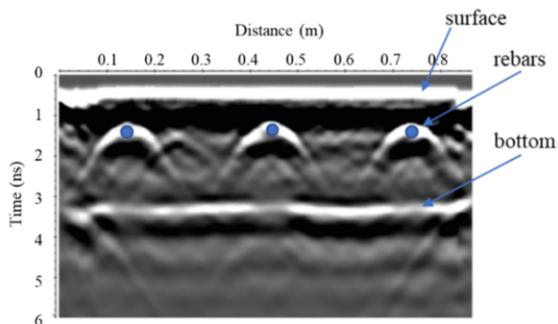
Figure 1. An example of pulse GPR detection B-scan on a concrete slab [9]

The hyperbolas seen in Figure 1 are due to the diffractions of the rebars. It can be observed that point sources appear as hyperbolas, because of the range between the antennas and the target changes while the radar is in motion. Reflections are due to differences in dielectric permittivity in the subsurface. A portion of the energy in the incident wave reflects from the object, and the remainder refracts through discontinuities, the respective amounts being determined by the ratio of refractive indices as indicated by the Fresnel equations. When the incident angle is zero (normal incidence on the ground surface),

$$R = \left| \frac{n_1 - n_2}{n_1 + n_2} \right|^2, T = 1 - R, \tag{1}$$

where R and T are the fractions of the incident power that are reflected and transmitted, respectively. For air-coupled systems, signals enter the receiver from three sources: 1) a direct wave from the transmitter through free space, 2) a wave reflecting from the ground surface and above ground clutter sources, 3) waves reflecting from discontinuities in the subsurface.

The vertical axis of the B-scan is the two-way travel time t_{wt}, typically given in nanoseconds, which is converted to depth (time-depth conversion) using

$$d = \frac{c t_{wt}}{2\sqrt{\varepsilon'_r}}, \tag{2}$$

where t_{wt} is in seconds, c is the velocity of light in vacuum and ε'_r is the real part of the relative permittivity (dielectric constant) of the subsurface medium.

2.2. Types of GPR systems

Currently, most of the commercial systems are pulse radar systems except for the stepped-frequency GPR from 3D-Radar®. The widespread of pulse radar systems is mainly due to their easiness of use and data interpretation. These systems can also be divided into two categories according to the configuration: cart-mounted system and vehicle-mounted system. The cart-mounted systems are the traditional systems that are pushed by operators. They are widely used in the field of civil engineering, hydrology, mining, archeology, geology, etc. [10]. The antennas can be either ground-coupled or air-coupled in different circumstances. The vehicle-mounted systems can be much more efficient and useful in the inspections of the road [11], tunnel [12], ballast railway [6], etc. In this configuration, the antennas are required to be air-coupled.

3. Ballastless Railways

Several types of ballastless track have been developed in different countries, which all use concrete in place of ballast. As a result, a ballastless track faces the same durability problems as concrete, such as the effects of temperature, freezing and thawing, corrosion of reinforcing elements, carbonation, cracks, etc. [13-14].

In China, the ballastless track types used in high-speed railways are listed as follows [15-16]:

- Using pre-cast slabs, CRTS I-III (CRTS: China railway track system);
- With cast in situ slabs, twin-block and sleeper buried ballastless track.

Most of the ballastless tracks in Chinese high-speed railways use pre-cast slabs. Current NDT inspections also focus on these types of ballastless tracks. A typical structure is shown in Figure 2, consisting of the support plate, CA mortar layer, track slab, fastener, and rail.
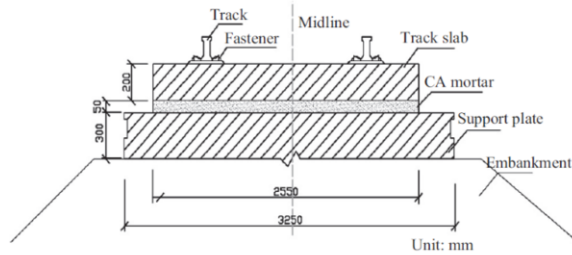
Figure 2. Transverse section of ballastless track [16]

3.1. Common defects of ballastless railways

With the construction and operation of high-speed railways, Chinese Railways found that many defects in ballastless track may affect the operational safety and durability of the railways, summarized in Table 1 [6]. What can be observed from this table is that many factors can cause different degrees of damage to a ballastless track. Therefore, it is necessary to carry out line inspection and maintenance frequently to eliminate potential security risks. More time and expertise must be devoted to the non-destructive detection of faults in the future, especially in China. Currently, NDT methods for defect detection of ballastless track include Ultrasonic methods [17], Impact echo [18], GPR [19], etc. GPR is considered the best NDT method for ballastless track since it is effective for both qualitative and quantitative evaluations of different defects at the same time.

Table 1. Main defects and causes of ballastless railways

Defect types	Causes	Consequences
Track slab cracks	Insufficient reinforcement, construction quality, etc.	Lateral separation cracks
CA mortar defects, interlayer gaps	Dry-wet cycles, temperature gradient, concrete under or over tamping, etc.	Heavier gaps and vertical cracks, precipitation accumulates in the gaps
Support layer cracks and deformation	Subgrade uneven settlement	Increment of tensile stress of track slab, shortened service life
Voids inside the layer	Uneven tamping, foreign matter doping, etc.	Breakdown of track slab or support plate

3.2. GPR inspections and challenges

The capability of GPR to detect defects in ballastless track or concrete slabs has been validated by many studies. Researchers in Germany [18-19] found it to be practical to combine several NDT methods, such as impact-echo, ultrasonic echo, and GPR, for the inspection of ballastless track. Li [20] applied GPR to the detection of interlayer gaps and produced effective results in evaluating the grouting effect. The use of low frequencies for ballastless track is limited due to the presence of rebars in track slabs

[17], results in limited penetration depth Moreover, although the vehicle-mounted GPR has been widely used in the inspection of ballast track [7,21], the GPR systems for ballastless track are usually hand-towed with the antennas ground-coupled to the surface of the trackbed.

From the above, some challenges and problems remain for the inspection of ballastless track using GPR. Firstly, GPR detection cannot be as accurate as other NDT methods in some circumstances, such as for distinguishing weak bonding and no bonding points. Secondly, existing research focuses on the use of the pulse GPR system, with which the penetration depth is limited by the required resolution. Thirdly, the system is usually hand-towed with the ground-coupled antennas. Despite the configuration, properly planned detection lines and suitable processing algorithms are necessary [22].

4. Newly developed GPR for ballastless track

To improve the signal resolution and testing efficiency of GPR systems, a radar system using SFCW signals was developed in this work. The SFCW system integrates a pair of air-coupled antennas, making it possible to be adapted to an integrated vehicle-mounted system for damage detection and safety assessment of high-speed railways in the future.

The developed SFCW system is shown in Figure 3. The horn antennas are used as the bi-static configuration for transmitting and receiving radar signals. Data are collected by sweeping frequency in the range of 1GHz - 4GHz. The idea of using SFCW for a GPR system is not new. It has already been applied to the detections of concrete, limestone, pavement, etc. [23-25]. Several advantages of the system facilitate the detection of high-speed railways, such as: 1) SFCW uses low-cost (low speed, low power) equipments compared to that of pulse GPR; 2) obtained information is richer as it contains magnitude and phase in frequency domain; 3) better resolution with wider operating bandwidth [26]. Moreover, the SFCW system is capable of the Quantitative Non-Destructive Evaluation (QNDE) of railway structural layers and other concrete structures [23, 27].

| (a)   (b) |
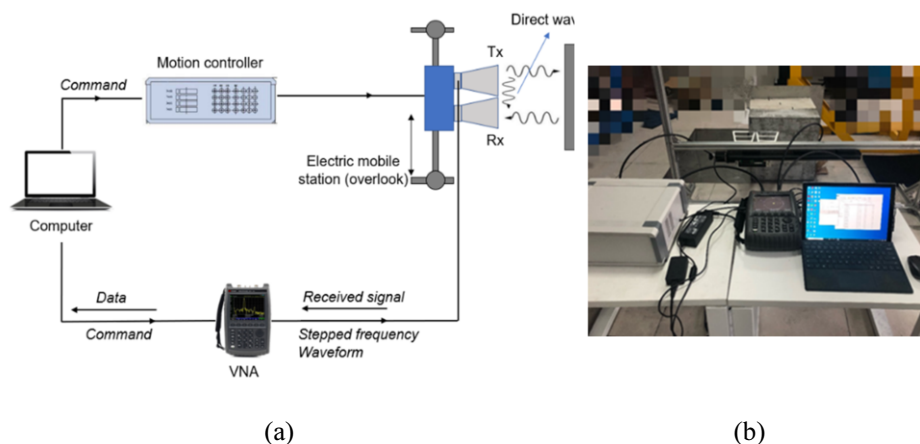
Figure 3. Schematic diagram (a) and photograph (b) of the SFCW system

4.1. Working principals of SFCW radar

The basic principles of SFCW radar systems are similar to FMCW except that the frequency changes in discrete steps rather than continuously. The step waveform is generated digitally and then converted to an analog signal that is high pass filtered and then drives a voltage-controlled oscillator (VCO). This results in the stepped frequency waveform $f_1(t)$ with an angular velocity of $\omega_0 + (\Delta\omega)N$, where ω_0 is the initial angular velocity, $\Delta\omega$ is the discrete angular frequency increment and N is the step number. The signal is then split into the transmitted signal (which is amplified and fed into the transmitting antenna) and $f_2(t)$ that is input to a mixer in the receiver segment.

The received signal is amplified and fed into a mixer. The amplified received signal $f_3(t)$ is mixed with $f_2(t)$ and the result is low pass filtered to yield the intermediate angular frequency $\omega_3 - \omega_2$. This signal is then digitized, which gives the frequency domain response.

4.2. Signal processing

The Vector Network Analyzer (VNA) based GPR system relies on the S parameters of the VNA to obtain the frequency response of the detected system. For the bi-static antenna configuration, the return loss $S_{21}(f)$ is collected. After analyzing the response, the characteristic information of the detection target is finally obtained. The following diagram illustrates the methodology we employ to acquire the time domain wave field from the raw data.
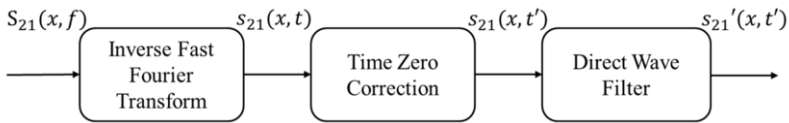
Figure 4. Block diagram of the signal processing procedure

First, the Inverse Fast Fourier Transform (IFFT) is used to transform the system response from the frequency domain $S_{21}(x, f)$ to the time domain $s_{21}(x, t)$. For digitized N points signal $S_{21}(N)$ in the frequency domain, the inverse discrete Fourier transform (IDFT) formula can be given by

$$s_{21}(n) = \frac{1}{N}\sum_{k=0}^{N-1} S_{21k}e^{i2\pi kn/N} \quad n = 0, \dots, N-1 \tag{3}$$

where $s_{21}(n)$ is the discrete signal in the time domain, plotting an A-scan at one scanning step. The set of A-scans forms a 2D B-scan image, with respect to the distance and the propagation time. Second, the distance between the centers of the two antennas is measured to be d=16.5cm. The propagation time of the direct wave from the transmitter to the receiver is calculated by t_0=d/c=0.55ns, where $c = 3 \times 10^8$ m/s is the wave's velocity in the air. So, the true time zero of the B-scan should be 0.55ns before the arrival of the direct wave. Last, the direct wave is filtered using a rectangular window to improve the image quality of the IFFT data.

4.3. Laboratory measurement

An experimental setup was designed in the lab, as shown in Figure 5(a). Concrete2

represents the concrete sample of track slab, fabricated with the C50 concrete (based on China's national standard GB50010-2010), with a dimension of $20 \times 50 \times 50 cm^3$. Concrete3 represents the sample of the support plate, fabricated with C15 concrete, with a dimension of $30 \times 50 \times 50 cm^3$, containing 3 artificial cracks of $0.5 \times 5 cm^2$ at different depths. Regarding crack2 as the scanning center, the antennas move simultaneously from the right to the left to obtain the frequency response S_{21} for each 1cm step, with X_{max}=40cm. The other experimental parameters are given in Table 2.

The generated B-scan in the time domain is shown in Figure 5(b). From this figure, the reflections from different interfaces are observed: interface1 between the air and the concrete, interface2 between the concrete2 and concrete3, steel plate of the bottom. Also, the scattering signals from the cracks can be found, as indicated in the figure. However, some unwanted noise is also recorded. It is caused by the heterogeneity of the concrete and the ringing noise between the antennas and the instrument.
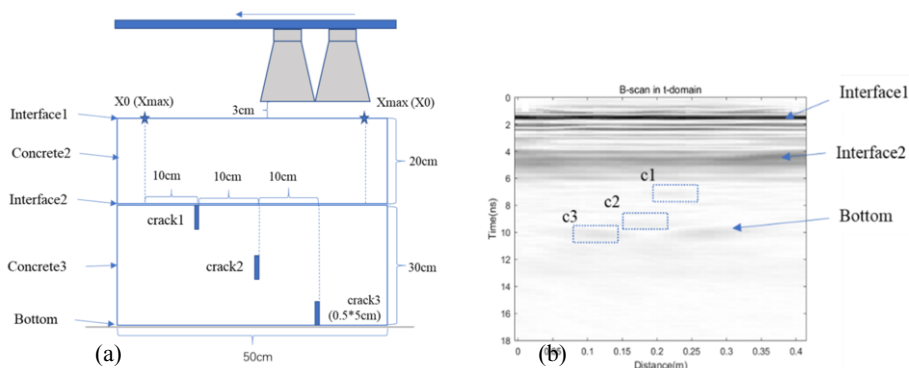
Figure 5. Experimental setup for cracks of different depths in concrete (a) and its generated B-scan (b)

Table 2. Experimental parameters

Component	Parameter	Definition
Antennas	Type	Brotex 1-4GHz horn
	Tx-Rx distance	16.5cm
VNA (N9913A)	Frequency range	1-4GHz
	Sampling points	201
	Required signal	$S_{21}(x, f)$
Motion controller	Step size	1cm
	Scanning distance	Xmax

5. Conclusions

This paper presents a brief review of GPR systems and the state-of-the-art of GPR applications on ballastless railways. The experimental results show that the proposed system can detect all the narrow cracks in the depth up to 50cm in the sample. More quantitative non-destructive evaluation of ballastless railways and optimization of the instrumental system will be undertaken in the future.

Acknowledgment

References

[1] W. Shao, A. Bouzerdoum, S. L. Phung, et al., Automatic classification of ground-penetrating-radar signals for railway-ballast assessment, *IEEE Transactions on Geoscience & Remote Sensing*, **10** (2011), 3961-3972.

[2] K. Ando, M. Sunaga, H. Aoki, O. Haga, Development of slab tracks for hokuriku shinkansen line, *Quarterly Report of RTRI*, **1** (2001), 35-41.

[3] Xinhuanet, China's high-speed rail will reach 39,000 kilometers by the end of 2020, **5** (2020). http://www.xinhuanet.com/2020-05/19/c_1126004736.htm

[4] C. Esveld. Recently developments in slab track, *European Railway Review*, **2** (2003), 81-85.

[5] Britpave, Infrastructure group calls for whole life concrete slab track solution, *Global Railway Review*, **10** (2016).

[6] X. Liu, P. Zhao, F. Dai, Advances in design theories of high-speed railway ballastless tracks, *Journal of Modern Transportation*, **3** (2011), 154-162.

[7] J. Hugenschmidt, Railway track inspection using GPR, *Journal of Applied Geophysics*, **2** (2000), 147-155.

[8] I. Al-Qadi, W. Xie, R. Roberts, Optimization of antenna configuration in multiple-frequency ground penetrating radar system for railroad substructure assessment, *NDT and E International*, **43** (2010), 20–28.

[9] X. Xiao, *Détermination de Gradients de Teneur en Eau dans les Bétons par Méthodes Électromagnétiques*, University of Nantes, France, 2015.

[10] W. W. L. Lai, X. Dérobert, P. Annan, A review of ground penetrating radar application in civil engineering: a 30-year journey from locating and testing to imaging and diagnosis, *NDT and E International*, **96** (2018), 58–78.

[11] S. Lahouar, and I. Al-Qadi, Automatic detection of multiple pavement layers from GPR data, *NDT& E International*, **41** (2008), 69-81.

[12] Y. Zan, Z. Li, G. Su and X. Zhang, An innovative vehicle-mounted GPR technique for fast and efficient monitoring of tunnel lining structural conditions, *Case Studies in Nondestructive Testing & Evaluation, Part A*, **6** (2016), 63-69.

[13] Association Française de Génie Civil (AFGC), *Concrete Design for A Given Structure Service Life: Durability Management with Regard to Reinforcement Corrosion and Alkali-Silica Reaction*, Paris, 2007.

[14] G. Villain, *Vers Une Évaluation des Indicateurs de Durabilité du Béton pour le Suivi de Ses Dégradations en Laboratoire et sur Ouvrage*, Ifsttar, Bouguenais, France, 2012. (*in French*)

[15] Z. Zeng, X. He, X. Meng and K. Zhu, Experimental study on mechanical characteristics of CRTSIII slab ballastless track under train load, *International Conference on Architectural, Civil and Hydraulics Engineering (ICACHE 2015)*, Guangzhou, China, November, 2015.

[16] P. E. Gautier, Slab track: Review of existing systems and optimization potentials including very high speed, *Construction and Building Materials*, **92** (2015), 9-15.

[17] H. Wang, A. Che, S. Feng, et al., Full waveform inversion applied in defect investigation for ballastless undertrack structure of high-speed railway, *Tunnelling & Underground Space Technology*, **51** (2016), 202-211.

[18] C. Colla, M. Krause, Ch, Maierhofer et al., Combination of NDT techniques for site investigation of non-ballasted railway tracks, *NDT & E International*, **35** (2002), 95-105.

[19] A. Gardei, K. Mittag, H. Wiggenhauser, B. Riple, M. Jovanovic: Inspection of concrete-embedded tracks process development for the quality assurance of concrete-embedded tracks using non-destructive testing methods. *Non-destructive Testing in Civil Engineering*, 2003.

[20] J. Li, Ground penetrating radar detection of voids and gaps at the bottom of support plate of high-speed railway ballastless track, *Road and Bridge Technology*, **18** (2015), 224-225. (*in Chinese*)

[21] S. Fontul, E. Fortunato, F. De Chiara et al., Railways track characterization using ground penetrating radar, *Procedia Engineering*, **143** (2016), 1193-1200.

[22] L. Pajewski, S. Fontul, M. Solla, Chapter 10 - Ground-penetrating radar for the evaluation and monitoring of transport infrastructures, *Innovation in Near-Surface Geophysics*, Elsevier, (2019), 341-398.

[23] A. Kalogeropoulos, J. van der Kruk, J. Hugenschmidt, et al., Full-waveform GPR inversion to assess chloride gradients in concrete, *NDT & E International*, **57** (2013), 74-84.

[24] X. Xiao, B. Guan, A. Ihamouten, et al., Monitoring water transfers in limestone building materials with water retention curve and ground penetrating radar: a comparative study, *NDT & E International*, **100** (2018),31-39.

[25] S. S. Todkar, C. Le Bastarda, V. Baltazart et al., Performance assessment of SVM-based classification techniques for the detection of artificial debondings within pavement structures from stepped-frequency A-scan radar data, *NDT & E International*, **107** (2019), 102128.

[26] X. Dérobert, C. Fauchard, Ph. Côte et al., Step-frequency radar applied on thin road layers, *Journal of Applied Geophysics*, **47** (2001), 317-325.

[27] Z. Khakiev, V. Shapovalov, A. Kruglikov, V. Yavna, GPR determination of physical parameters of railway structural layers, *Journal of Applied Geophysics*, **106** (2014), 139-145.

Instrumental Configuration of Electromagnetic Thermography and Optical Thermography

Haoran Li[a], Yuming Zhang[a], Shunyao Wu[a], Bin Gao[a,1], Guiyun Tian[b], Yang Yang[c], Yongjie Yu[c]

[a] *School of Automation Engineering, University of Electronic Science and Technology of China, China*
[b] *School of Engineering, Newcastle University, UK*
[c] *Chengdu aircraft industry Co., Ltd.*

Abstract. Electromagnetic thermography and optical thermography are both important non-destructive testing (NDT) methods that have been widely used in the fields of modern aerospace, renewable energy, nuclear industry, etc. The excitation modes are crucial whose performances have a decisive effect on the detection results. Previous studies mainly focused on the physics mechanism, applications, and signal processing algorithms. However, the instrument configuration is rarely presented. This paper is to introduces the recently designed excitation sources of electromagnetic thermography and optical thermography detection systems, respectively. These instruments involved L-shaped and Shuttle-shaped sensor structures for electromagnetic thermography and multi-modes excitation for optical thermography. Besides, the topologies and operating principles are shown in detail. Experimental results are carried out to verify the practicability and reliability of the proposed systems.

Keywords. Electromagnetic thermography, optical thermography, excitation system, non-destructive testing (NDT)

1. Introduction

Thermography instruments and modes have been widely used in the sensing and detection fields as a part of the system, such as laser detection [1], electromagnetic thermography testing [2], ultrasound inspection [3], plasma detection [4] and optical thermography testing [5]. In particular, there are many commercial products in electromagnetic thermography field such as EASYHEAT series produced from Ameritherm, automatic eddy current thermography system designed by Starmans [6], integrated system of eddy current and eddy current thermography developed by Laval University [7] and automatic inspection system developed by Siemens for motor components [8]. In addition, Thermal Wave Imaging (TWI) has developed an optical thermography system for NDT since different excitation modes are integrated. This paper particularly interprets the instrumental configuration for electromagnetic thermography and optical thermography systems to enhance the quality of NDT.

---

[1] Corresponding Author: Bin Gao, E-mail: bin_gao@uestc.edu.cn.

2. Instrument configuration and detection results of the thermography NDT systems

2.1. Configuration and detection results of electromagnetic thermography system

1) Configuration

The electromagnetic thermography excitation system [9] is composed of an inductive heating device, a synchronizer trigger, a working head and an excitation magnet yoke. Especially, according to different application scenarios, the shape of the magnet yoke can be selected as L-Shaped [10] or Shuttle-shaped [11]. Both of them have good performance in natural micro-crack detection applications.

Figure 1 shows the diagram of the electromagnetic thermography system. When the control device generates a signal to activate the system, high-frequency pulsed current flows through the helix coil and generates an alternating magnetic field. The ferrite core collects the magnetic flux and the flux is transmitted to the sample between the two poles of the core through a magnetic circuit. These include ferrite core, the air gap and the sample. If a defect exists in the conductive material, the distribution of the magnetic field, the eddy current intensity, and the process of thermal diffusion will be affected. Consequently, the transient time-spatial characteristics of radiative heat transfer modes over the plate surface can be captured by an infrared camera.
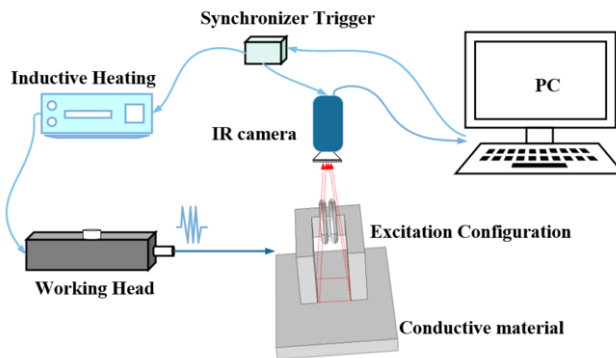
Figure 1. Diagram of the electromagnetic thermography system

Figure 2 presents the experimental system. As shown in Figure 2, the inductive heating device can be further divided into a full-bridge LC resonant circuit, an FPGA control board, a high-power DC power supply, and an auxiliary power supply. The topology of the full-bridge LC resonant circuit is shown in Figure 3. S_1-S_4 are four power MOSFETs, V_s is the voltage provided by DC power supply and its value is adjustable from 0-60 V.
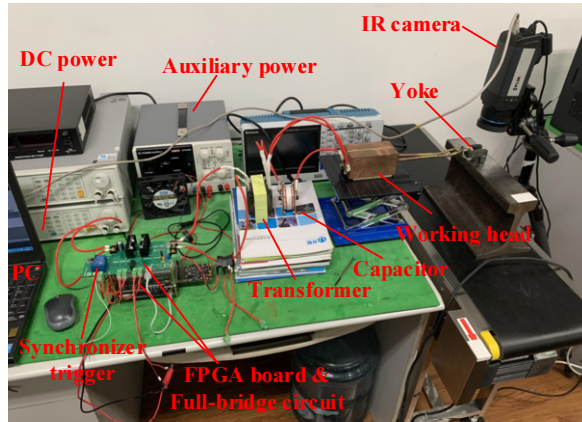
Figure 2. Experimental system
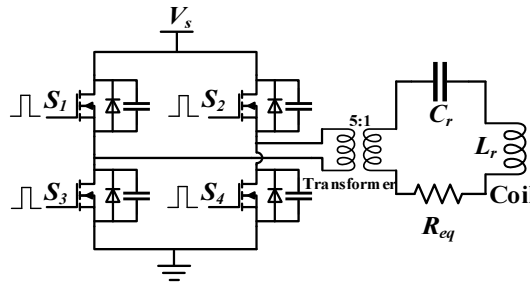
Figure 3. The topology of the full-bridge LC resonant circuit

In addition, R_{eq} denotes the equivalent resistance of the circuit, it is typically ranged from several dozen to several hundred mΩ. C_r denotes the resonant capacitor and the value is 0.4 µF. L_r denotes the resonant inductance and the value is 1 µH. The turns ratio of the transformer is 5:1. When the circuit works at the resonant state, the current flowing through the excitation coil reaches a peak value, and the magnetic field generated by the coil is the strongest. The resonant frequency of the series resonant circuit f_r can be described as:

$$f_r = \frac{1}{2\pi\sqrt{L_r C_r}} \tag{1}$$

The working logic of the excitation system can be summarized as follows: Firstly, the FPGA is programmed as the drive frequency sweep from 300 kHz-50 kHz and acquire the secondary current of the transformer during this process. Secondly, if this current value is greater than a set threshold, it means that the frequency is close to the resonant frequency and mark this value. Finally, the FPGA will stop sweeping and output at the marked frequency. Thus, the system will find the resonant frequency automatically and generate the maximum output power which is important to inspection. At this working state, the maximum peak-to-peak value of output current is ±180 A which is suitable for electromagnetic thermography testing.

2)   Detection results

The verification experiments are performed by using the proposed excitation configuration model with L-shaped and Shuttle-shaped yoke respectively to detect natural microcracks on different samples. The excitation current is set to 180 A and frequency is matched on 220 kHz. Thermal images are captured by the infrared camera as shown in Figure 4 and Figure 5, respectively. It can be seen that the multiple natural cracks in complex geometry can be visualized effectively.
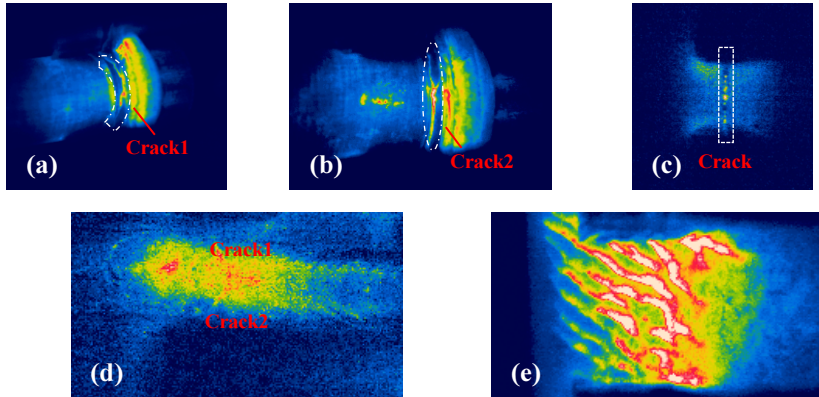
Figure 4. Detection results of (a)(b) screw (c) stainless steel plate (d) weld crack and (e) RCFs by using L-shaped yoke
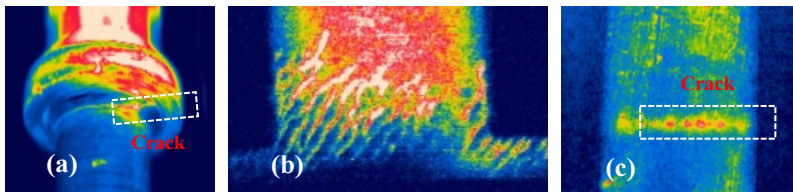
Figure 5. Detection results of (a) screw (b) RCFs (c) stainless steel plate by using Shuttle-shaped yoke

2.2. Configuration and detection results of potable optical thermography system

1)   Configuration

Carbon fiber reinforced polymer (CFRP) has become an indispensable structural material in the aircraft manufacturing industry. However, quality issues in CFRP may be caused by cyclic stress, impact damages and any other anomaly buried within the composite structure. Defects associated with composite materials will lead to a significant reduction of the load capacity and degradation of mechanical properties. Therefore, it is necessary to conduct a reliable nondestructive testing analysis to guarantee safety.

To meet this demand, Portable Optical Pulsed Thermography (POPT) system is designed for defect detection in carbon fiber reinforced composite in reflection mode, using halogen lamps as an excitation source. As shown in Figure 6(a), it includes an excitation source and a CPU, a display screen, six halogen lamps with a power of 900 W, an IR camera, and a grip. The temperature sensitivity is 0.06°C, and the maximum resolution is 288×384. Figure 6(b) illustrates the new configuration of human-computer interaction interface which is developed using C#.
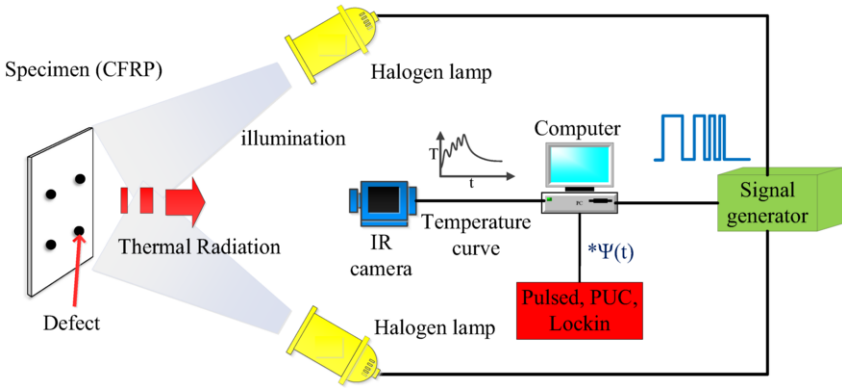
(a) Diagram of the POPT system
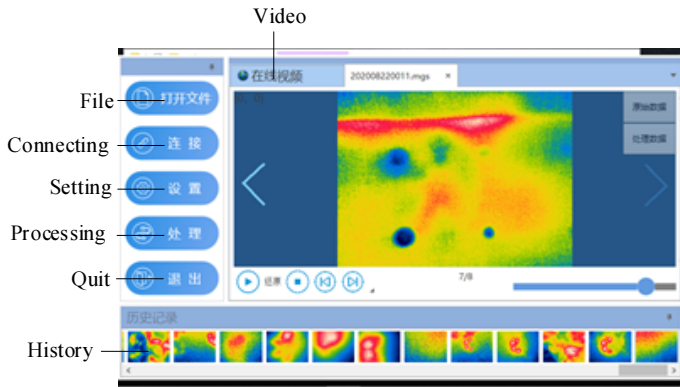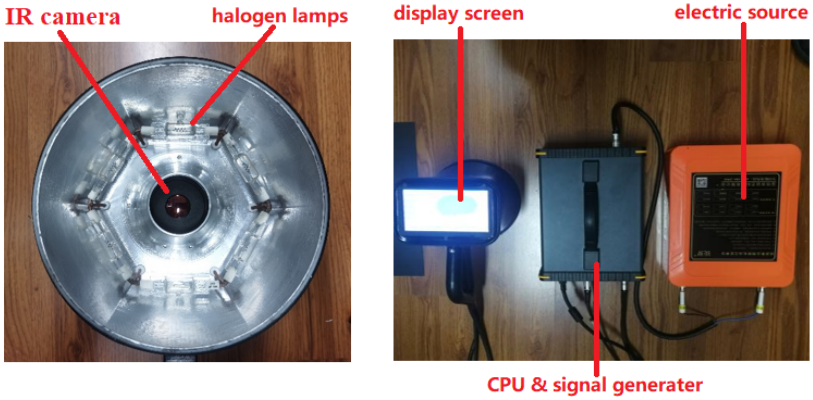
(b) The physical picture of POPT system

Figure 6. The components and structure of the POPT system

After setting the parameters on the touch screen, the excitation source sends signals to the halogen lamps, and the IR camera records the heating and cooling stages of the specimen, which are stored in the form of video and processed by the tensor decomposition [12] algorithms and deep learning methods.

2) Detection results

The detection results of carbon fiber board with buried defects are shown in Figure 7, which provides the evidence of the reliability of the POPT system. Large curvature surface can be captured and detected. More quantitative analysis and comparison can be found in [13]. It should be noted that in these experiments long pulse excitation is chosen and the heating time is set to 3 s. Furthermore, the excitation power is 900 W and the cooling time is 3-4 s.
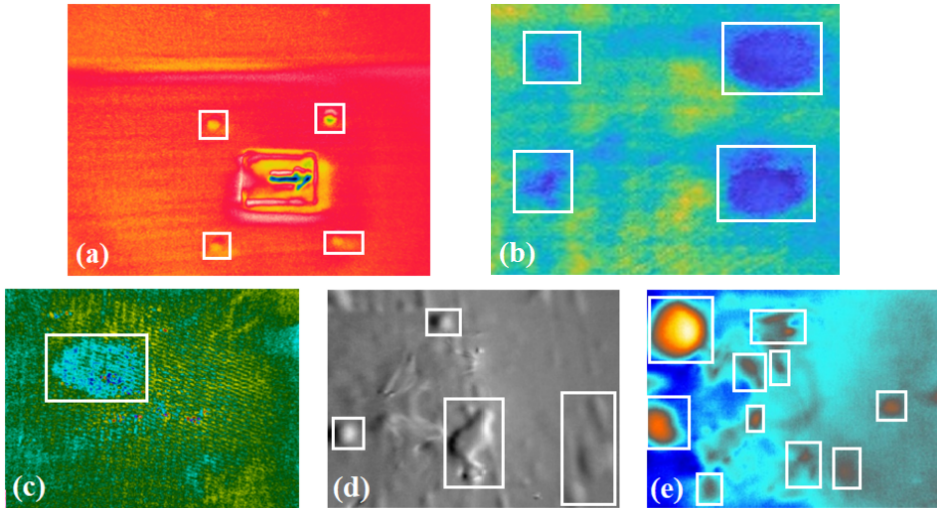
Figure 7. Detection results of artificial defects (a) (b) delamination （b） bubble (c) and debonding (d)&(e)

3. Conclusion

This paper presents the instrumental configuration of two modes of thermography NDT system. The natural micro-cracks on different samples can be detected obviously through the electromagnetic thermography excitation system. In addition, the POPT system can effectively separate the defect information from thermal diagrams by using the tensor decomposition method [14]. Both of the two systems have the advantage of small volume which means they have the potential to be portable and more conducive to non-laboratory condition testing. However, it is still a challenge for these systems to distinguish all the defects especially in some irregular shape components.

4. Acknowledgement

References

[1] Asher S A. "Some Important Considerations in the Selection of a Tunable UV Laser Excitation Source, " *Applied Spectroscopy*, **vol. 38**(2), pp. 276-278, Mar 1984.

[2] Sfarra, Stefano, et al. "Quantitative Infrared Thermography (IRT) and Holographic Interferometry (HI): Nondestructive Testing (NDT) for Defects Detection in the Silicate Ceramics Industry." *Advances in Science & Technology*, **vol. 68**, pp. 102-107, Oct 2010.

[3] Poelzleitner, Wolfgang. "Ultrasound lock-in thermography: feasibilies and limitations," *Proc Spie*, **vol. 3827**, pp. 10-15, Sep 1999.

[4] Abdallah M H, Coulombe S, Mermet J M, et al. "An assessment of an atmospheric pressure helium microwave plasma produced by a surfatron as an excitation source in atomic emission spectroscopy," *Spectrochimica Acta Part B Atomic Spectroscopy*, **vol. 37**(7), pp. 583-592. 1982.

[5] Y. Zhu et al., "Nondestructive Testing for Multi-Layer Metal-Metal Bonded Structure by Using Inductive Lock-In Thermograhy," *IEEE Sensors Journal*, **vol. 17**, no. 20, pp. 6716-6723, 15 Oct.15, 2017, doi: 10.1109/JSEN.2017.2741581.

[6] Staeman S, Matz V. "Automated System for Crack Detection Using Infrared Thermographic Testing." *In 17th World Conference on Nondestructive Testing.* **Shanghai: 2008**.

[7] Grenier M, et al. "Development of a hybrid non-destructive inspection system combining induction thermography and eddy current techniques." *In 10th international conference on quantitative infrared thermography.* **Quebec: 2010**.

[8] Goldammer M, et al. "Automated Induction Thermography of Generator Components." *AIP Conference Proceedings,* **1211**(2010):451-457.

[9] H. Li, et al., "Multiphysics Structured Eddy Current and Thermography Defects Diagnostics System in Moving Mode," *IEEE Transactions on Industrial Informatics*, doi: 10.1109/TII.2020.2997836.

[10] Z. Liu, B. Gao and G. Y. Tian, "Natural Crack Diagnosis System Based on Novel L-Shaped Electromagnetic Sensing Thermography," *IEEE Transactions on Industrial Electronics*, **vol. 67**, no. 11, pp. 9703-9714, Nov. 2020, doi: 10.1109/TIE.2019.2952782.

[11] X. Li, B. Gao, Z. Liu and G. Y. Tian, "Microcracks Detection Based on Shuttle-shaped Electromagnetic Thermography," *IEEE Sensors Journal*, doi: 10.1109/JSEN.2020.3001305.

[12] L. Liu, et al., "Structured Iterative Alternating Sparse Matrix Decomposition for Thermal Imaging Diagnostic System," *Infrared Physics and Technology*, **vol. 107**, no. 2020, pp. 1-14, Apr 2020.

[13] Z. Wang, J. Zhu, G. Y. Tian and F. Ciampa, "Comparative analysis of eddy current pulsed thermography and long pulse thermography for damage detection in metals and composites," *NDT & E International* **vol. 107**, 102155, 2019.

[14] J. Ahmed, B. Gao, W. L. Woo and Y. Zhu, "Ensemble Joint Sparse Low Rank Matrix Decomposition for Thermography Diagnosis System," *IEEE Transactions on Industrial Electronics*, doi: 10.1109/TIE.2020.2975484.

Subject Index

Author Index